U.S. DEPARTMENT OF COMMERCE
National Institute of Standards and Technology
(Formerly National Bureau of Standards)
National Engineering Laboratory
Center for Building Technology
Gaithersburg, MD 20899

NISTIR 88-4007

Punching Shear Resistance of Lightweight Concrete Offshore Structures for the Arctic: Results of Experimental Study

Long T. Phan and H. S. Lew

November 1988

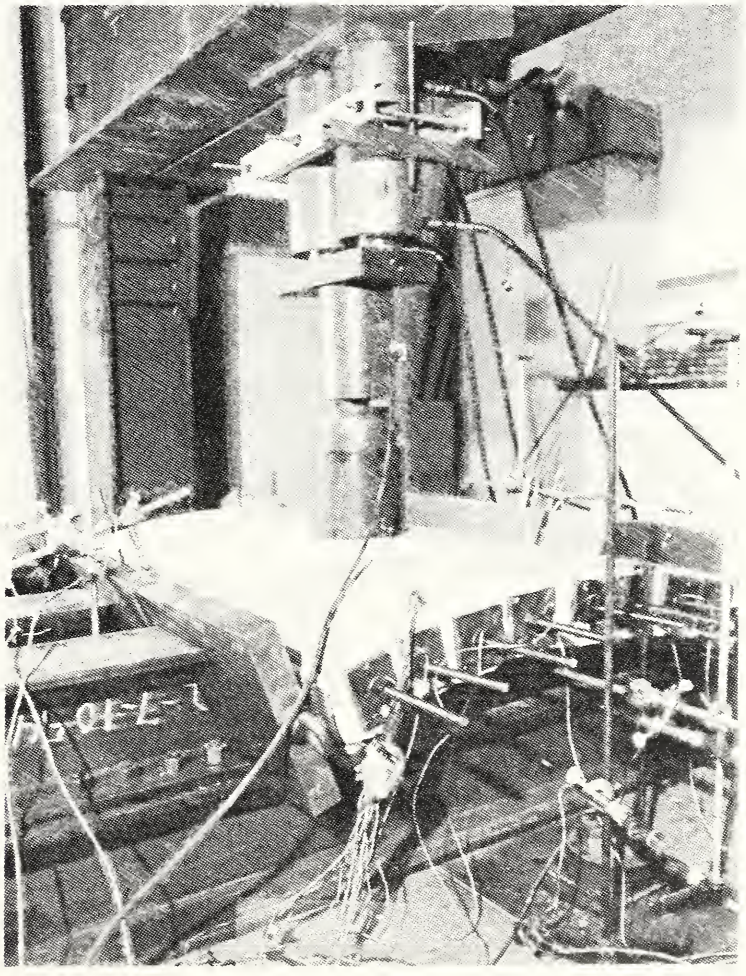

Sponsored by:
Technology Assessment and Research Branch
Mineral Management Service
U.S. Department of the Interior
Reston, Virginia 22091

NISTIR 88-4007

Punching Shear Resistance of Lightweight Concrete Offshore Structures for the Arctic: Results of Experimental Study

Long T. Phan and H. S. Lew

U.S. DEPARTMENT OF COMMERCE
National Institute of Standards and Technology
(Formerly National Bureau of Standards)
National Engineering Laboratory
Center for Building Technology
Gaithersburg, MD 20899

November 1988

National Bureau of Standards became the National Institute of Standards and Technology on August 23, 1988, when the Omnibus Trade and Competitiveness Act was signed. NIST retains all NBS functions. Its new programs will encourage improved use of technology by U.S. industry.

Sponsored by:
Technology Assessment and Research Branch
Mineral Management Service
U.S. Department of the Interior
Reston, Virginia 22091

U.S. DEPARTMENT OF COMMERCE
C. William Verity, Secretary

NATIONAL INSTITUTE OF STANDARDS
AND TECHNOLOGY
Ernest Ambler, Director

ABSTRACT

This report presents the results of the experimental investigation on punching shear behavior of heavily reinforced, thick, lightweight concrete plates and shells. Eighteen concrete plate and shell specimens of 1/6- and 1/4-scale were tested. These were designed to represent typical panels of the perimeter walls of Arctic offshore structures. The specimens were subjected to high-intensity, concentrated load, applied at the center of each specimen. The results of tests indicated that shear reinforcement ratio (ρ_v) and curvature (R/t ratio) are the two most influencing factors affecting the punching shear strength and ductility of the specimens. Prestressing with uniform compressive prestress of 500 psi, either in one or two orthogonal directions, was found to have very little effect in terms of improving the punching shear capacity of the specimens. Further, unlike the plates where ultimate punching shear failures were preceded by yielding of shear reinforcement across the crack surfaces, the presence of curvature-induced membrane compression in shells resulted in brittle failure which was caused by crushing of concrete in the compression zone. More importantly, the test results showed that the current ACI Code provisions for punching shear are extremely conservative in predicting the punching shear strength of the specimens of this test program.

Keywords: Arctic offshore structures; experimental study; lightweight concrete; prestressing; punching shear; prototype; reinforced concrete; scale models.

EXECUTIVE SUMMARY

With the global depletion of known oil reserves in temperate climates, exploration for oil and gas in harsher climatic regions, including in the Arctic Ocean, have increased during the past decade. Design and construction of platform structures in such regions pose formidable challenges in that these structures must withstand extreme environmental conditions such as cold temperature, large wind and wave forces, and significant forces generated by moving ice.

To protect against the impact of moving ice, Arctic offshore platform structures are commonly constructed with a strong exterior wall. The wall must resist both global ice forces on the structure and local concentrated loads produced by impacting of ice floes which could raise local contact pressures in excess of 2000 psi (14 MPa).

In order to overcome a short construction period in the Arctic, drilling platforms are commonly built in temperate climates such as in the Pacific Northwest, then towed through the Bering Sea and into the Arctic Ocean. High strength lightweight concrete has been considered to be one of the better materials for this type of construction since it provides improved buoyancy and resistance to ice abrasion and freeze and thaw attacks.

This report presents the results of two series of experimental studies on the punching shear behavior of heavily reinforced lightweight concrete plates and shells. The first series consisted of plates and shells of 1/6-scale model wall sections, and the second series consisted of plates of 1/4-scale. A total of fifteen 1/6-scale specimens, including nine plates and six shells, and three 1/4-scale plates were tested.

In selecting the prototype sections of the exterior ice wall, linear elastic computer analyses were carried out to match the boundary conditions in the actual structure. Two different scales for physical modelling were selected to examine the influence of scale factor on the experimental results.

Lightweight concretes with densities of 120 - 125 lb/cu.ft (1920 - 2000 kg/cu.m) were produced using North Carolina Solite, condensed silica fume, superplasticizer, and air-entraining agent. The compressive strength of concrete at the time of testing ranged from 6000 - 9300 psi (41 -64 MPa). Flexural reinforcement consisted of ASTM Grade 60 steel which had a mean yield strength of 60 ksi (414 MPa). Special T-headed stirrups were used as shear reinforcement with a mean yield strength of 52 ksi (359 MPa).

Several 1/6-scale specimens were post-tensioned to produce an in-plane stress of 500 psi (3.5 MPa) in addition to the provision of shear reinforcement. The purpose of the prestressing was to examine its effects on the resistance to punching shear and the associated modes of failure. One plate specimen was post-tensioned in a single direction, one plate

specimen in two othogonal directions, and one shell specimen in a single direction.

In general, the plate and shell specimens failed in two distinct modes. The plate specimens mobilized all three post-cracking shear resistance mechanisms: namely, (1) axial resistance provided by shear reinforcement; (2) interface aggregate interlock; and (3) dowel action. Because final failure was brought about by yielding and fracture of shear reinforcement, the test specimens failed in a gradual manner. On the other hand, because of the presence of membrane compression associated with the curvature of the shell, the shell specimens failed in a shear-compression mode, and collapsed suddenly due to crushing of concrete in the compression zone.

Test results indicated that the punching shear strength for plate specimens ranged between 1.4 to 3.1 times greater than the shear strength predicted by the ACI code, while that for shell specimens exceed the ACI code predicted values by a factor between 3 to 4.9. These results clearly indicate that the ACI code provisions for punching shear are excessively conservative.

The upper limit of shear strength, as specified in ACI code 11.11.3.2, is not appropriate for the types of wall sections tested in this program, since all specimens with shear reinforcement showed much higher punching shear capacities.

The results of the prestressed specimens tested were inconclusive: an in-plane prestress of 500 psi (3.4 MPa) contributed very little to improve the punching shear capacity of the specimens tested.

ACKNOWLEDGEMENTS

The authors wish to acknowledge the valued technical guidance provided by the project advisory group. The members of the group comprised of representatives of the Minerals Management Service, U.S. Department of the Interior; Mobil Research and Development Corporation; Chevron Corporation; Standard Oil Company of Ohio; Exxon Production Research Company; and Shell Oil Company; and Professor Richard N. White of Cornell University; and Professor Thomas G. Harmaon of Washington University.

The authors would like to extend special appreciation to Mr. Charles E. Smith of the Minrasls Management Service and Dr. George C. Hoff for their continued support and encourgement throught the project.

Finally, we wish to thank Drs. William Stone and John Gross of the Center for Building Technology who reviewed and provided valuable comments for this report.

TABLE OF CONTENTS

LIST OF FIGURES

LIST OF FIGURES (Continued)

LIST OF FIGURES (Continued)

LIST OF FIGURES (Continued)

LIST OF FIGURES (Continued)

LIST OF FIGURES (Continued)

LIST OF FIGURES (Continued)

LIST OF TABLES

NOTATION

b_o	=	Perimeter of critical section for slabs and footings
b_w	=	Web width, or diameter of circular section
d	=	Distance from extreme compression fiber to centroid of longitudinal tension reinforcement
f'_c	=	Specified compressive strength of concrete
f_y	=	Specified yield strength of flexural and shear reinforcement
M_u	=	Factored moment at section
R	=	Radius of curvature
S_1	=	Geometric scale factor
t	=	Thickness
v_{cr}	=	Nominal shear cracking stress
v_{test}	=	Nominal ultimate shear stress
V_{cr}	=	Nominal shear strength at onset of shear cracking
V_c	=	Nominal shear strength of concrete
V_s	=	Nominal shear strength of reinforcement
V_n	=	Nominal punching shear strength
V_{test}	=	Nominal measured shear strength
V_u	=	Factored shear force at section
ρ_v	=	Shear reinforcement ratio

1. INTRODUCTION

1.1 BACKGROUND

Despite the harsh environmental conditions, the Arctic Ocean has been found to be a potentially great source of oil and natural gas. Tapping these reserves requires permanent drilling platforms that can be used both as living facilities and as temporary oil storage in year-round operations. In the past several years, many Arctic offshore structures have been built with structural configurations and construction materials substantially different from standard construction.

A typical Arctic offshore structure is usually surrounded by an exterior wall, also known as ice wall. The main purpose of this exterior wall is to protect the Arctic structure from the impact of moving sea ice. The exterior wall consists mainly of either flat plate or curved structural elements, stiffened by a system of bulkheads and thrust beams (Figure 2.1). These elements are usually built on-shore in temperate climates using lightweight concrete, and then transported by sea and assembled at installation sites in the Arctic Ocean. Concrete has been used extensively since it offers the durability and stability these structures need to withstand the extreme loading and environmental conditions.

In addition to the normal loading conditions such as static and cyclic loading due to current, waves, and wind forces, Arctic structures may also be subjected to concentrated impact loads due to ship collisions and/or local ice impacts. While ship collisions might be rare, local ice impacts, with pressures of up to 2500 psi (17 MPa, ACI Committee 347, 1984), are common for these types of structures. The exterior walls of these structures must be designed to resist not only the extremely large global ice forces exerted on them by moving sea ice, but, also the high local ice pressure so that sudden punching shear failure can be prevented. The requirement for adequate punching shear resistance usually produces concrete structures with very large thickness and large amount of

reinforcement if the provisions pertaining to punching shear resistance in the existing ACI building code are to be followed.

Incomplete understanding, due to lack of technical information, on the behavior of concrete structures of this type subjected to high intensity concentrated load currently hinders the development of safe and economical design guidelines for Arctic offshore structures. To satisfy this need, an experimental investigation into the punching shear behavior of physical models of real Arctic structures was conducted by the National Institute of Standards and Technology (formerly National Bureau of Standards) on behalf of the Minerals Management Service of the U.S. Department of the Interior and the following five oil companies:

- Chevron Oil Company;
- Exxon Company, U.S.A.;
- Mobil Corporation;
- Shell Oil Company; and
- Standard Oil Company of Ohio.

The results of this experimental investigation are presented in this report.

1.2 OBJECTIVES AND SCOPE OF RESEARCH

The experimental program included physical model tests of two series of concrete specimens representative of typical Arctic offshore structures. The first series consisted of both plate and shell specimens of 1/6-scale. The second series consisted of only plate specimens of 1/4-scale. The main objectives of this study were:

1. To investigate experimentally the punching shear behavior of thick, heavily reinforced, lightweight concrete plates and shells, and to quantitatively study the influence of several key parameters on the punching shear performance of these structures.

2. To examine the applicability of the provisions of the current ACI Code pertaining to the punching shear behavior of structures with large thickness, high percentage of reinforcement, and curvature. This examination is necessary since the Code provisions were derived from tests conducted on thin and lightly reinforced sections.

1.3 ORGANIZATION OF THE REPORT

This report is organized in 6 chapters:

Chapter 2 describes the rationale used in the selection of the geometry, materials, dimensions, and boundary conditions for the prototypes and the scaled specimens. The overall test program and the instrumentation are also introduced in this chapter.

Chapter 3 describes the behavior of each specimen with respect to its entire loading history.

Chapter 4 explains the mechanics of punching shear observed in this test program.

Chapter 5 examines the effect on punching shear of the 6 selected variables listed in chapter 2.

Chapter 6 summarizes the current ACI code provisions for punching shear, presents quantitative comparisons of the test results and the ACI predictions, and discusses the applicability of the current ACI code to punching shear prediction of heavily reinforced, lightweight concrete structures with configurations and dimensions similar to those of Arctic offshore structures.

Chapter 7 summarizes the findings in this investigation and presents conclusions and recommendation for future research.

2. PUNCHING SHEAR TESTING PROGRAM

2.1 INTRODUCTION

The NBS punching shear testing program consisted of two test series. The first series included fifteen 1/6-scale concrete plate and shell specimens. The second series included three 1/4-scale plate specimens. All specimens were designed to represent portions of typical concrete perimeter walls (or ice walls) of Arctic offshore structures. The program was designed to study the influence of the following variables on the punching shear behavior of concrete plates and shells:

1. Area of loading.
2. Shell radius-to-thickness ratio (R/t ratios).
3. Shear reinforcement ratio.
4. Effect of multiple span versus single span.
5. Prestressing.
6. Scale effect.

This chapter describes the rationale used in the selection of test parameters for this study. In the sections to follow, the selection of the following experimental factors are discussed:

1. Geometry, dimensions, and boundary conditions of the prototype structures and of the reduced-scale test specimens.
2. Scale factors and materials used for the test specimens.
3. Flexural and shear reinforcement ratios, and prestress force used in the specimens.
4. Area and method of loading.
5. Instrumentation, and data acquisition.

2.2 SELECTION OF PROTOTYPE STRUCTURES

The term "prototype structures" is used in this study to refer to typical portions of the Arctic ice walls that were isolated and scaled down for testing. These isolated portions of the ice walls, hereafter referred to as prototype structures, must have similar configurations and boundary conditions with the real walls to ensure behavioral similarity. More importantly, the dimensions of the prototype must be properly selected so that the punching shear behavior in the real ice walls can be adequately captured by testing the scaled models of these prototypes. The selection of geometries, dimensions, and boundary conditions of the prototypes in this study were based on:

1. Typical dimensions and configurations of existing and proposed designs of Arctic offshore concrete structures (Figure 2.1), and
2. Results of linear elastic finite element analyses (reference 2.1).

2.2.1 GEOMETRY AND THICKNESS OF PROTOTYPES

a) Geometry

The exterior wall of an Arctic offshore structure is generally supported by a combination of vertical bulkheads and horizontal thrust beams to enhance its resistance to ice pressures (see Figure 2.1). The concrete segments between two adjacent vertical bulkheads are either flat plates or arched shells. To maintain similarity with real Arctic offshore structures, two typical configurations, flat plate and arched shell, were selected for the prototypes in this program. Two curvatures, corresponding to R/t ratios of 6 and 12, were selected for the shell prototypes to study the contribution of arch action to punching shear resistance in shells.

b) Thickness

Review of literature relevant to the design of Arctic offshore structures [references 2.2,2.6,2.8,2.9,2.10,2.11,2.12] indicates that the plate and shell concrete segments between the supporting bulkheads have typical thicknesses of 2 to 5 ft (0.6 to 1.5 m). This review also indicates a

typical spacing between two vertical bulkheads (or span length) of 15 to 25 ft (4.6 to 7.6 m), and a typical unsupported transverse wall length of at least 40 ft (12 m). Based on these typical dimensions, the thickness of a prototype plate in this study was selected to be 3.5 ft (1.07 m), and the thickness of a prototype shell was selected to be 2.5 ft (0.76 m).

2.2.2 SPAN LENGTH AND NUMBER OF SPANS FOR PLATE PROTOTYPE

a) Span Length

As has been indicated, the span length of a prototype is defined as the spacing between two adjacent vertical bulkheads of Arctic ice walls. This spacing ranges typically from 15 to 25 ft (4.6 to 7.6 m). A span length of 20 ft (6.0 m) was therefore selected for the plate prototype.

To adequately represent the behavior of the real ice walls under punching shear, both the continuity of the wall (multi-span structure) and the supporting bulkheads must be appropriately modeled. In the sections to follow, the selections of these experimental factors for the plate prototype are discussed.

b) Modeling of Suppporting Bulkheads

To select the support condition that best simulates the reaction in the supporting bulkheads, a unit width, five-span section of a flat plate ice wall with equal span lengths of 20 ft (6 m) was analyzed using the finite element technique for two cases:

- Case 1: Supporting bulkheads were modeled as actual members with realistic dimensions, and
- Case 2: Supporting bulkheads were idealized as pin supports.

A concentrated load was applied at the center of the middle span and distributions of bending moments along the five-span beams were plotted for both cases as shown in Figure 2.2. The comparison showed that the differences in moments between the two cases are insignificant (less than 3 percent). This indicated that the vertical supporting bulkheads of the

prototype plate can be adequately simulated in the laboratorty using pin supports.

c) Modeling Span Continuity

The number of spans needed for the prototype plate to sufficiently represent the continuity of a flat plate ice wall was also determined by linear elastic finite element analyses. In this analysis, a five-span plate with equal span lengths of 20 ft (6.0 m) was assumed to be large enough to represent the continuity of the ice wall. A uniform pressure was applied over a small area at the center of the middle span.

The analyses showed that lines of zero moment exist in the two spans adjacent to the middle span. These lines were located at 16 ft (5 m), or 0.8 times the span length (0.8 x 20 ft), away from the lines of support of the middle span. Based on this observation, a three-span plate was analyzed for the same loading and support conditions. The center span of the three-span plate was 20 ft (6 m) and the two outer spans were 16 ft (5 m). The distribution of span bending moments obtained from the three-span plate analysis was compared with that obtained from the five-span plate analysis. This comparison, shown in Figure 2.3, indicated that there is less than one percent difference in the distribution of bending moments for the two cases. Thus, a simply-supported, three-span plate of 20-ft (6-m) central span and 16-ft (5-m) end spans was considered as sufficient in representing the multi-span flat ice walls, and therefore was selected as the prototype plate in this study.

2.2.3 SPAN LENGTH AND NUMBER OF SPANS FOR ARCHED SHELL PROTOTYPE

A typical span length of 20 ft (6 m) was also selected for the shell prototype. Analyses similar to those performed for the flat plate were also carried out for the arched shell. In the analyses of the shells, the lateral stiffness provided by the supporting bulkheads had a significant influence on the distribution of moments and in-plane thrust in the loaded span of the arched wall. It is difficult to duplicate this influence in the laboratory unless supporting bulkheads with realistic dimensions are

modeled. In addition, unlike the flat plate, no simple set of boundary conditions could be prescribed for the prototype shell which could properly account for the multi-span nature in the horizontal direction of arched shell ice walls.

For these reasons, it was decided to study the arched shells using simple boundary conditions that could easily be established both experimentally and analytically. A pinned support, single span arched shell with a 20-ft (6-m) span length was therefore selected as the prototype shell in this study.

2.2.4 TRANSVERSE LENGTH

a) Transverse Length of Flat Plate Prototype

In this report, the term transverse length denotes the vertical dimension of the ice walls. This vertical dimension is either the distance between two horizontal thrust beams or the distance from the top to the bottom of a wall. An appropriate transverse length must be selected for the prototypes so that their punching shear behavior will be similar to the behavior of an Arctic ice wall under local, concentrated load. In this study, the transverse length of the prototypes was selected by the following procedure:

> A series of three-span plates having different transverse lengths were analyzed using the finite element techniques. All plates had the same thickness and span lengths as those selected for the prototypes. The transverse length of the plate in which bending moments converge to those calculated for a very large wall would be selected as transverse length of the plate prototype.

The results of the plate analyses are shown in Figure 2.4. It can be seen that a three-span plate having a transverse length (2L) of 28 ft (8.5 m) revealed only about a 3% difference in bending moments in the region local to the loaded area as compared to plates having transverse lengths of 40 ft or larger. This insignificant difference in moments indicates that a three-span plate with a transverse length of 28 ft (8.5 m) can be considered

sufficient to represent the very large dimension of a typical ice wall. The 28 ft (8.5 m) transverse length was therefore selected as the transverse length for all the flat plate prototypes.

b) Transverse Length of Arched Shell Prototype

The same criterion and procedure used in selecting the transverse length of the flat plate prototypes were used to select the transverse length of the shell prototypes. A series of single-span arched shells with different transverse lengths were analyzed and the results are shown in Figure 2.5. About 3% difference in bending moments in the vicinity of the loaded area can be observed for the shell of 28 ft (8.5 m) transverse length and the shell with infinite transverse length. Thus, the tranverse length of 28 ft (8.5 m) was also selected for all shell prototypes.

2.3 SELECTION OF REDUCED-SCALE TEST SPECIMENS

For practical reasons, it was decided that reduced-scale specimens would be tested in this program to predict the punching shear behavior of the larger structures. A reduced-scale specimen had the advantages of being less costly to fabricate and test, and it did not require a large testing facility. In the following sections, selections of scale factors and materials for the reduced-scale specimens are discussed.

2.3.1 SCALE FACTORS AND DIMENSION OF TEST SPECIMENS

In modeling, the reduced-scale specimen is related to the larger scale prototype by a set of similitude requirements. These requirements, if satisfied, allow a direct extrapolation of the behavior of the reduced-scale specimen to the prototype structure. The set of similitude requirements governing the modeling of a reinforced concrete structure is given in References 2.3 and 2.4 and is reproduced in Table 2.1.

It may be seen from Table 2.1 that the similitude requirements for a reinforced concrete model are specified solely by the geometric scale factor S_1, provided the stress-strain relationship of model concrete and its

elastic modulus are identical with those of the real structure. The choice of this geometric scale factor is governed by such factors as the loading capacity of the testing facilities, the practical dimensional limitations, and the cost of testing. Taking the above factors into consideration, two geometric scale factors S_1 of 6 and 4 were selected for this experimental study, with the majority of the test specimens having a scale factor of 6. The overall dimensions of the 1/6 and 1/4-scale specimens were obtained by directly scaling the prototype dimensions by the appropriate scale factor (either 6 or 4). The 1/6-scale three-span flat plate specimens thus had a uniform thickness of 7 in (18 cm), a 40-in (102-cm) center span and two 32-in (81-cm) end spans, and a transverse length of 56 in (142 cm). The 1/6-scale shell specimens had a uniform thickness of 5 in (13 cm), a span length of 40 in (102 cm), and a transverse length of 56 in (142 cm). And finally, the 1/4-scale three-span plate specimens had a uniform thickness of 10.5 in (27 cm), a 60-in (152-cm) central span and two 48-in (122-cm) adjacent spans, and a transverse length of 84 in (213 cm). Figure 2.6 shows the configurations, dimensions, and boundary conditions of the specimens in this experimental study.

2.3.2 CONCRETE MATERIALS

In this study, the concrete and the reinforcement used for the 1/6 and 1/4-scale specimens were selected to have the same properties as the materials used for Arctic offshore structures. Information obtained from literature on Arctic offshore structures [reference 2.2] shows that high-strength lightweight concrete is used extensively as the principle building material for these structures. Lightweight concrete is required for economic and practical reasons, and is achieved by using lightweight coarse aggregate with a typical nominal maximum aggregate size of 3/4 in (19 mm). The use of many additives, including condensed silica fume, high-range water reducing agents or "superplasticizers", and air-entraining agents, is also reported. These additives are used to improve both the workability of the concrete mix and the strength and durability of the offshore structures. Based on this information, the following materials were selected for concrete:

1. North Carolina Solite lightweight aggregate with a nominal maximum size of 1/2 in (13 mm).
2. Acceptable proportions of condensed silica fume (10 percent replacement of cement), superplasticizer, and air-entraining agent.

The typical concrete mix design used for all specimens is listed in Table 2.2. The mix design produced concrete with a compressive strength f'_c of at least 7,000 psi (48 MPa) and a mean density of 120-125 lb/cu.ft. This compressive strength was determined by testing 4x8 in (101x203 mm) cylinders according to recommendations of ACI Committee 444 [2.5].

2.3.3 FLEXURAL REINFORCEMENT

Available literature on the design of Arctic offshore structures indicates that flexural reinforcement ratios in these structures range from 1.5 to 2.5 percent [reference 2.6]. This ratio represents the amount of flexural reinforcement in one direction on one face of the cross-sectional area of each specimen. A previous experimental investigation on punching shear [reference 2.7] concluded that differences in punching shear strength due to varying amounts of flexural reinforcement in structures of this type is insignificant (an increase of 43% in flexural reinforcement caused only a 2% increase in punching shear strength). Therefore, flexural reinforcement was not considered as a variable in this study. Two flexural reinforcement ratios were selected for the 1/6 and 1/4-scale specimens: 1.75 percent and 2.5 percent. The high percentage of flexural reinforcement and the practical dimensions of the specimens dictated the use of #4 (0.5 in diameter) deformed reinforcing bars for the 1/6-scale plate specimens, #3 (3/8 in diameter) deformed bars for the 1/6-scale shell specimens, and #6 (0.75 in diameter) deformed bars for the 1/4-scale plate specimens. The bars were placed in groups of two in both directions of each layer of flexural reinforcement as shown in Figure 2.7. A mean yield strength of 60 ksi (414 MPa) was specified for these reinforcing bars.

2.3.4 SHEAR REINFORCEMENT

The contribution of shear reinforcement to punching shear resistance in offshore concrete structures is one of the variables examined in this study. No rational basis currently exists for the selection of shear reinforcement ratios in the design of Arctic offshore structures. Shear reinforcement ratios as high as 1 percent have been suggested. To study the contribution of shear reinforcement to punching shear resistance, three ratios of shear reinforcement were selected: 0, 0.22, and 0.44 percent. There is a trend in industry toward using mechanically-headed stirrups as shear reinforcement in Arctic offshore structures due to the congestion of reinforcement. To achieve similarity, T-headed bars, stamped out from steel plate, with a mean measured yield stress of 52 ksi (359 MPa) were selected for use as shear reinforcement in this study. The T-headed bars were anchored to the top and bottom layers of flexural reinforcement as shown in Figure 2.7. Dimensions of the T-headed bars are given in Figure 2.8.

2.3.5 PRESTRESSING

Most Arctic offshore structures, due to their large dimensions, are built segmentally. The concrete wall segments are usually assembled at the site and connected by post tensioning. Tensioning values ranging from 300 to 1000 psi (2 to 7 MPa) have been reported in the design of Arctic structures. The tensioning force, by creating a state of triaxial compression in the prestressed walls, is expected to have an effect on the punching shear behavior of the walls. Influence on punching shear of a prestressing force of 500 psi (3.5 MPa) in one and two directions for both plate and shell specimens was therefore selected for study in this experimental program.

Finely-threaded bars, 7/8 in (22 mm) in diameter, with a yield strength of 125 ksi (862 MPa) were used as post-tensioning tendons. These tendons were equally spaced across the concrete section to provide uniform distribution of 500 psi (3.5 MPa) compressive stress in the specimens. Tendons with a fine pitch of thread were selected to minimize prestressing losses due to

end anchorage slip, which otherwise can be significant due to the short length of the prestressing tendons.

Grouting of the post-tensioning ducts is usually performed in real Arctic structures to protect the post-tensioned tendons from being damaged by corrosion. However, it was believed that the absence of grout would not affect the punching shear strength of the post-tensioned structures. Therefore, to simplify the construction of the test specimens, the tendon ducts were not grouted in this study .

Prestress force in the tendons was applied sequentially and monitored using a strain gage mounted on each of the tendons. Sequential tensioning of the tendons helped reduce loss of prestress due to elastic shortening of concrete.

2.3.6 AREA OF LOADING & LOADING SYSTEM

a) Area of Loading

The size of the loaded area in this test program was selected based on the following two criteria:

1. The size of the loaded area should be selected such that the contact pressure for punching shear failure to occur in the test specimens is within the range of realistic local ice pressures. The upper limit of a realistic ice pressure acting on an Arctic structure is approximately 3500 psi (24 MPa).
2. The size of the loaded area should be selected so that a punching shear failure will occur prior to flexural failure in all test specimens.

A relationship between the applied punching shear pressure and the loaded area was developed for different values of nominal ultimate shear stress as shown in Figure 2.9. The ultimate shear stress was assumed to act on a critical section defined by the ACI Code. For a circular loaded area, the critical section is a circle with the perimeter, b_o, located a distance

equal to half of the effective depth, d, away from the perimeter of the loaded area [reference 6.1]. Figure 2.9 shows that the size of the loaded area is inversely proportional to the ultimate applied pressure, i.e. if the area of loading becomes smaller, the required pressure for a punching shear failure will increase. If the area of loading is too small, the pressure at punching shear failure will become unrealistically large. However, if the loaded area is made too large, flexural failure of the specimen will occur instead of a punching shear failure.

Results of other punching shear studies indicated that the nominal ultimate shear stress acting on the ACI critical section of reinforced concrete plates and shells with normal weight aggregate varied between $9\sqrt{f'_c}$ to $18\sqrt{f'_c}$. In order to satisfy the above stated criteria, a nominal shear strength of $15\sqrt{f'_c}$ was assumed for all specimens in this test program. This assumption is reasonable for lightweight concrete since the contribution of aggregate interlock in structures with this type of aggregate is anticipated to be less than that of a normal weight aggregate concrete structure. This assumed ultimate shear stress corresponds to a loaded area of 50 in^2 in the 1/6-scale specimens (see Figure 2.9).

For this experimental program, a circular loaded area of 50 in^2 was selected for the majority of the 1/6-scale specimens, with two 1/6-scale specimens and all 1/4-scale specimens were tested with a circular loaded area of 100 in^2.

b) Loading System

A loading system designed to provide a uniformly distributed pressure on a circular area was selected for use in this testing program (Figure 2.10). Load was applied through a solid steel piston contained in a steel cylinder. At the bottom of the steel piston, several layers of natural rubber and leather pads were placed. The rubber was used to simulate fluid behavior to impart a uniform pressure on the specimens. The leather pads were used to contain the rubber within the cylinder.

Molybdenum grease was applied on the inner surface of the steel cylinder to minimize friction between the piston and the cylinder. Calibration tests on the loading system showed that loss of applied load transmitted through the loading system due to friction was approximately 1 percent and therefore was considered negligible.

2.3.7 TESTING PROGRAM

The list of the specimens in this test program is presented in Table 2.3. The program consisted of fifteen 1/6-scale specimens and three 1/4-scale specimens. Of the 1/6-scale specimens, six were open cylindrical shells with two radius-to-thickness ratios (R/t of 6 and 12); the other specimens included eight three-span continuous flat plates and one single span flat plate (specimen FP1). Two of the three-span continuous plates (FP2-1 and IFP2-1) were duplicated to check the variability of test results. Of the three 1/4-scale specimens, two were duplicates of specimens FP2-1 and FP2-2 (named 4FP2-1 and 4FP2-2) and one was duplicate of specimen FP3 (named 4FP3). The specimens were different from each other either in configuration or properties. They were grouped as follows to facilitate the study of the influence on punching shear of the variables listed in section 2.1:

1.	Effect of area of loading:	Specimens FP2-1 and FP2-2 versus IFP2-1 and IFP2-2.
2.	Effect of radius-to-thickness ratio:	Specimens FP1 vs. AS7 vs. AS8; Specimens AS10 vs. AS12.
3.	Effect of shear reinforcement ratio:	Specimens FP2s vs. FP3 vs. FP4; Specimens AS9 vs. AS7 vs. AS11; Specimens FP7s vs FP8; Specimens 4FP2s vs. 4FP3.
4.	Effect of multiple span:	Specimens FP1 vs. FP3.

5. Effects of prestressing:

a) One way prestressing:	Specimens FP3 vs. FP5;
	Specimens AS7 vs. AS10;
	Specimens AS8 vs. AS12.
b) Two way prestressing:	Specimens FP3 vs. FP6;
	Specimens FP5 vs. FP6.

6. Scale Effect: Specimens FP2s vs. 4FP2s;
Specimens FP3 vs. 4FP3.

2.4 TEST SETUP

2.4.1 PLATE SPECIMENS

The test setups for the 1/6 and 1/4-scale plate specimens are similar in nature. Therefore only the test setup for the 1/6-scale three-span plate specimens, as shown in Figure 2.11, is described in this section.

Each three-span plate had one pin and three roller supports. The plate specimens were set on top of two interior supports, spaced 40 in (102 cm) on center. Each support consisted of a 4x1 in steel bearing plate, a 3 in-diameter half-round steel bar, and a W8x67 beam. At one of the two interior supports, two layers of Teflon were placed between the bearing plate and the half-round bar to provide a friction-free surface. Similarly, the assembly of the exterior supports consisted of a 4x1 in bearing plate, Teflon layers, a 3 in-diameter half-round bar, and a W12x53 beam. These exterior supports were placed on top of the specimens, 32 in (81 cm) away from the interior supports. They were tied down to the test floor to prevent vertical displacement of the specimen at the exterior supports. Half-round steel bars and Teflon were used to allow rotational and horizontal displacements at the supports, simulating a roller support condition. In the one interior support where Teflon was not used, friction was assumed to prevent horizontal displacement and allow only rotational displacement, thus simulating a pin support.

2.4.2 SHELL SPECIMENS

A steel test bed was used for testing the arched shell specimens. A schematic of the test setup is shown in Figure 2.12. The test bed consisted of three wide flange beams (W10x60), 78 in long, placed parallel to the span direction of the shell specimens. Two cut-off beams (W8x58), cut with two different angles to accommodate two R/t ratios of the shell specimens, were bolted onto the top flange of each of the wide flange beams by eight 7/8 in-diameter bolts to accommodate the thrust forces. The wide flange beams were tied down to the test floor at the center to prevent upward displacement of the test bed. A 2x12 in steel plate, 56 in long, was placed against the three cut-off beams on each side of the test bed to provide continuous supports along the straight edges of the shells.

2.5 INSTRUMENTATION

Monitoring the behavior of the specimens during testing included making the following observations and measurements:

1. Ultimate failure load and mode of failure.
2. Strain in the shear and flexural reinforcement and in the prestressing tendons in the vicinity of the loaded area.
3. Crack development and crack patterns.
4. Deflections under the load and at points along the major axes of the test specimens.
5. Support rotation in the shells.

The test load was applied to the specimens incrementally using a 12,000 kip capacity universal testing machine and monitored by both the load indicator on the testing machine and a 400 kip-capacity load cell. Strains in the reinforcement and specimen displacements were recorded at each increment of load using an electronic data acquisition system capable of scanning and recording 128 data channels in 1/100 of a second.

Electrical resistance foil strain gages were used to measure strain in the shear and flexural reinforcement and in the prestressing tendons. All gages were temperature-compensating gages. The gages were mounted on the reinforcement using a Cyano-Acrylate adhesive and protected from moisture with layers of protective coating. Strain in the shear reinforcing steel (T-headed bars) was measured using small strain gages attached to the stem section of the bars. Two gages were mounted at mid-height and on opposite sides of each T-headed bar. For the 1/6-scale specimens without shear reinforcement, four T-headed bars with gages were placed along the two major axes of each specimen at a distance of approximately half effective depth away from the edge of the loaded area (8 in from center of the specimen). In the 1/6-scale specimens with shear reinforcement, an additional four gaged shear bars were placed at a distance equal to the effective depth (12 in from center of the specimen). For the three 1/4-scale plates, eight gaged shear bars were placed in two layers along the two major axes of the plates. The first layer was placed at approximately half the effective depth away from the perimeter of the loaded area (12 in from center of the 1/4-scale specimen), and the second layer was placed at a distance equal to the effective depth from the perimeter of the loaded area (17 in from center). These gaged shear bars were greased after they were placed so that bond stresses on the bars would be minimized. Strain readings from the T-headed bars and the flexural reinforcement were used to determine the initiation of inclined shear cracking and the flexural strain profiles in each specimens. Locations of strain gages in the flexural and shear reinforcements are shown in Figures 2.13 to 2.16.

Strain gages were also used in monitoring the tension force in the post-tensioning tendons. One strain gage was mounted on each tendon. These gages indicated loss of prestress in the post-tensioning process and also indicated any stress changes in the tendon during testing, although it was expected that little change would occur.

Deflections of the test specimens were measured using linear-variable-differential-transformers (LVDTs). Measurements were taken on the underside of the specimens at distances of 0 and 12 in (30 cm) away from the center

of the 1/6-scale specimens; and 0 and 18 in away from the center of the 1/4-scale specimens, and at the supports. Figure 2.17 shows the locations of LVDTs in the specimens.

Externally-mounted dial gages were used to monitor the support rotations of the shell specimens during testing. Monitoring of the support rotations provided information on the behavior of the test setup.

Cracks and crack patterns in the specimens were visually monitored during testing. After testing to failure, the 1/6-scale specimens were to be removed and sectioned in both directions to facilitate examination of the crack patterns on the cross sections of these specimens. For the 1/4-scale specimens, this examination was inhibited due to the difficulty involved in sectioning specimens of this scale.

2.6 SUMMARY

The results of finite element analyses of centrally-loaded multi-span plates and shells with various boundary conditions showed that flat ice walls can be best represented by three-span continuous, simply-supported flat plates, whereas curved ice walls can be best represented by pinned support, single-span open cylindrical shells. Two scale factors, being 6 and 4, were selected for the plate specimens. The scale factor of 6 was selected for all shell specimens.

The 1/6-scale plate had a 40 in (102 cm) center span, two 32 in (81 cm) end spans, and an uniform thickness of 7 in (18 cm). The 1/6-scale shell was pin supported along the straight edges (transverse direction) and had an uniform thickness of 5 in (13 cm) and a span length of 40 in (102 cm). All 1/6-scale specimens had 56 in (142 cm) transverse lengths. The 1/4-scale plate had a 60 in (152 cm) center span, two 48 in (122 cm) end spans, a uniform thickness of 10.5 in (27 cm), and a transverse length of 84 in 213 cm).

Lightweight aggregate (North Carolina Solite) with a nominal maximum sizes of 1/2 in (13 mm) and 3/4 in (19 mm) were used to produce lightweight concrete for the 1/6 and 1/4-scale specimens, respectively. Condensed silica fume, an air-entraining agent, and a superplasticizer were also used to achieve similarity with the material of real Arctic offshore structures.

Reinforcing bars, with 3/8, 1/2 and 3/4 in diameters (#3, #4, and #6) and a specified yield strength of 60 ksi (414 MPa), were used as flexural reinforcement. Two flexural reinforcement ratios of 1.75 and 2.5 percent were selected. T-headed bars with a measured yield strength of 52 ksi (359 MPa) were used as shear reinforcement. Three ratios of shear reinforcement, 0, 0.22, and 0.44 percent, were selected.

For the 1/6-scale specimens, two circular loaded areas of 50 and 100 in^2 (300 and 600 cm^2), with the majority of specimens have 50 in^2 (300 cm^2) loaded area, were selected. For the 1/4-scale specimens, a loaded area of 100 in^2 (600 cm^2) was used for all three specimens.

3. TEST RESULTS

3.1 INTRODUCTION

A considerably large volume of raw data was obtained in this test program. These data were reduced to engineering units and plotted to facilitate examination of the performance of each specimen. The results of each specimen are shown by the following plots:

1. Load-center deflection relationship.
2. Load-strain relationships for the gaged T-headed bars.
3. Flexural strain profiles, plotted for the tension reinforcement in both span and transverse directions. For the 1/6-scale arched shell and the 1/4-scale plate specimens, strain profiles of the compression reinforcement are also provided.

Discussion regarding the performance of each specimen is based largely on the above plots and the observations made during testing. In addition, pictures of crack patterns on the underside and on the cross sections of the specimens are also shown. Descriptions of the test specimens in this test program are summarized in Table 2.3, and the test results of all specimens are given in Table 3.1.

3.2 RESULTS OF 1/6-SCALE PLATE TESTS

3.2.1 PLATE SPECIMENS WITHOUT SHEAR REINFORCEMENT

a) Specimen FP2-1 and FP2-2

Specimens FP2-1 and FP2-2 were identical in every aspect except for their concrete compressive strengths at testing. They were designed to provide some measure of the variability of the test results in this test program. The difference in concrete compressive strengths of the specimens at testing was taken into account by normalizing the loads with respect to the square root of the measured compressive strengths ($\sqrt{f'_c}$). To monitor the initiation and development of internal shear cracking in each of these

specimens, four gaged shear bars were placed along the two major axes of each specimen at distances of 12 inches (30.5 cm) away from the center.

For specimen FP2-1, the flexural strain profiles were not obtained, therefore only the load-deflection curve and the load-strain curves for the gaged shear bars are shown in Figures 3.1 and 3.2.

The initiation of internal shear cracking in this specimen was first detected by the two gaged shear bars on the transverse axis at approximately 90 kips (400 KN, 78% of ultimate load) as seen in Figure 3.2. At this load level, a slight deviation of the load-deflection curve from the original linear relationship was observed (see Figure 3.1), indicating a degradation of stiffness due to cracking.

Cracks continued to develop and completion of the circumferential crack was estimated at 100 kips (445 KN, 87% of ultimate), as evidenced by the sudden increase of strain in the two gaged shear bars on the span axis. Ultimate load was recorded at 114.9 kips (511 KN), at which point the strain in all four gaged bars increased rapidly. The applied load dropped slightly at 114.9 kips (511 KN) before climbing back to the same peak of 114.9 kips (511 KN, see Figure 3.1).

The specimen was cut along the center line in both the span and transverse directions after failure and the cross-sections are shown in Figures 3.3a and b. From these cross sections, it was observed that cracking was in the form of multiple shear cracks which were not necessarily parallel to each other. The primary shear cracks were determined as those with the largest width. Measurements of the angles of these primary cracks with respect to a horizontal plane gave angles of approximately 27^{o} in the span direction and 28^{o} in the transverse direction.

For specimen FP2-2, the load-deflection curve, load-strain curves for gaged shear bars, and flexural strain profiles are shown in Figures 3.4, 3.5 and 3.6, respectively.

The load-strain curves for the gaged shear bars (Figure 3.5) of this specimen indicate that internal shear cracking occurred first in the transverse direction as in specimen FP2-1 at 98 kips (436 KN, 77% of ultimate load). The flexural strain profiles of the tension reinforcement in both directions of this specimen (Figures 3.6a and b) show proportional increases in strain with increasing load up to 90 kips (400 KN). However, at the initial cracking load of 98 kips (436 KN), redistribution of flexural strain in both directions of the specimen was observed. Smaller increase of strain was recorded at the center of the specimen compared with the increase of strain at 8 inches (20.3 cm) from the center of the specimen in both directions. This is an indication of shear cracks intersecting with the tension reinforcement in the region of 8 inches (20.3 cm) away from the center of the specimen. At 113 kips (503 KN), a decrease in flexural strain at the center of the specimen was seen on the transverse strain profiles (Figure 3.6b). At this same load level, significant increase of strain in all gaged shear bars developed (Figure 3.5), indicating the completion of circumferential crack and an increase of crack width. Further opening of cracks at 113 kips (503 KN) is also evidenced by a drop in the applied load while the center deflection was still increasing (see Figure 3.4).

Load was again increased and the ultimate capacity of FP2-2 was recorded at 126.9 kips (564 KN). Flexural strain profiles at ultimate load show that there was further decrease in flexural strains at the center of FP2-2 in both directions while the strains at locations of 8 inches (20.3 cm) and further away from the center continued to increase (Figures 3.6a and b).

Crack patterns on the span and transverse cross sections and on the underside of FP2-2 are shown in Figures 3.7a, b and c. Cracks, almost circular in form, can be observed on the underside of FP2-2. The two cross sections also show similar crack patterns to those observed in specimen FP2-1.

Essentially similar load-deflection behavior was observed for specimens FP2-1 and FP2-2. Both specimens displayed the same stiffness up to ultimate. The difference between ultimate loads of these two specimens, when normalized with respect to the ACI critical section $b_o d$ (defined in section 2.3.6) and expressed in terms of $\sqrt{f'_c}$, was small ($4.8 b_o d\sqrt{f'_c}$ and $5.4 b_o d\sqrt{f'_c}$, respectively). Yielding of the tension steel did not occur in either specimens.

b) Specimens IFP2-1 and IFP2-2

Similar to specimens FP2-1 and FP2-2, IFP2-1 and IFP2-2 were not reinforced in shear. However, both specimens had larger amounts of flexural reinforcement and loaded areas than the rest of the specimens tested in this program. Specimen IFP2-1 had a flexural reinforcement ratio of 2.5 percent and an area of loading of 138 in^2 (890 cm^2), and specimen IFP2-2 had the same amount of flexural reinforcement and an area of loading of 100 in^2 (600 cm^2). The larger loaded area of 138 in^2 (890 cm^2) in specimen IFP2-1 resulted from load being transferred by friction to the outer cylinder of the loading system. This problem was corrected for specimen IFP2-2 by applying lubricant at the interfaces of the loading system. Since these two specimens were designed to provide guidances for the overall test program, they were not monitored to the same extent that the rest of the specimens in the testing program were. The test results for these two specimens included the measured ultimate loads and observations made during testing.

The ultimate capacities of specimens IFP2-1 and IFP2-2 were 127.4 kips and 117.6 kips (567 KN and 523 KN), respectively. These loads corresponded to normalized shear stresses, v_{test}, of $4.3\sqrt{f'_c}$ and $4.4\sqrt{f'_c}$. Yielding did not occur in the tension reinforcement at ultimate. The crack patterns on

the underside and transverse cross-sections of one of these specimens are shown in Figures 3.8a and b. No significant differences in the failure mechanism or crack patterns were observed between the two specimens.

It was observed in the failed specimens that shear cracks propagated along the flexural steel layers and came out to the sides of the specimens rather than penetrating through the bottom surface. This partial delamination was due in part to the larger amount of flexural reinforcement and loaded area in IFP2-1 and IFP2-2. Ultimate failures in these two specimens occurred due to the combined actions of beam and punching shear.

3.2.2 PLATE SPECIMENS WITH SHEAR REINFORCEMENT

Two specimens, FP3 and FP4, were designed to study the influence of the amount of shear reinforcement on the punching shear capacities and the failure mechanisms of the plate specimens. The only difference between these two specimens and specimens FP2-1 and FP2-2 was the inclusion of shear reinforcement. FP3 contained a shear reinforcement ratio of 0.22 percent, and FP4 contained a shear reinforcement ratio of 0.44 percent.

a) Specimen FP3

The load-deflection curve, load-strain curves for gaged shear bar, flexural strain profiles, and pictures of crack patterns of this specimen are shown in Figures 3.9, 3.10, 3.11a and b, and 3.12a, b and c.

Internal shear cracking was first detected in the transverse direction at 90 kips (400 KN, 46% of ultimate load) as indicated by the load-strain curves (Figure 3.10). At this load level, gradual degradation of stiffness, indicated by the deviation of the load-deflection relationship from the original linear relationship, was observed on the load-deflection curve (Figure 3.9). Shortly after reaching 90 kips (400 KN), redistribution of flexural strains occurred in both directions of the tension reinforcement (Figures 3.11a and b). The flexural strain profiles in both directions of FP3 show a smaller increase of strain at the center of the specimen and a larger increase in the region of 8 inches (20.3 cm)

away from the center. The inflection points seen in both directions before the load reached 90 kips (400 KN) disappeared.

The strain redistribution process in this specimen, however, was less extensive when compared with the redistribution process seen in FP2-2 (Figures 3.6a and b). The flexural strain at the center of FP3 continued to increase with increasing load up to ultimate at a slower and no longer proportional rate, but it did not decrease as observed in FP2-2. This is due to the presence of the shear reinforcement in FP3. The shear reinforcement bridging the crack surfaces provided restraint from further crack opening and therefore slowed down the rate of crack propagation. Additional load had to be applied to overcome this restraining force before ultimate failure could occur, thus increasing the load carrying capacity of the specimen and making the failure process of FP3 more gradual than that of FP2-2. Gradual progression of shear cracks in FP3 is also evidenced by the fact that the sudden development of strain in different gaged shear bars in this specimen occurred at significantly different load levels (from 90 kips to approximately 160 kips).

The ultimate capacity of FP3 was 195.1 kips (868 KN). Yielding did not occur in the tension reinforcement prior to ultimate failure. Also, greater strains carried in the span direction of the specimen indicate that the stiffness in the span direction was greater than that in the transverse direction. This observation is consistent with the behavior shown in the flexural strain profiles of specimen FP2-2 and with the fact that cracks always occurred first in the transverse direction.

Similar to specimens FP2-1 and FP2-2, multiple cracks formed in the region local to the failure surface as shown on the cross-sections of FP3 (Figures 3.12b and c). Cracking on the underside of the specimen was diffused and included many fine cracks (Figure 3.12a). The slope of the shear cracks appeared to be steeper in the transverse direction than in the span direction with primary crack angles of 27^{o} in the span direction and 32^{o} in the transverse direction.

b) Specimen FP4

The load-deflection curve, load-strain curves for gaged shear bars, flexural strain profiles, and crack patterns of specimen FP4 are shown in Figures 3.13, 14, 15a and b, 16a, b and c.

Internal shear cracking was first evidenced by the sudden increase of strain in two gaged shear bars, one in the span and one in the transverse direction (Figure 3.14), at approximately 100 kips (445 KN, 40% of ultimate).

Although this specimen displayed higher punching shear strength than specimen FP3 (ultimate load was recorded at 251.9 kips) and higher yield load (180 kips, see Figures 3.15a and b), the failure process of this specimen was essentially the same as that observed in specimen FP3. Shortly after internal shear cracking was detected by the gaged shear bars, a deviation of the load-deflection relationship from the original linear trend was observed. The beginning of the flexural strain redistribution in the tension reinforcement in both directions also became evident at this load level. The wide range of loads at which significant strain levels were detected among the various gaged shear bars (100 kips to 230 kips, Figure 3.14) indicated that failure of FP4 was more gradual than FP3. The load dropped slightly at 246 kips (1094 KN) while the center deflection was still increasing, indicating the development of major cracks at this load level. This load decrease also implied that most of the shear reinforcement crossing the cracks had failed at this load stage. The load then increased again to the indicated peak load of 251.9 kips (1120 KN, Figure 3.13). Figures 3.16a, b and c show the crack patterns on the cross sections and underside of this specimen. Cracking on the underside of the specimen was also diffused, similar to the cracking in specimen FP3. The primary shear crack angles were approximately 27° in the span direction and 36° in the transverse direction.

3.2.3 PLATE SPECIMENS WITH PRESTRESSING

Two specimens, FP5 and FP6, were constructed to study the effects of prestressing on punching shear behavior in the plate specimens. Like specimen FP3, each of these two specimens had a shear reinforcement ratio of 0.22 percent. The only difference between these two specimens and specimen FP3 was the presence of compressive prestress. For specimen FP5, a compressive prestress of 500 psi (3450 kPa) was applied uniformly in the transverse direction of the specimen. For specimen FP6, the same value of prestress was applied in both span and transverse directions.

a) Specimen Prestressed in Transverse Direction: FP5

The test results of this specimen and pictures of crack patterns on the span and transverse cross-sections and on the underside are shown in Figures 3.17, 18, 19a and b, and 20a, b and c.

Internal shear cracking occurred first in the span direction of FP5 at 87 kips (387 KN, 43% of ultimate load) as indicated on the load-strain curves for the shear reinforcement (Figure 3.18). Due to the effect of prestressing in the transverse direction, this cracking was different from that of the non-prestressed specimens in which cracking began in the transverse direction. After initiation of cracking at 87 kips (387 KN), radial and circumferential cracks propagated gradually down and outward. Major crack openings, marked by the sudden increases of strain in the gaged shear bars, developed at approximately 150 kips (667 KN, 74% of ultimate).

On the load-deflection curve (Figure 3.17), evidence of the initiation of internal shear cracking was observed by the gradual degradation of stiffness beginning at 87 kips (387 KN). The development of major shear cracking was confirmed by a sudden shift of the load-deflection relationship at 150 kips (667 KN).

The flexural strain profile in the span direction of specimen FP5 indicates the beginning of the strain redistribution process at 90 kips (400 KN, Figure 3.19a and b). Yielding of tension reinforcement in the span

direction occurred shortly before the ultimate load was reached. These strain profiles also indicate that more load was carried in the span direction than in the transverse direction of this specimen. Ultimate punching shear capacity of FP5 was recorded at 202.2 kips (900 KN).

The underside and cross-sections of specimen FP5 are shown in Figures 3.20a, b and c. Cracks on the underside were diffused, but not to the extent observed in specimens FP3 and FP4. The primary crack angle in the span direction (perpendicular to the direction of prestress) was approximated as 42°. This angle was much greater than the angles observed in specimens FP3 and FP4. In contrast, cracks in the transverse direction were at angles of approximately 16° and 23°, which were less than the angles observed in the transverse directions of FP3 and FP4.

The behavior of specimen FP5 was similar to that of specimen FP3. Internal shear cracking initiated in both specimens at almost the same load level: 90 kips for FP3 and 87 kips for FP5 (400 KN and 387 KN, or 46% and 43% of ultimate loads), respectively. Sudden development of strain in all gaged shear bars, an indication of major crack opening, occurred at 160 kips for FP3 and at 150 kips for FP5. This was also marked by the shifts in the load-deflection relationships in both specimens at these load levels. The normalized punching shear strength of specimen FP5, however, was 8 percent higher than that of FP3.

b) Specimen Prestressed in Both Direction: FP6

A compressive prestress of 500 psi (3.45 MPa) was applied uniformly in both directions of specimen FP6. Information from strain gages mounted on the tension reinforcement was not obtained for this specimen, therefore the flexural strain profiles for specimen FP6 are not presented. The load-center deflection curve and the load-strain curves for the shear reinforcement are shown in Figures 3.21 and 3.22.

The load-strain curves (Figure 3.22) show that internal shear cracking first developed at 85 kips (378 KN, 38% of ultimate). Around this load level, gradual degradation of stiffness was indicated by the load-

deflection curve (Figure 3.21). The load-deflection behavior of this specimen was essentially similar to that of FP3 and FP5. Ultimate load was recorded at 221.3 kips (984 KN) for specimen FP6.

Figures 3.23a, b and c show the crack patterns on the cross-sections and on the underside of specimen FP6. The primary shear crack angles were measured as 37° in the span direction and 23° in the transverse direction. In both specimens FP5 and FP6, the locations of the post-tensioning ducts were seen to have influenced the formation of the cracks.

3.2.4 SINGLE SPAN PLATE SPECIMEN

In a three-span specimen, the two end spans provide the center span with restraint that makes the specimen stiffer in the span direction. The lack of this restraint in a single span specimen makes it more flexible, which may in turn affect the load carrying mechanism. To better understand the influence of this restraint condition on the punching shear behavior of the specimens in this test program, a single-span plate specimen, FP1, was tested. Except for being a single-span specimen, FP1 was identical to FP3 (shear reinforcement ratio of 0.22 percent). The test results for this specimen are shown in Figures 3.24, 25, 26a and b.

The flexibility of specimen FP1 is reflected in its load-deflection curve and its flexural strain profiles (Figures 3.24, 3.26a and b). The load-displacement relationship of this specimen deviated more from the original linear relationship at a much lower load than in any of the three-span plate specimens, and the flexural strain profiles show that there was more bending action, especially in the span direction, in FP1 than in its three-span counterpart, specimen FP3. Yielding of the tension reinforcement in the span direction was observed at approximately 140 kips (623 KN, 65% of ultimate load). Yielding also occured in the transverse tension reinforcement at ultimate load.

Ultimate load was recorded at 216.8 kips (964 KN). Internal shear cracking occurred at approximately 76 kips (338 KN, 35% of ultimate) as indicated

by the load-strain curves for the shear reinforcement. Shortly after the initial cracking load was reached, redistribution of strain was seen in the span direction as indicated by the larger increase of strain at locations 8 inches (20.3 cm) away from the center of the specimen compared with the increase of strain at the center.

Even though yielding in the tension reinforcement occurred at a relatively low load level in this specimen (at 65% of ultimate load), the initiation of internal shear cracking at a lower load level (35% of ultimate load), and the distributions of strain in the tension reinforcement indicate that punching shear was the primary mode of failure in specimen FP1.

The measured punching shear strength of FP1 was 20 percent higher than that of FP3. This increase in punching shear strength can be attributed to the flexibility of this specimen. Since FP1 was more flexible in the span direction than FP3, its ability to deform with increasing load was greater than that of FP3. The greater deformability allowed FP1 to deflect more than FP3 or any other three-span specimen after cracking had formed. This deflection helped reduce the tensile stress in the shear reinforcement crossing the crack. Additional applied load was required to fail this shear reinforcement, resulting in a higher shear load-carrying capability in the single-span specimen. This is further confirmed by the significantly wider range of loads at which sudden strain increases in the gaged shear bars occured in FP1 (from 76 kips to ultimate) as seen in Figure 3.25.

Crack patterns on the underside and on the span cross-section of this specimen are shown in Figures 3.27a and b. The underside of this specimen shows extensive flexural and shear cracks, and the cross-sections show primary crack angles of approximately 27^{o} in the span direction and 24^{o} in the transverse direction.

3.3 RESULTS OF 1/6-SCALE SHELLS WITH R/t RATIO OF 12

3.3.1 SHELL SPECIMEN WITHOUT SHEAR REINFORCEMENT AS9

For all shell specimens, the strain profiles of the compression reinforcement in the span direction are provided in addition to the load-deflection curve, the load-strain curves for shear reinforcement and the strain profiles of the tension reinforcement. The test results of specimen AS9, which had an R/t ratio of 12 and contained no shear reinforcement, are shown in Figures 3.28, 29, 30a, b and c, and 31a, b and c.

Only information from three of the four gaged shear bars, placed on the two major axes of this specimen, was obtained for this specimen. Load-strain histories for these are given in Figure 3.29. According to these load-strain curves, internal shear cracking initiated at approximately 92 kips (409 KN, 74% of ultimate load). However, the beginning of the strain redistribution process in both directions took place at approximately 85 kips (378 KN, Figures 3.30a and b), indicating that internal shear cracking might have occurred at this load level rather than at 92 kips (409 KN) as given by the load strain curves. The load-deflection curve (Figure 3.28) shows a linear relationship up to the level of the initial shear cracking load (92 kips). Gradual degradation of stiffness, marked by the decrease of the slope of the load-deflection curve, occurred shortly after that load level. The ultimate punching shear capacity was recorded at 124.3 kips (553 KN). The sudden development of strain in the gaged shear bars, an indication of the extension of crack to their locations, occurred between 85 kips to approximately 118 kips (378 KN to 525 KN, Figure 3.29).

The flexural strain profiles (Figures 3.30a, b and c) show that bending action was equally distributed in both directions. Neither tension nor compression reinforcement yielded at ultimate load. More importantly, the strain profiles in Figure 3.30 show a similar strain redistribution process to the plate specimen without shear reinforcement (FP2-2). As load continued to increase after 85 kips (378 KN), a decrease of strain in the tension reinforcement near the center of the specimen and a large, disproportionate increase of strain in the portion of the tension

reinforcement approximately 8 inches (20.3 cm) away from the center were observed. This indicates that shear cracks intersected the tension reinforcement approximately 8 inches from the center of the specimen. This behavior, which is similar to the behavior displayed by the plate specimen FP2-2, may be explained as follows:

As a shear crack extended downward and intersected the tension reinforcement, additional tension created by the opening of crack was introduced into the portion of the tension reinforcement local to the crack. This resulted in an increase of tensile strain in that portion. At the same time, compression created by the decrease in volume of the solid concrete between the cracks due to crack opening was introduced to the tension reinforcement between the cracks (at the center of the span specimen), thus releasing some tension in this portion. This is evidenced by the decrease of tensile strain at the center of the specimen.

More information on how this specimen behaved is offered in the strain profiles of the compression reinforcement (Figure 3.30c). These profiles show a steady, almost proportional increase of compressive strain in the compression reinforcement under increasing load up to 120 kips (96 percent of ultimate load). This compressive strain was evidence of the existence of a compressive zone, extending from the top surface of the specimen to the two supports.

Figures 3.31a ,b and c show the crack patterns on the underside and on the cross-sections of AS9. Again, multiple shear cracks developed prior to the final collapse of the specimen (Figures 3.30b and c). Evidence of crushing of concrete was observed in the region near to the top of the specimen. The primary shear crack angles were approximated to be 25^{o} and 18^{o} in the span direction and 22^{o} in the transverse direction.

3.3.2 SHELL SPECIMENS WITH SHEAR REINFORCEMENT

Two specimens, AS7 and AS11, were constructed to study the influence of shear reinforcement on punching shear capacity and failure mechanism of the shell specimens. Both AS7 and AS11 had an R/t ratio of 12. The only difference between these two specimens and specimen AS9 was the inclusion of shear reinforcement. AS7 contained 0.24 percent of shear reinforcement and AS11 contained 0.48 percent.

a) **Specimen AS7**

A total of eight gaged shear bars were placed along the two major axes of AS7, four were placed on the two major axes at the same distance of 8 inches from the center of the specimen and the other four were placed at 12 inches from the center. Test results for this specimen are shown in Figures 3.32, 33, 34, and 35.

Despite visual observation of sudden failure, the load-strain curves for the gaged shear bars (Figure 3.33) revealed a gradual process of crack development. Initiation of internal shear cracking was detected at approximately 93 kips (414 KN, 49% of ultimate load) by a gaged shear bar placed at 8 inches from the center of the specimen in the span direction. Cracking then slowly propagated circumferentially and radially, as evidenced by the development of strain in the gaged shear bars placed further from the center at higher loads (see Figure 3.33). In one of the gaged shear bars placed 12 inches (31 cm) from the center of the specimen, no significant strain development was detected, indicating that at least some of the shear reinforcement crossing the crack was not fully activated at ultimate load.

The flexural strain profiles (Figures 3.34a and b) showed that redistribution of strain in the transverse direction of this specimen occurred shortly after 90 kips (400 KN). The strain redistribution process in this specimen was less extensive when compared with the strain redistribution process that occurred in the specimen without shear reinforcement, AS9. Strains in the tension reinforcement in the transverse

direction were greater than they were in the span direction, and yielding of the tension reinforcement in the transverse direction occurred at approximately 150 kips (667 KN, 79% of ultimate load).

The strain profiles for the compression reinforcement (Figure 3.34c) showed a steady, proportional increase in compressive strain with increasing load. Strain in the compressive reinforcement reached levels near yielding at ultimate load.

The load-deflection curve of this specimen (Figure 3.32) displayed an essentially linear relationship between load and center displacement. No clear sign of stiffness degradation due to cracking was indicated. The ultimate punching shear capacity of this specimen was 190.6 kips (848 KN).

Crack patterns on the underside and on the cross-sections of AS7 are shown in Figures 3.35a, b and c. Cracking on the underside was in the form of a single, circular crack. Multiple cracks also formed on the cross-sections with evidence of concrete crushing on top of the specimen. The primary crack angles were estimated as 31^{o} in both the span and transverse directions.

b) Specimen AS11

AS11 contained 0.48 percent of shear reinforcement, twice the amount contained in AS7. The test results of this specimen are shown in Figures 3.36, 37, 38 and 39.

The load-strain curves for the gaged shear bars (Figure 3.37) showed that internal shear cracking developed first at the locations of the four inner gaged shear bars (8 inches from center) at 95 kips (423 KN, 49% of ultimate load). Internal shear cracking propagated radially outward, and at 133 kips (592 KN) reached the four outer gaged shear bars (12 inches from the center). The development of strain in all gaged shear bars was much more gradual compared with that of AS7 and AS9, indicating a more restrictive crack opening in AS11. This was due to the larger amount of shear reinforcement crossing the cracks. The fact that cracks were less free to

open and propagate is also evidenced in the strain profiles (Figures 3.38a, b and c). These profiles show an even less extensive strain redistribution process when compared with the process seen in specimen AS7. Like AS7, the load-strain curves for the gaged shear bars in this specimen also indicated that some shear reinforcement bridging the crack did not fail when the ultimate load was achieved.

Yielding of the tension reinforcement occurred in the span direction shortly after 120 kips (534 KN), and in the transverse direction shortly after 150 kips (667 KN), as indicated in Figures 3.38a and b. Yielding of the compression reinforcement in the compression zone occurred at ultimate (Figure 3.38c). The strain profiles for the tension reinforcement also showed that bending action was more equally distributed in both directions of this specimen than it was in specimen AS7. The strain profiles of the compression reinforcement showed a steady, proportional increase of compressive strain in the compression zone up to ultimate load.

The load-deflection behavior of AS11 is almost identical to that of AS7. Essentially, a linear relationship between load and center displacement was observed throughout the loading history. No clear sign of stiffness degradation due to cracking was indicated by the load-deflection curve (Figure 3.36). Sudden rupture marked ultimate failure of this specimen; and the ultimate load was recorded at 192.4 kips (856 KN), almost the same load level with AS7.

Crack patterns on the cross-sections of the failed specimen are shown in Figures 3.39a anb b. Formation of circular cracks was seen on the underside of AS11. Similar to AS7 and AS9, cracks on the cross-sections of AS11 were in the form of multiple cracks with evidence of concrete crushing on top of the specimen. The primary crack angles were measured as 34^{o} in the span direction and 37^{o} in the transverse direction.

3.3.3 SHELL SPECIMEN WITH PRESTRESSING AS10

The influence of prestressing on punching shear behavior of the shell specimens was examined in specimen AS10. Except for a uniform transverse prestress of 500 psi (3447 KPa), AS10 was identical to AS7. It contained 0.24% shear reinforcement and had an R/t ratio of 12. The test results of AS10 are shown in Figures 3.40, 41, 42, and 43.

Unlike specimen AS7, in which cracking was seen to propagate slowly (internal shear cracks initiated at 93 kips at locations of the inner gaged shear bars and did not reach the locations of the outer gaged shear bars until 143 kips), the propagation of cracks in AS10 was rapid. Initial shear cracking load in AS10 was approximately 87 kips (387 KN), and extension of cracks to the outer gaged shear bars (12 inches from center) was observed at approximately 100 kips (445 KN, see Figure 3.41). Shortly after reaching the initial cracking load of 87 kips (387 KN), redistributions of strain in the tension reinforcement in both directions of AS10 were observed on the flexural strain profiles as shown on Figures 3.42a and b. The distribution of strain in the compression reinforcement was proportional to the applied load up to approximately 120 kips (534 KN, 79% of ultimate load). Beyond this load level, redistribution of compressive strain in the compression reinforcement occurred as observed in the strain profiles shown in Figure 3.42c.

At the initial cracking load (87 kips, 387 KN), the load-deflection curve (Figure 3.40) showed a slight deviation from the original linear relationship. Ultimate punching shear capacity of specimen AS10 was 152.1 kips (677 KN). Crack patterns on the underside and on the cross-sections of AS10 are shown in Figures 3.43a, b and c. Cracking was in a circular form on the underside, and multiple cracks developed on the cross-sections prior to complete failure of the specimen. The primary shear crack angles were 47^{o} and 36^{o} in the span direction and 31^{o} in the transverse direction. Influence of the locations of the post-tensioning ducts on the formation of cracks was also visible on the cross-sections.

3.4 RESULTS OF 1/6-SCALE SHELLS WITH R/t RATIO OF 6

The influence of compressive membrane action (arching action) on punching shear behavior of the test specimens was further studied by testing two shell specimens with larger curvature, AS8 and AS12. Both specimens had an R/t ratio of 6. AS8 contained no shear reinforcement and AS12 contained 0.24 percent shear reinforcement.

3.4.1 SPECIMEN AS8

Except for the larger curvature, this specimen was identical to specimen AS9. The test results of this specimen are shown in Figures 3.44, 45, 46, and 47.

Internal shear cracking was detected by three gaged shear bars, two on the transverse axis and one on the span axis (Figure 3.45), at 108 kips (480 KN, 71% of ultimate load). The completion of the circumferential crack, indicated by the development of strain in the remaining gaged shear bar, was recorded at 128 kips (569 KN, 84% of ultimate load). The beginning of the flexural strain redistribution process, which was similar to that for AS9, was observed on the strain profiles of the tension reinforcement in both span and transverse directions (Figures 3.46a and b) shortly after the initial cracking load was reached. Proportional increases of compressive strain in the compression reinforcement up to ultimate were indicated on the strain profiles for the compression reinforcement (Figure 3.46c). Ultimate load was recorded at 152.0 kips (676 KN). The load-deflection curve showed an essentially linear relationship between the applied load and the center deflection up to ultimate load.

Crack patterns on the underside of this specimen are shown in Figure 3.47. Crack patterns on the cross-sections are not shown here due to the difficulty in cutting this specimen.

3.4.2 SPECIMEN AS12

The only difference between AS12 and AS7 was the larger curvature in specimen AS12. The test results of this specimen are shown in Figures 3.48, 49, 50, and 51.

As for other specimens with shear reinforcement, the development of strain in the gaged shear bars in AS12 was gradual, with the development of strain in the inner gaged shear bars occurring first (Figure 3.49). The initial shear cracking load was recorded at 106 kips (472 KN, 62% of ultimate load). Like specimen AS7, one of the gaged shear bars of AS12 did not fail at ultimate, indicating that ultimate failure of this specimen occurred prior to complete failure of all shear reinforcement crossing the crack.

The strain profiles for the tension reinforcement (Figures 3.50a and b) showed that yielding did not occur prior to ultimate load. Redistribution of strain in the tension reinforcement in both directions was evidenced shortly after 106 kips (472 KN). The strain redistribution in this specimen was also less extensive than that of specimen AS8, which contained no shear reinforcement. Compressive strain in the compression reinforcement increased proportionally with increasing load up to ultimate as shown in Figure 3.50c.

The load-deflection curve (Figure 3.48) displayed an essentially linear relationship between the applied load and the center deflection, with no clear sign of degradation of stiffness due to internal shear cracking. Ultimate load was recorded at 170.1 kips (757 KN) for AS12.

Crack patterns on the underside of AS12 are shown in Figure 3.51. Primary crack angles were estimated to be 60^{o} in the span direction and 30^{o} in the transverse direction.

3.5 RESULTS OF 1/4-SCALE PLATE TESTS

As discussed in chapter 2, three 1/4-scale plates were tested to study the effect of scale on the behavior of the specimens and the feasibility of extrapolating the 1/6-scale test results to predict the response of larger structures. Two of the 1/4-scale plates, 4FP2-1 and 4FP2-2, contained no shear reinforcement and were identical to the 1/6-scale FP2s. The remaining 1/4-scale plate, 4FP3, contained 0.22% shear reinforcement and was identical to the 1/6-scale specimen FP3. The behavior of these specimens are described in the following sections.

3.5.1 1/4-SCALE PLATES WITHOUT SHEAR REINFORCEMENT

a) Specimen 4FP2-1

Unlike the 1/6-scale test series, the strain profiles for the compression reinforcement were obtained for the 1/4-scale specimens. The load-deflection curve, the load-strain curves for the gaged shear bars, and the flexural strain profiles in both the tension and compression reinforcements for specimen 4FP2-1 are shown in Figures 3.52, 53, 54a and b, and 55a and b.

Two layers of gaged shear bars, arranged as shown in Figure 2.14, were used to monitor the initiation and development of internal shear cracks in this specimens. From the load strain curve of an inner gaged shear bar (Figure 3.53), inclined shear cracking was determined to have initiated at approximately 167 kips (743 KN, corresponding to a normalized cracking stress, v_{cr}, of $3.1\sqrt{f'_c}$). As load was increased to about 180 kips (800 KN), redistribution of flexural strain in the tension reinforcement occurred as indicated on the flexural strain profiles (Figures 3.54a and b). Ultimate load was reached at 271 kips (1205 KN), corresponding to a normalized ultimate shear stress, v_{test}, of $5.0\sqrt{f'_c}$. The strain profiles for the compression reinforcement (Figures 3.55a and b) showed that prior to shear cracking, the top reinforcement in both span and transverse directions were under minor compression. At approximately 180 kips (800 KN), redistribution of strain also took place in the compression

reinforcement. These redistributions were marked by changes from compression to tension in the top reinforcement in regions approximately 12 inches (31 cm) from the center of this specimen (Figures 3.55a and b).

Crack formation on the bottom of 4FP2-1 (Figure 3.56) indicated a similar failure surface as for the 1/6-scale FP2s. The crack patterns on the cross sections were not obtained due to the difficulty involved in sectioning the 1/4-scale specimens.

b) Specimen 4FP2-2

For specimen 4FP2-2, The test results are presented in Figures 3.57, 58, 59a and b, and 60a and b. In this specimen, determination of shear cracking load was inhibited by the loss of four gaged shear bars. The information obtained from the remaining gaged shear bars was considered insufficient to facilitate a reliable prediction of the onset of shear cracking. Therefore, the shear cracking load will not be speculated for this specimen. The ultimate shear strength and the flexural strain profiles of 4FP2-2, however, indicated the punching shear behavior for this specimen was similar to 4FP2-1.

The ultimate load in 4FP2-2 was measured at 270 kips (1200 KN, corresponding to an ultimate punching shear stress, v_{test}, of $5.2\sqrt{f'_c}$). Redistribution of flexural strain in the tension reinforcement occurred first in the span direction shortly after 180 kips (800 KN, see Figure 3.59a). In the transverse direction, redistribution did not take place until after 240 kips (1068 KN, see Figure 3.59b). The compression reinforcement, however, showed that the top layer of this specimen was essentially in compression up to ultimate load (Figure 3.60a and b). The crack patterns on the underside of this specimen was similar to that of specimen 4FP2-1 (Figure 3.61).

3.5.2 1/4-SCALE PLATE WITH SHEAR REINFORCEMENT: 4FP3

The load-deflection curve, load-strain curve for the gaged shear bars, flexural strain profiles in the tension and compression reinforcement for specimen 4FP3 are shown in Figures 3.62, 63, 64a and b, and 65a and b.

The development of strain in a gaged shear bar at 158 kips (703 KN, corresponding to a normalized shear stress, v_{cr}, of $3.2\sqrt{f'_c}$), as seen on the load-strain curves (Figure 3.63), marked the initiation of internal shear cracking in 4FP3 at this load level. Like the 1/6-scale plate FP3, the flexural strain profiles in the tension reinforcement of this specimen did not show a significant redistribution of strain after cracking. The strain profile of the compression reinforcement in the span direction (Figure 3.65a) showed a change from compression to tension of the compression reinforcement in region approximately 12 inches (31 cm) from the center of 4FP3. This change occurred at about 270 kips (1200 KN), indicating the propagation of shear cracking to the location of the compression reinforcement at this load level. The load-deflection curve (Figure 3.62) showed that, after ultimate load was reached at 404.2 kips (1800 KN, corresponding to a normalized punching shear stress, v_{test}, of $8.1\sqrt{f'_c}$), this specimen was still able to deform without a significant drop of load. In fact, at displacement of approximately three times the ultimate-load displacement (0.9 in), this specimen was still able to withstand 78% of the ultimate load. The circular crack patterns on the underside of this specimen (see Figure 3.66) also indicated the formation a conical failure surface in 4FP3.

3.6 SUMMARY

Experimental results and general observations obtained from this test program have been presented in the above sections. Discussion regarding the behavior of each specimen was given with respect to load history. Test results of all specimens were summarized and presented in Table 3.1. The behavior of the specimens in this testing program is summarized here:

1. In most cases, the load level at which internal shear cracking was first detected by the gaged shear bars was lower or almost the same as the load level at which the redistribution of flexural strain was observed. This established confidence in relying on the gaged shear bars to determine initial cracking loads.

2. The strain redistribution process, marked by the disproportionate increases of strain in the flexural reinforcement at locations near the cracks and the disproportionate decreases of strain at the center of the specimens, was more extensive in specimens without shear reinforcement than for those with shear reinforcement. This process was also more extensive in shell specimens than in plate specimens.

3. Failure in plate specimens that contained shear reinforcement was more gradual than in those without shear reinforcement. In the latter specimens, sudden rupture occurred shortly after initiation of internal shear cracking, while in the former specimens ultimate punching shear failure did not occur until a significant increase of load and center deflection had been achieved. The ductility of the specimens increased with increasing amounts of shear reinforcement.

4. Not all shear reinforcement crossing the crack in shell specimens (AS7, AS11, and AS12) was fully activated at ultimate load, especially those shear bars at locations further from the center of the specimen. This indicates that failure in these specimens occurred mainly due to compressive failure of concrete.

5. The rate of radial propagation of shear cracks was much slower for the shell specimens than for the plate specimens, indicating the influence of the compressive membrane forces in restraining crack opening.

6. In all shell specimens, the strain profiles for compression reinforcement showed a steady, proportional increase of compressive strain with increasing applied load up to ultimate. This increase in strain indicates that a compressive dome existed in all shell specimens throughout the loading process. In the shell specimens with 0.24 and 0.48 percent shear reinforcement (AS7 and AS11), yielding of the top flexural reinforcement in compression occurred prior to failure of the specimens.

7. Non-linear behavior of the load-center deflection relationship, an indication of stiffness degradation due to internal shear cracking, was more apparent for plate specimens than for shell specimens.

8. Increasing shell curvature resulted in a slower rate of crack propagation and less extensive flexural strain redistribution. Further, increasing shell curvature resulted in higher punching shear capacity. However, the presence of curvature-induced membrane compressive forces also resulted in a marked reduction in shell ductility.

9. Increasing shell curvature resulted in an increase in normalized shear cracking stress, v_{cr}. The ranges of shear cracking stress is listed as follows:

-For Plates (R/t = 0): $v_{cr} = 3.4\sqrt{f'_c}$ to $4.2\sqrt{f'_c}$

-For Shells with R/t = 6: $v_{cr} = 7.2\sqrt{f'_c}$ to $7.6\sqrt{f'_c}$

-For Shells with R/t =12: $v_{cr} = 8.6\sqrt{f'_c}$ to $9.3\sqrt{f'_c}$

10. Normalized shear cracking stress, v_{cr}, is not affected by the amount of shear reinforcement.

11. In all specimens, the primary shear crack angles were less than 45° when measured with respect to a horizontal plane. For non-prestressed plates, the mean crack angle in the span direction was 27°, and the crack angle in the transverse direction ranged from 24 to 36°. For prestressed plates, the crack angle in the span direction was greater, 37 to 42°, and the crack angle in the transverse direction was less, 16 to 23°. The crack angles for the shells were generally greater than for the plates. Crack angles for shells with R/t ratio of 6 ranged from 25° to 60° in the span direction, and 22° to 37° in the transverse direction.

12. The single span plate specimen (FP1) had slightly lower shear cracking stress v_{cr} ($3.4\sqrt{f'_c}$) but higher ultimate shear strength V_{test} ($9.8b_o d\sqrt{f'_c}$) when compared with its three span counterpart FP3 ($3.7\sqrt{f'_c}$ and $8.0b_o d\sqrt{f'_c}$). The higher ultimate shear strength was attributed to the greater flexibility in the span direction of FP1.

4. FAILURE MECHANISMS

4.1 INTRODUCTION

Experimental results are used in this chapter to identify the failure mechanisms of the test specimens and to explain the processes that led to ultimate punching shear failures. Since more complete information was obtained for the shell specimens, the failure mechanism for shells is explained first.

4.2 FAILURE MECHANISM FOR SHELL SPECIMENS

Substantial empirical evidence indicated that shear-compression was the mechanism of failure in all the shell specimens. This mechanism of failure can be better explained if the progression of internal shear cracking in the shells is understood.

The region where internal shear cracks first occurred was determined by examining the strain profiles of both the tension (bottom flexural steel) and compression reinforcement (top flexural steel). These profiles indicated that there existed a dome-like compression zone, extending from the supports to the top layer of the shell specimens as idealized in Figure 4.1, throughout the loading history of the shells. The strain profiles of the compression reinforcement for all shells showed steady and proportional increases of compressive strain up to ultimate load (Figures 3.30c, 3.34c, 3.38c, 3.42c, 3.46c, 3.50c). Redistribution of flexural strain in the compression reinforcement was minor and occurred just before ultimate load was achieved. The proportional increase of compressive strain up to ultimate in the compression reinforcement clearly indicated that internal shear cracking could not have initiated first in the region close to the top of the specimens, where this reinforcement was located. If this had occurred, a major strain redistribution in the compression reinforcement would have resulted. On the other hand, the strain profiles of the tension reinforcement showed a significant redistribution shortly after internal

shear cracking was detected by the gaged shear bars. As explained in chapter 3, the redistribution of strain in the tension reinforcement was caused by the intersection of shear cracks with the bottom steel layer. The redistribution of strain in the tension steel only occurred in most cases after internal shear cracking had been detected by the shear bars. This also ruled out the possibility that shear cracks initiated first at the bottom of the specimens. Consequently it is clear that internal shear cracking first developed in the mid-depth region of the specimens.

Having determined the region where internal shear cracks first developed, it is now possible to explain the progression of shear cracking in shells by examining the behavior of one typical shell specimen, specimen AS7. AS7 had an R/t ratio of 12 and 0.24 percent shear reinforcement. Two layers of gaged shear bars were placed on the two major axes of the specimen, the inner layer 8 inches (20 cm) away from the center and the outer layer 12 inches (31 cm) away from the center. The following successive events describe the failure process of AS7:

During the period before any internal shear cracks developed in AS7 (from 0 to 93 kips), the gaged shear bars experienced only minor compressive or bending stresses as a result of elastic deformation in the specimen. This resulted in a very small amount of either tensile or compressive strain as can be seen from the load-strain curves (Figure 3.33). Elastic bending action was evidenced during this period by the proportional distributions of flexural strain with respect to the applied load in both the tension and compression reinforcement (Figures 3.35a, b and c). Furthermore, a dome-like compression zone, extending from the supports to the top layer of the specimen, was clearly indicated by the strain profiles of both the tension and the compression reinforcement.

At 93 kips (414 KN) and shortly thereafter, sudden development of tensile strain in the shear reinforcement, an indication of internal shear cracking, was detected by the inner layer gaged shear bars (Figure 3.33). As discussed earlier, these internal shear cracks first

initiated in the mid-depth region of the specimen. These cracks then propagated outward, as evidenced by the detection of cracks at 143 kips (636 KN) by an outer layer gaged shear bar placed in the span direction. The shear cracks also propagated downward and intersected the tension reinforcement, evidenced by the redistribution of strain in the tension reinforcement (Figures 3.35a and b). This redistribution was marked by a sudden increase of strain at crack locations (approximately 8 inches from the center of the specimen) and by a decrease in rate-of-strain-increase at the center of AS7. The increase of strain at locations local to the shear crack in the tension reinforcement was caused by the opening of cracks. This opening also resulted in a release of tension in the concrete portion in between the cracks, as reflected by the decrease of tensile strain at the center of the specimen (see Figure 4.2).

During the period when strain redistribution was taking place in the tension reinforcement, the strain profiles of the compression reinforcement still showed a proportional distribution (Figure 3.35c). This proportional distribution persisted until ultimate load was reached, indicating that shear cracks were not present in the compression region of AS7. Similar indications were observed for all other shell specimens.

Redistribution of strain in the tension reinforcement continued to take place until ultimate failure occurred at 190.6 kips (848 KN). The failure appeared to be very sudden, even though the detection of shear cracks at much lower load (93 kips or 414 KN) indicated a more gradual development of shear cracks.

At failure, one interesting observation was made concerning the load-strain curves for the gaged shear bars (Figure 3.33). These load-strain curves showed that some of the shear bars crossing the cracks did not yield at ultimate. Similar observations were made for other shell specimens with shear reinforcement, AS11 and AS12 (Figures 3.37 and 3.49). This suggests that failure of the shell specimens was controlled by the crushing of

concrete in the compression zone. Photographs of crack patterns on the cross-sections of this specimen (Figures 3.35 b, and c) also suggest that failure was due to crushing of concrete in the compression zone. This crushing occurred in the region immediately beneath the loaded area, where the area of the compression zone was smallest. The inclined cracks which had developed earlier created a tied-arch system, where compression was resisted by the compression dome and tension was resisted mainly by the tension reinforcement. Yielding of more shear bars across the crack surfaces resulted in continuing reduction of the compression area as shear cracks opened wider. This gradual reduction of area eventually led to overloading of the compression zone which led to crushing failure of concrete. It should also be noted that in specimens with shear reinforcement, AS7 and AS11, the compression reinforcement in the span direction of the specimens yielded under compressive loads prior to the ultimate load being achieved.

4.3 FAILURE MECHANISM FOR PLATE SPECIMENS

Unlike the shell specimens, where failure occurred due to crushing of concrete in the compression zone without the necessity of complete failure of the shear reinforcement, plate specimens failed in a different mode due to the lack of membrane compressive forces.

The difference between the behavior of the plates and the shells was illustrated by the load-strain curves of the gaged shear bars. Figures 3.10, 14, 18, and 22 show the load-strain curves of specimens FP3, FP4, FP5, and FP6. All these specimens contained shear reinforcement with ratios of 0.22 to 0.44 percent. These load-strain curves show that most if not all the shear bars had yielded at load levels much lower than ultimate load. For example, both layers of gaged shear bars in specimen FP3 yielded at approximately 150 kips (667 KN), while FP3 did not fail until 195 kips (867 KN, see Figure 3.10). The complete yielding of shear reinforcement at significantly lower load levels suggests that failures in the plate specimens were caused by the successive failures of the shear reinforcement, the interface shear transfer, and the dowel action. In

other words, failure in plate was due mainly to shear. The applied shear force overcame the combined action of the three basic shear resistance mechanisms, thus ultimately led to punching shear failures in plates.

4.4 SUMMARY

The progression of shear cracks and the causes of failure for the test specimens were explained using experimental results obtained from this test program. The presence of in-plane compression in shell specimens resulted in crushing failures of concrete in the compression zone without the complete failure of shear reinforcement. Thus, the failure mechanism of the shells was identified as that of shear-compression type. The lack of this in-plane compressive force in the plates resulted in failures due to failure of the shear resistance mechanisms.

5. EFFECTS OF TEST PARAMETERS ON PUNCHING SHEAR STRENGTH

5.1 INTRODUCTION

The effects of different parameters on punching shear strength of specimens in this test program are investigated in this chapter. Direct comparisons of normalized shear strengths are provided in order to examine the effects of the following test parameters:

1. Shear reinforcement ratio (ρ_v).
2. Radius-to-thickness ratio (R/t).
3. Span continuity.
4. Prestressing.
5. Size of area of loading.
6. Scale effect.

5.2 EFFECT OF SHEAR REINFORCEMENT RATIO

Plotted in Figure 5.1 are the normalized punching shear strengths of the test specimens versus the shear reinforcement index, $\rho_v f_y$. Three curves are shown in this figure. The first curve represents the normalized shear strengths of four plate specimens, FP2-1, FP2-2, FP3 and FP4. As indicated, the only difference between these specimens was the amount of shear reinforcement (0.0 to 0.44 percent). The second curve represents results of three shell specimens with R/t ratio of 12. These specimens, AS9, AS7 and AS11, contained 0, 0.24 and 0.48 percent shear reinforcement, respectively. The third curve represents results of two shell specimens with R/t ratio of 6, AS8 and AS12, which contained 0 and 0.24 percent shear reinforcement. The shear reinforcement index, $\rho_v f_y$, was used to account for the slight difference in the yield strength of the T-headed bars used in the plate and the shell specimens.

From the curve for the plate specimens, it is apparent that within the range of 0 to 0.44 percent shear reinforcement, the punching shear strength of the plate specimens increased proportionally with increasing shear

reinforcement ratio (or reinforcing index), with a rate of increase of approximately $1.3\sqrt{f'_c}$ per every additional 0.1 percent of shear reinforcement. The linear relationship between the punching shear strength and the shear reinforcing index suggests that, within the indicated range of shear reinforcement ratio, the shear reinforcement in the plate specimen was effectively utilized. This relationship further confirms that ultimate failure in plate specimens was the result of complete failure of all three basic shear resistance mechanisms, i.e. the restraint provided by the shear reinforcement, aggregate interlock, and dowel action. It is anticipated that at some point, the benefit from increasing the amount of shear reinforcement in the plate specimen would diminish. However, it is difficult to assess the optimum level of shear reinforcement in plate specimens without further testing of plates with shear reinforcement ratios higher than 0.44 percent.

Different from the plate specimens, the normallized shear strength-shear reinforcement index curve for the shell specimens with an R/t ratio of 12 shows an initially larger contribution of shear reinforcement to the punching shear strength of the shells, with a mean rate of increase in punching shear capacity of $1.9\sqrt{f'_c}$ for every 0.1 percent increase of shear reinforcement up to 0.24 percent. The rate of increase in punching shear strength in these shells, however, decreased significantly as the shear reinforcement ratio increased from 0.24 percent to 0.48 percent. This decrease, coupled with the fact that not all the shear bars bridging the cracks in specimens AS7 and AS11 had failed at ultimate load, is consistent with the explanation given for the failure mechanism of the shells. That is, complete failures in the shells were controlled by crushing of concrete in the compression zone. Since not all the shear bars in specimen with 0.24 percent shear reinforcement failed at ultimate load, the effective level of shear reinforcement for shells with R/t ratio of 12 is apparently smaller than 0.24 percent. This effective level of shear reinforcement can be considered the optimum level beyond which the contribution of shear reinforcement in punching shear strength is no longer significant.

For shells with R/t ratios of 6, only two data points were obtained (Figure 5.1). However, if a linear relationship can be assumed between these two data points, then the rate of increase in punching shear strength with increasing shear reinforcement ratio for these shells is consistent with the rate obtained for the plate specimens ($1.2\sqrt{f'_c}$ to compare with $1.3\sqrt{f'_c}$ in the plates). Like shells with an R/t ratio of 12, the shear reinforcement ratio of 0.24 percent in these shells also exceeds the optimum level since some of the shear bars bridging the cracks in specimen AS12 did not fail at ultimate.

5.3 EFFECT OF CURVATURE

The normalized shear strengths of four sets of data are plotted against the inverse of R/t ratios in Figure 5.2 to facilitate examination of effects of shell curvature on punching shear strength. The four curves shown in Figure 5.2 correspond to data obtained from specimens with: (1) no shear reinforcement (FP2's, AS9, and AS8), (2) 0.22 and 0.24 percent of shear reinforcement (FP3, AS7 and AS12), (3) 0.44 and 0.48 percent of shear reinforcement (FP4 and AS11), and (4) 0.22 and 0.24 percent of shear reinforcement and a prestress of 500 psi (FP5 and AS10).

In general, the curves that correspond to the cases of 0 and 0.44 percent of shear reinforcement show a consistent increase of $5\sqrt{f'_c}$ in punching shear strength as the curvature (t/R ratio) increases from 0 to 0.0833 (R/t of 12). Within this range of curvature, however, the line for specimens with prestress shows a smaller increase of approximately $4\sqrt{f'_c}$ and the line for specimens with 0.22 percent shear reinforcement shows a larger increase in punching shear strength of $6.7\sqrt{f'_c}$. This inconsistency appears to be caused by the high normalized shear strength obtained for specimen AS7.

Examination of lines corresponding to 0 and 0.22 percent shear reinforcement revealed that higher punching shear strength can be achieved by increasing the curvature of the specimens. However, the rate of increase in punching shear strength appears to decrease as the curvature increases. Further, in one of the shell specimens with larger curvature,

specimen AS8, a somewhat different crack pattern was observed. Lines of cracks developed on top and bottom of this specimen, parallel to the lines of supports. This appears to be the result of a combined in-plane compression and bending action. This development, which occurred only in AS8, coupled with the observation that the rate of increase in punching shear strength decreases with increasing curvature, suggests that further increase of shell curvature beyond the R/t ratio of 6 would result in a different mode of failure in the shell and no significant benefit in terms of shear strength could be achieved.

5.4 EFFECT OF SPAN CONTINUITY

The effect of span continuity is examined by comparing test results of the single span plate specimen FP1 and its three-span counterpart FP3. Specimen FP1 had a normalized punching shear strength that was approximately 20 percent higher than that of specimen FP3. This is due to the greater flexibility in the span direction of FP1. As explained in chapter 3, greater flexibility in the span direction allowed FP1 to undergo greater deformation. This deformation helped reduce stress in the shear reinforcement bridging the cracks. Higher load was therefore required to fail the shear reinforcement in this specimen in order to achieve complete failure, resulting in a higher punching shear capacity.

From this comparison, it is apparent that the relative stiffness of a specimen has an important influence on its shear carrying capability and the results obtained from the single span specimen must be considered as being unconservative when applied to the real multi-span structures.

5.5 EFFECT OF PRESTRESSING

Prestressing achieved little in improving the punching shear capacity of the specimens in this test program. Three comparisons were made regarding the effects of prestressing: (1) effect of one-way prestressing in plates, specimens FP3 and FP5, (2) effect of two-way prestressing in plates, specimens FP3 and FP6, and (3) effect of one-way prestressing in shells, specimens AS7 and AS10.

The test results in Table 3.1, show that the initial cracking loads for specimens with and without prestressing were nearly the same. This indicates that the concrete shear cracking load was not affected by the 500 psi prestress. In terms of punching shear capacity, one-way prestressing resulted in an increase in strength of approximately 9 percent and two-way prestressing resulted in an increase of approximately 19 percent in the plate specimens. However, one-way prestressing in shells resulted in a 14 percent decrease in punching shear strength. The contradictory effect of prestressing on the ultimate punching shear capacity of the plates and the shells in this testing program inhibited a definitive conclusion regarding the effect of prestressing.

Examination of the crack patterns on the cross-sections of the prestressed specimens revealed an influence of the tendon ducts on the orientation of shear cracks. The angle of cracks in the direction parallel to the direction of prestressing was steeper than the crack angle in the other direction. The primary shear cracks in all cases intersected the post-tensioning ducts.

5.6 EFFECT OF SIZE OF LOADED AREA

As the size of the loaded area increases relative to the surface area of concrete plate, at some point a transition from slab behavior to wide beam behavior takes place. It is common knowledge that the shear strength of concrete beams, due to many reasons such as the lack of natural restraint in the circumferential direction, the stress conditions in the concrete in the compression zone, and the smaller dowel forces, is less than that of a slab of similar dimensions. Thus, it is anticipated that the punching shear capacity of concrete slabs would diminish with the increase of size of loaded area. This is confirmed in this study by comparing the results of four plates with loaded areas of 50 in^2 (FP2-1 and FP2-2), 100 in^2 (IFP2-1), and 138 in^2 (IFP2-2). The normalized shear strengths of the above four specimens were plotted against their areas of loading to facilitate the examination of the influence of size of loaded area on punching shear strength, as shown on Figure 5.3. It can be seen that the normalized shear strength decreased with increasing area of loading.

5.7 SCALE EFFECT

The effect of scale is examined by superimposing the strength-displacement curves of the 1/4-scale specimens onto those of their 1/6-scale counterparts, as shown in Figures 5.4 and 5.5. Figure 5.4 shows the normalized shear strength-displacement curves of specimens 4FP3 and FP3. Figure 5.5 shows the normalized shear strength-displacement curves of specimens 4FP2s and FP2s. It should be noted that the displacements of the 1/4-scale specimens in these Figures have been reduced by a factor of 1.5 (6/4) in accordance with the similitude laws to facilitate comparison with the 1/6-scale specimens.

The normalized shear strength-displacement behavior and the ultimate normalized shear stresses in these specimens are essentially similar, with the exception that the initial stiffness of the 1/4-scale specimens are slightly higher than that of the 1/6-scale specimen. The measured shear stresses in the specimens with 0.22% of shear reinforcement (FP3 and 4FP3)

are $8\sqrt{f'_c}$ for the 1/6-scale and $8.15\sqrt{f'_c}$ for the 1/4-scale (a difference of approximately 2%). The measured shear stresses in specimens without shear reinforcement are $4.8\sqrt{f'_c}$ and $5.4\sqrt{f'_c}$ for FP2-1 and FP2-2, respectively, and $5.0\sqrt{f'_c}$ and $5.2\sqrt{f'_c}$ for 4FP2-1 and 4FP2-2 (a mean difference of approximately 0%). Thus, from these results it is reasonable to conclude that the effect of scale on the punching shear behavior of specimens in this test program is very minimal. The test results can therefore be reliably extrapolated to predict the responses of larger structures.

6. COMPARISON OF TEST RESULTS WITH ACI PREDICTIONS

6.1 INTRODUCTION

The applicability of the ACI code provisions for punching shear on high-strength lightweight concrete structures is examined in this chapter. To facilitate comparison of the test results and the ACI predictions, key provisions for punching shear of the ACI 318-83 building code [reference 6.1] are summarized. Discussions regarding limitations of ACI 318-83 are given in the following section.

6.2 SUMMARY OF THE ACI PROVISIONS FOR PUNCHING SHEAR

The current ACI code provisions offer two methods for the calculation of shear strength in concrete members. Both methods treat the maximum shear strength, V_n, as the sum of two independent quantities, V_c and V_s, where V_c is the shear strength provided by the concrete and V_s is the shear strength provided by the shear reinforcement.

The first method, outlined in the "special provisions for slabs and footings" (section 11.11 in reference 6.1), includes provisions which place an upper limit of $6b_o d\sqrt{f'_c}$ on the nominal shear strength V_n of all two-way, reinforced slabs, regardless of the amount of shear reinforcement. Further, this method limits the concrete shear strength V_c to $4b_o d\sqrt{f'_c}$ in slabs without shear reinforcement and $2b_o d\sqrt{f'_c}$ in slabs with shear reinforcement. The shear strength provided by the shear reinforcement V_s is computed by summing the forces required to yield all shear reinforcement crossing a 45^o failure surface defined by the ACI code. Finally, this method does not yet allow the shear enhancement benefit of the curvature-induced membrane compression to be accounted for.

The second method includes provisions that are considered more applicable to beams or one-way slabs (wide beams). As such, the component shear strengths V_s and V_c in this method are expressed in terms of the full effective cross section $b_w d$ instead of a critical circular section $b_o d$.

In this method, the calculation of V_s is essentially the same as in the first method. However, it should be noted that the effects of shear span versus effective depth ratio (represented by $M_u/V_u d$) and axial compression are allowed in the calculation of V_c. A summary of the ACI 318-83 provisions relevant to both methods is given in Table 6.1.

6.3 COMPARISON WITH ACI 318-83

The component shear strengths, V_c and V_s, and the nominal shear strength, V_n, of the specimens in this test program, calculated in accordance with the two ACI methods, are given in Tables 6.2 and 6.3. It should be noted that the concrete strength components, V_c, listed in these tables have been multiplied by a strength reduction factor of 0.85 to account for sand-lightweight concrete. To facilitate an examination of the ACI predictions, the code-predicted $V_{n(ACI)}$ and the measured normalized shear strengths of all specimens V_{test} were plotted against the shear reinforcement index ($\rho_v f_y$) as shown in Figure 6.1, and against the inverse of the R/t ratio as shown in Figure 6.2.

The thickened lines in Figures 6.1 and 6.2 represent the code-predicted shear strength, V_n, of the specimens in this test program. It can be seen from Figure 6.1 that, by placing an upper limit of $6b_o d\sqrt{f'_c}$ on the nominal shear strength of reinforced slabs, the "special provisions for slabs and footings" (first method) neglects any benefit from the additional shear reinforcement when the shear reinforcement ratio exceeds an effective level. For specimens in this test program, that effective level corresponds to a shear reinforcing index ($\rho_v f_y$) of 393 psi (or a shear reinforcing ratio ρ_v of 0.75 percent). Since the largest amount of shear reinforcement tested was 0.44 percent in the plate specimens (corresponding to a reinforcing index of 228 psi), and the shear strength of the plates increased linearly with increasing shear reinforcing index within the range examined, it is difficult to make a conclusive statement regarding the effective level of shear reinforcement implied by the code for reinforced slabs. More tests on plates with a larger shear reinforcing index may be needed to further examine this code-implied upper limit.

It is also apparent from Figures 6.1 and 6.2 that the code predictions using the first method become more conservative with increasing shear reinforcement ratio and curvature. This conservatism is due two reasons:

1. The limit of $2b_o d\sqrt{f'_c}$ imposed on V_c of slabs with shear reinforcement. By reducing the contribution of V_c from $4b_o d\sqrt{f'_c}$ to $2b_o d\sqrt{f'_c}$ when shear reinforcement is included, the code does not recognize any contribution of shear reinforcement unless a minimum amount of shear reinforcement is provided. For these specimens, this minimum amount is 0.31 percent (corresponding to a shear reinforcement index of 160 psi). In contrast, the test results for the plate specimens show that even with a modest increase of shear reinforcement index (less than 160 psi), the benefit in terms of increasing the punching shear strength can clearly be observed.
2. The "special provisions for slabs and footings" do not include the benefit of curvature-induced membrane compression.

The broken line in Figures 6.1 and 6.2 represent the ACI's strength predictions using the second method. The predicted V_n obtained from this method are less conservative than those predicted by the first method. However, the benefit of membrane compression allowed by this method is still insignificant when compared to the test results.

The conservativeness of the code can be quantitatively examined by comparing the measured component shear strengths and the component shear strengths predicted by the code. The measured shear strengths of the specimens V_{test} were divided into two components, V_c and V_s. V_c was determined as the measured punching shear strength of the unreinforced specimen, and V_s was computed as the difference between V_{test} and V_c. There are three reasons that led to this treatment. Firstly, since more than one shear crack developed on the cross-sections of all specimens and because the failure surfaces were not exactly conical, the area of the failure surfaces could not be computed accurately. Therefore the total amount of shear reinforcement passing through the failure surface of a

specimen could not be determined accurately. Second, it was observed that an undetermined amount of shear reinforcement in the shells did not yield at ultimate. This makes it more difficult to estimate the exact amount of shear reinforcement activated at failure. Third, such treatment ignored the interaction between the shear reinforcement and the concrete, making comparisons of experimental results and the ACI predictions more appropriate since similar treatment was used by the code.

The measured component shear strengths of the test specimens are listed in Table 6.4. Listed also in Table 6.4 are the ratios of the measured to code-predicted component shear strengths, and ratios of the measured shear strength V_{test} to shear strengths predicted by the two methods of ACI V_n. Several conclusions can be drawn by examining these ratios:

1. In reinforced and unreinforced slabs, the ratios V_c/V_{cACI} and V_s/V_{sACI} show that the code was more conservative in predicting the concrete shear strength V_c than in predicting the shear strength provided by the shear reinforcement V_s. This is the direct result of the minimum shear reinforcement requirement implied in the "special provisions for slabs and footings" which in effect reduces V_c in reinforced slab by halves. For the unreinforced slabs (specimens FP2-1 and FP2-2), the ratio V_c/V_{cACI} was equal to 1.5. However, this ratio doubled (V_c/V_{cACI} = 3.0) when shear reinforcement was present. The ratio V_s/V_{sACI} for slabs with shear reinforcement showed that the code underestimated the strength provided by the shear reinforcement by a factor of approximately 2.1 (FP3 and FP4). This was 30 percent less conservative than the prediction for concrete strength V_c. However, when the effects of prestressing and single span were accounted for, the V_s/V_{sACI} ratio increased to 2.7.

2. The code predictions using the "special provisions for slabs and footings" were more conservative in predicting strength of shells since these provisions exclude the benefit of the curvature-induced membrane compression. In unreinforced shells, the concrete strength

components, V_c, of specimens with R/t ratio of 12, were underestimated by a factor of 3.0. This factor increased to 3.6 when the curvature of the shell was doubled (R/t of 6). In reinforced shells, a mean V_c/V_{cACI} ratio of 5.9 was obtained for shells with R/t of 12, and a ratio of 7.1 was obtained for shells with R/t of 6. By comparing the rate of increase of these ratios with respect to increasing curvature, it is apparent that the code became less conservative with increasing curvature. An average V_s/V_{sACI} ratio of 2.3 was obtained for all shell specimens with shear reinforcement. This ratio was slightly smaller than that of the plates (2.7), which reflects the fact that not all the shear reinforcement crossing the crack in the shell specimens yielded at ultimate load.

3. The underestimation of V_s can be attributed to: a) the assumption by ACI that shear cracks are at a 45^o angle with the horizontal plane and, b) the disregard by ACI of the influence the shear reinforcement might have on the growth of inclined cracking. The presence of shear reinforcement across the crack results in larger interface shear transfer capacity, which ultimately enhances the shear strength. In addition, it was observed from the cross-sections of the specimens that the crack angles on the failure surface in all cases were less than 45^o. This means that more shear reinforcement had been activated to resist the applied shear stress than the amount recognized by ACI.

4. The ratio V_{test}/V_{nACI} was 1.5 for unreinforced plates, 3.0 for unreinforced shells with R/t of 12, and 3.6 for unreinforced shells with R/t of 6. For specimens with shear reinforcement, this ratio is 2.8 for plates, 4.1 for shells with R/t of 12, and 4.2 for shells with R/t of 6.

6.4 SUMMARY

Quantitative comparisons of the experimentally-obtained normalized shear strengths and the ACI predictions are provided in this chapter. In most cases, the code was more conservative in predicting the shear strength provided by the concrete (V_c) than the strength provided by the shear reinforcement (V_s). The conservatism of the code is amplified by the provision which implied a minimum effective ratio of shear reinforcement (0.31 percent) for reinforced slabs. The lack of consideration for the contribution of membrane action in the "special provisions for slabs and footings" resulted in more conservative estimates for curved specimens. Finally, the assumption of a 45^{o} angle shear crack and the disregard of the ability of crack to transfer shear, especially when shear reinforcement is present, were identified as the reasons for the underestimations of shear strength provided by the shear reinforcement V_s.

7. SUMMARY AND CONCLUSIONS

7.1 SUMMARY

A total of fifteen 1/6-scale specimens, including nine flat plates and six arched shells, and three 1/4-scale plates were tested to study the punching shear behavior of lightweight concrete plates and shells. Two distinct modes of punching shear failure resulted in the plates and the shells. In the plates, failure was due to the failure of all three basic shear resistance mechanisms: resistance provided by the steel reinforcement, aggregate interlock, and dowel action. In the shells, the presence of membrane compression associated with the curvature of the shell resulted in a mode of failure similar to the shear-compression mode in deep beams. Ultimate failure in the shells was governed by the crushing of concrete in the compression zone.

For all specimens, experimental evidence indicated that internal shear cracking developed first in the mid-depth region of the specimens. The redistribution of flexural strain was more extensive in specimens without shear reinforcement than it was in specimens with shear reinforcement. This indicated the influence of shear reinforcement in restraining growth of inclined shear cracks. Visual observations made during tests of the shell specimens indicated a brittle mode of failure. However, empirical evidence indicated that cracks developed gradually in these specimens.

7.2 CONCLUSIONS

The following conclusions regarding the ACI code provisions for punching shear and the effects of major variables studied in this program were drawn from the test results:

1. Within the range of shear reinforcing ratios examined in this test program (0 to 0.48 percent), any increase in the amount of shear

reinforcement will result in a proportional increase in the punching shear capacity of plates. In shells, the rate of increase in punching shear strength decreases with increasing amount of shear reinforcement.

2. Punching shear strength is greatly increased when the curvature-induced membrane compression is present. However, the rate of increase in punching shear strength due to membrane compression decreases with increasing curvature. The presence of curvature in the shell specimens resulted in brittle failure which was governed by the crushing of concrete in the compression zone. Total failure occurred in shells without complete yielding of the shear reinforcement on the failure surface.

3. Failures in the shells were very sudden. There was neither clear sign of the impending collapse nor much reserve capacity after ultimate load was reached. However, substantial empirical evidence suggested that inclined shear cracks in the shells developed at lower loads, and the radial and circumferential propagation of shear cracks in the shells were gradual with respect to the increase of loading.

4. The ACI code provisions are very conservative with respect to the results obtained from this test program. Further, the code is more conservative in predicting the shear strength of concrete than in predicting the shear strength provided by the shear reinforcement. Underestimation of shear strength provided by the concrete is amplified by the reduction of V_c by half when shear reinforcement is included. This reduction implies that the code does not recognize the contribution of shear reinforcement until a minimum amount is provided, corresponding to 0.31 percent in this test program. In contrast, test results showed that significant increases in shear strength can be achieved even with a modest increase of shear reinforcement. Underestimation of V_s was due to

the steeper crack angle assumed by the Code (45^{o}) and the disregard of the concrete-shear reinforcement interaction.

5. The upper limit of shear strength imposed by the code ($6b_{o}d\sqrt{f'_{c}}$) is not particularly meaningful with respect to this study, since all specimens with shear reinforcement showed much higher punching shear capacities.

6. The results of the prestressed specimen tests were inconclusive. Prestressing with 500 psi (3.45 MPa) achieved very little in terms of improving the punching shear capacity of the specimens in this testing program.

7.3 FUTURE RESEARCH NEEDS

This research has provided insight into the mechanics of punching shear in thick, lightweight concrete plates and shells typical of Arctic offshore structures. Effects of several key variables on the punching shear behavior of these specimens, and the effectiveness of T-headed bars as shear reinforcements were investigated. Conservatism in the current ACI code provisions for punching shear when applied to heavily reinforced, thick plates and shells was identified. In light of the results of this study, the following areas are suggested for further investigation:

1. Effects of prestressing with smaller tendon ducts and higher prestress (higher than 500 psi).

2. Smaller shear-span/effective-depth ratio (a/d or $V_{u}d/M_{u}$).

3. Parameter study using analytical model which can account for the nonlinear behavior of cracked concrete.

8. BIBLIOGRAPHY

2.1 Phan, L.T., Lew, H.S., Mclean, D.I., "Punching Shear Resistance of Lightweight Concrete Offshore Structures for the Arctic: Planning of Experimental Study", NBSIR 86-3440, National Bureau of Standards.

2.2 Mclean, D.I., Lew, H.S., Phan, L.T. and Sansalone, M., "Punching Shear Resistance of Lightweight Concrete Offshore Structures for the Arctic: Literature Review", NBSIR 86-3388, National Bureau of Standards.

2.3 Sabnis, G.M., Harris, H.G., White, R.N. and Mirza, M.S., "Structural Modeling and Experimental Techniques", Prentice-Hall, 1983.

2.4 Harris, H.G., "Use of Structural Models as an Alternative to Full Scale Testing", Full-Scale Load Testing of Structures, ASTM STP 702, Shriever, W.R., Ed., American Society for Testing and Materials, 1980, pp. 25-44.

2.5 American Concrete Institute Committee 444, "Models of Concrete Structure", SP-24, ACI, Detroit, Mich., 1970.

2.6 Bhula, D.N., Birdy, J.N. and Bruen, F.J., "Design of Concrete Gravity Structures to Withstand Concentrated Ridge and Flow Impact Loads". Proceedings 1984 Offshore Technology Conference, OTC 4708, Houston, Texas.

2.7 "Experimental Work on Punching Shear Resistance of Concrete Structures for the Arctic", Brian Watt Associates, Inc. AOGA project no. 152.

2.8 Buslov, V.M., and Krahl, N.W. (Brown and Root Inc.), "Fifty-One New Concepts for Arctic Drilling and Production". Part 1, Ocean Engineering, 1983.

2.9 Schlecten, J.R., Fernandes, R.L., Dolan, D.K., and Bivens, H.R., "Analysis and Design of an Ice Wall Framing System for an Arctic Drilling Structure". Proceedings, 1984 Offshore Technology Conference, OTC 4691, Houston, Texas.

2.10 Byrd, R.C., Coleman, R.K., Weiss, R.T., Boaz, I.B., Sauve, E.R., and White, R.M., "The Arctic Cone Exploration Structure: A Mobile Offshore Drilling Unit for Heavy Ice Cover". Proceedings 1984 Offshore Technology Conference, OTC 4800, Houston, Texas.

2.11 Wetmore, S.B., "The Concrete Island Drilling System: Super Series (Super CIDS)". Proceedings 1984 Offshore Technology Conference, OTC 4801, Houston, Texas.

2.12 Gerwick, B.C., Potter, R.E., and Rojansky, M., "Development of a Structural Concept to Resist Impacts from Multi-Year Ice Floes, Ridges, and Icebergs". Proceedings 1984 Offshore Technology Conference, OTC 4799, Houston, Texas.

6.1 "Building Code Requirements for Reinforced Concrete, ACI 318-83". Reported by ACI Committee 318, American Concrete Institute, Detroit, Michigan, 1983.

Table 2.1 Similitude Requirements for Reinforced Concrete Modeling

QUANTITY	DIMENSION	SCALE FACTOR FOR PRACTICAL TRUE MODEL
Concrete stress	FL^{-2}	1
Concrete strain	-	1
Modulus of concrete	FL^{-2}	1
Poisson's ratio	-	1
Mass density	FL^{-3}	$1/S_1$
Reinforcing stress	FL^{-2}	1
Reinforcing strain	-	1
Modulus of Reinforcing	FL^{-2}	1
Bond stress	FL^{-2}	1
Linear dimension	L	S_1
Displacement	L	S_1
Angular displacement	-	1
Area of reinforcement	L^2	S_1^2
Concentrated load	F	S_1^2
Line load	FL^{-1}	S_1
Pressure	FL^{-2}	1
Moment	FL	S_1^3

Table 2.2 Typical Concrete Mix Design

MATERIALS	WEIGHT PER CU. YARD (lbs)
Portland Cement Type I	806
Solite Lightweight Aggregate, 1/2 in. max	1025
Sand	1076
Corrocem	96
Water	210.4
Daravair AEA (Oz)	30

TABLE 2.3 DESCRIPTIONS OF TEST SPECIMENS

Specimen No.	Scale	Thickness (in)	Area of Loading (in^2)	Shear Reinforcing Ratio (%)	Flexural Reinforcing Ratio * (%)	Prestress (500 psi)	R/t Ratio	Geometry
FP1	1/6	7	50	0.22	1.75	NO	-	Single-Span Plate
FP2-1	1/6	7	50	0	1.75	NO	-	Three-Span Plate
FP2-2	1/6	7	50	0	1.75	NO	-	Three-Span Plate
FP3	1/6	7	50	0.22	1.75	NO	-	Three-Span Plate
FP4	1/6	7	50	0.44	1.75	NO	-	Three-Span Plate
FP5	1/6	7	50	0.22	1.75	One-Way	-	Three-Span Plate
FP6	1/6	7	50	0.22	1.75	Two-Way	-	Three-Span Plate
IFP2-1	1/6	7	138	0	2.50	NO	-	Three-Span Plate
IFP2-2	1/6	7	100	0	2.50	NO	-	Three-Span Plate
AS7	1/6	5	50	0.24	1.75	NO	12	Arched Shell
AS8	1/6	5	50	0	1.75	NO	6	Arched Shell
AS9	1/6	5	50	0	1.75	NO	12	Arched Shell
AS10	1/6	5	50	0.24	1.75	One-Way	12	Arched Shell
AS11	1/6	5	50	0.48	1.75	NO	12	Arched Shell
AS12	1/6	5	50	0.24	1.75	NO	6	Arched Shell
4FP2-1	1/4	10.5	100	0	1.75	NO	-	Three-Span Plate
4FP2-2	1/4	10.5	100	0	1.75	NO	-	Three-Span Plate
4FP3	1/4	10.5	100	0	1.75	NO	-	Three-Span Plate

* Ratio of flexural reinforcement on one face and in one direction

TABLE 3.1 SUMMARY OF TEST RESULTS

Specimen No.	Compressive Strength (psi)	Initial cracking load P_{cr} (Kips)	V_{cr} $(P_{cr}/b_o d\sqrt{f'_c})$	Ultimate load P_u (Kips)	Nonmalized shear strength $V_{test} = P_u/bod\sqrt{f'_c}$
FP1	7780	76	3.4	216.8	9.8
FP2-1	9010	90	3.8	114.9	4.8
FP2-2	8810	98	4.2	126.9	5.4
FP3	9320	90	3.7	195.1	8.0
FP4	8810	100	4.2	251.9	10.7
FP5	8610	87	3.7	202.2	8.7
FP6	8610	85	3.6	221.3	9.5
AS7	7790	93	7.2	190.6	14.7
AS8	7310	108	8.6	152.0	12.1
AS9	7030	92	7.5	124.3	10.1
AS10	6750	87	7.2	152.1	12.6
AS11	7200	95	7.6	192.4	15.4
AS12	6010	106	9.3	170.1	14.9
4FP2-1	8988	167	3.1	271.0	5.0
4FP2-2	8332	-	-	270.0	5.2
4FP3	6875	158	3.2	404.2	8.1

Table 6.1 ACI PUNCHING SHEAR PROVISIONS

Parameters	Special Provisions For Slabs & Footings	General Provisions For Concrete Members	
		Shear & Flexure Only	Shear, Flexure & Axial Compression
Critical Section	d/2	d/2	d/2
Critical Perimeter, b_o	$\pi(D + d)$	$\pi(D + d)$	$\pi(D + d)$
Active Shear Rein. Zone	$\pi d(D + d)$	$\pi d(D + d)$	$\pi d(D + d)$
Area of Active Shear Rein., ΣA_v	$\pi\rho_v d(D + d)$	$\pi\rho_v d(D + d)$	$\pi\rho_v d(D + d)$
Shear Strength of Concrete, V_c (w/o Shear Rein.)	$(2 + 4/\beta_c)b_o d\sqrt{f'_c}$	$(1.9\sqrt{f'_c} + 2500\rho_w V_u d/M_u)b_w d$	$(1.9\sqrt{f'_c} + 2500\rho_w V_u d/M_m)b_w d$ $M_m = M_u - N_u(4h - d)/8$
Shear Strength of Concrete, V_c (w/ Shear Rein.)	$2b_o d\sqrt{f'_c}$	"	"
Shear Strength of Rein., V_s	$\Sigma A_v f_y$	$\Sigma A_v f_y$	$\Sigma A_v f_y$
Conditions	$\beta_c \geq 2.0$ $V_n \leq 6.0b_o d\sqrt{f'_c}$	$V_c \leq 3.5b_w d\sqrt{f'_c}$ $V_s \leq 8.0b_o d\sqrt{f'_c}$	$V_c \leq 3.5b_w d\sqrt{f'_c}/(1 + N_u/500$ $V_s \leq 8.0b_o d\sqrt{f'_c}$

Table 6.2 Predicted Component and Nominal Shear Strengths for Test Specimens According to ACI's Special Provisions for Slabs and Footings.

Specimen No.	$V_{c_{ACI}}$(*) (x $b_o d\sqrt{f'_c}$)	$V_{s_{ACI}}$ (x $b_o d\sqrt{f'_c}$)	$V_{n_{ACI}}$ ($V_c + V_s$)
FP1	1.7	1.3	3.0
FP2-1	3.4	0	3.4
FP2-2	3.4	0	3.4
FP3	1.7	1.3	3.0
FP4	1.7	2.6	4.3
FP5	1.7	1.3	3.0
FP6	1.7	1.3	3.0
IFP2-1	3.4	0	3.4
IFP2-2	3.4	0	3.4
AS7	1.7	1.3	3.0
AS8	3.4	0	3.4
AS9	3.4	0	3.4
AS10	1.7	1.3	3.0
AS11	1.7	2.6	4.3
AS12	1.7	1.3	3.0
4FP2-1	3.4	0	3.4
4FP2-2	3.4	0	3.4
4FP3	1.7	1.3	3.0

(*) All V_c terms were multiplied by a factor of 0.85 to account for sand-lightweight concrete.

Table 6.3 Predicted Component and Nominal Shear Strengths for Test Specimens According to ACI's Second Method.

Specimen No.	$V_{c_{ACI}}$ (*) ($x\ b_o d\sqrt{f'_c}$)	$V_{s_{ACI}}$ ($x\ b_o d\sqrt{f'_c}$)	$V_{n_{ACI}}$ ($V_c + V_s$)
FP1	2.6	1.3	3.9
FP2-1	2.6	0	2.6
FP2-2	2.6	0	2.6
FP3	2.6	1.3	3.9
FP4	2.6	2.6	5.2
FP5	2.6	1.3	3.9
FP6	2.6	1.3	3.9
IFP2-1	2.9	0	2.9
IFP2-2	2.9	0	2.9
AS7	3.0	1.3	4.3
AS8	3.1	0	3.1
AS9	3.0	0	3.0
AS10	3.0	1.3	4.3
AS11	3.0	2.6	5.6
AS12	3.1	1.3	4.4
4FP2-1	2.6	0	2.6
4FP2-2	2.6	0	2.6
4FP3	2.6	1.3	3.9

(*) All V_c terms were multiplied by a factor of 0.85 to account for sand-lightweight concrete.

Table 6.4 Ratios of Measured versus Code-Predicted Shear Strength

SPECIMEN No.	$\frac{V_{test}}{V_{nACI}}$	$\frac{V_c}{V_{cACI}}$	$\frac{V_s}{V_{sACI}}$
FP1	3.2	3.0	3.46
FP2-1	1.4	1.4	-
FP2-2	1.6	1.6	-
FP3	2.6	3.0	2.1
FP4	2.4	3.0	2.1
FP5	2.8	3.0	2.6
FP6	3.1	3.0	3.2
AS7	4.8	5.9	3.4
AS8	3.6	3.6	-
AS9	3.0	3.0	-
AS10	4.1	5.9	1.9
AS11	3.5	5.9	1.9
AS12	4.9	7.1	2.1
4FP2-1	1.5	1.5	-
4FP2-2	1.53	1.53	-
4FP3	2.7	3.0	2.3

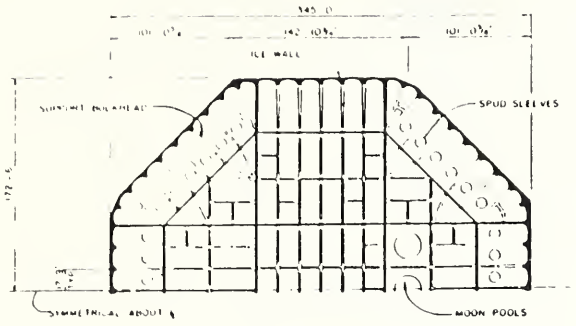

plan view

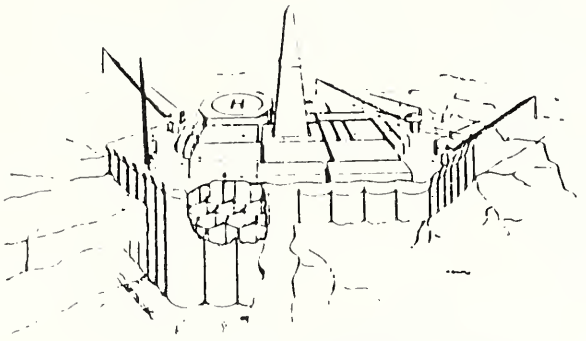

perspective view

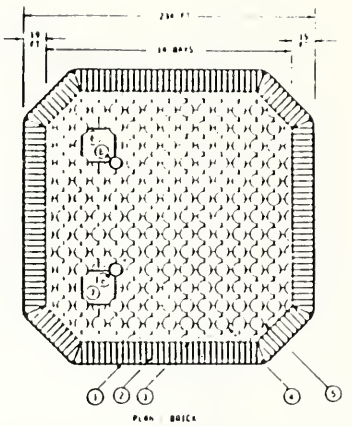

brick structural arrangement

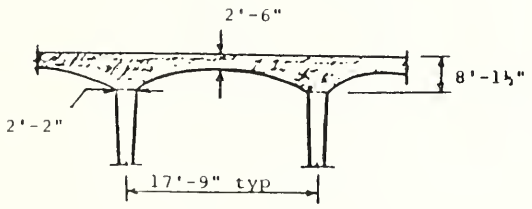

detail of wall

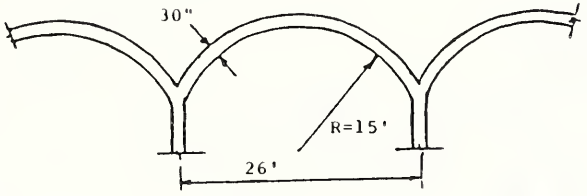

wall detail

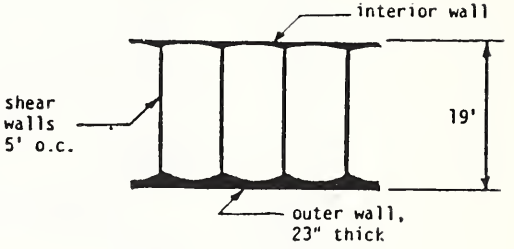

outer wall dimensions

(a) (b) (c)

Figure 2.1 Typical Arctic Offshore Concrete Structures
(a) Sohio Arctic Mobile Structure (SAMS)
(b) Brian Watts Associates Caisson System (BWACS)
(c) Concrete Island Drilling System: Super Series (Super CIDS)

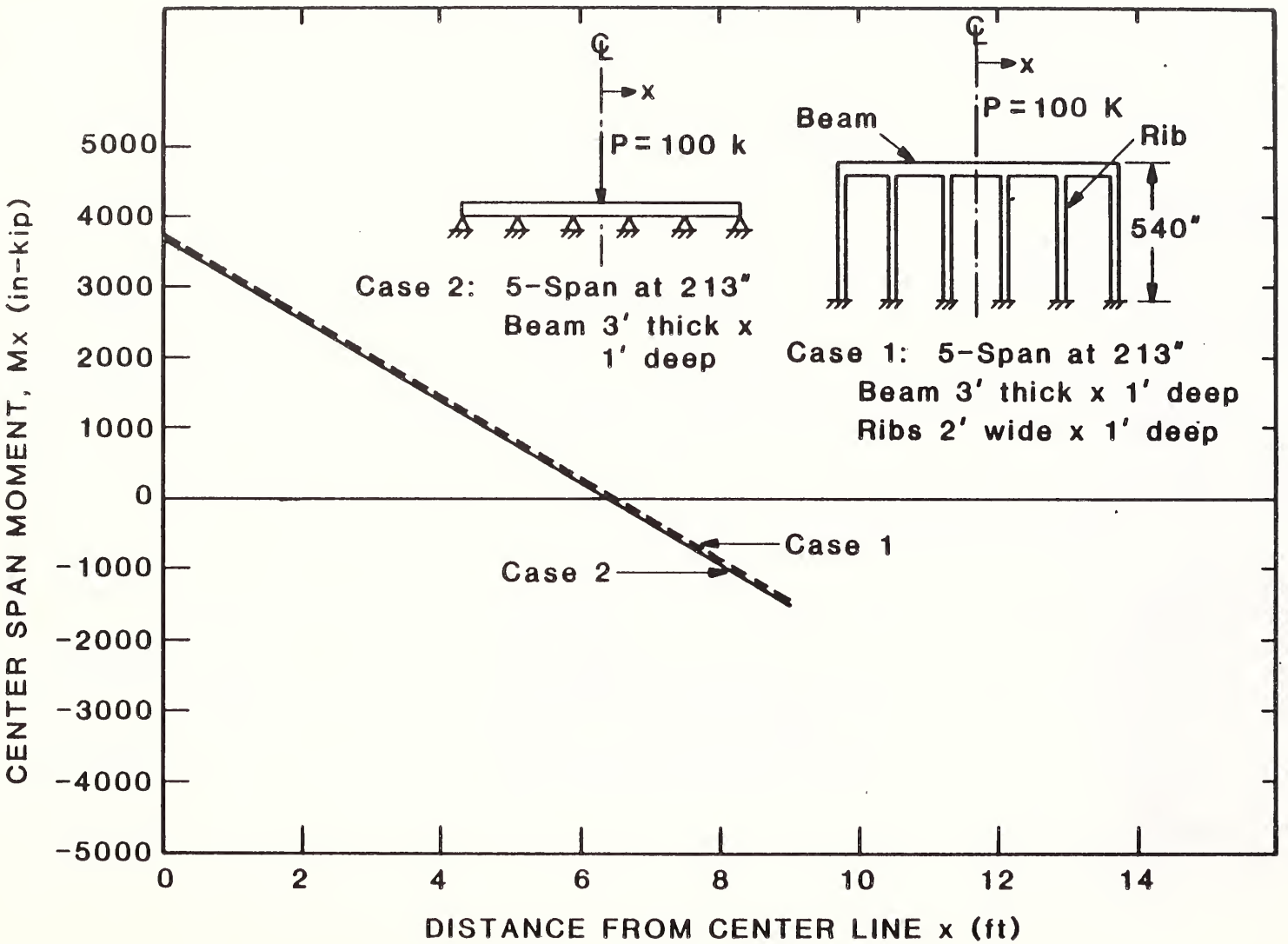

Figure 2.2 Distribution of Center Span Moment in Beams with Different Support Conditions

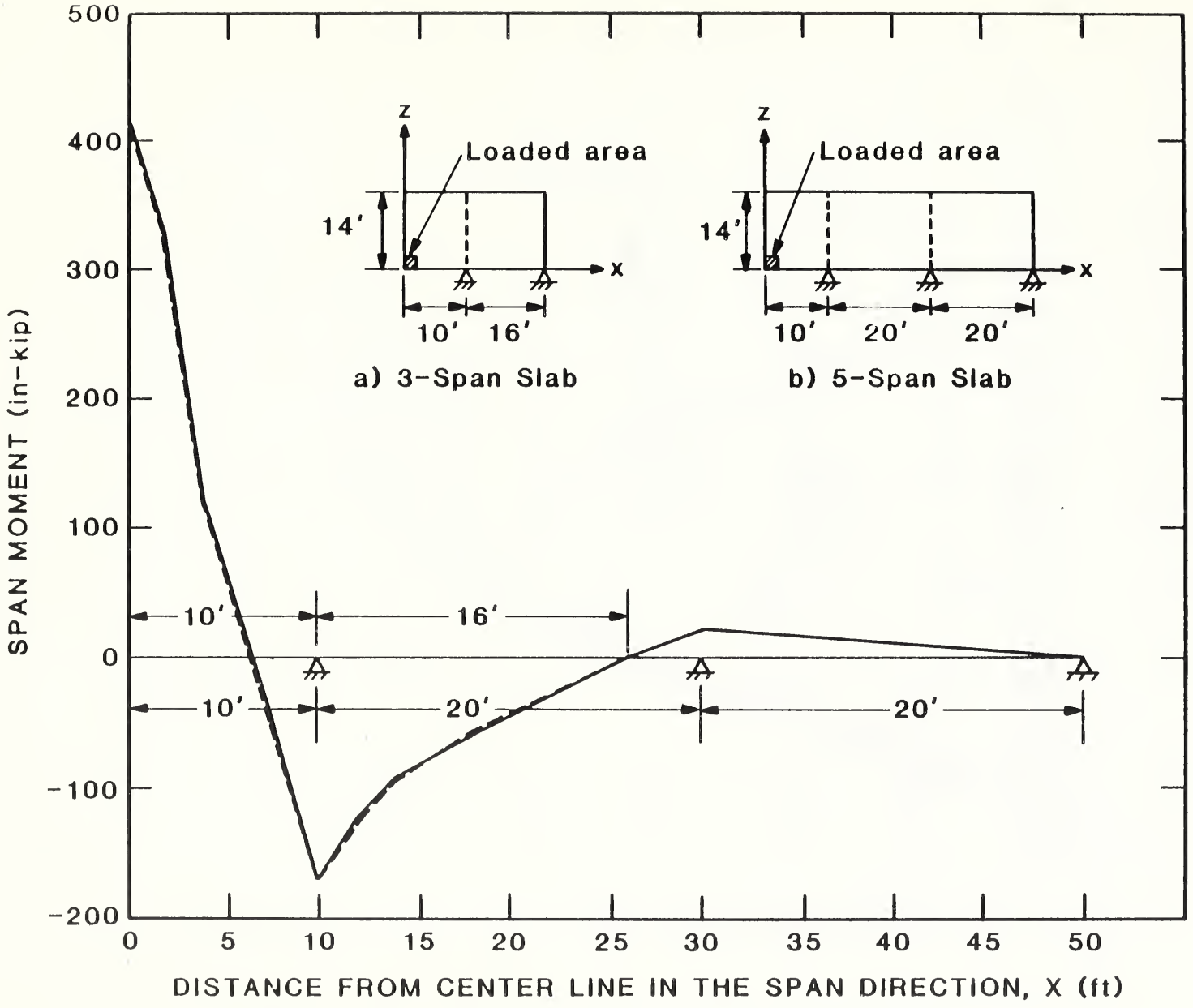

Figure 2.3 Distribution of Center Span Moment in Three and Five-Span Plates

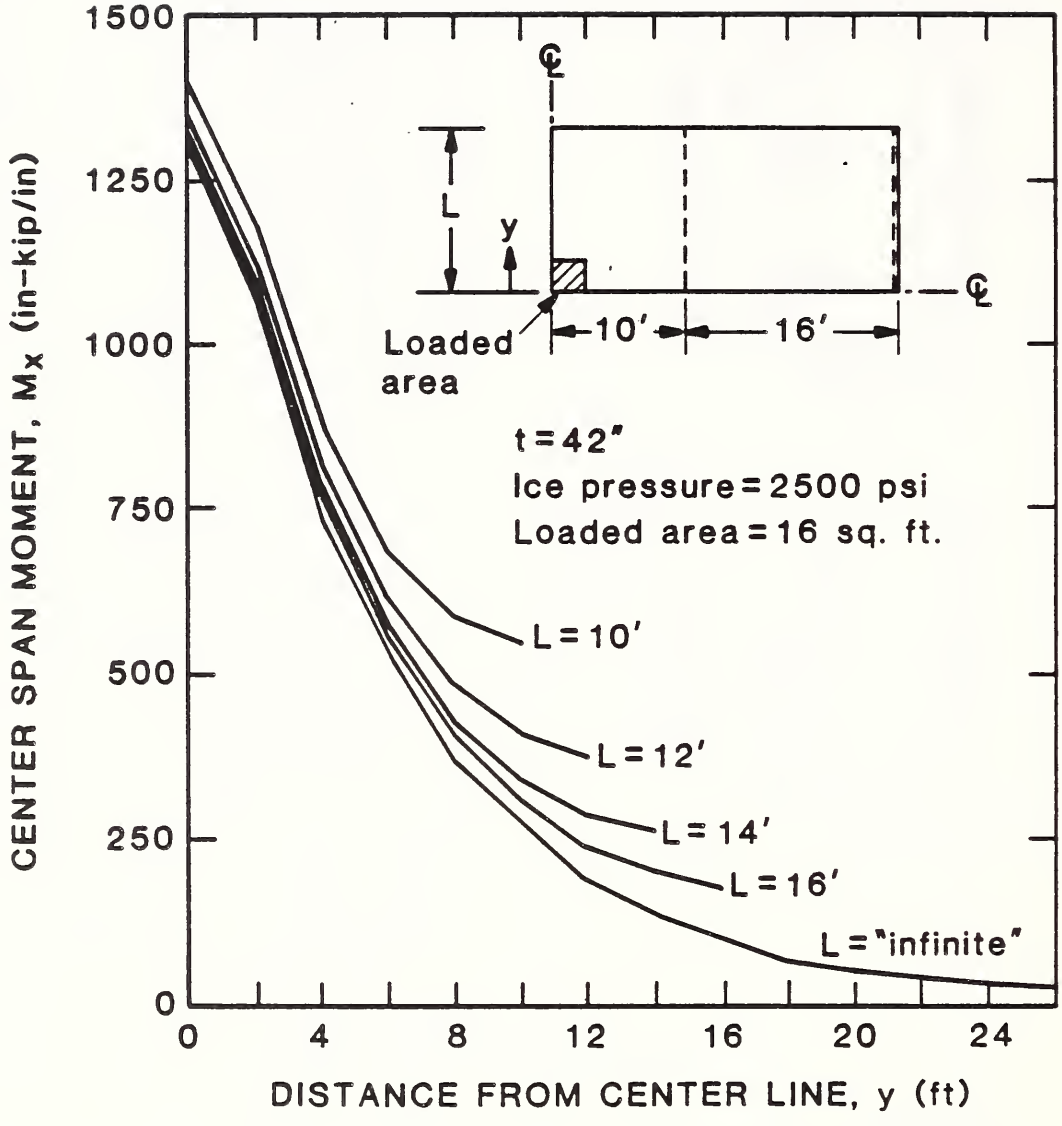

Figure 2.4 Distribution of Center Span Moment in the Transverse Direction of Plates with Different Transverse Lengths

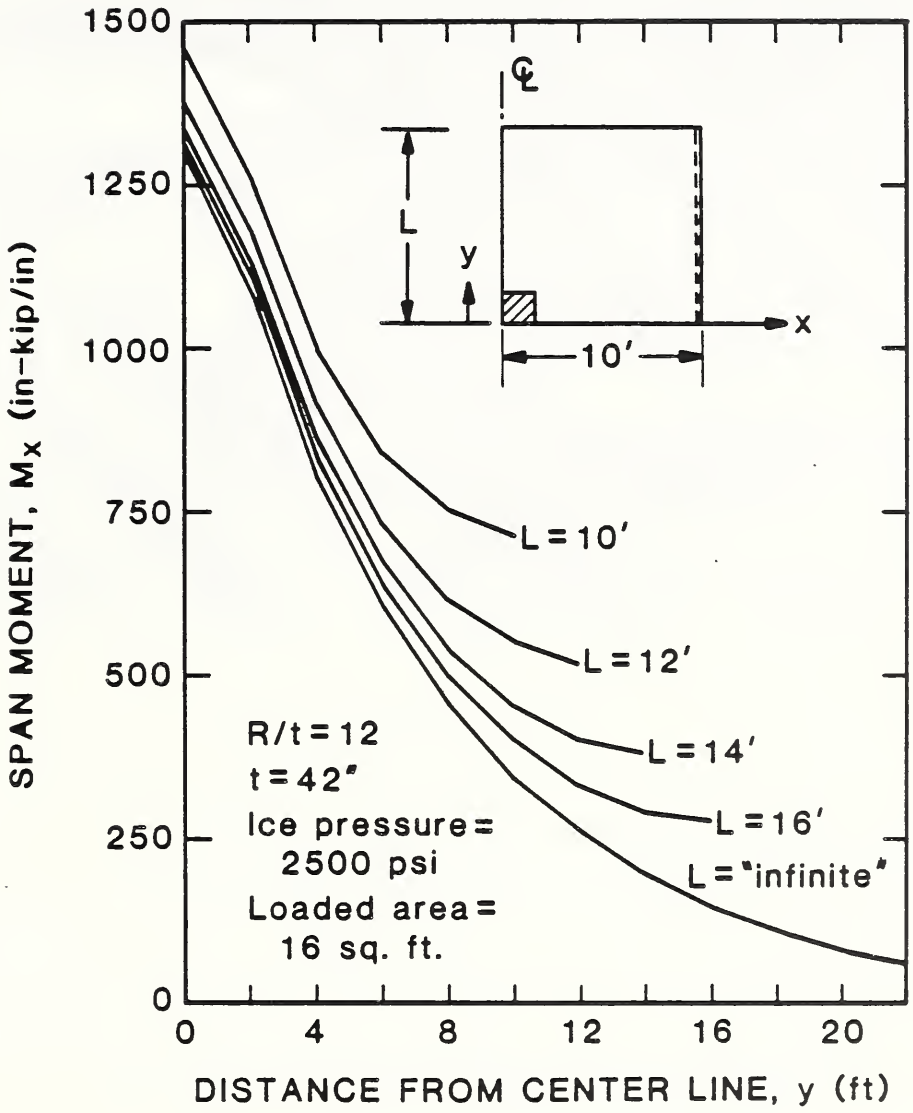

Figure 2.5 Distribution of Center Span Moment in the Transverse Direction of Shells with Different Transverse Lengths

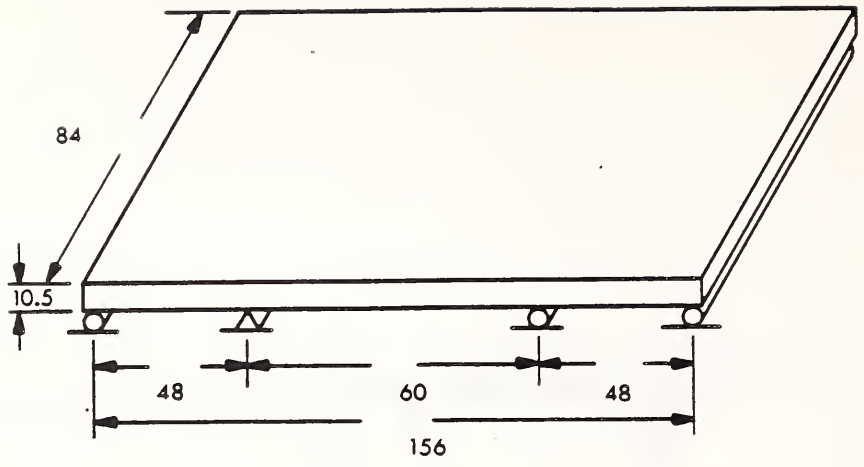

(1) Three-Span Plate (1/4-Scale)

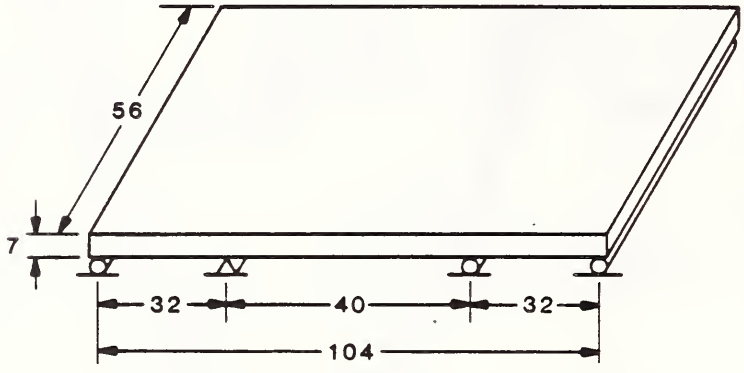

(2) Three-Span Plate (1/6-Scale)

All dimensions in inches

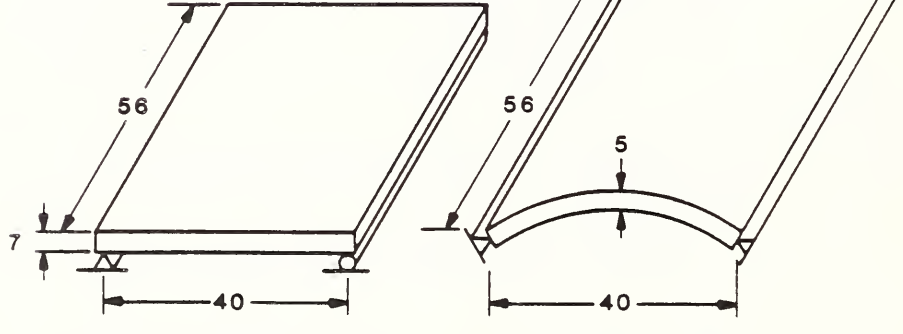

(3) Single Span Plate (4) Arched Shell Plate

Figure 2.6 Geometries, Dimensions, and Boundary Conditions of the 1/6 and 1/4-Scale Specimens

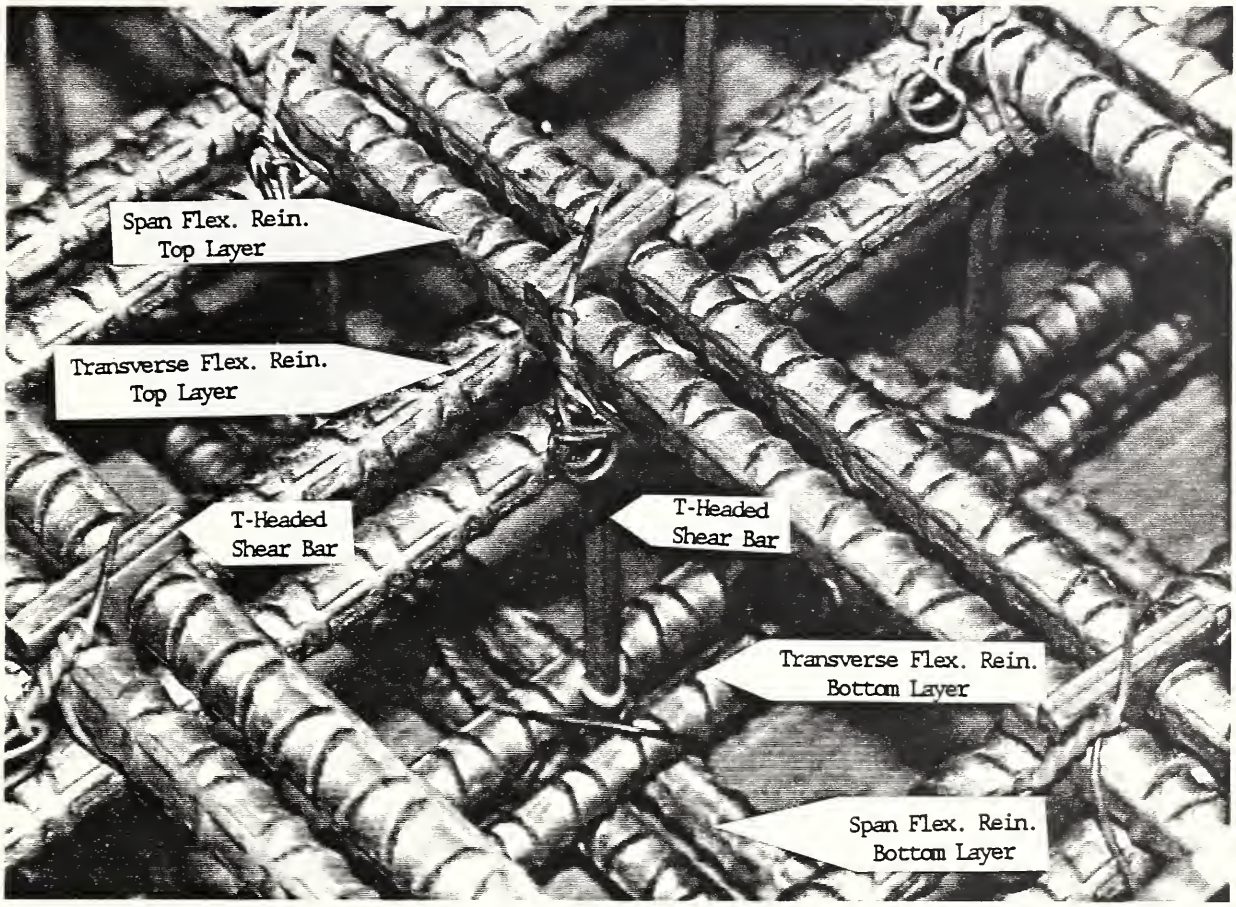

(a)

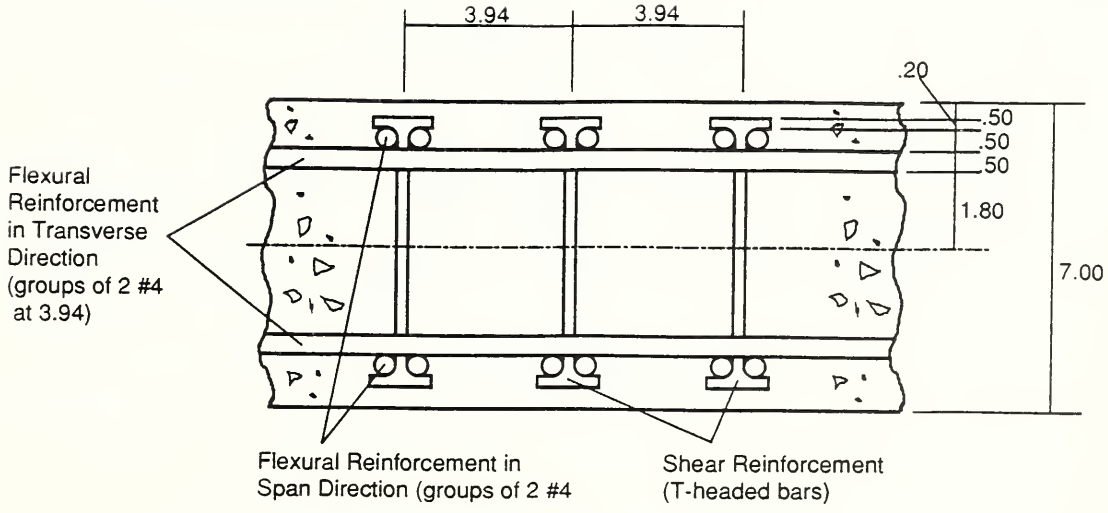

(b)

Figure 2.7 Arrangments of Flexural and Shear Reinforcements in the 1/6- and 1/4-Scale Specimens
(a) General Arrangement
(b) 1/6-Scale Plate
(c) 1/4-Scale Plate
(d) 1/6-Scale Shell

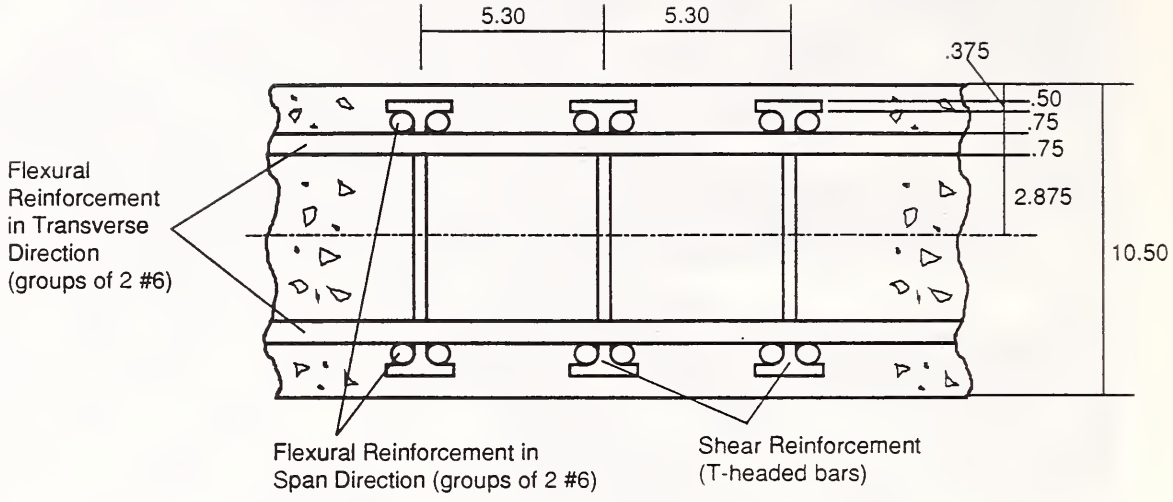

(c)

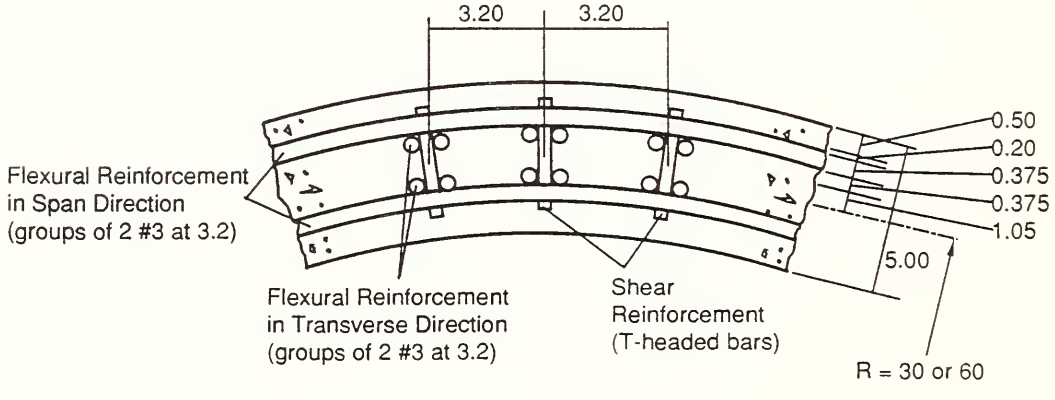

(d)

Figure 2.7 (continued)

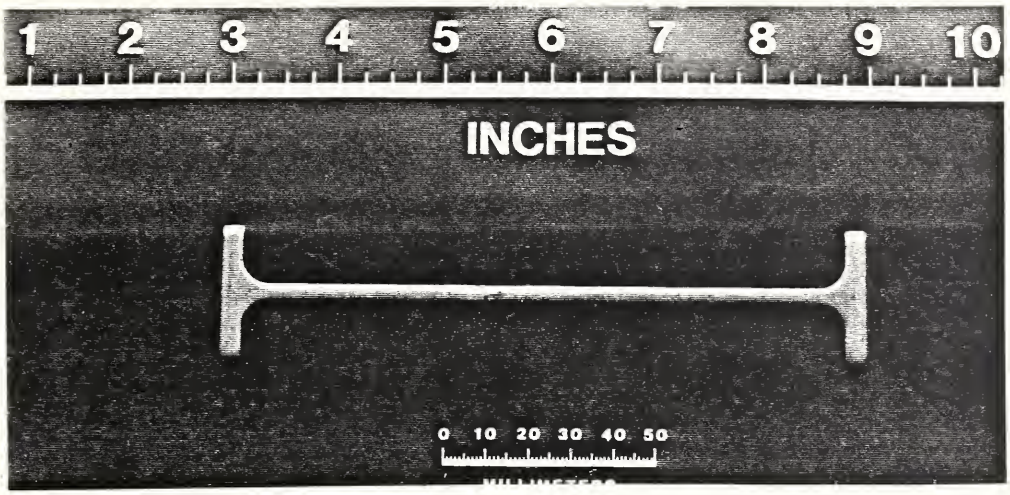

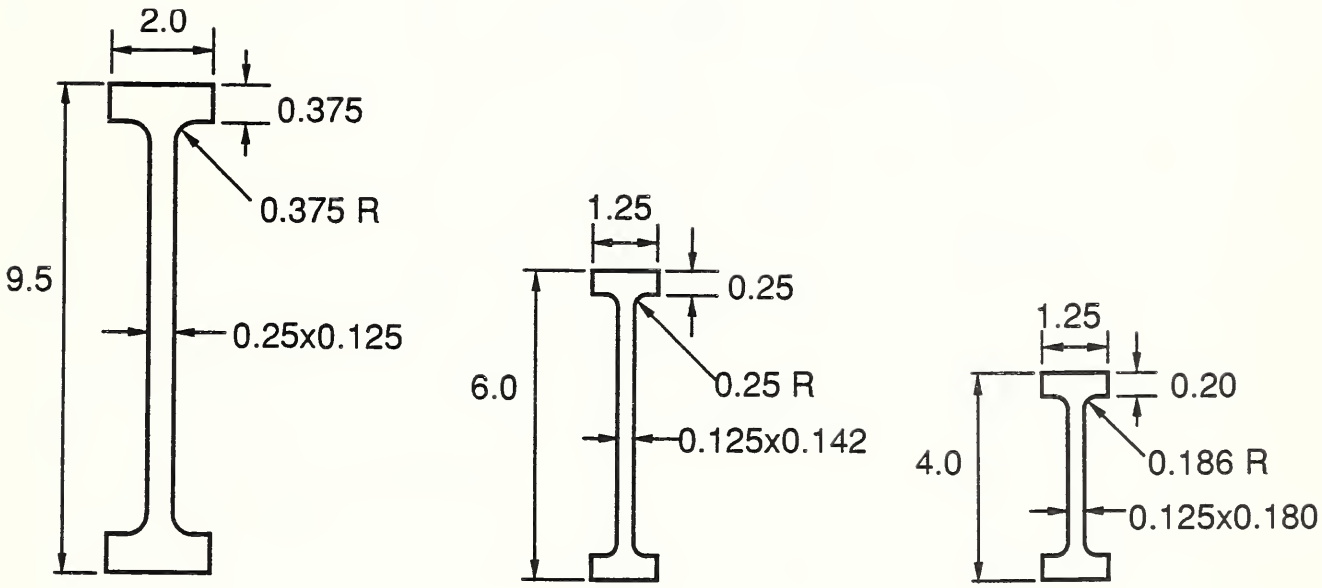

Figure 2.8 Dimensions and Configuration of the T-Headed Shear Bars used in the 1/6- and 1/4-Scale Specimens
(a) Shear Bar in 1/4-Scale Plate
(b) Shear Bar in 1/6-Scale Plate
(c) Shear Bar in 1/6-Scale Shell

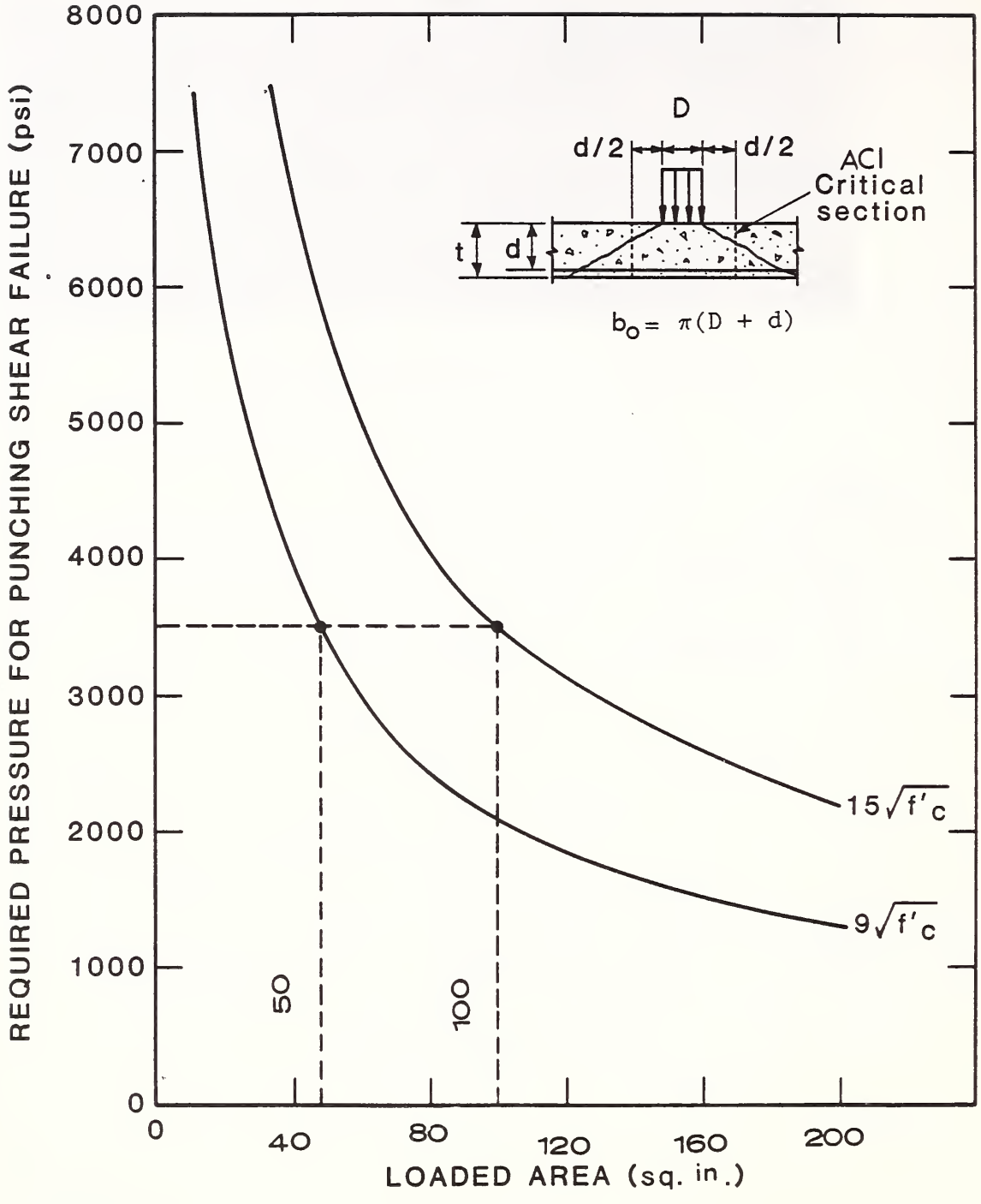

Figure 2.9 Predicted Punching Shear Pressure versus Loaded Area

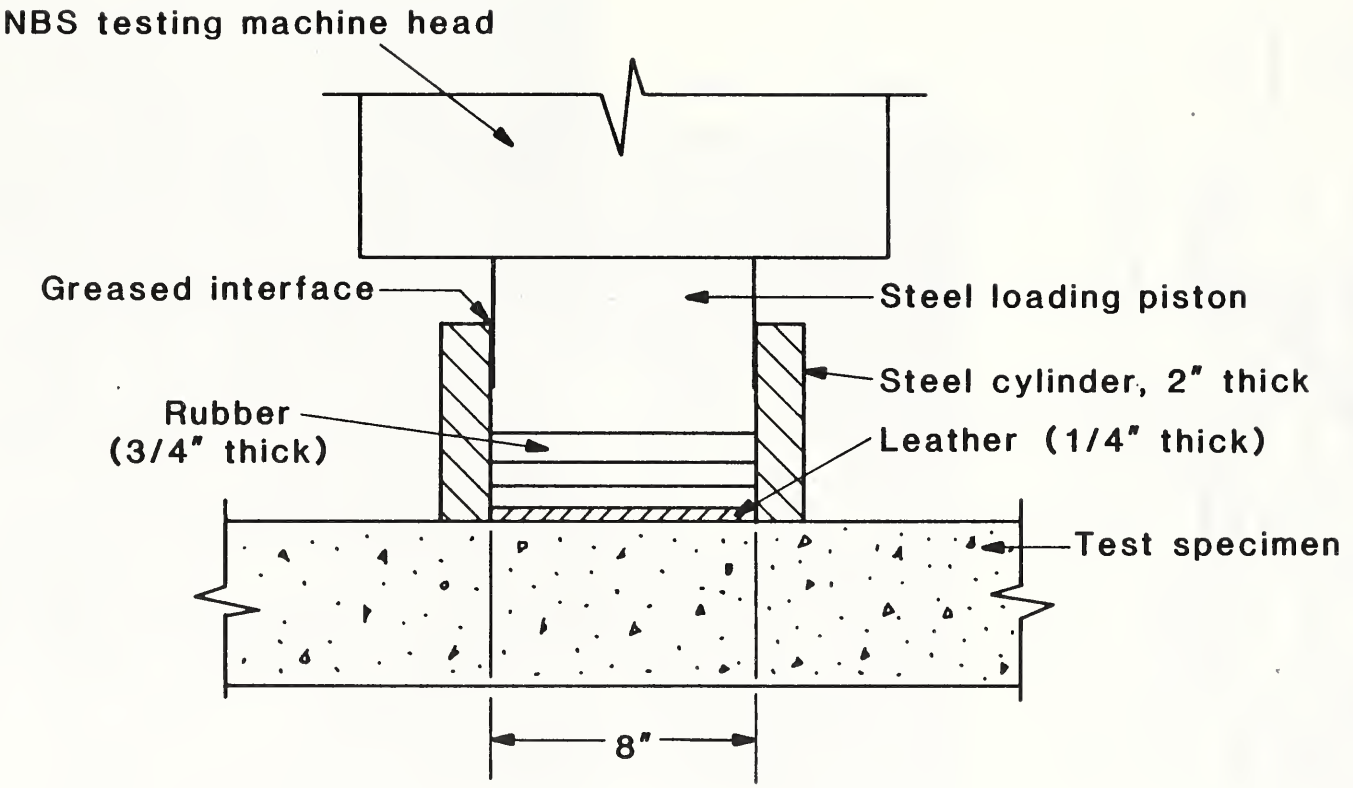

Figure 2.10 Loading System

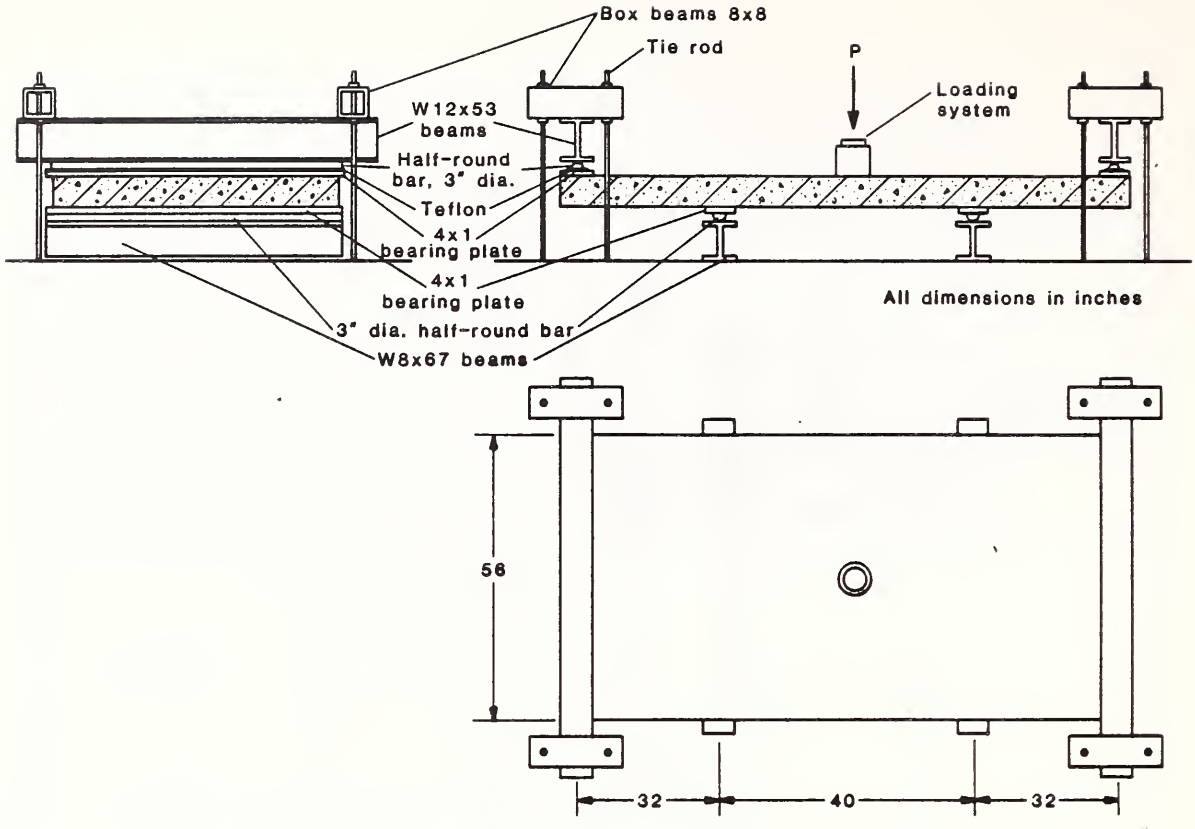

Figure 2.11 Flat Plate Test Setup

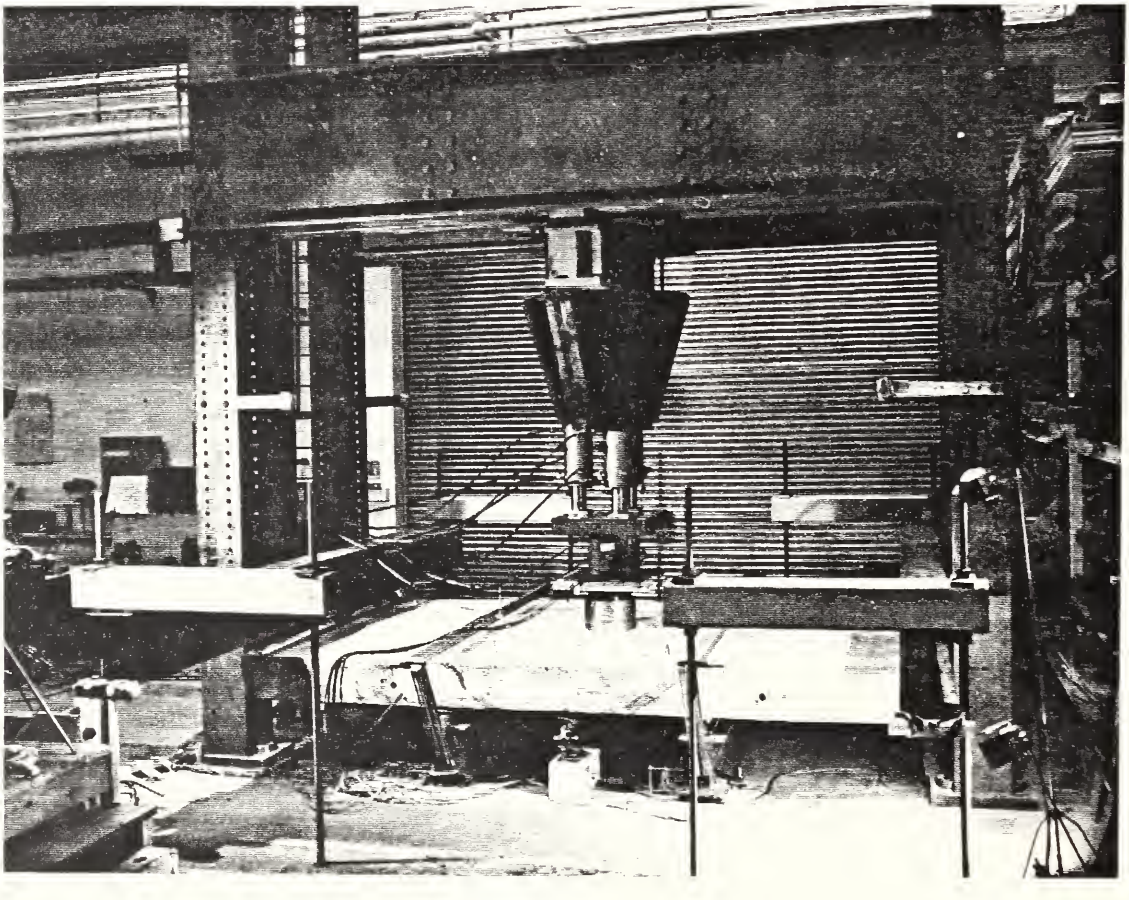

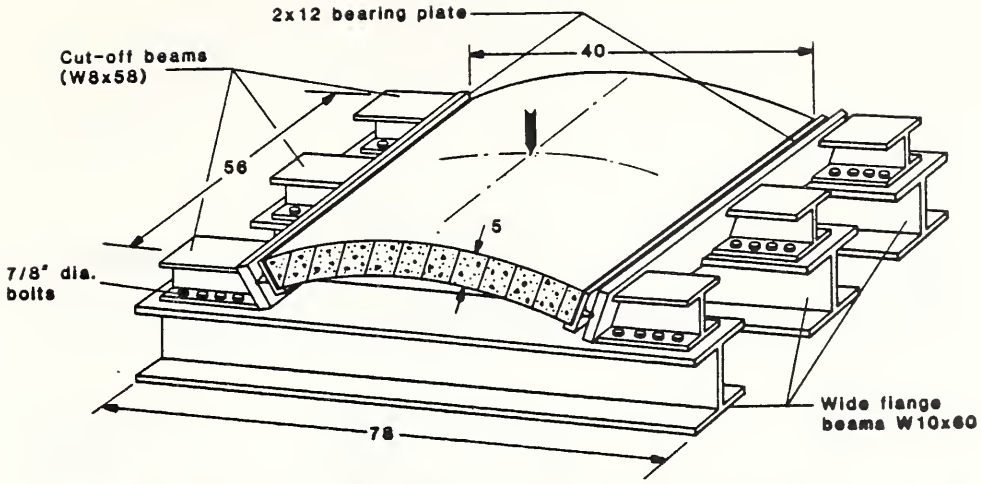

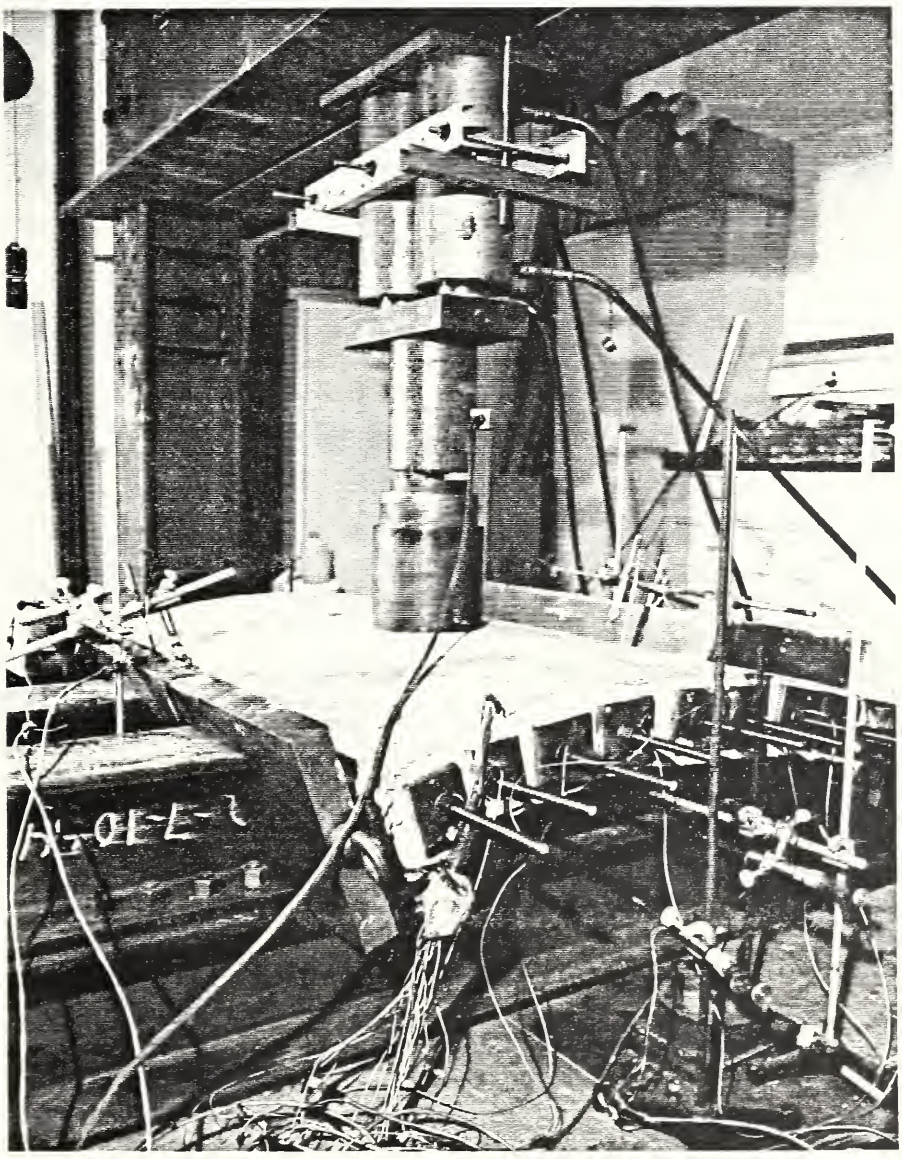

Figure 2.12 Arched Shell Test Setup

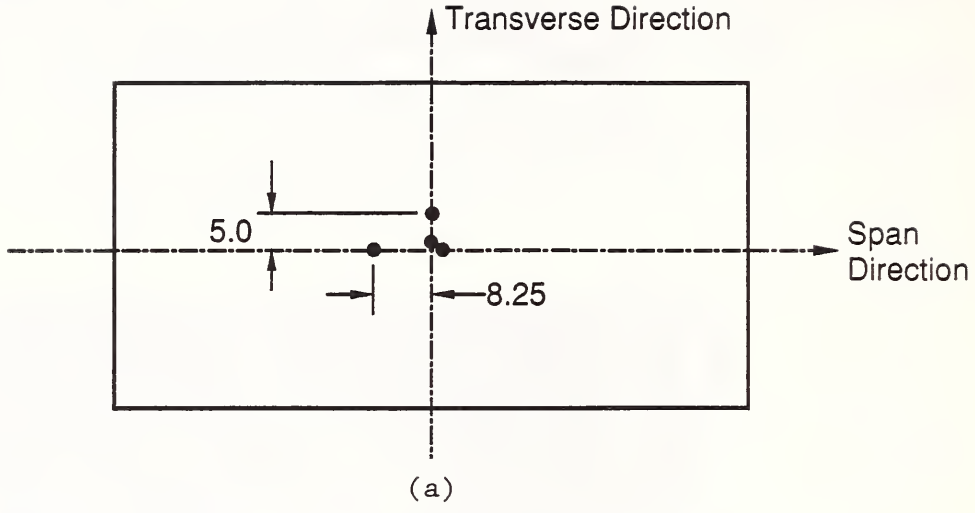

(a)

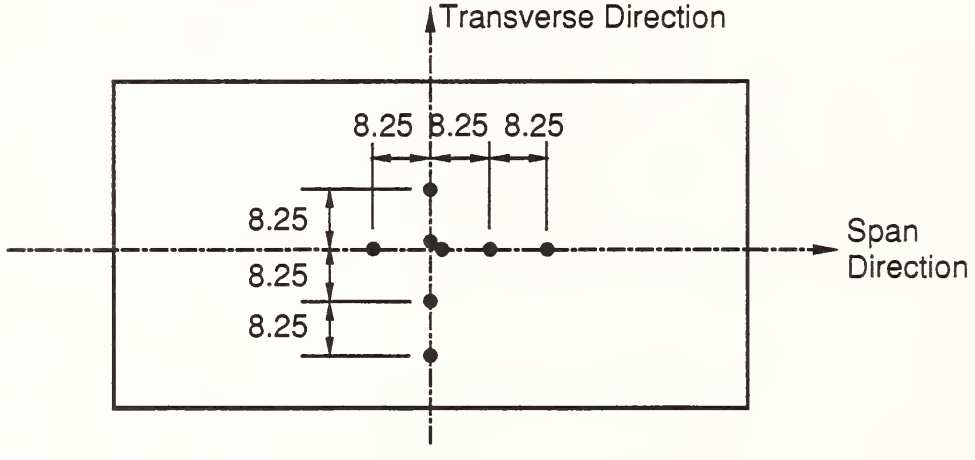

(b)

Figure 2.13 Locations of Flexural Strain Gages in 1/6-scale PLate
(a) on top flexural reinforcement
(b) on bottom flexural reinforcement

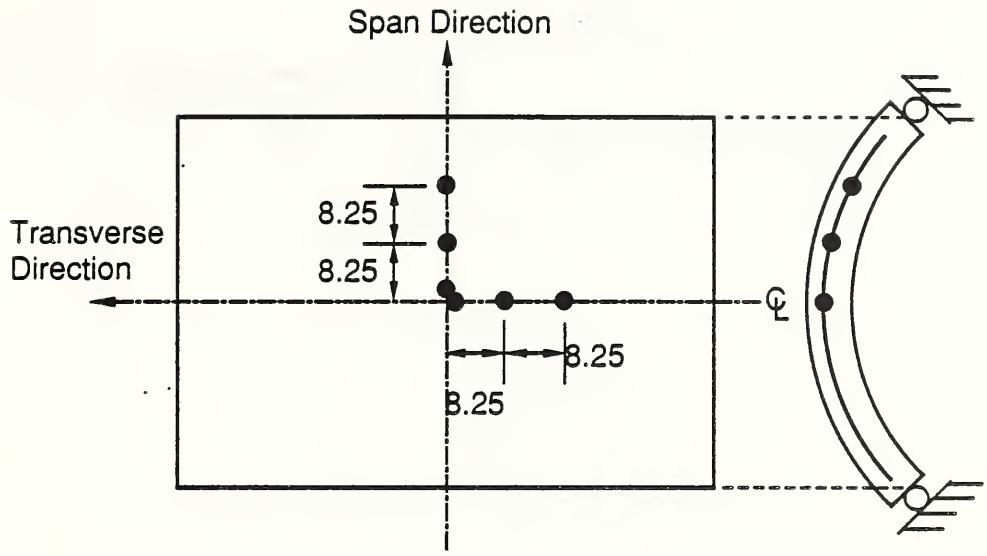

(a)

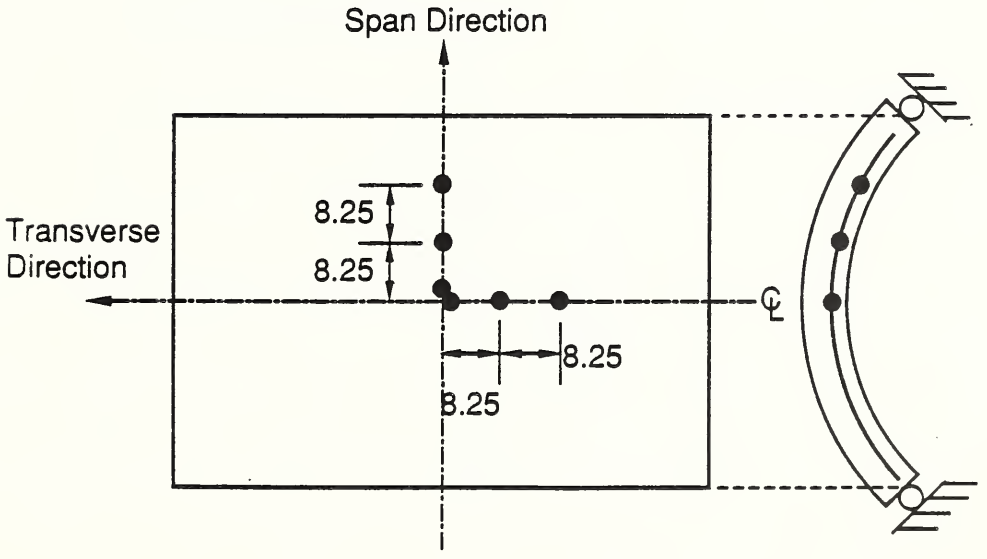

(b)

Figure 2.14 Locations of Flexural Strain Gages in 1/6-scale Shells
a) on top flexural reinforcement
b) on bottom flexural reinforcement

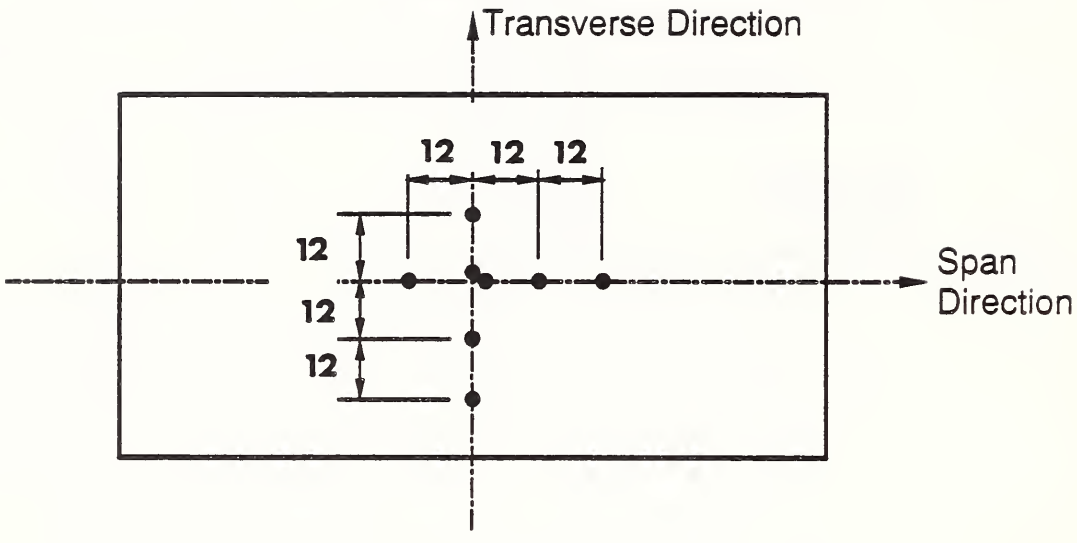

(a)

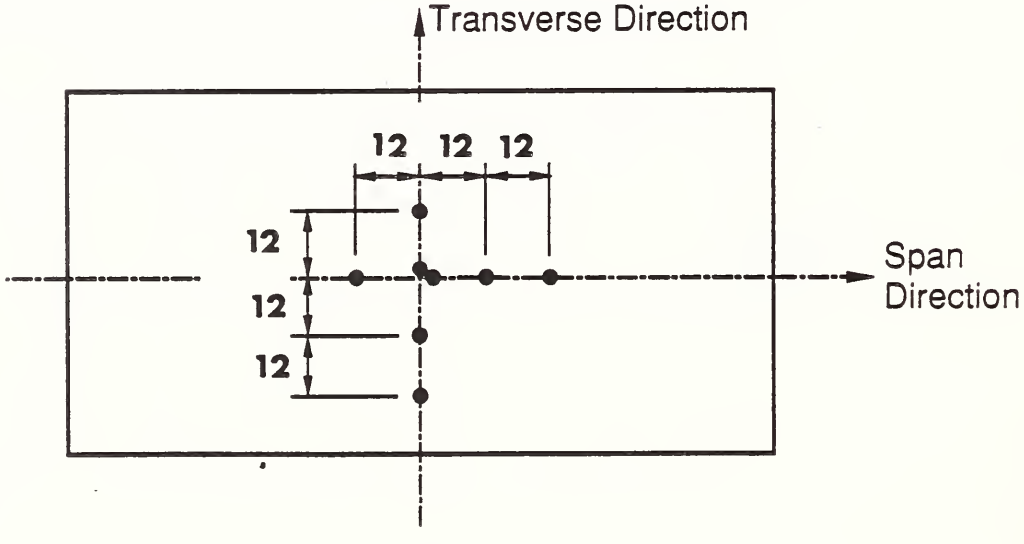

(b)

Figure 2.15 Locations of Flexural Strain Gages in 1/4-scale Plate
(a) on top flexural reinforcement
(b) on bottom flexural reinforcement

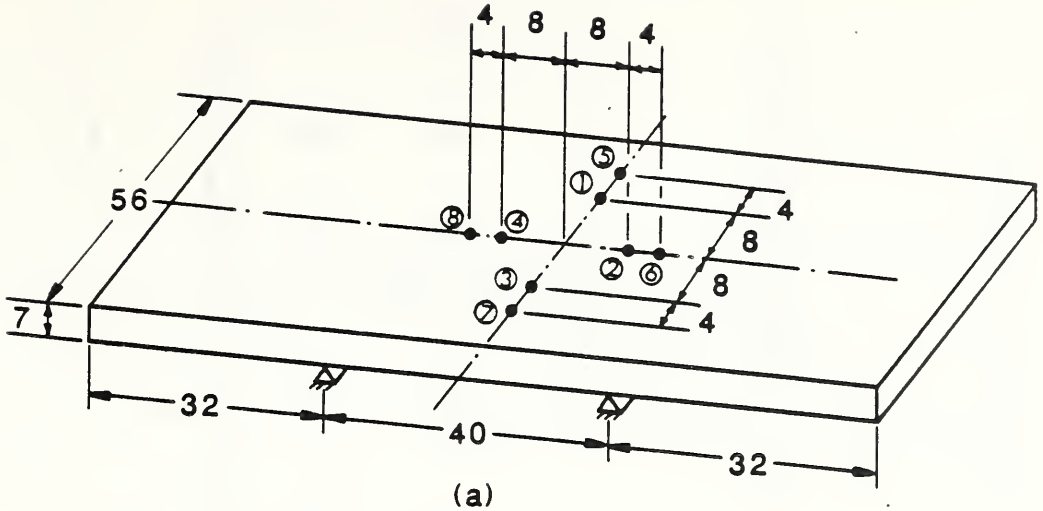

(a)

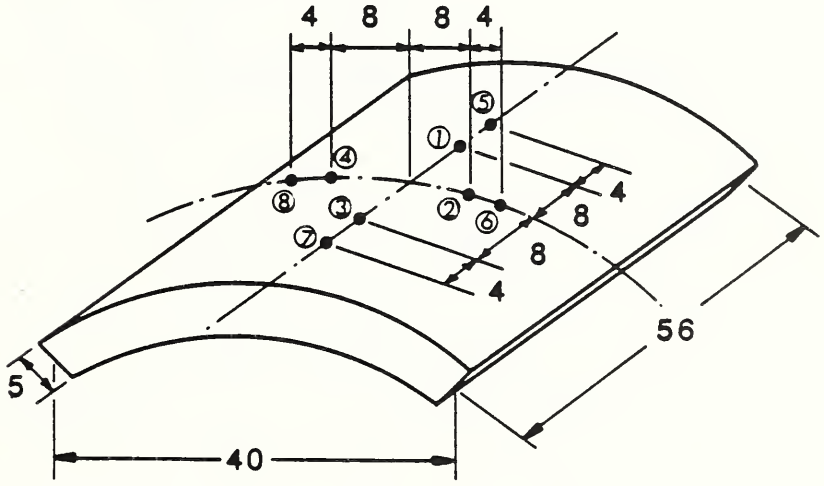

(b)

All dimensions in inches

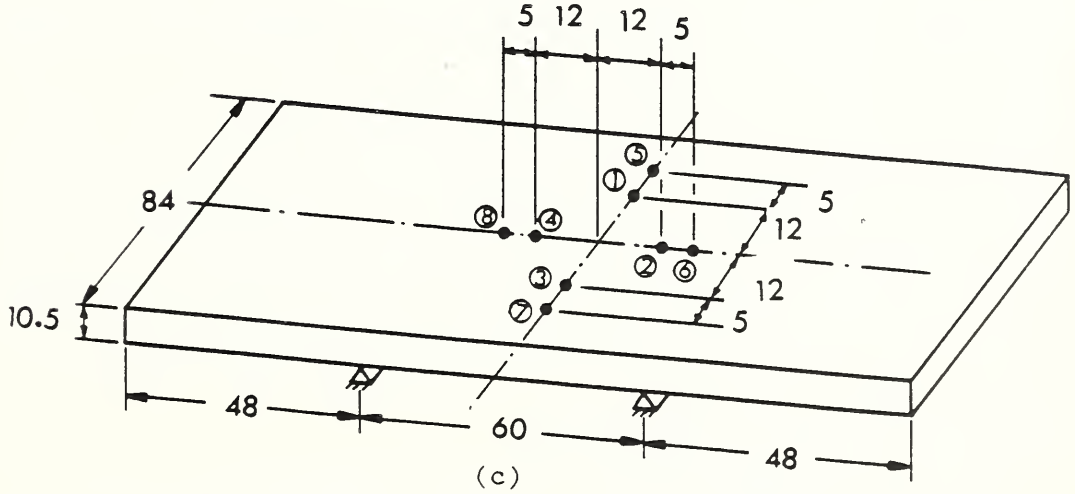

(c)

Figure 2.16 Locations of Gaged Shear Bars
(a) in 1/6-scale plates
(b) in 1/6-scale shells
(c) in 1/4-scale plates

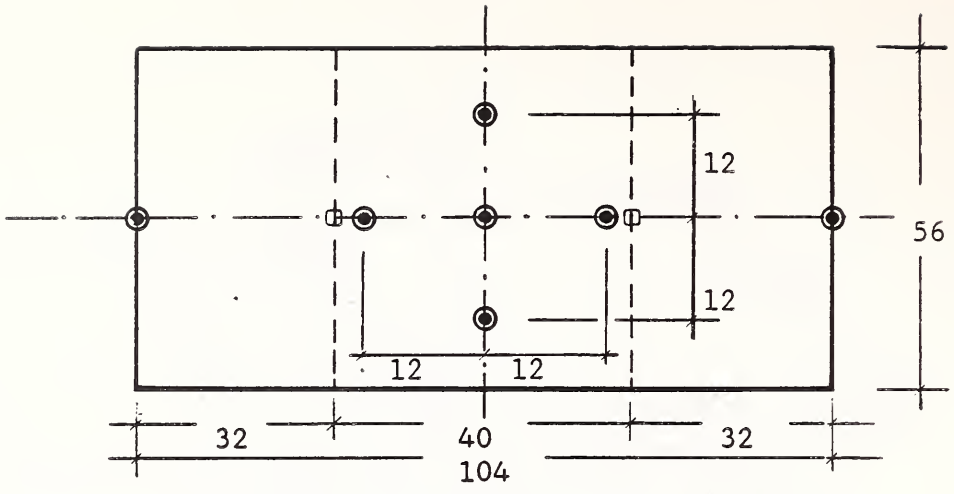

a) Locations of LVDTs in 1/6-Scale Plate

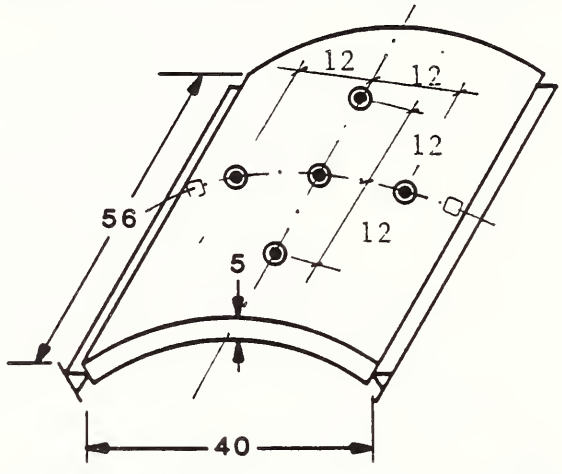

b) Locations of LVDTs in 1/6-Scale Shell

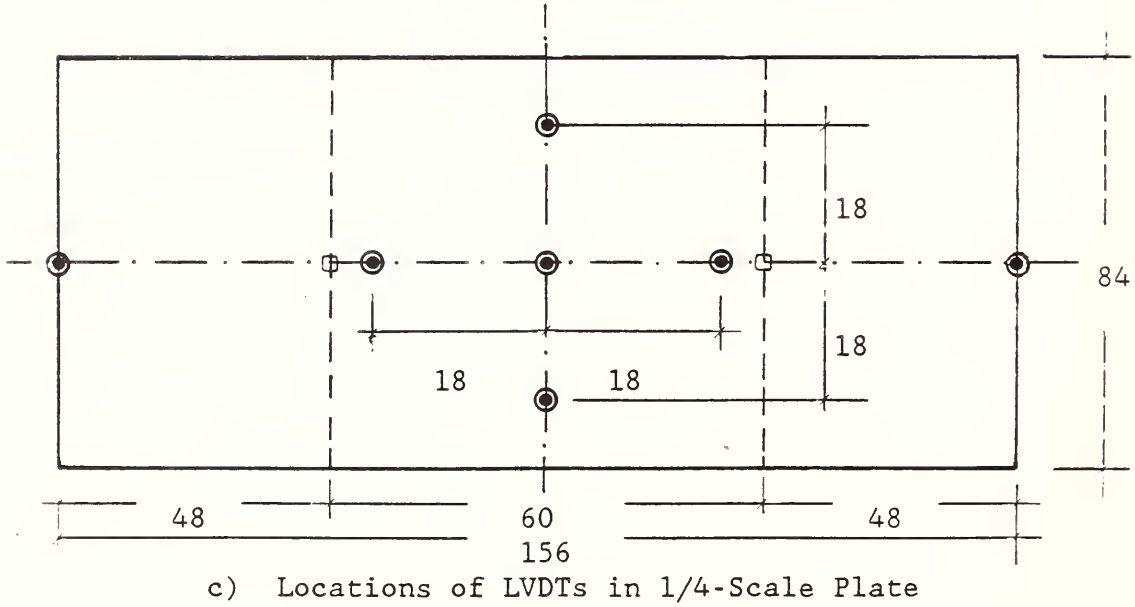

c) Locations of LVDTs in 1/4-Scale Plate

All Dimensions in inches

□ Top Surface LVDTs

◉ Bottom Surface LVDTs

Figure 2.17 Locations of Linear-Diferential-Variable-Transformers (LVDT)
(a) in 1/6-scale plates
(b) in 1/6-scale shells
(c) in 1/4-scale plates

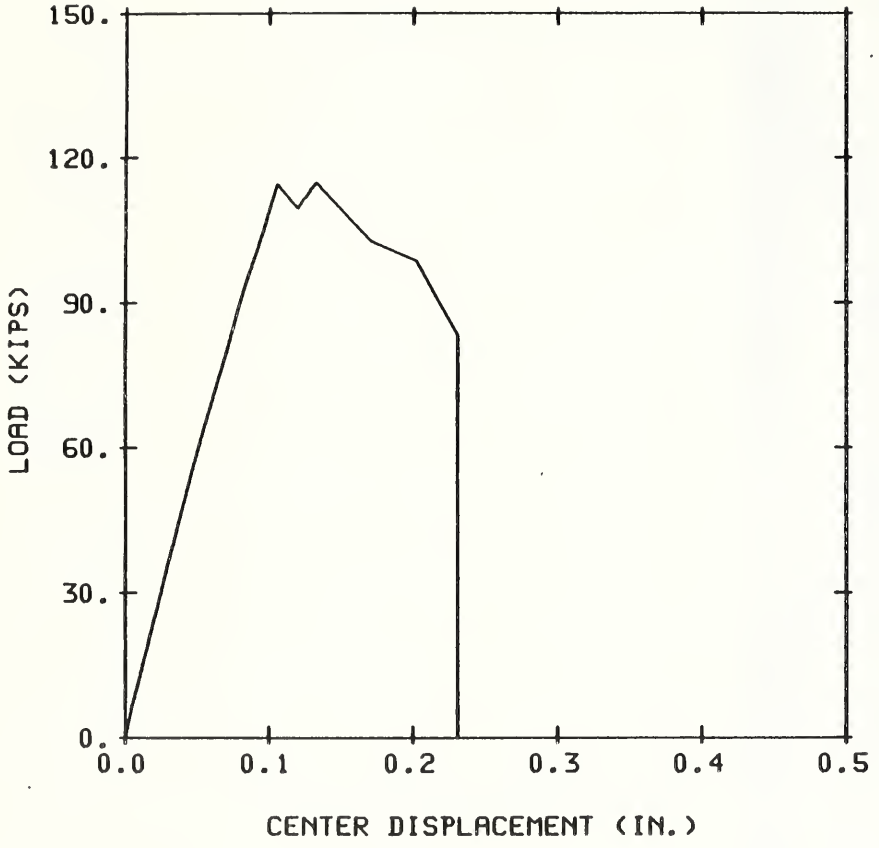

Figure 3.1 Load-Center Deflection Curve of Specimen FP2-1

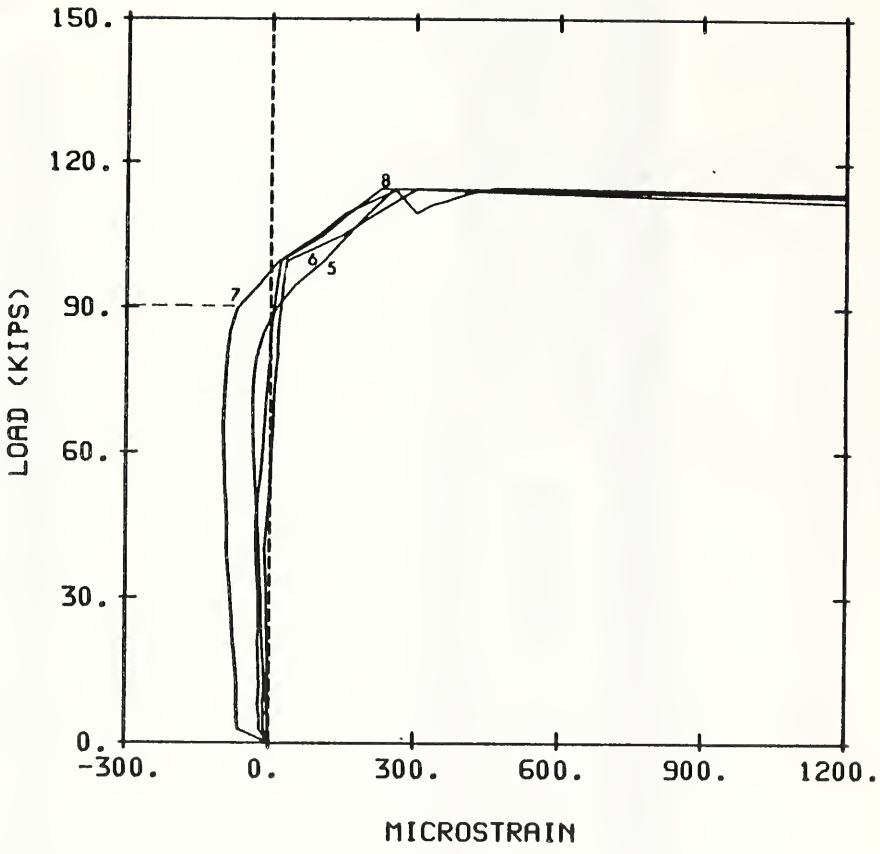

Figure 3.2 Load-Strain Curves for Gaged Shear Bars in FP2-1

(a)

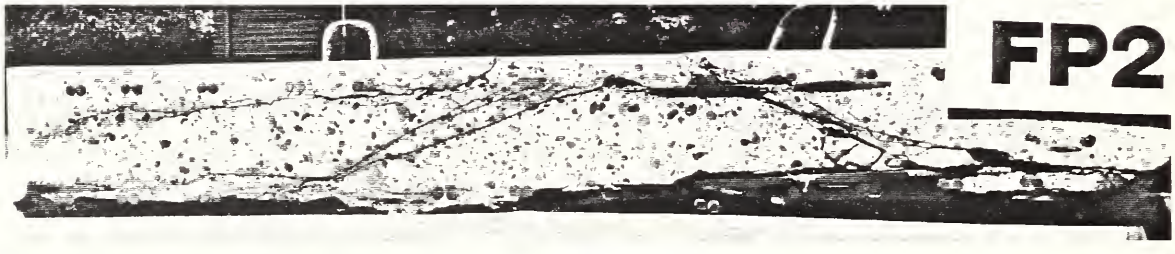

(b)

Figure 3.3 Crack Patterns in Specimen FP2-1
(a) Span Cross-Section
(b) Transverse Cross-Section

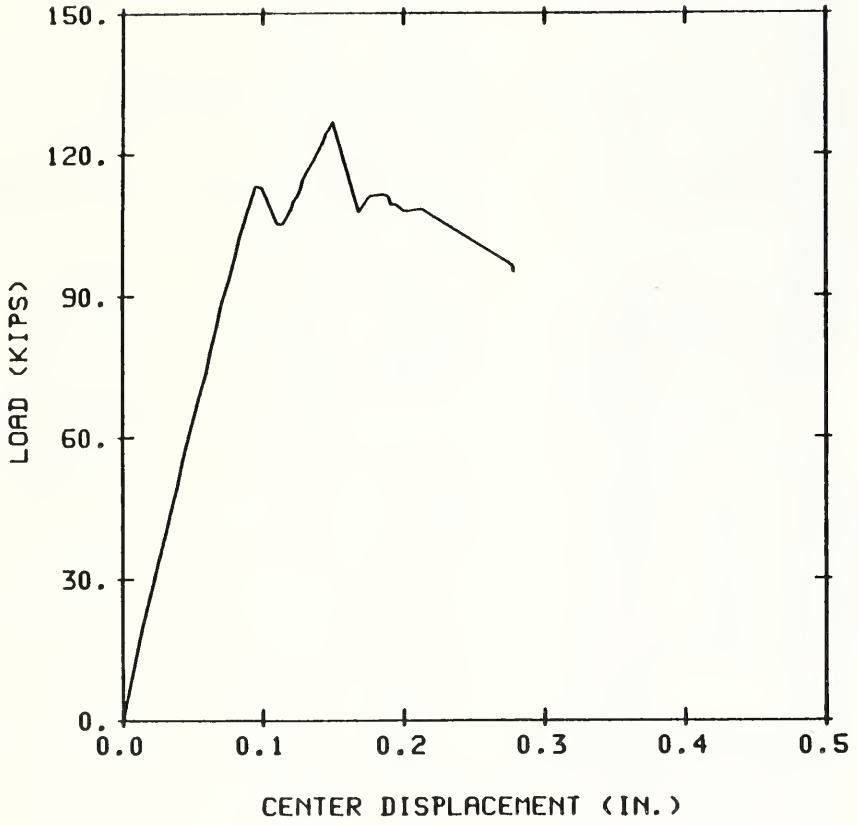

Figure 3.4 Load-Center Deflection Curve of Specimen FP2-2

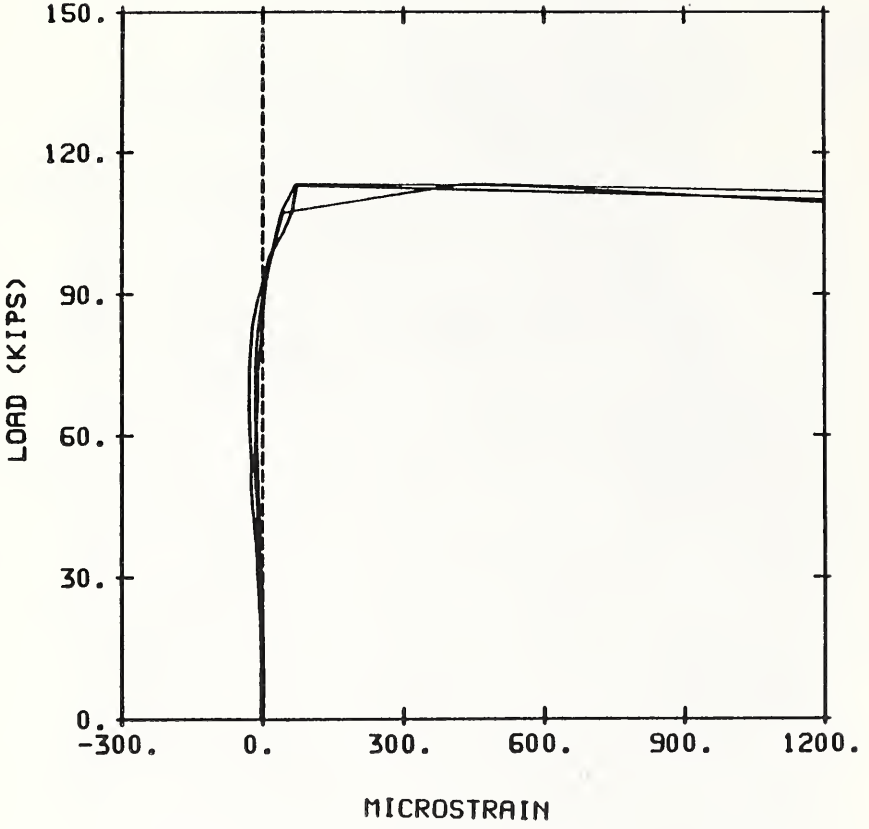

Figure 3.5 Load-Strain Curves for Gaged Shear Bars in FP2-2

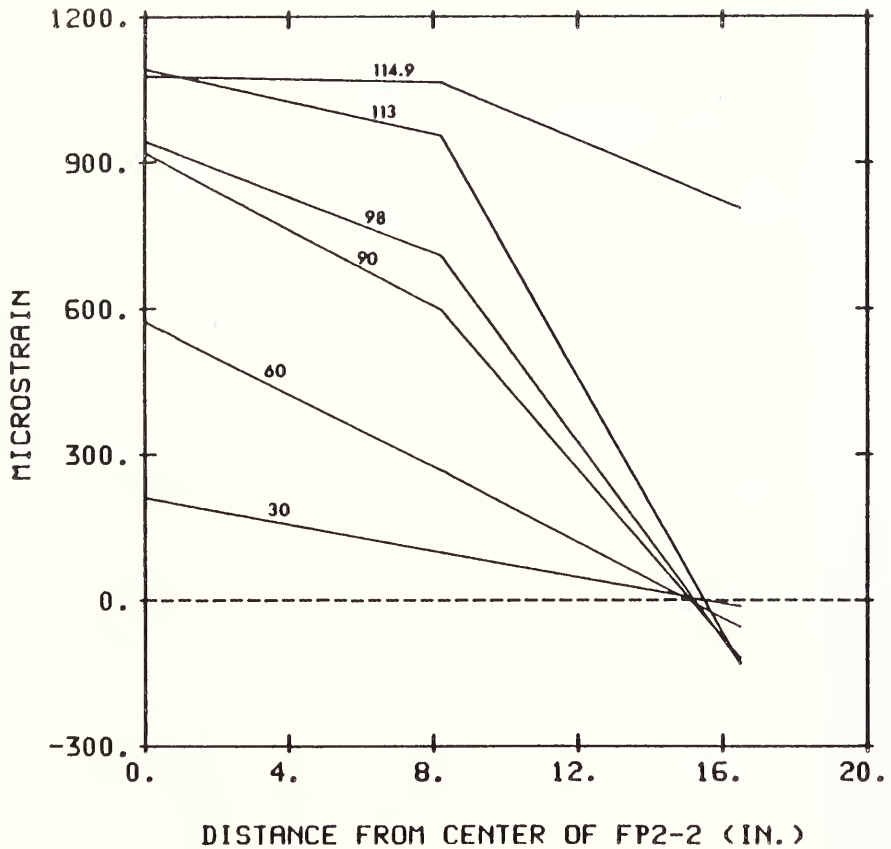

(a)

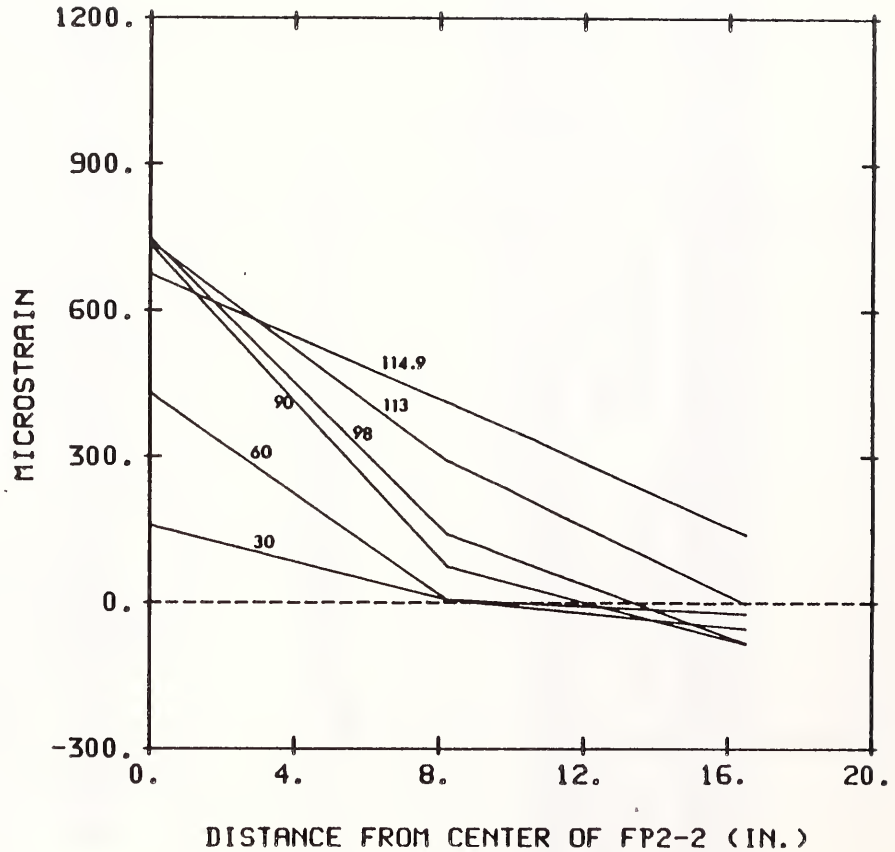

(b)

Figure 3.6 Flexural Strain Profiles of FP2-2
(a) in Span Tension Reinforcement
(b) in Transverse Tension Reinforcement

(a)

(b)

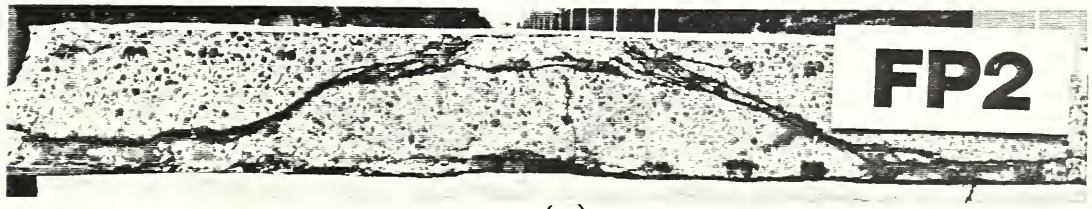

(c)

Figure 3.7 Crack Patterns in Specimen FP2-2
(a) Underside
(b) Span Cross-Section
(c) Transverse Cross-Section

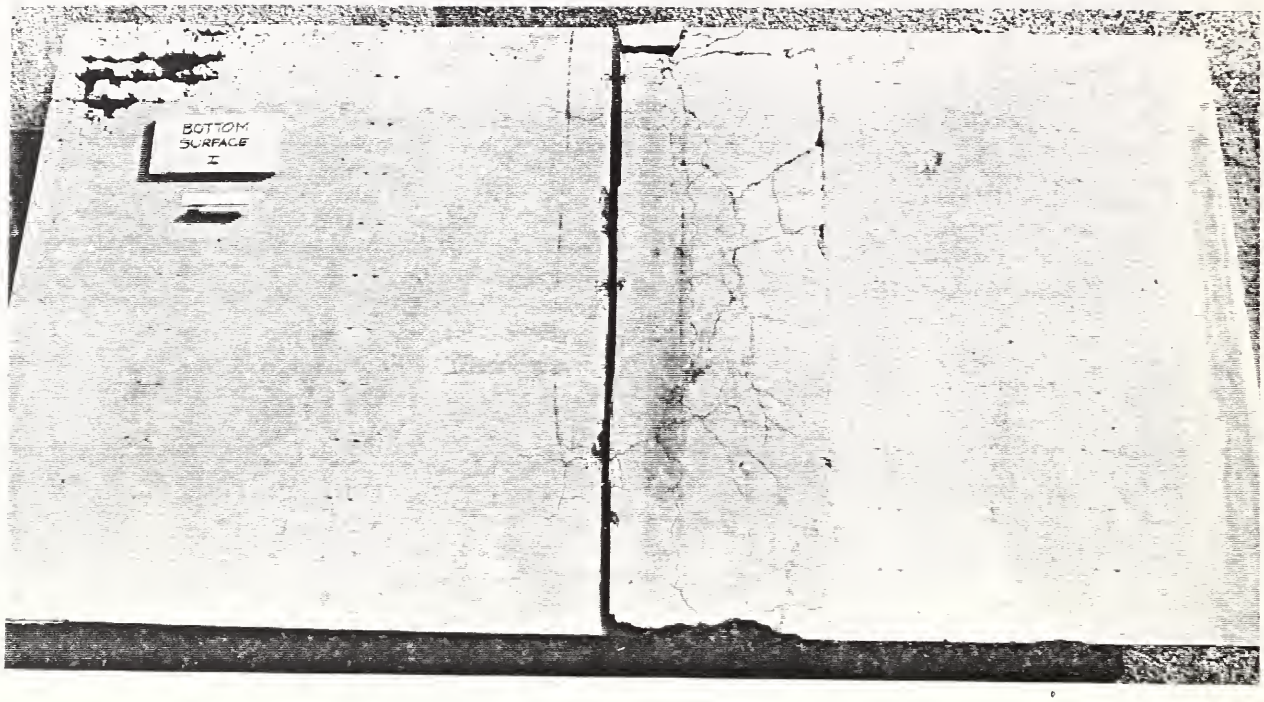

(a)

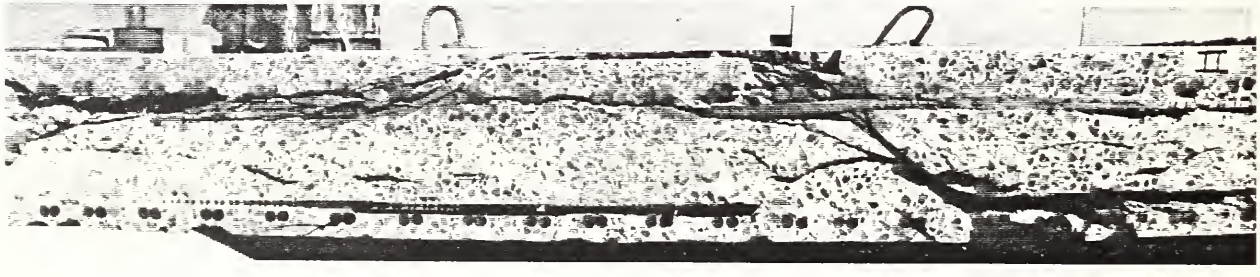

(b)

Figure 3.8 Crack Patterns in Specimen IFP2-2
(a) Underside
(b) Transverse Cross-Section

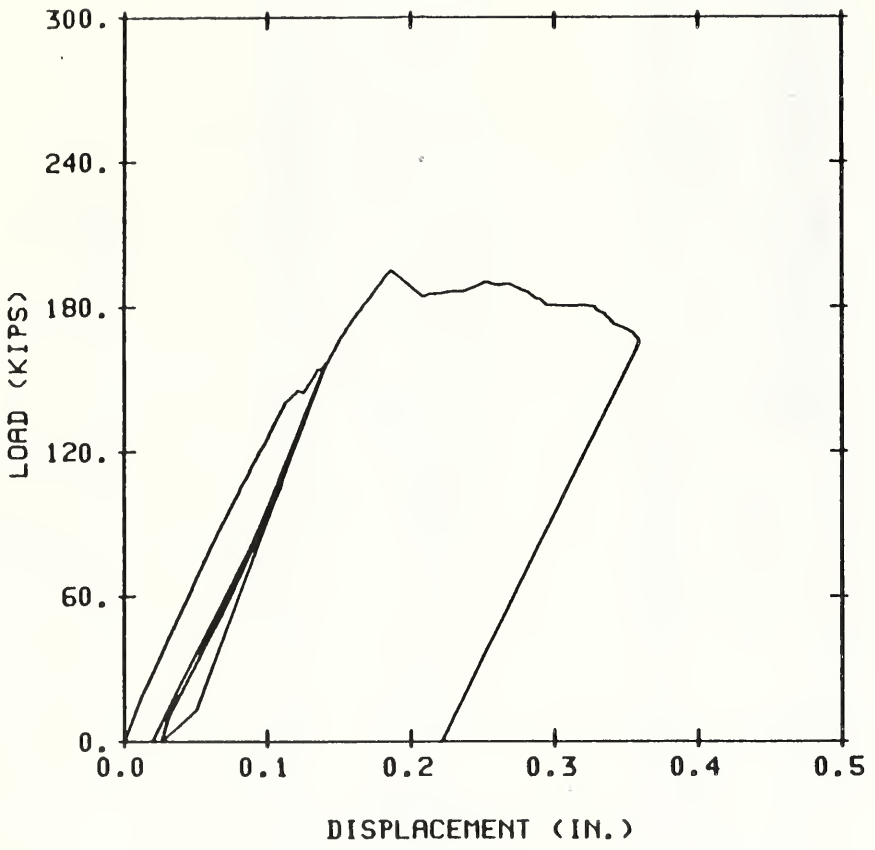

Figure 3.9 Load-Center Deflection Curve of Specimen FP3

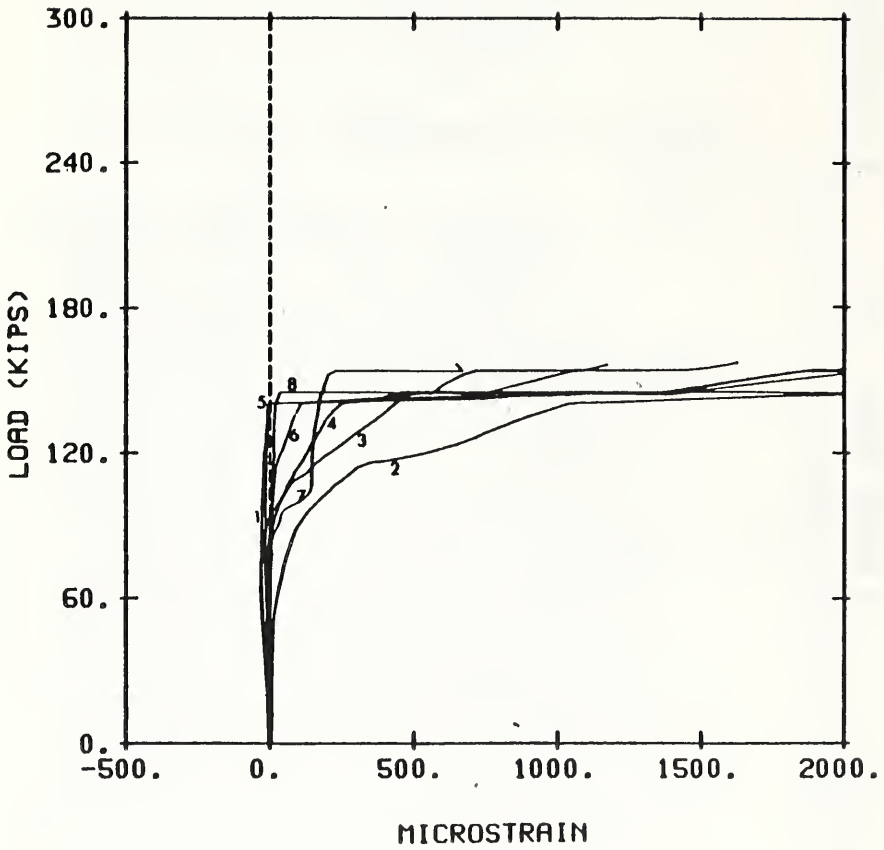

Figure 3.10 Load-Strain Curves for Gaged Shear Bars in FP3

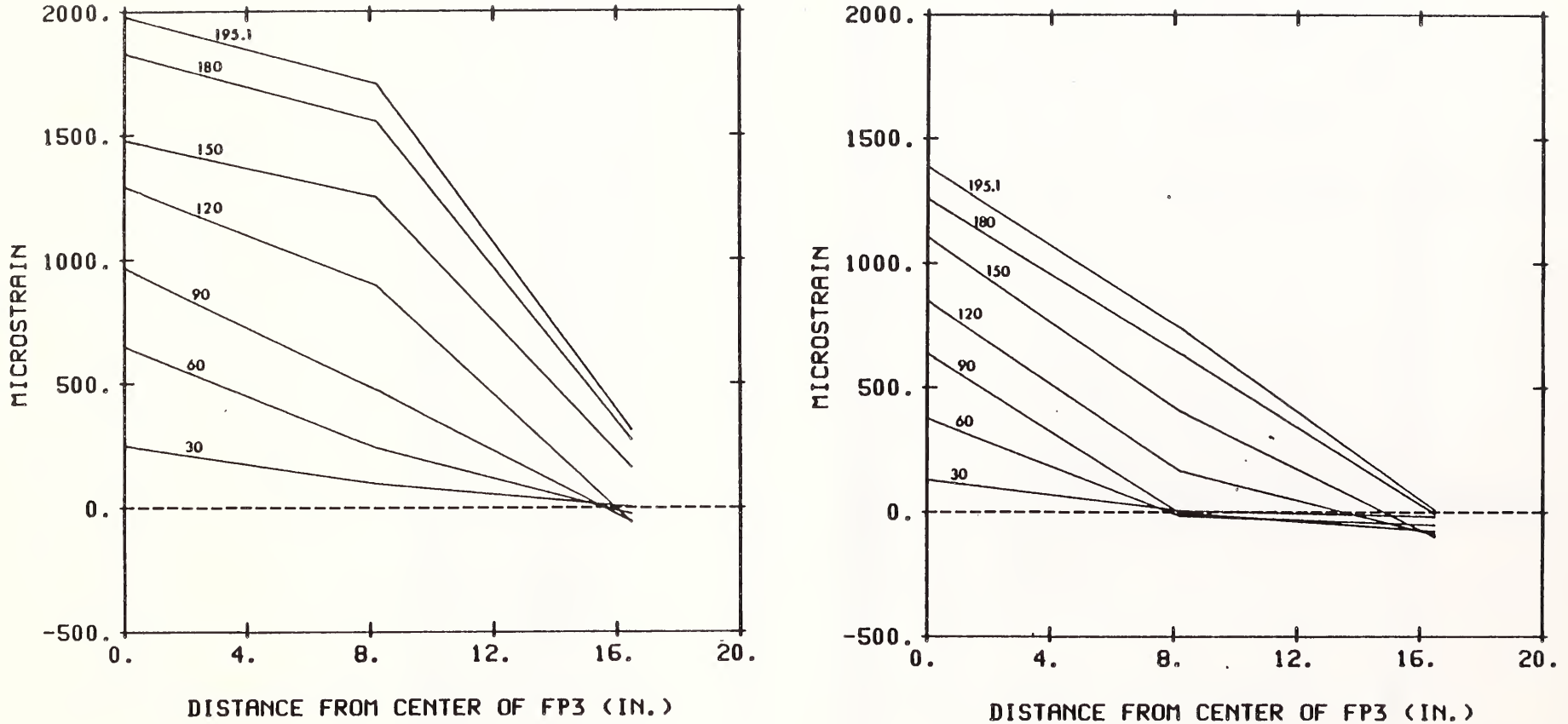

Figure 3.11 Flexural Strain Profiles of Specimen FP3
(a) in Span Tension Reinforcement
(b) in Transverse Tension Reinforcement

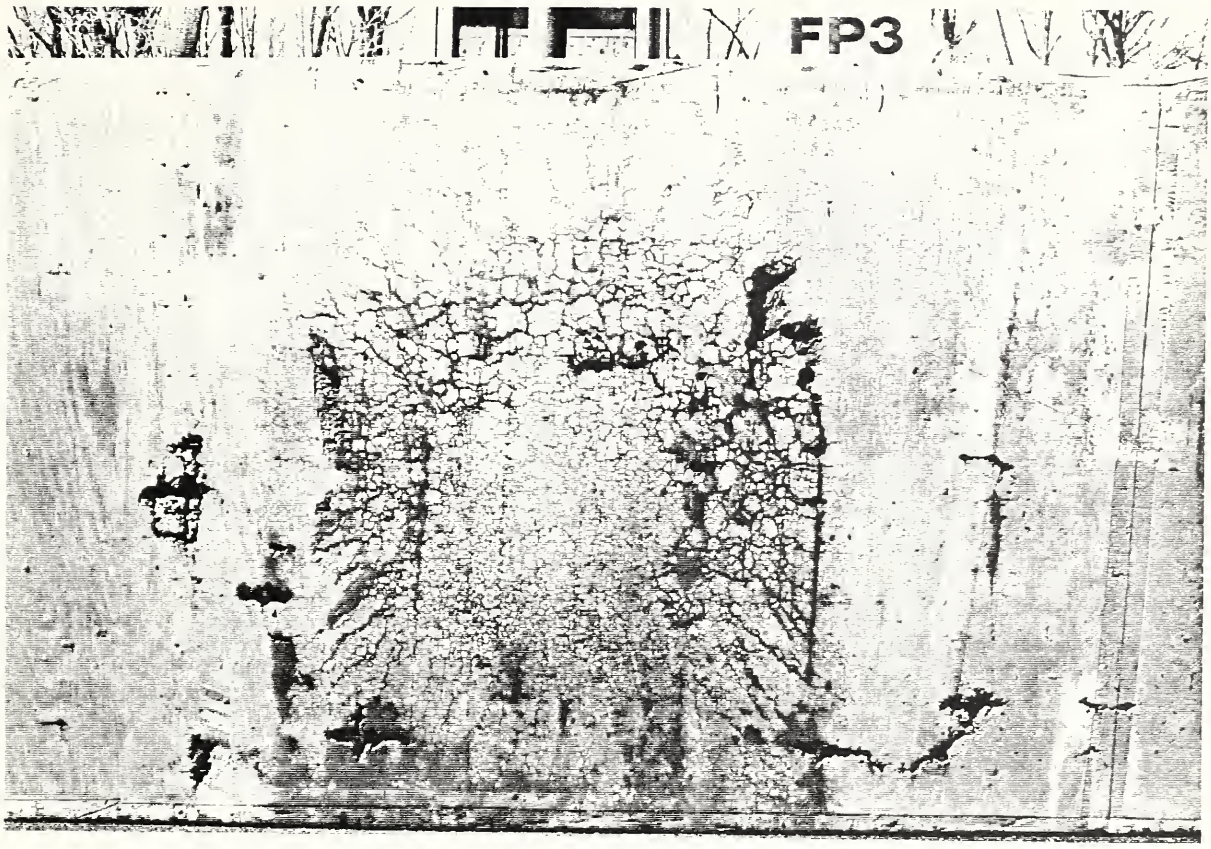

(a)

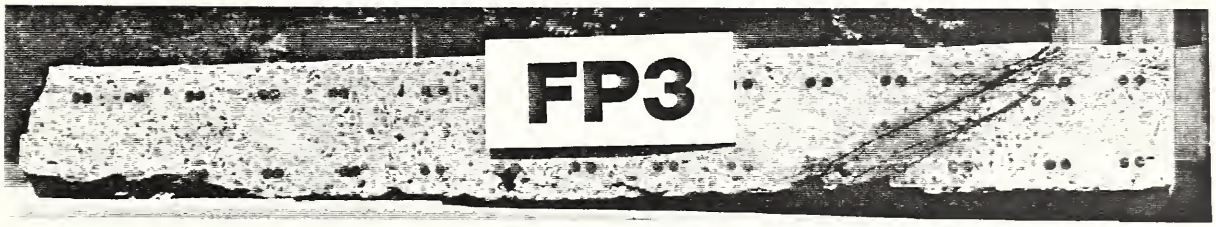

(b)

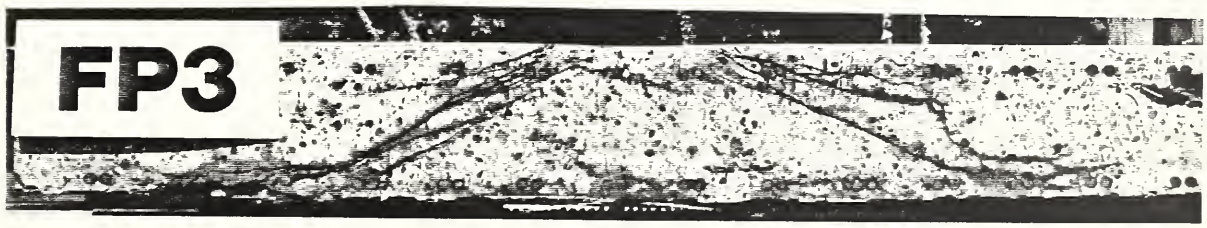

(c)

Figure 3.12 Crack Patterns in Specimen FP3
(a) Underside
(b) Span Cross-Section
(c) Transverse Cross-Section

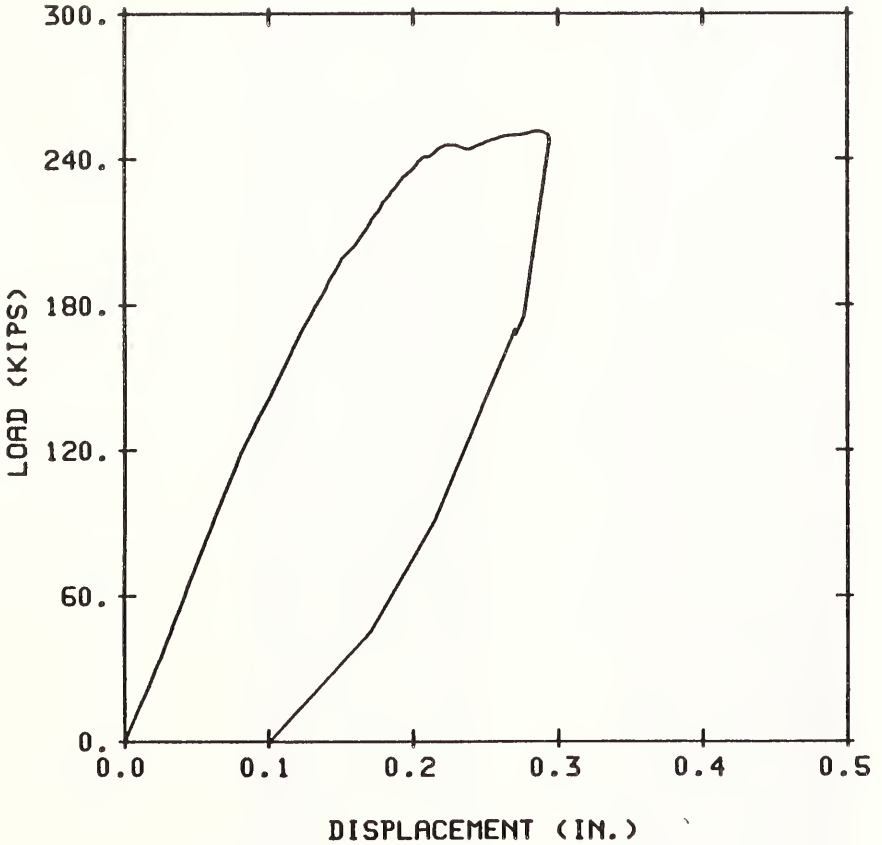

Figure 3.13 Load-Center Deflection Curve of Specimen FP4

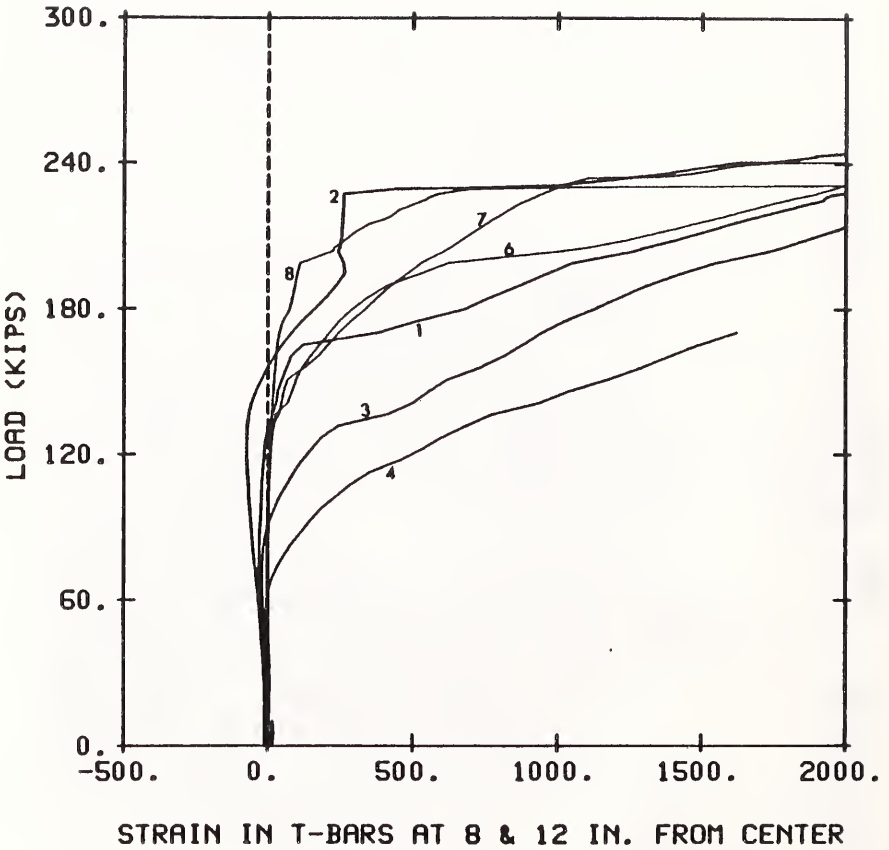

Figure 3.14 Load-Strain Curves for Gaged Shear Bars in FP4

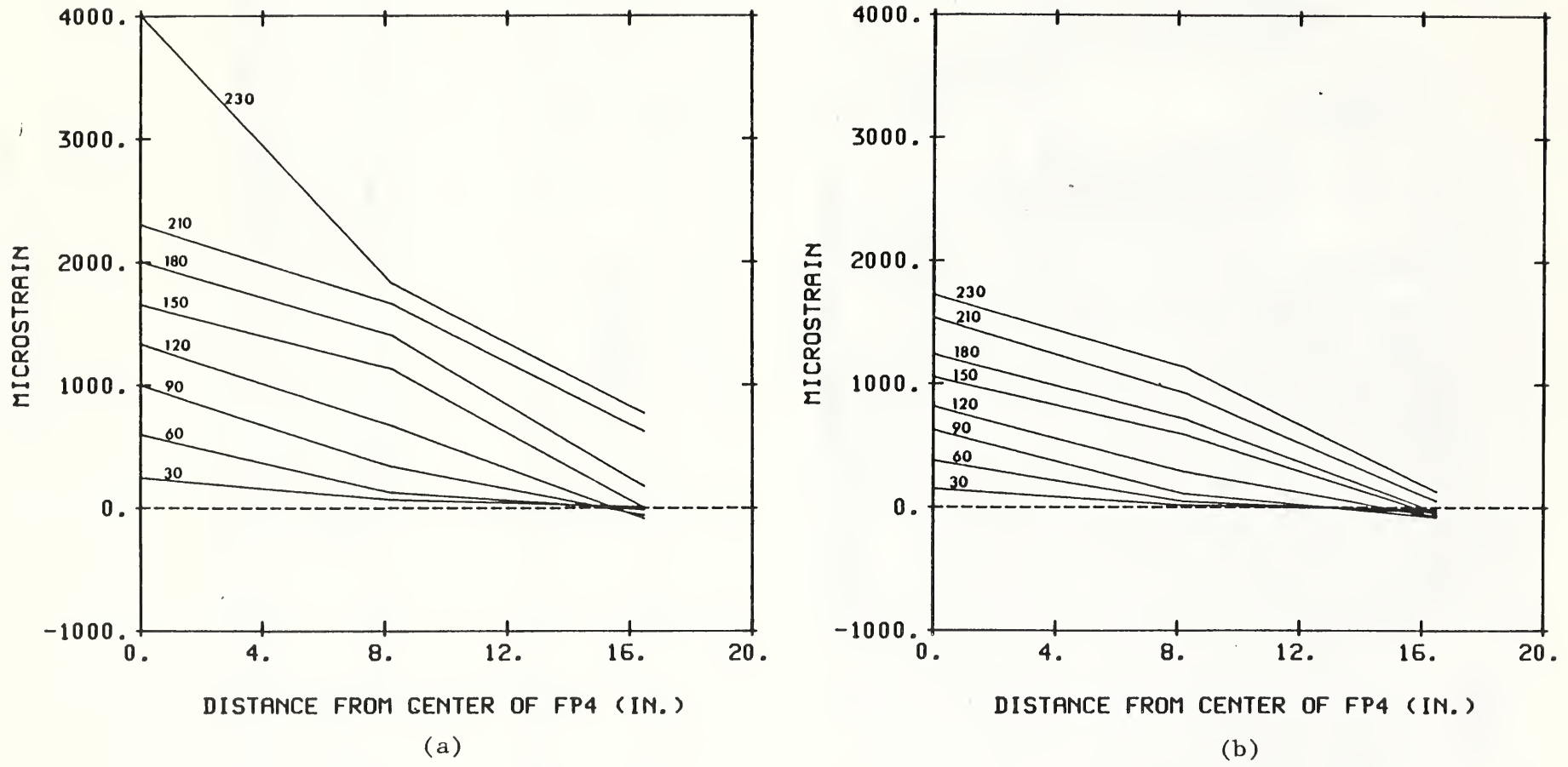

Figure 3.15 Flexural Strain Profiles of Specimen FP4
(a) in Span Tension Reinforcement
(b) in Transverse Tension Reinforcement

Figure 3.16 Crack Patterns in Specimen FP4
(a) Underside
(b) Span Cross-Section
(c) Transverse Cross-Section

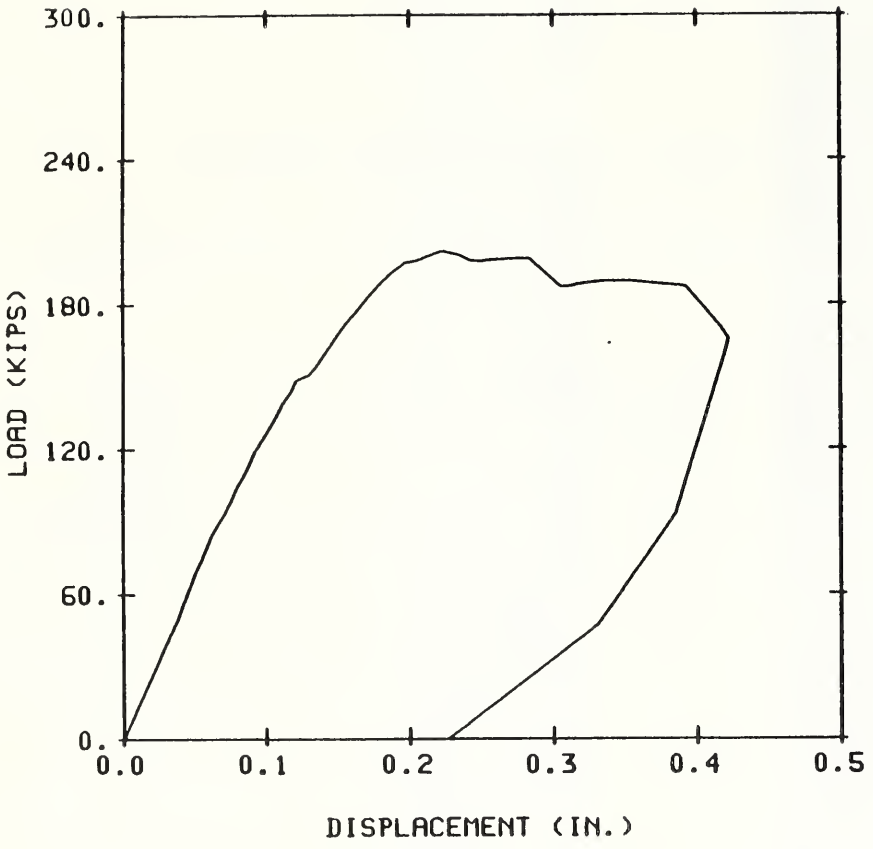

Figure 3.17 Load-Center Deflection Curve of Specimen FP5

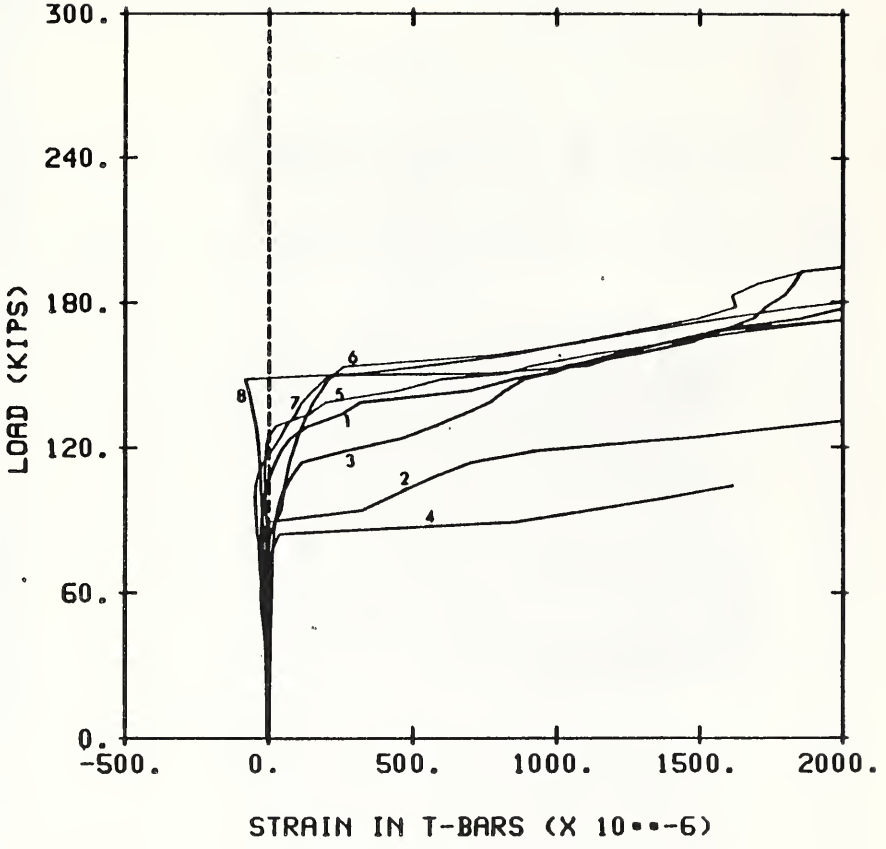

Figure 3.18 Load-Strain Curves for Gaged Shear Bars in FP5

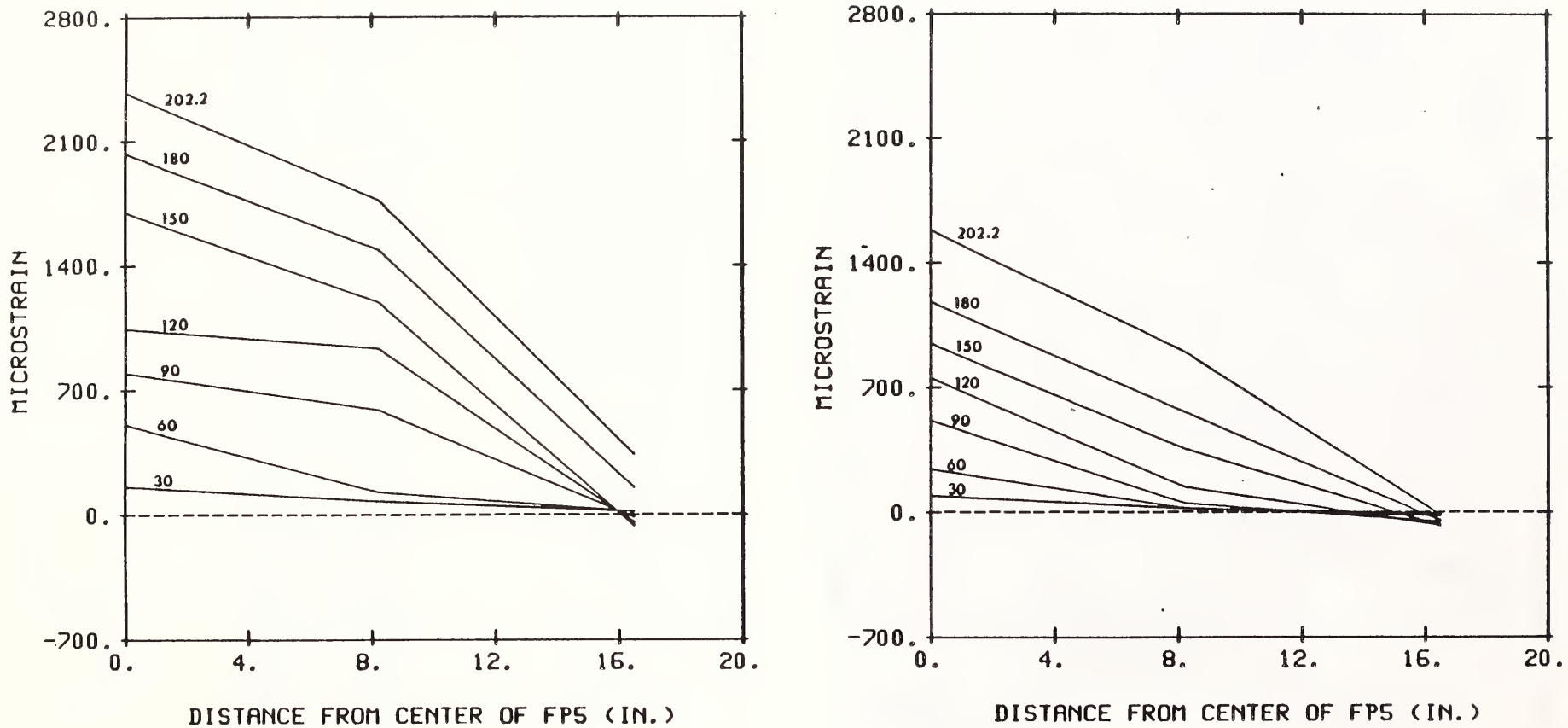

Figure 3.19 Flexural Strain Profiles of Specimen FP5
(a) in Span Tension Reinforcement
(b) in Transverse Tension Reinforcement

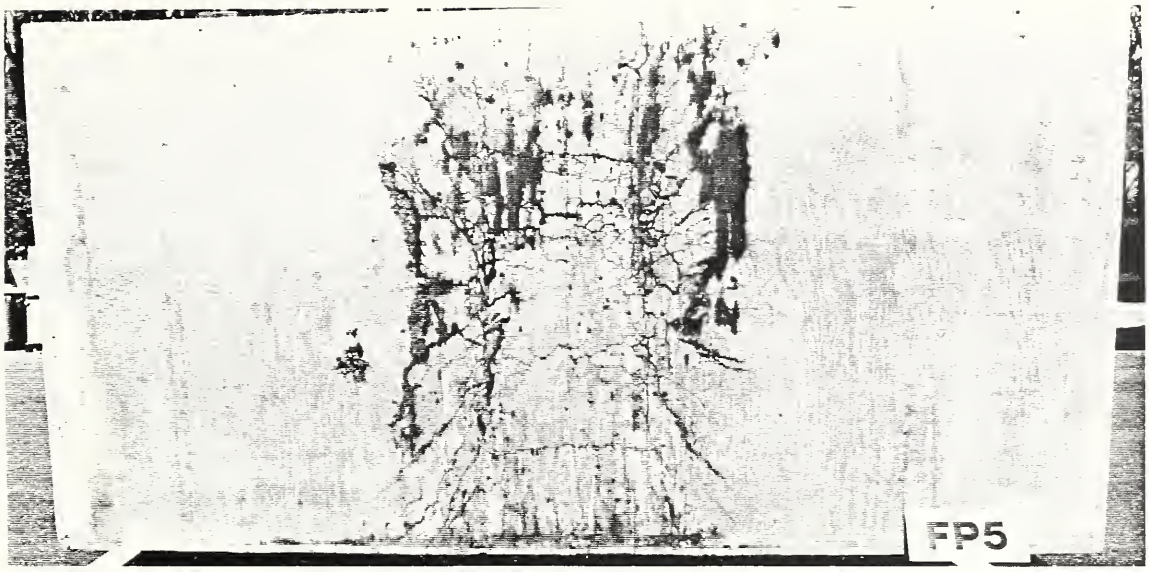

(a)

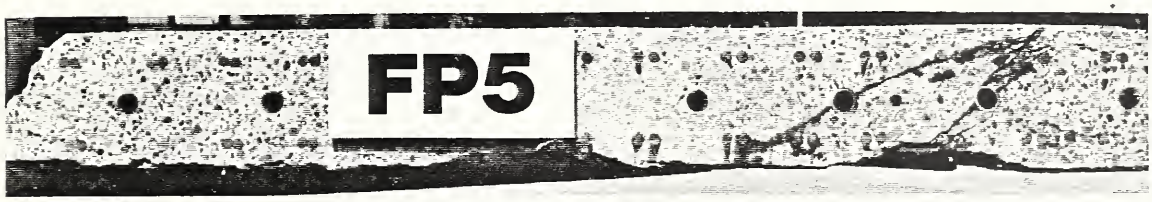

(b)

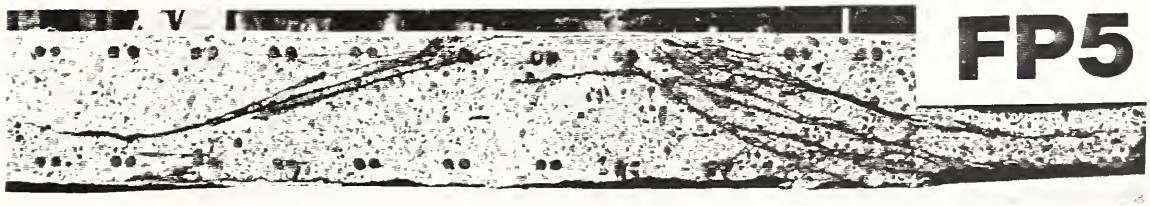

(c)

Figure 3.20 Crack Patterns in Specimen FP5
(a) Underside
(b) Span Cross-Section
(c) Transverse Cross-Section

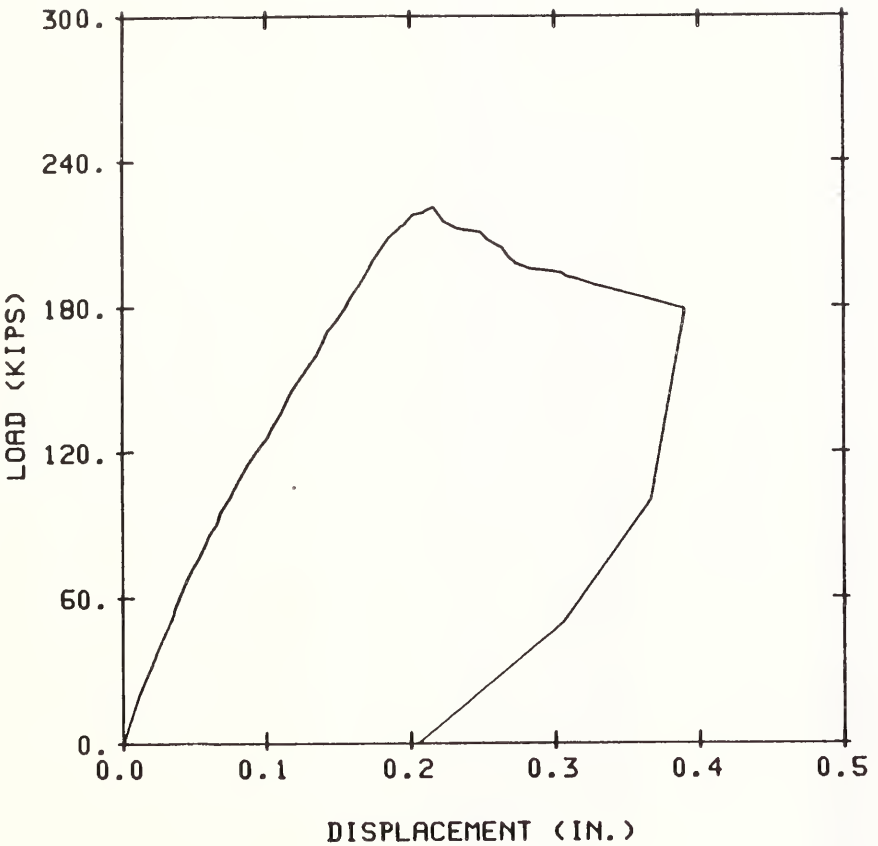

Figure 3.21 Load-Center Deflection Curve of Specimen FP6

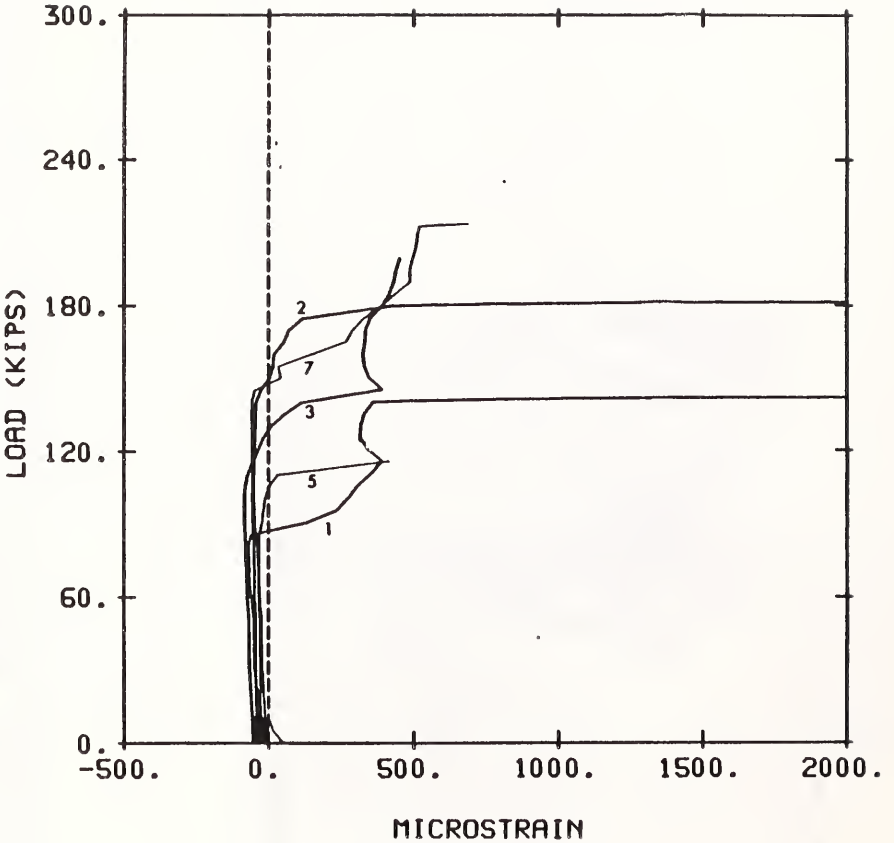

Figure 3.22 Load-Strain Curves for Gaged Shear Bars in FP6

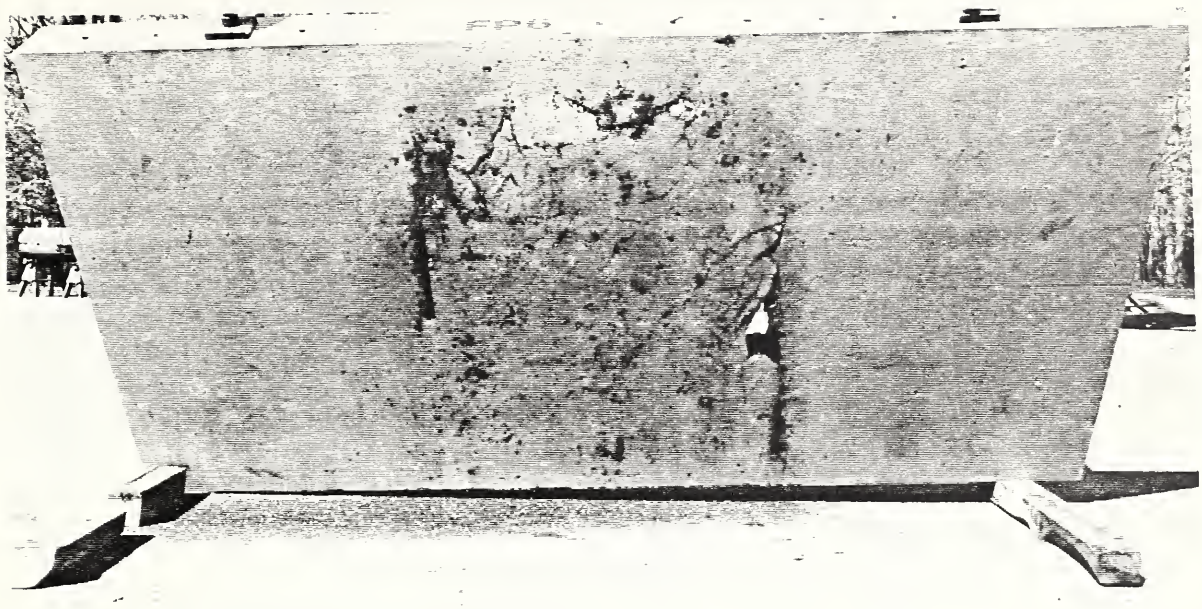

(a)

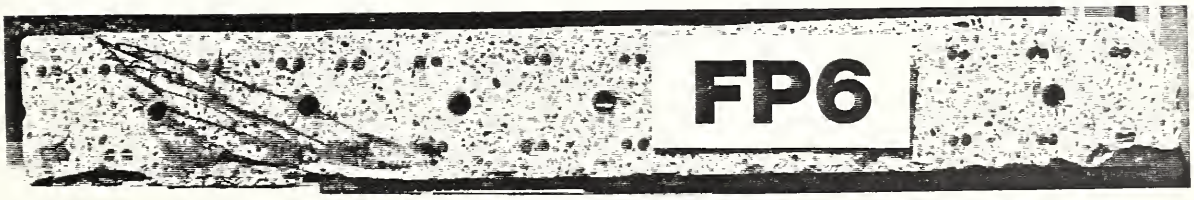

(b)

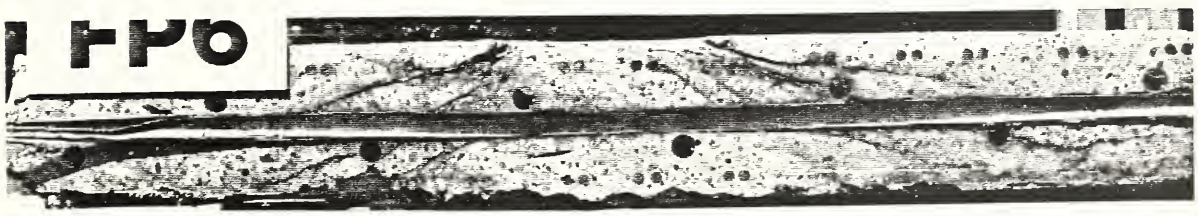

(c)

Figure 3.23 Crack Patterns in Specimen FP6
(a) Underside
(b) Span Cross-Section
(c) Transverse Cross-Section

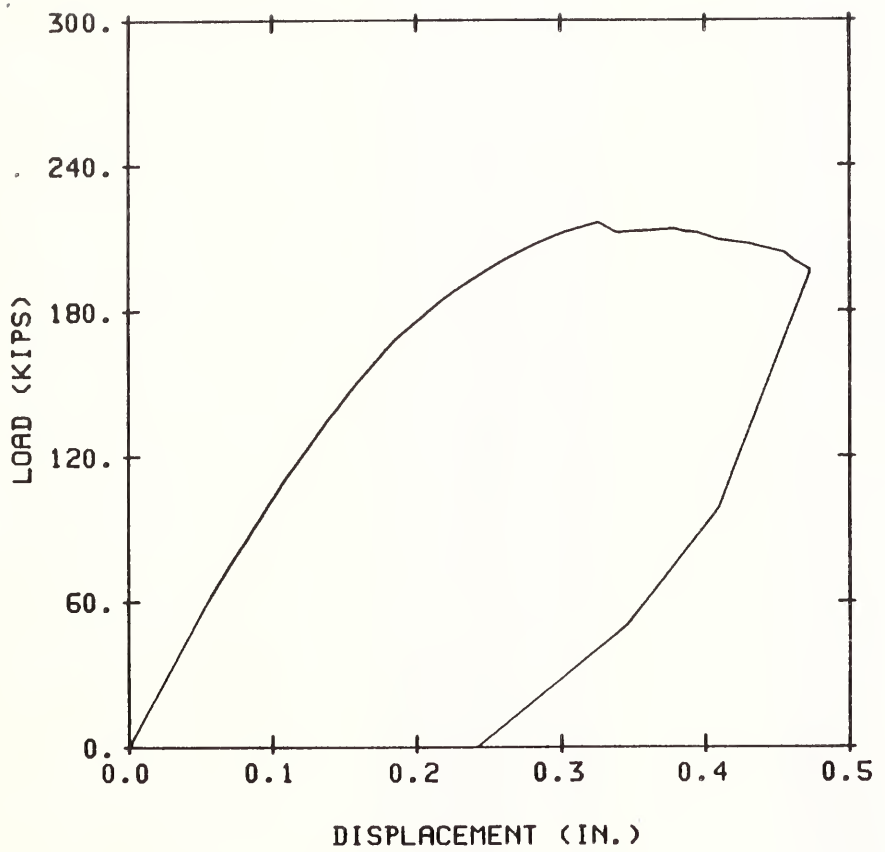

Figure 3.24 Load-Center Deflection Curve of Specimen FP1

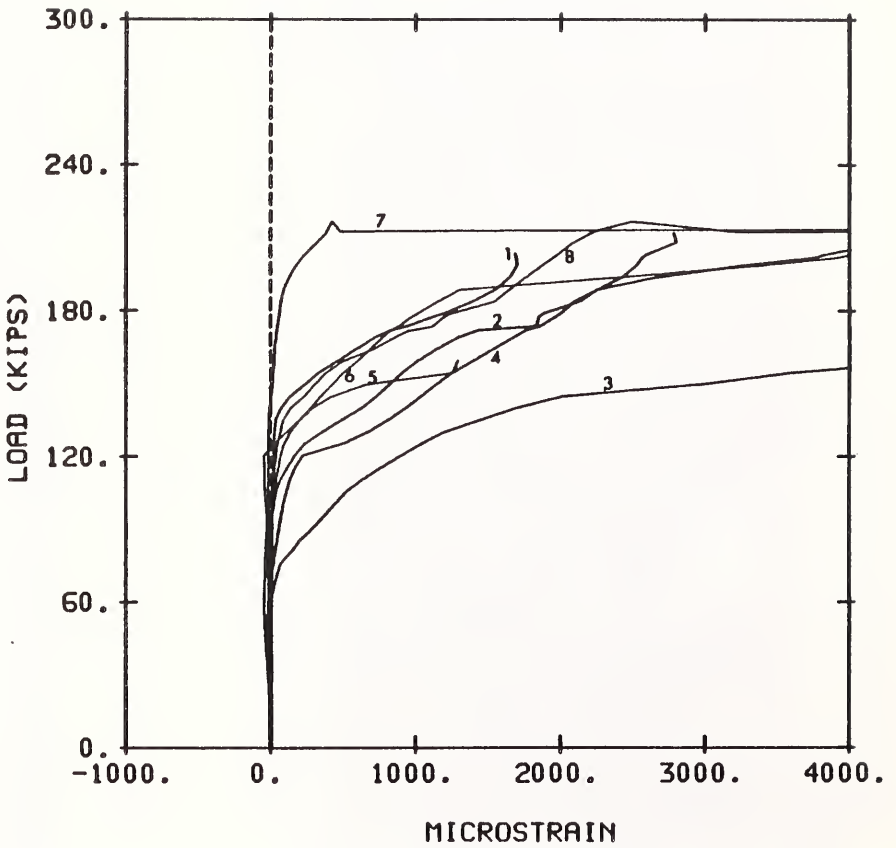

Figure 3.25 Load-Strain Curves for Gaged Shear Bars in FP1

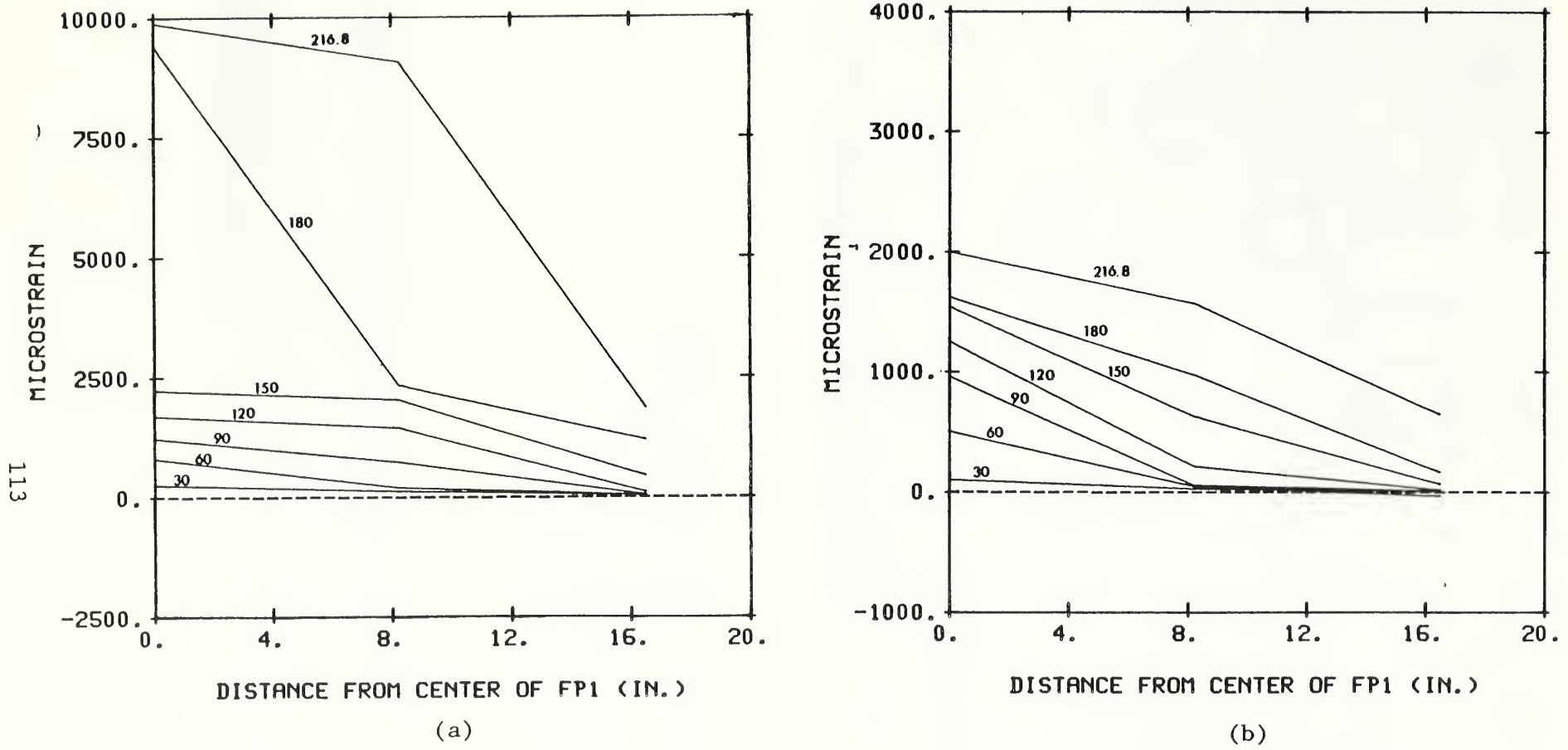

Figure 3.26 Flexural Strain Profiles of Specimen FP1
(a) in Span Tension Reinforcement
(b) in Transverse Tension Reinforcement

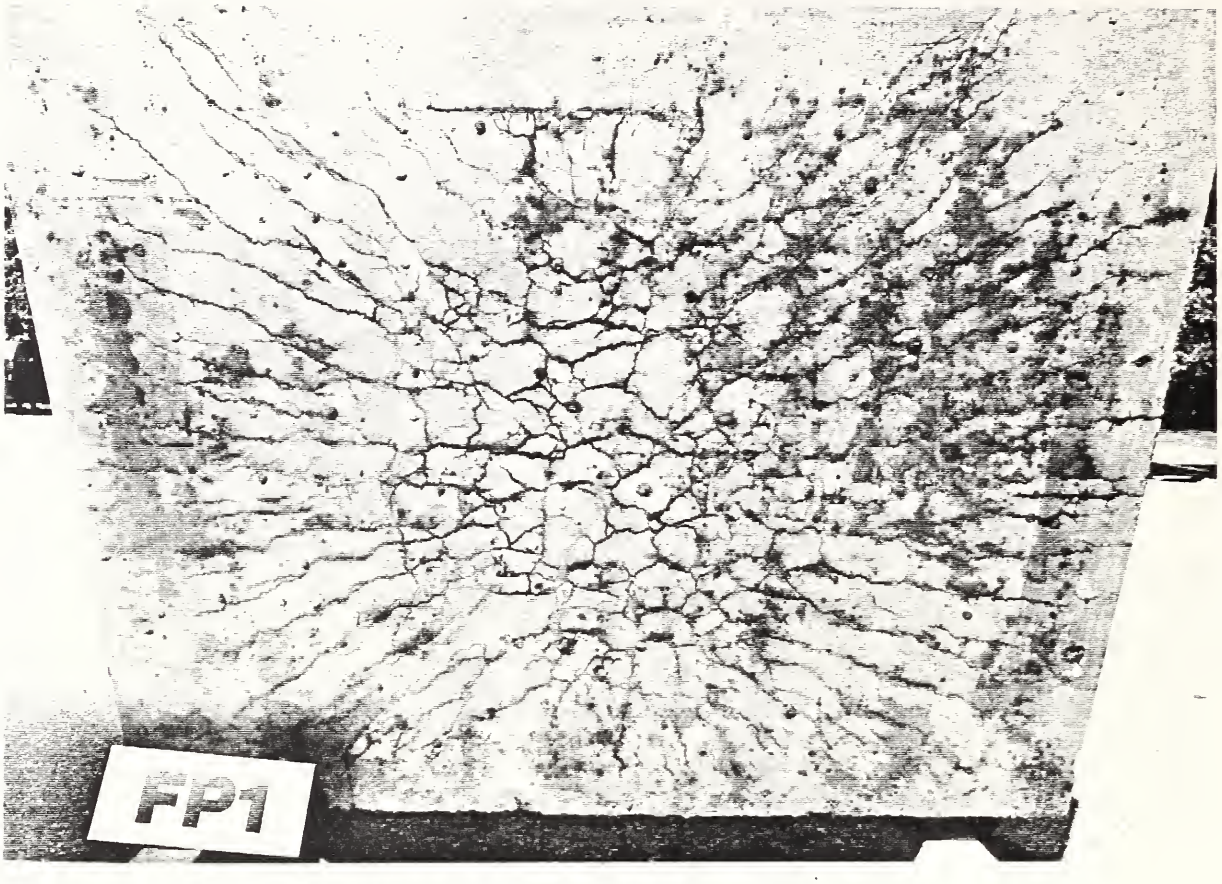

(a)

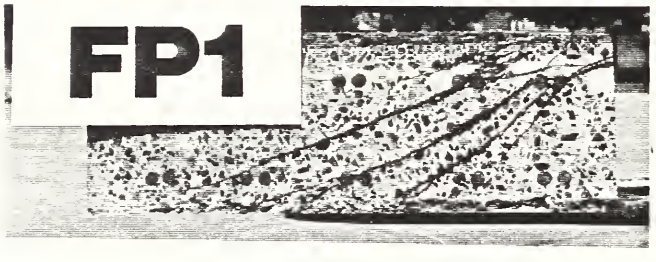

(b)

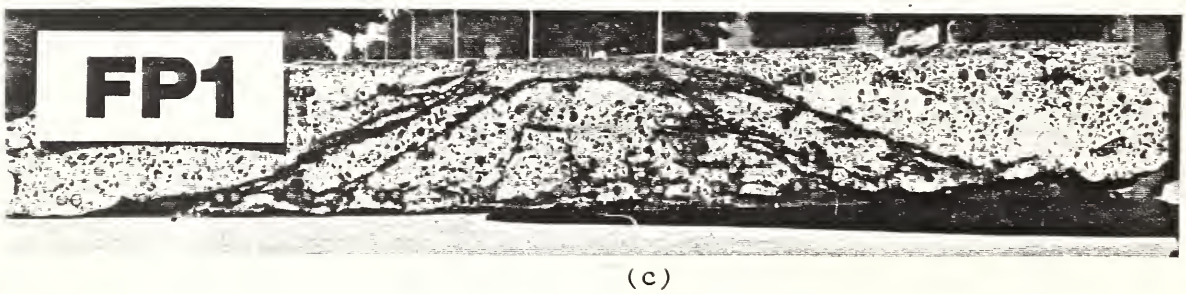

(c)

Figure 3.27 Crack Patterns in Specimen FP1
(a) Underside
(b) Span Cross-Section
(c) Transverse Cross-Section

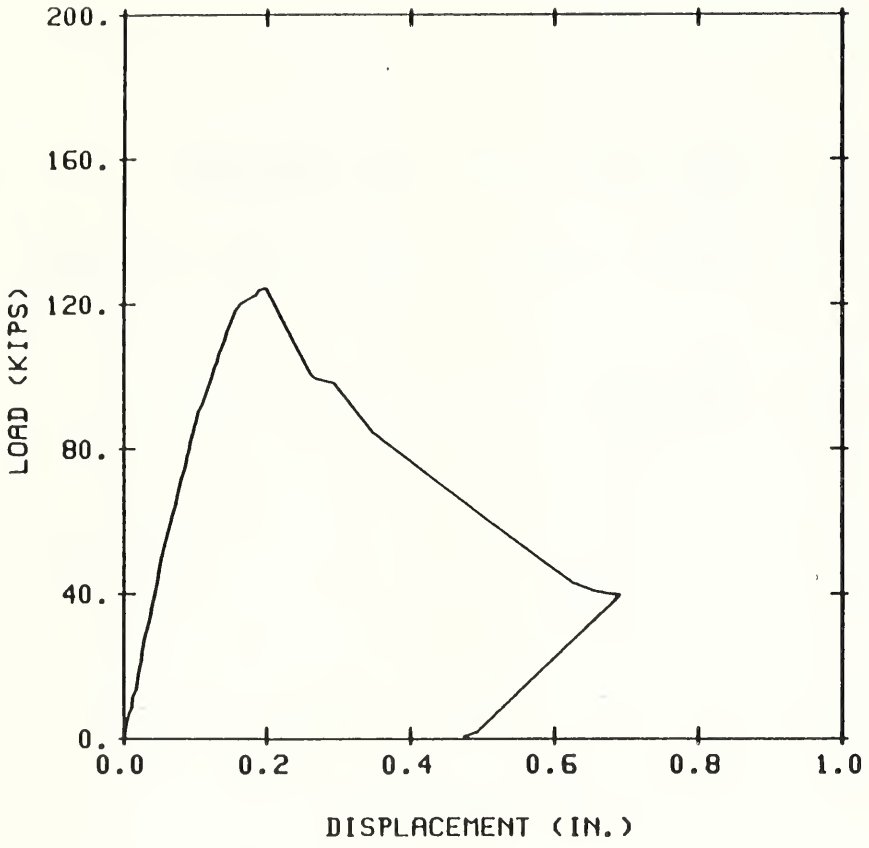

Figure 3.28 Load-Center Deflection Curve of Specimen AS9

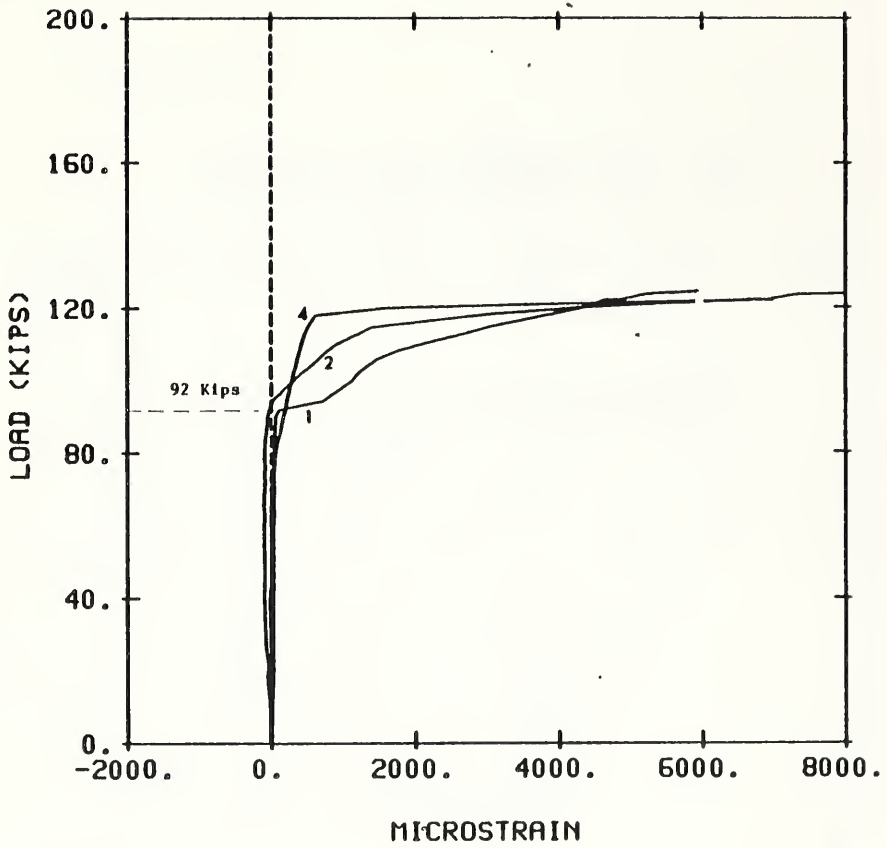

Figure 3.29 Load-Strain Curves for Gaged Shear Bars in AS9

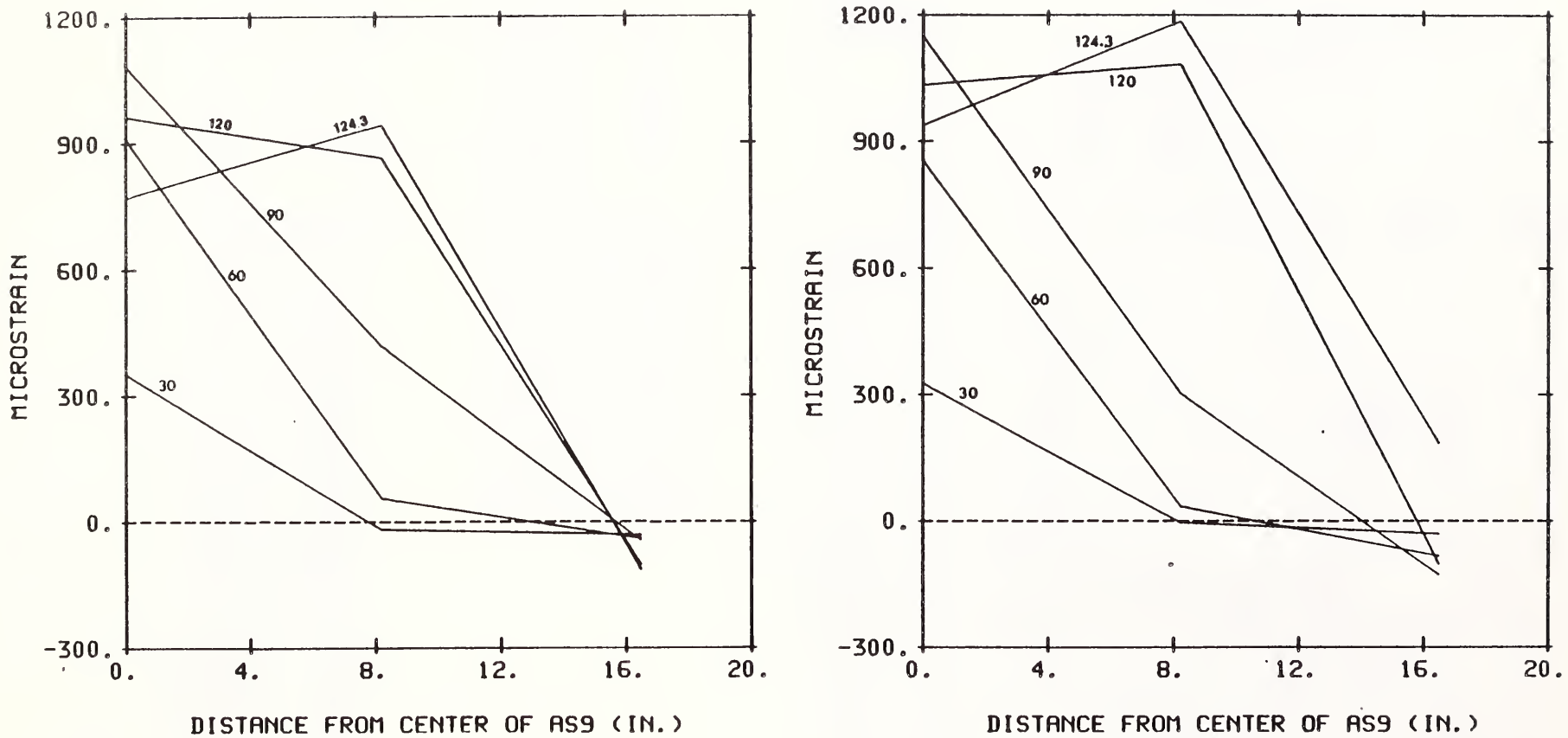

Figure 3.30 Flexural Strain Profiles of Specimen AS9
(a) in Span Tension Reinforcement
(b) in Transverse Tension Reinforcement
(c) in Span Compression Reinforcement

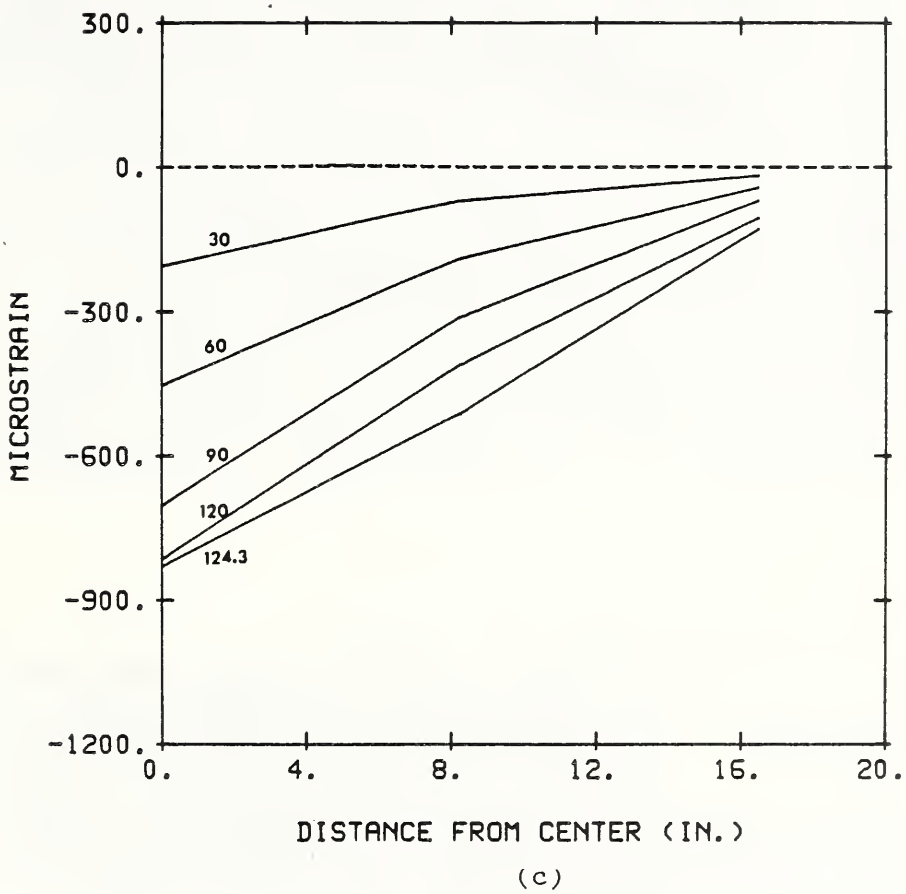

(c)

Figure 3.30 (continued)

(a)

(b)

(c)

Figure 3.31 Crack Patterns in Specimen AS9
(a) Underside
(b) Span Cross-Section
(c) Transverse Cross-Section

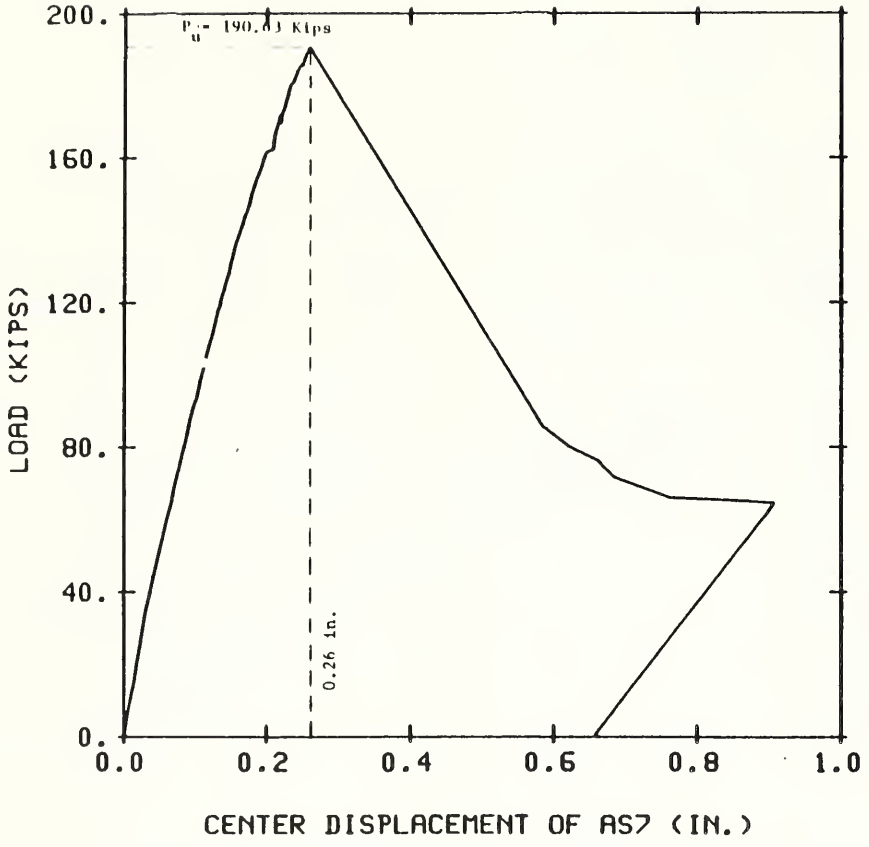

Figure 3.32 Load Center Deflection Curve of Specimen AS7

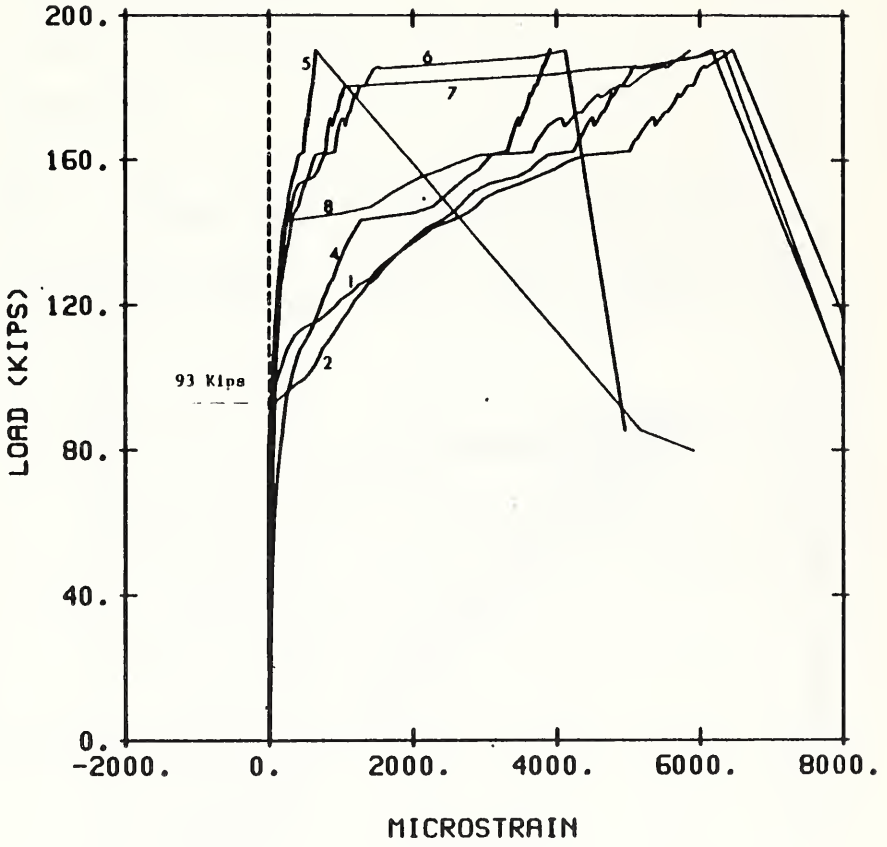

Figure 3.33 Load-Strain Curves for Gaged Shear Bars in AS7

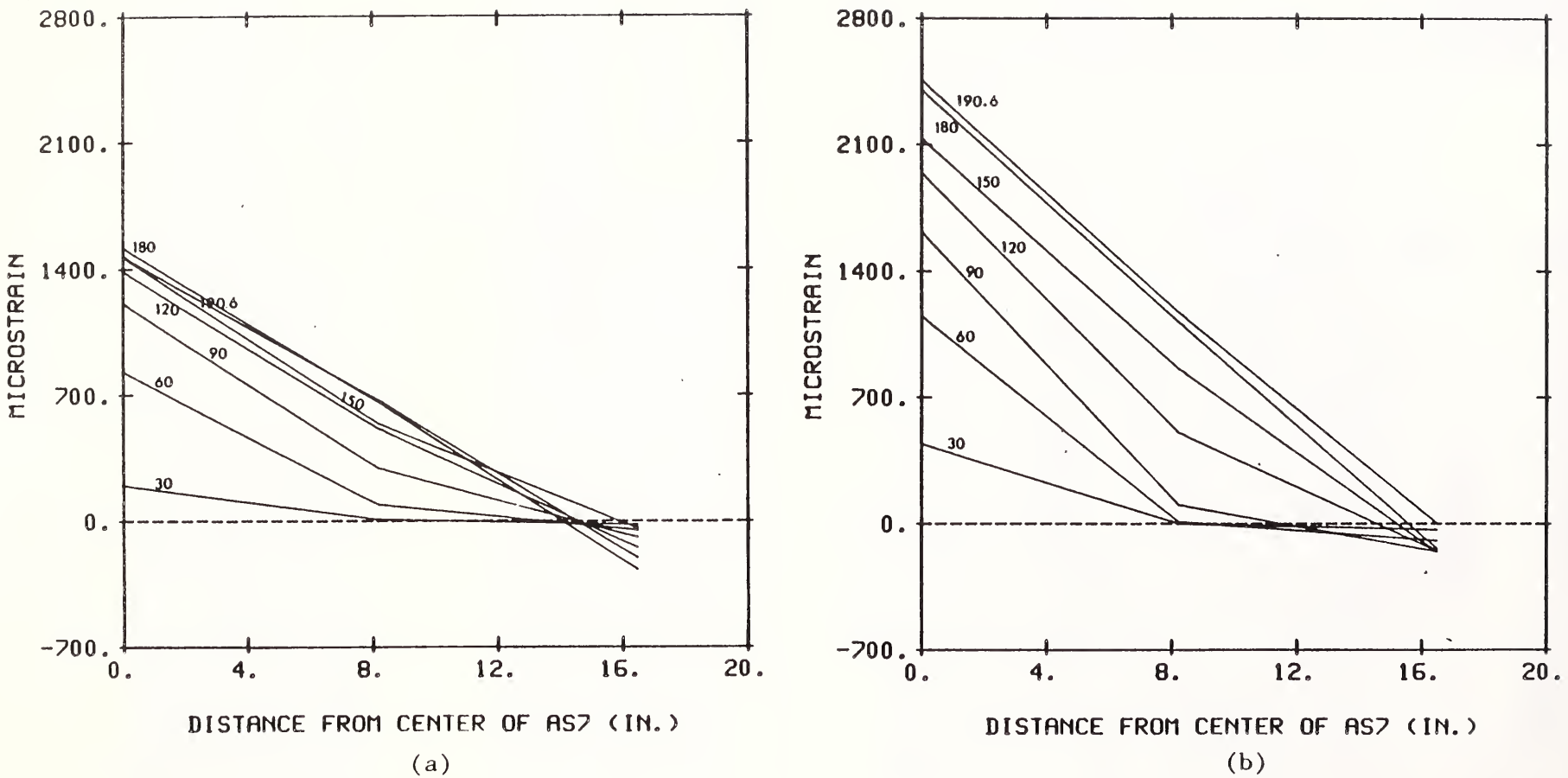

Figure 3.34 Flexural Strain Profiles of Specimen AS7
(a) in Span Tension Reinforcement
(b) in Transverse Tension Reinforcement
(c) in Span Compression Reinforcement

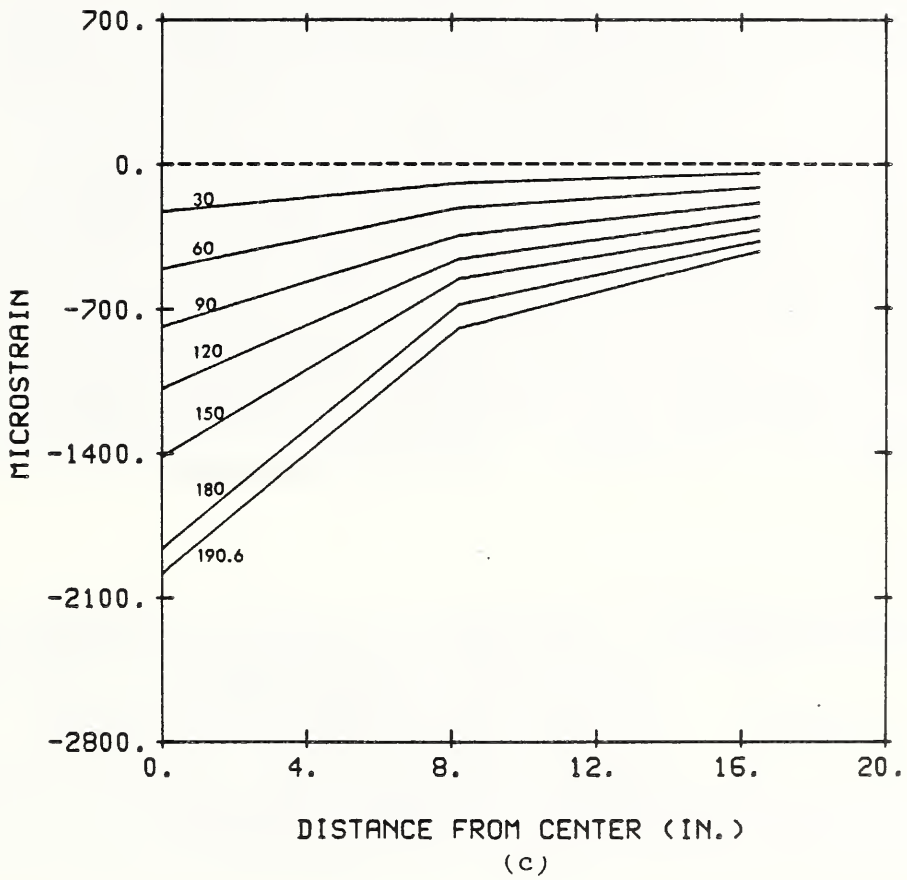

(c)

Figure 3.34 (continued)

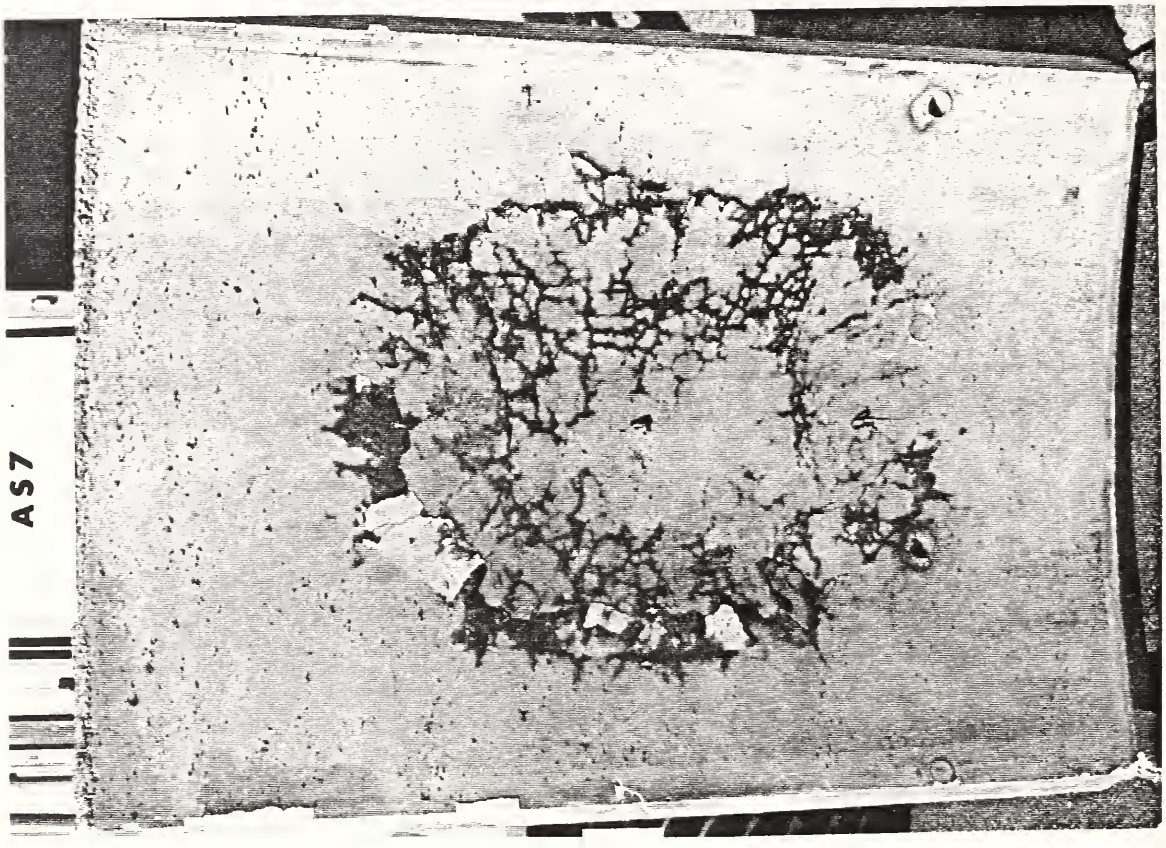

(a)

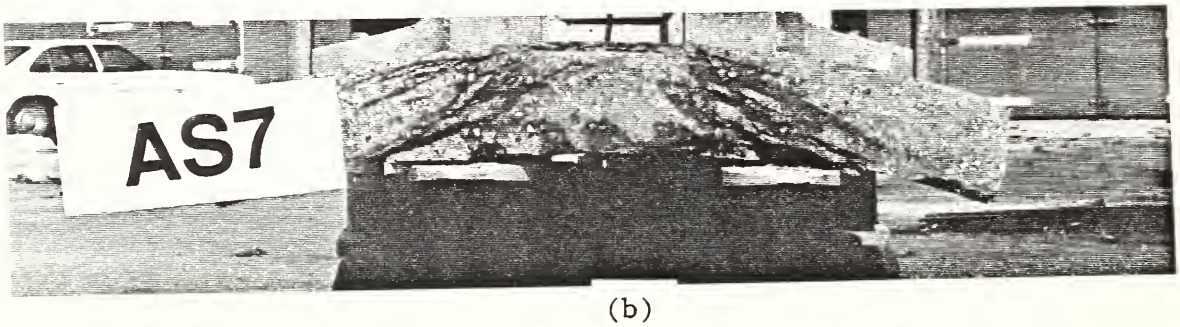

(b)

(c)

Figure 3.35 Crack Patterns in Specimen AS7
(a) Underside
(b) Span Cross-Section
(c) Transverse Cross-Section

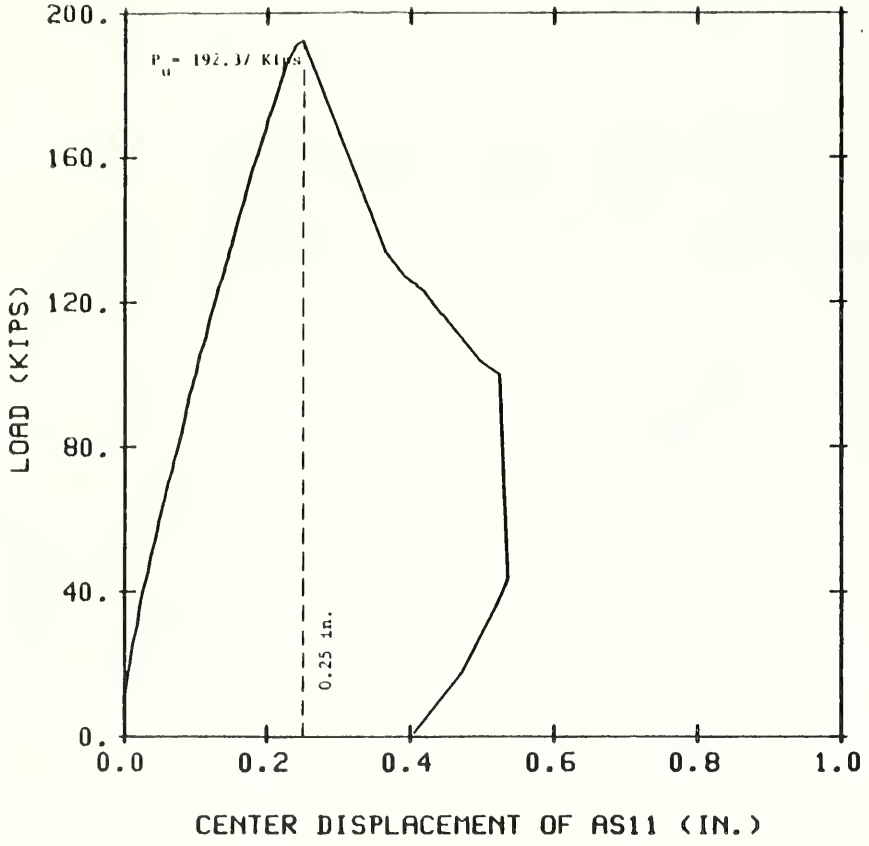

Figure 3.36 Load-Center Deflection Curve of Specimen AS11

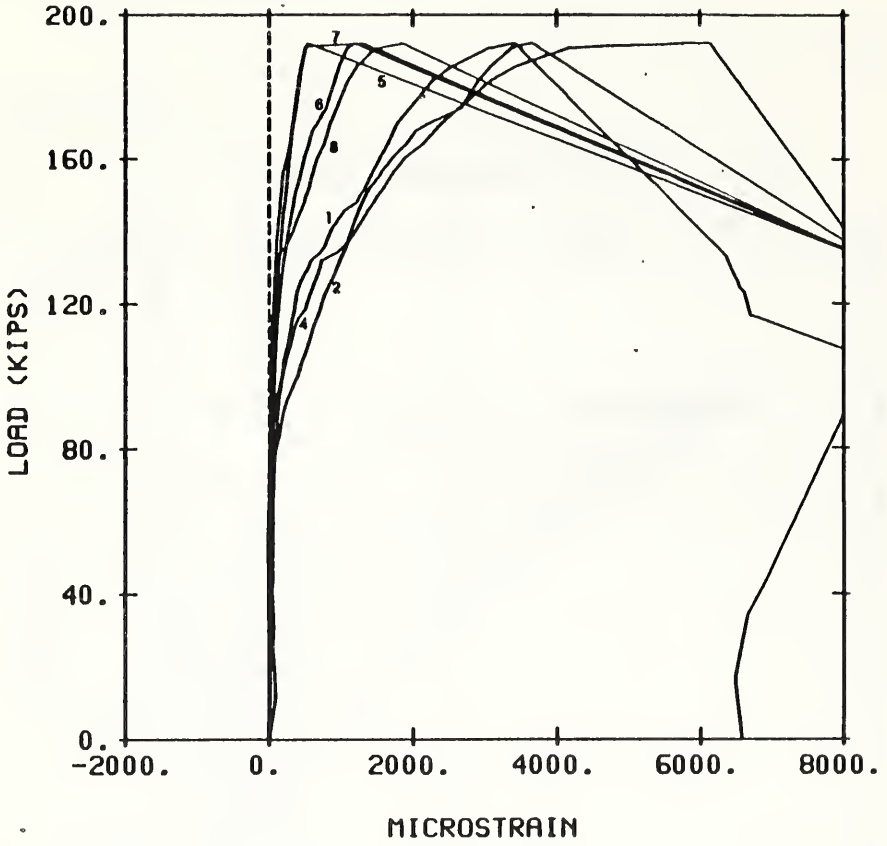

Figure 3.37 Load-Strain Curves for Gaged Shear Bars in AS11

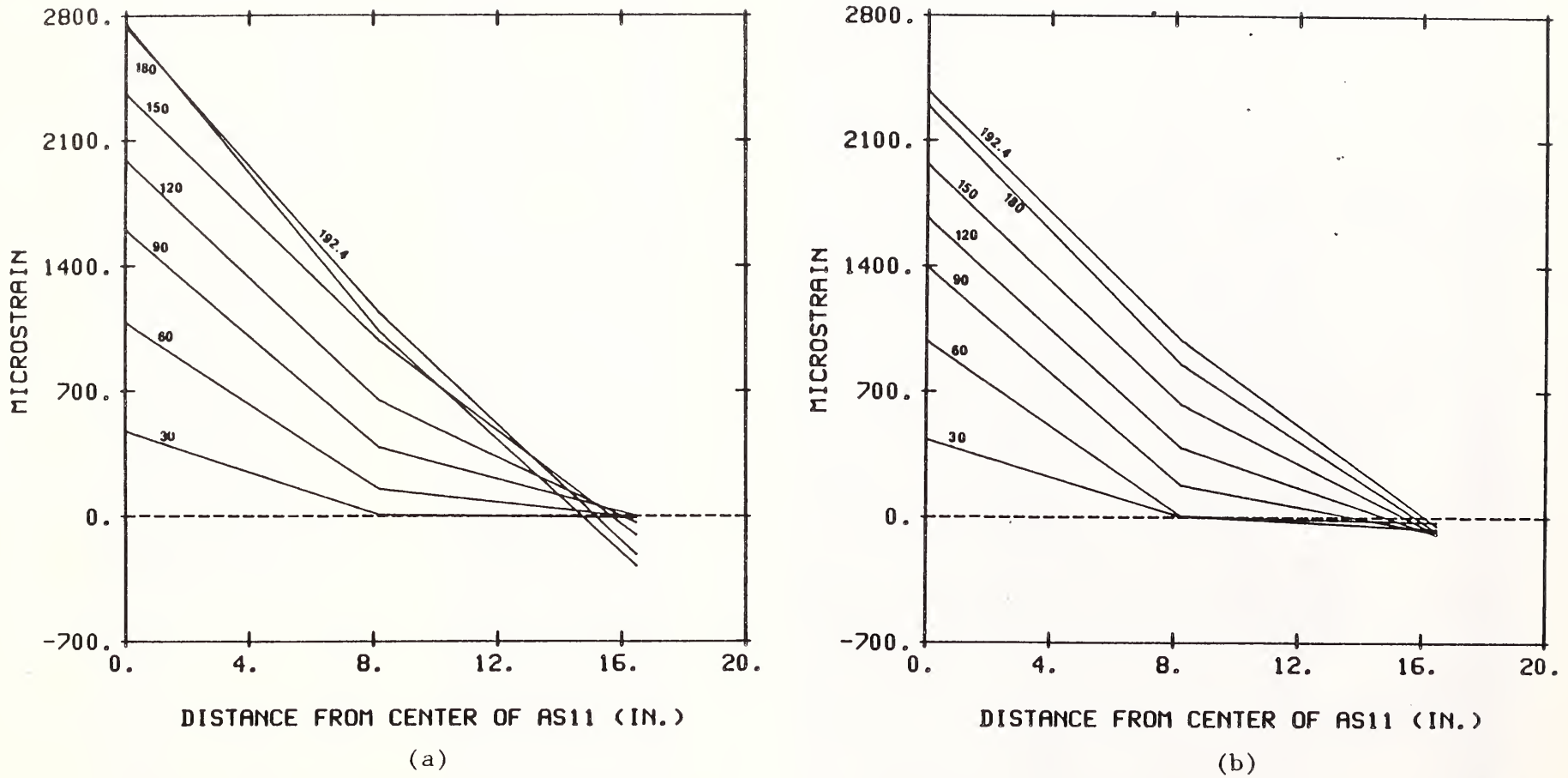

Figure 3.38 Flexural Strain Profiles of Specimen AS11
(a) in Span Tension Reinforcement
(b) in Transverse Tension Reinforcement
(c) in Span Compression Reinforcement

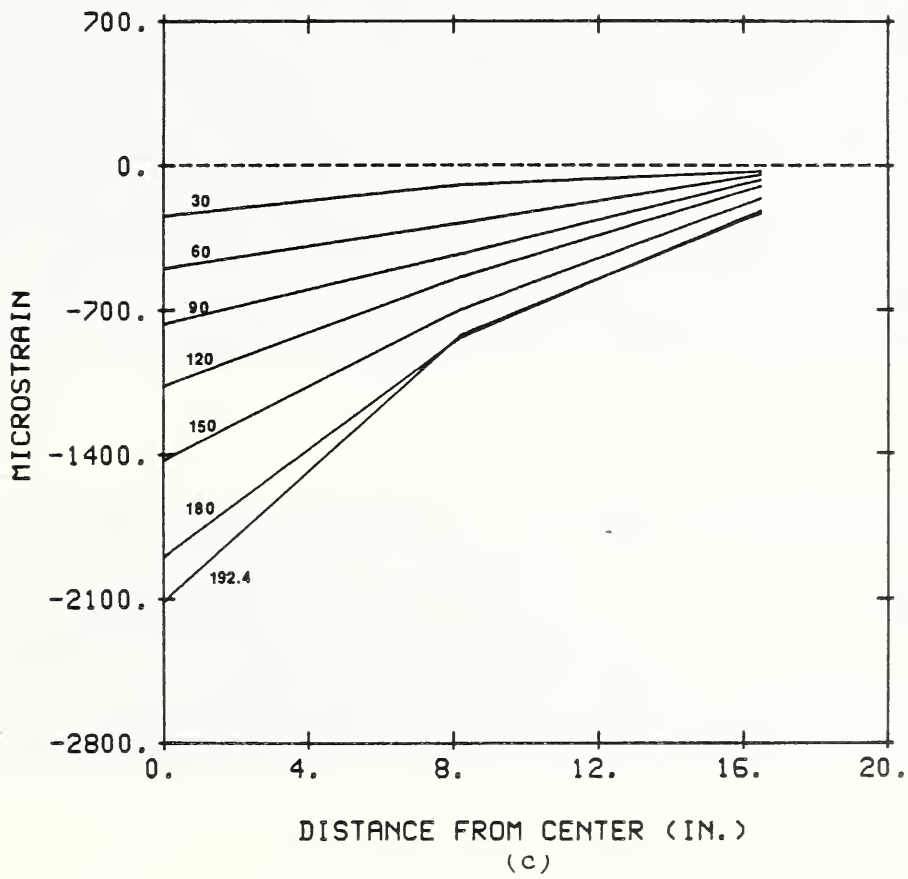

Figure 3.38 (continued)

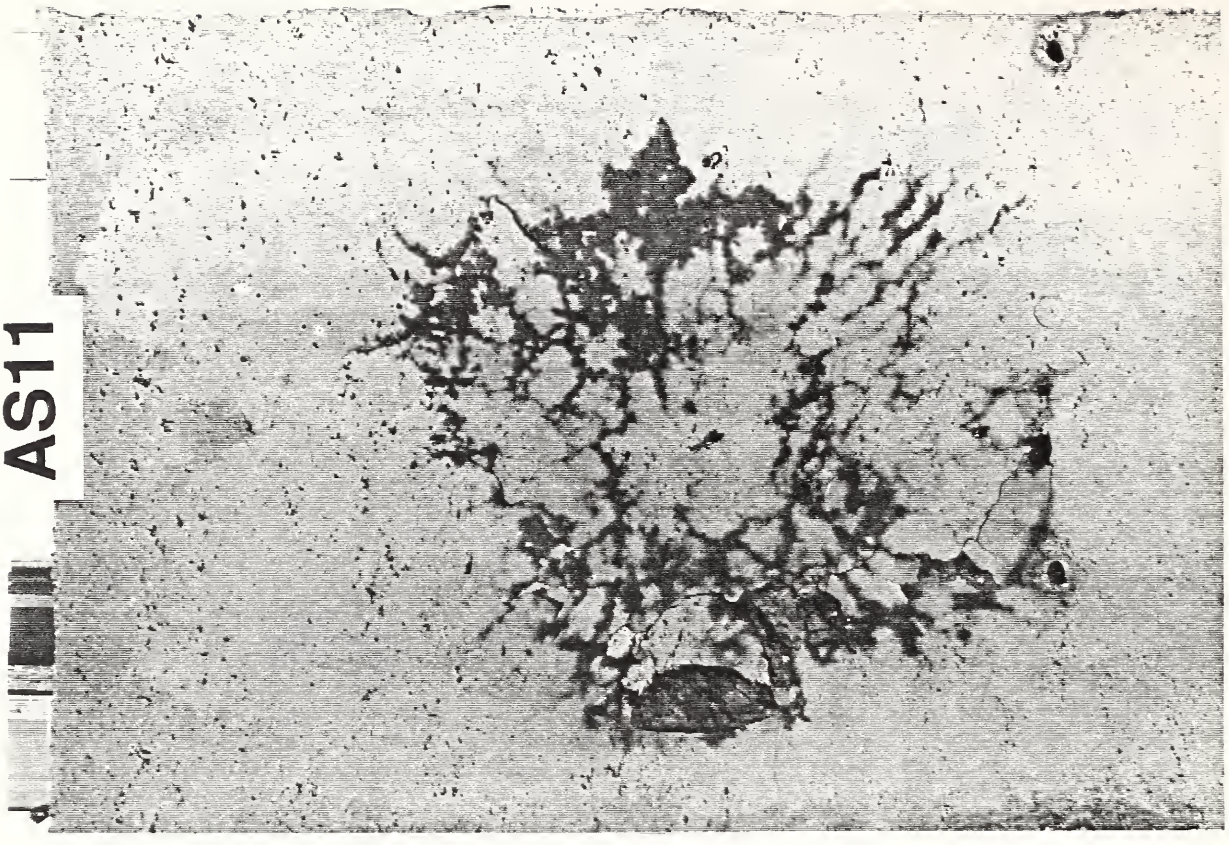

(a)

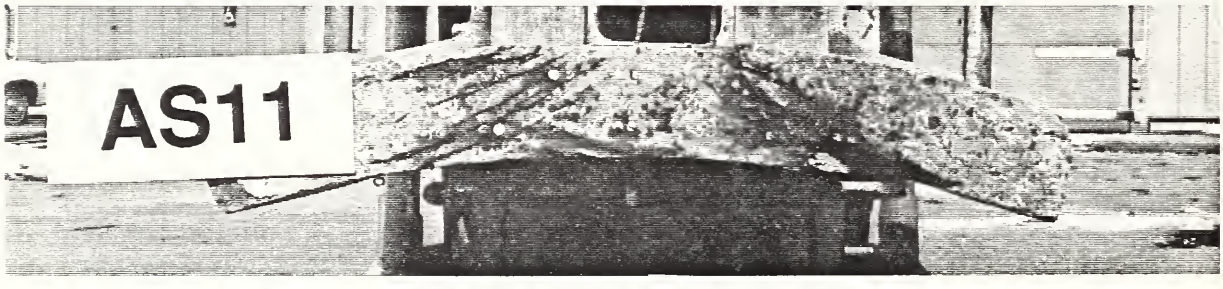

(b)

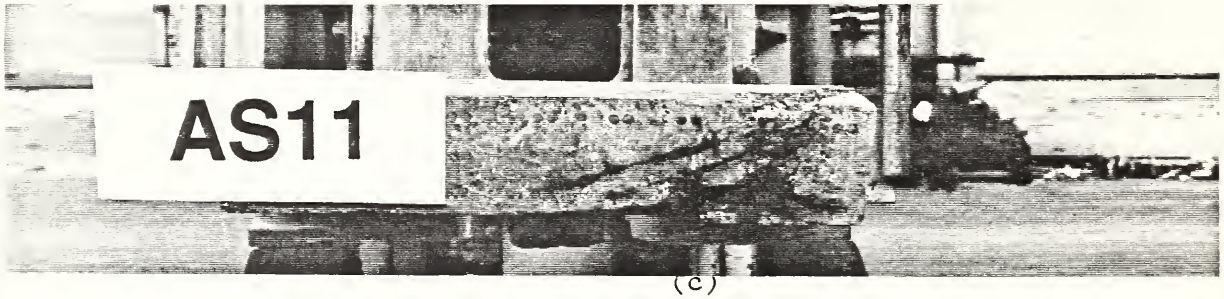

(c)

Figure 3.39 Crack Patterns in Specimen AS11
(a) Underside
(b) Span Cross-Section
(c) Transverse Cross-Section

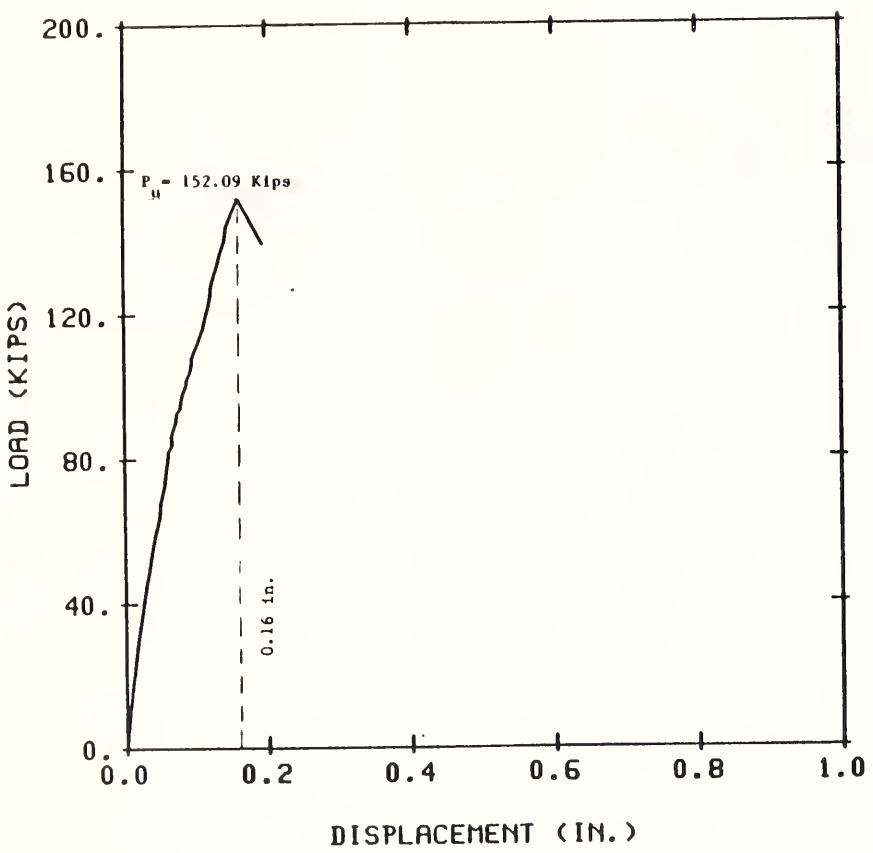

Figure 3.40 Load-Center Deflection Curve of Specimen AS10

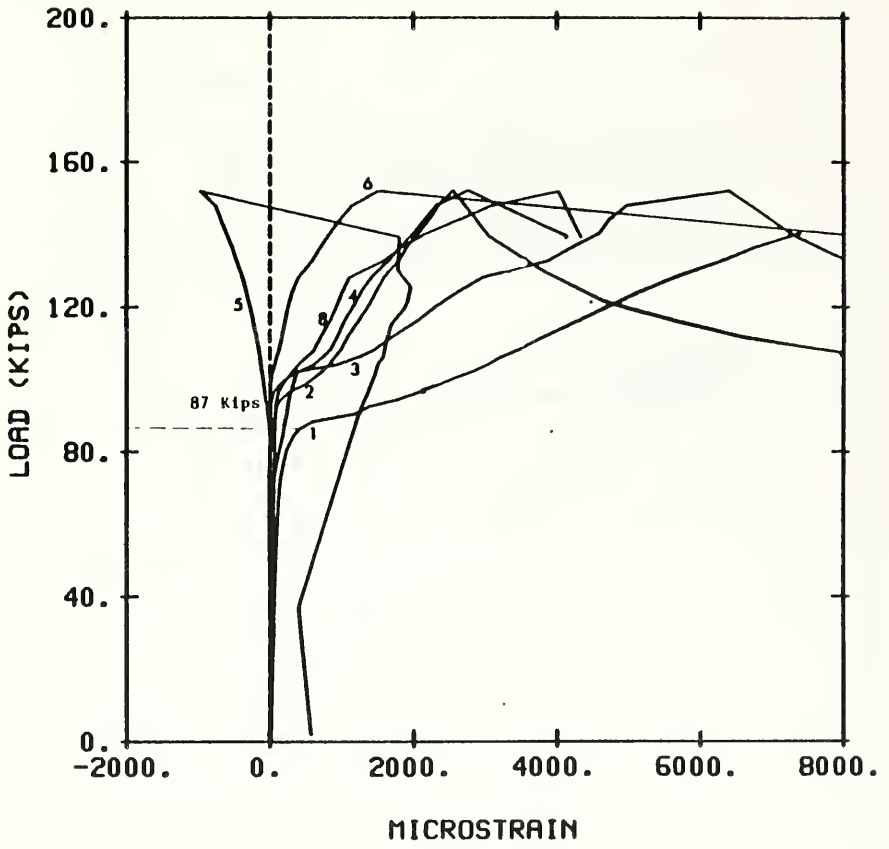

Figure 3.41 Load-Strain Curves for Gaged Shear Bars in AS10

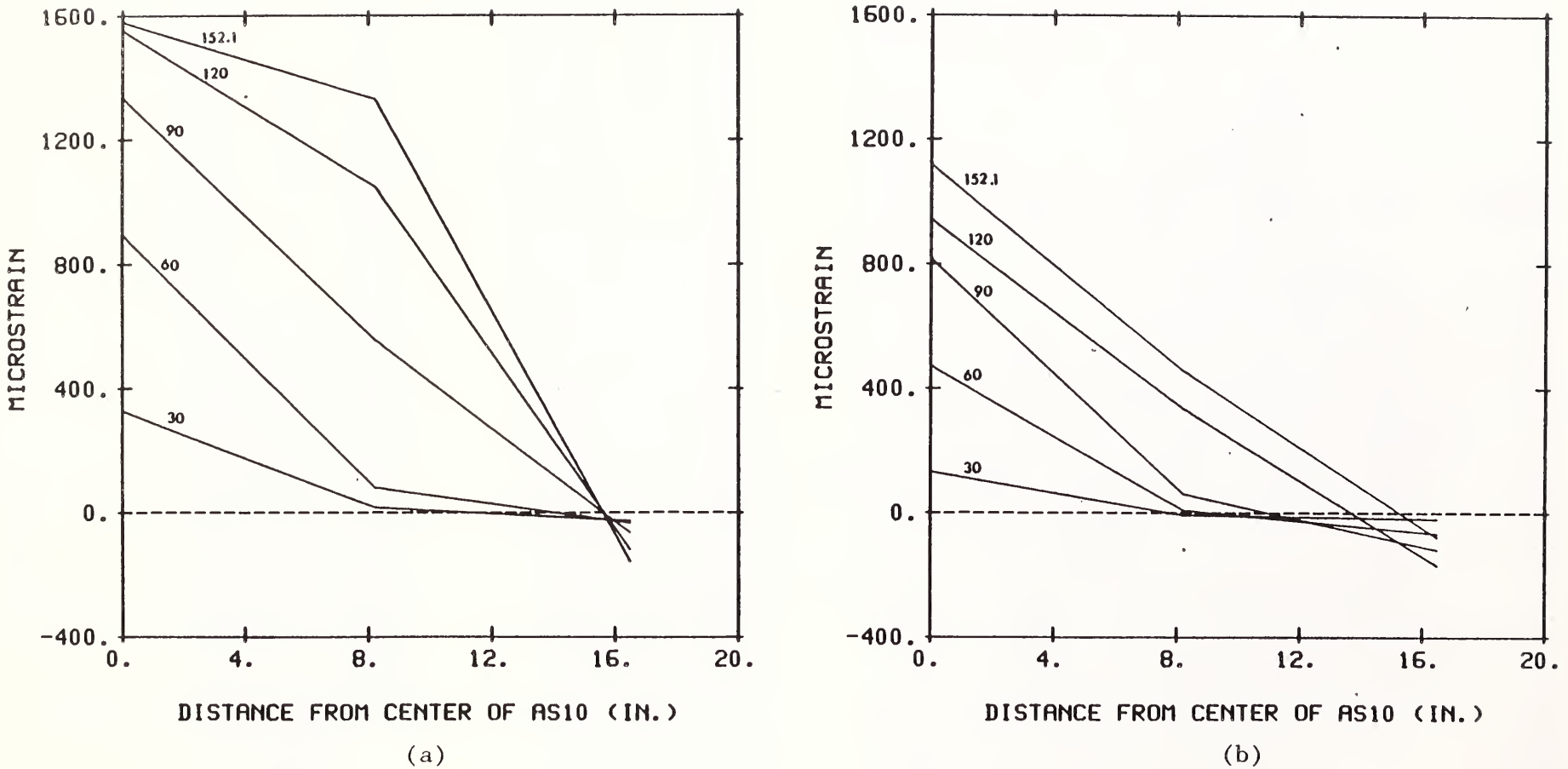

Figure 3.42 Flexural Strain Profiles of Specimen AS10
(a) in Span Tension Reinforcement
(b) in Transverse Tension Reinforcement
(c) in Span Compression Reinforcement

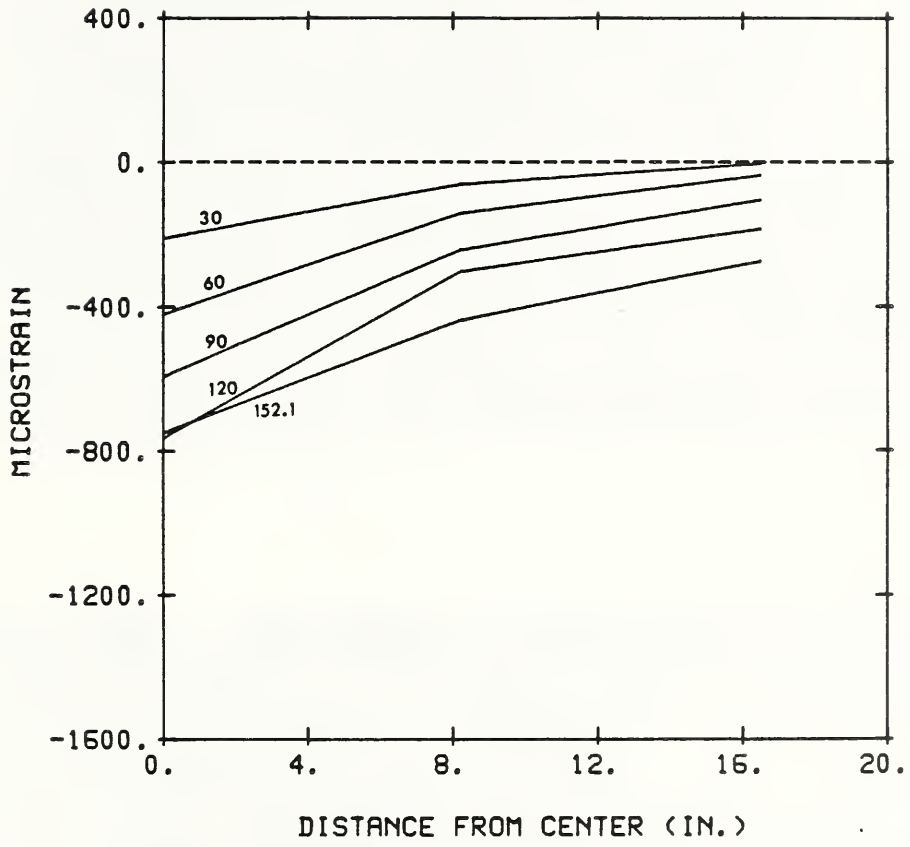

(c)

Figure 3.42 (continued)

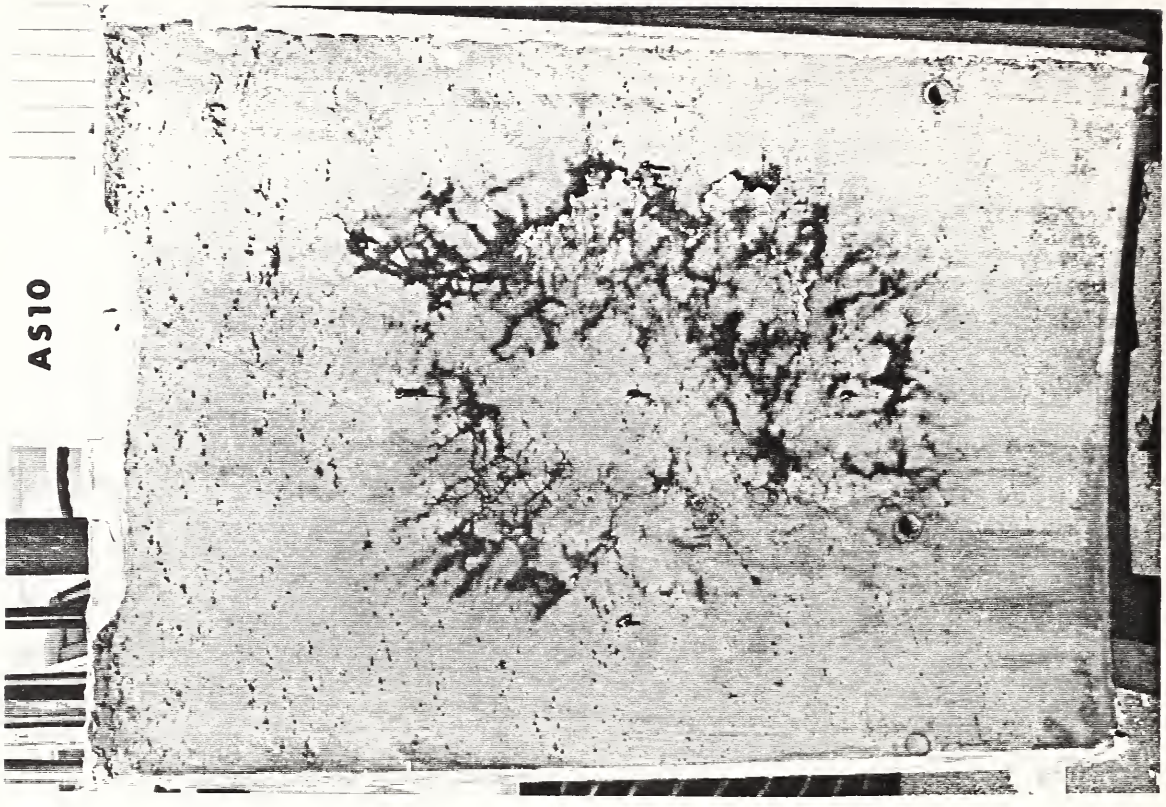

(a)

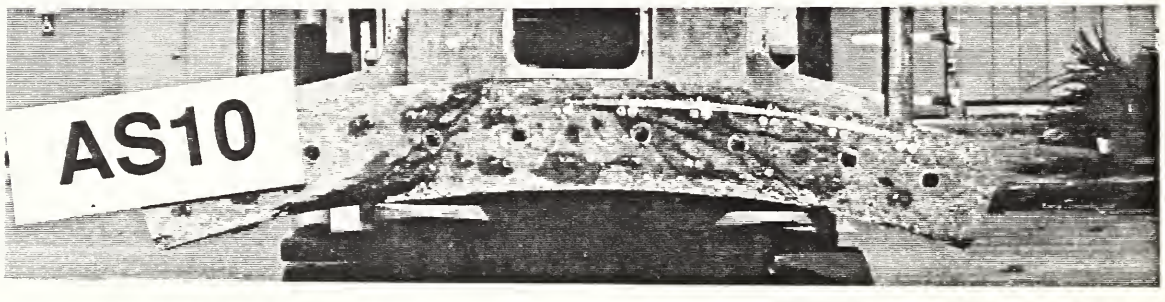

(b)

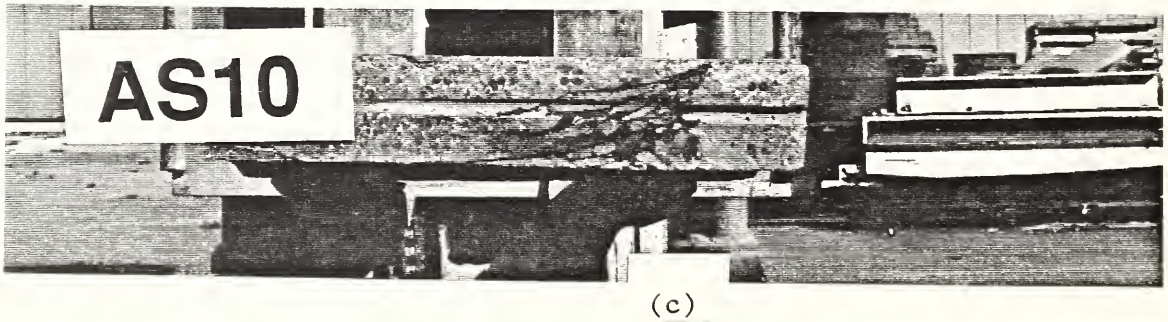

(c)

Figure 3.43 Crack Patterns in Specimen AS10
(a) Underside
(b) Span Cross-Section
(c) Transverse Cross-Section

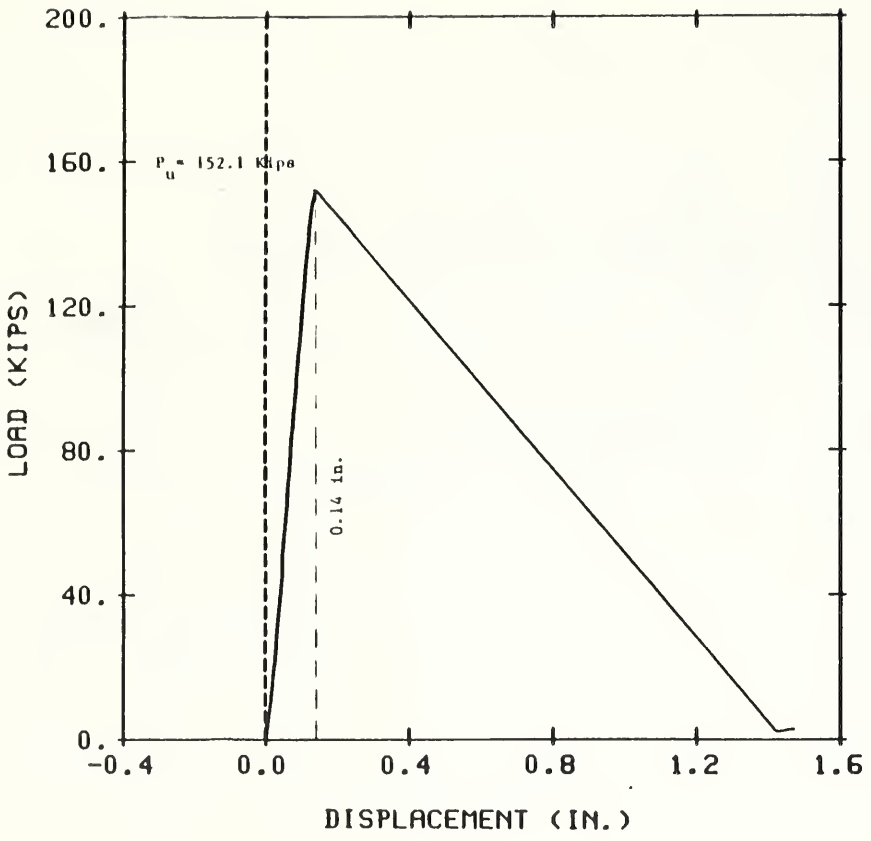

Figure 3.44 Load-Center Deflection Curve of Specimen AS8

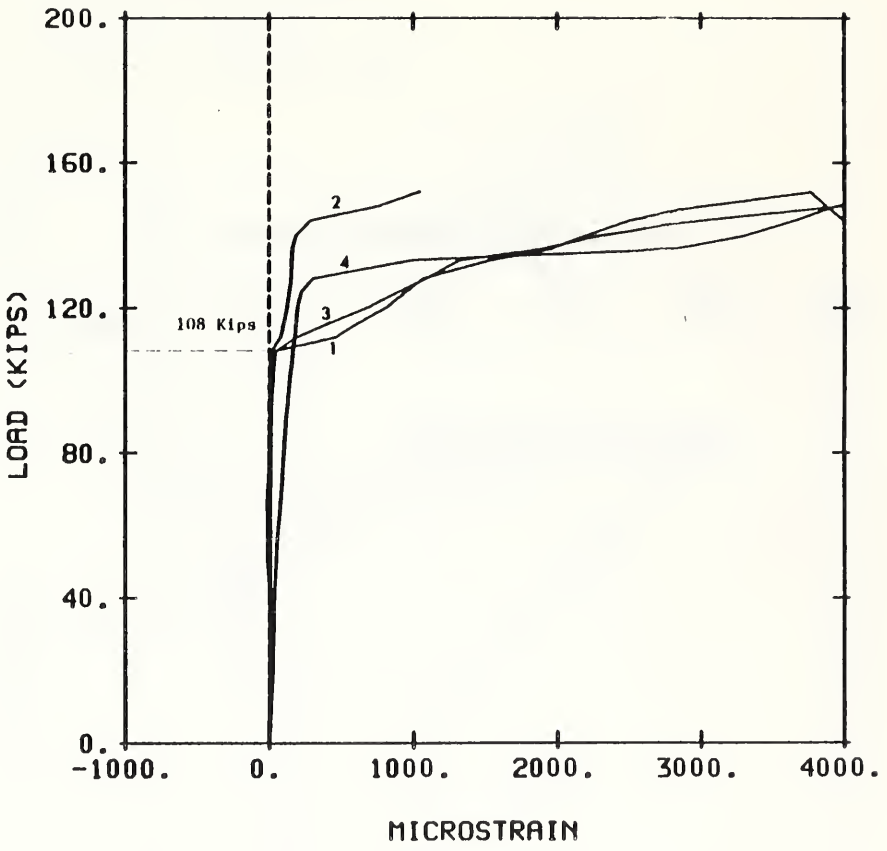

Figure 3.45 Load-Strain Curves for Gaged Shear Bars in AS8

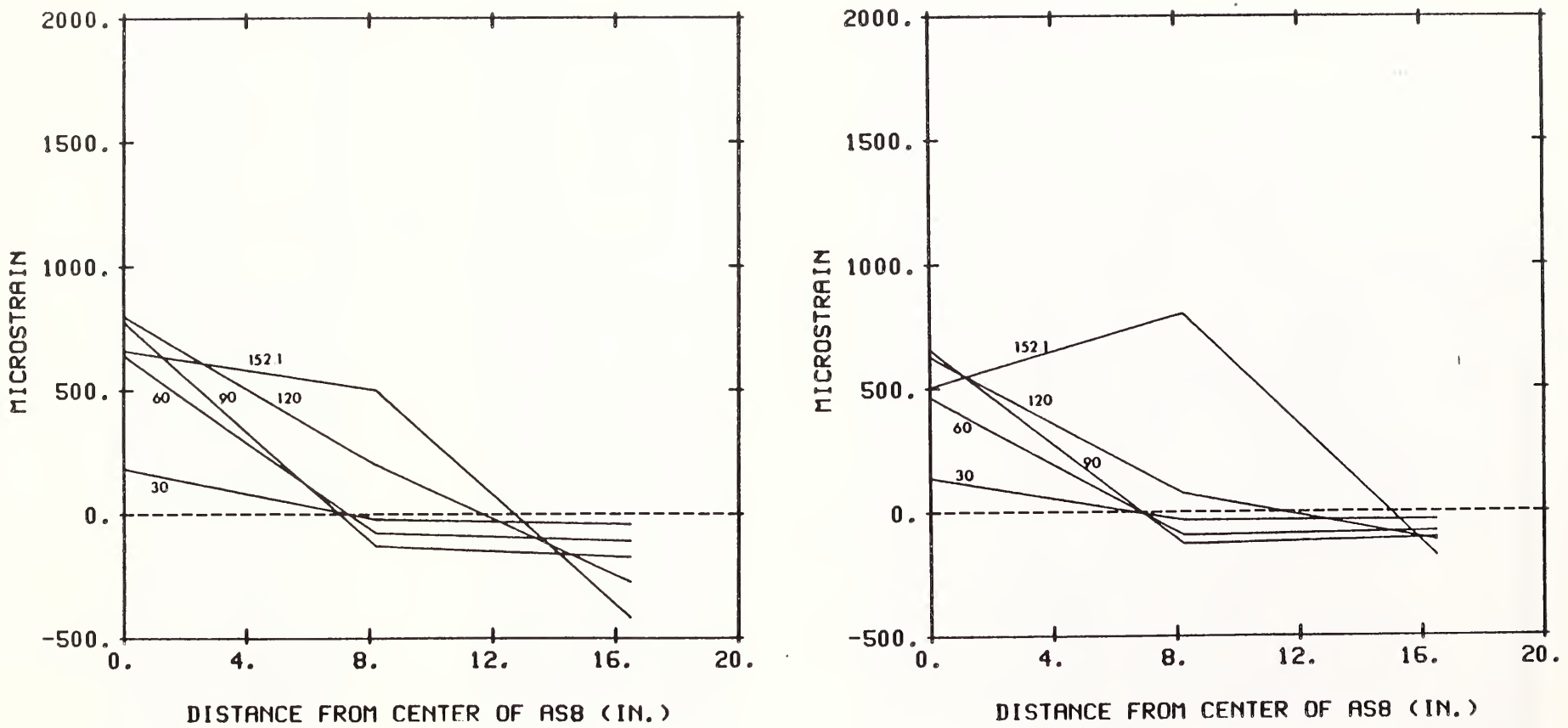

Figure 3.46 Flexural Strain Profiles of Specimen AS8
(a) in Span Tension Reinforcement
(b) in Transverse Tension Reinforcement
(c) in Span Compression Reinforcement

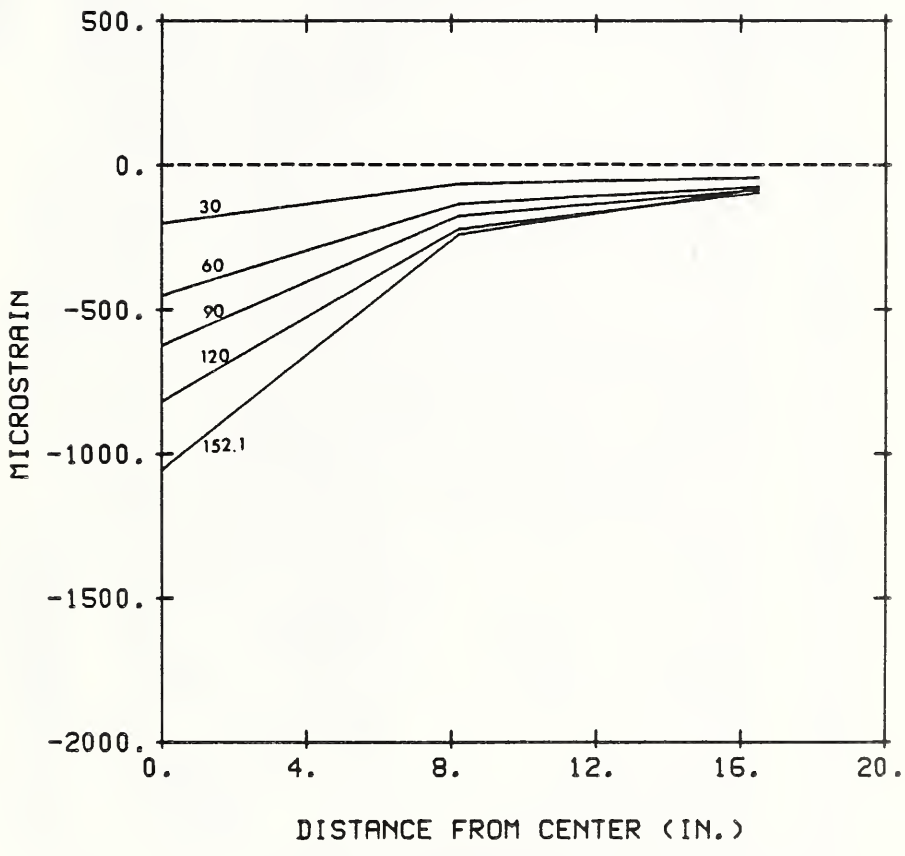

(c)

Figure 3.46 (continued)

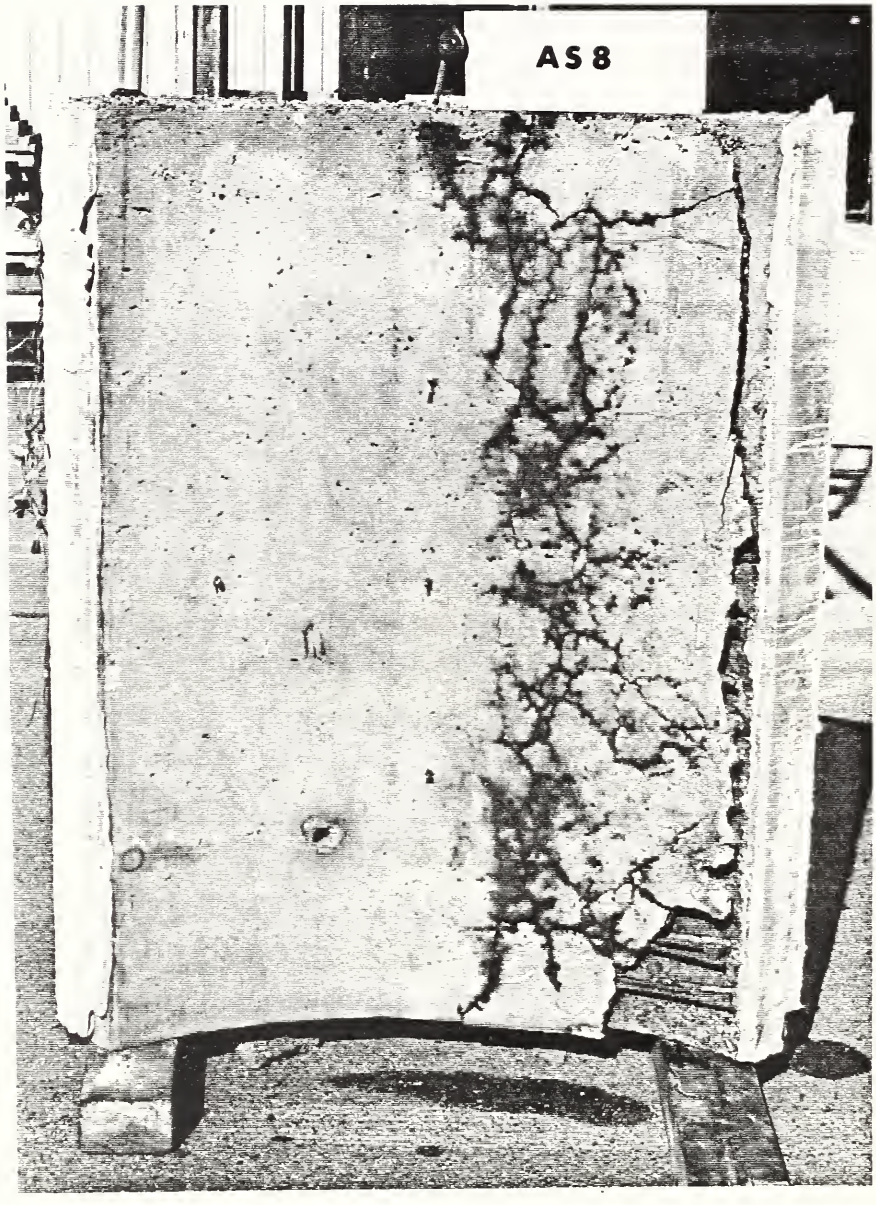

Figure 3.47 Crack Patterns on the Underside of Specimen AS8

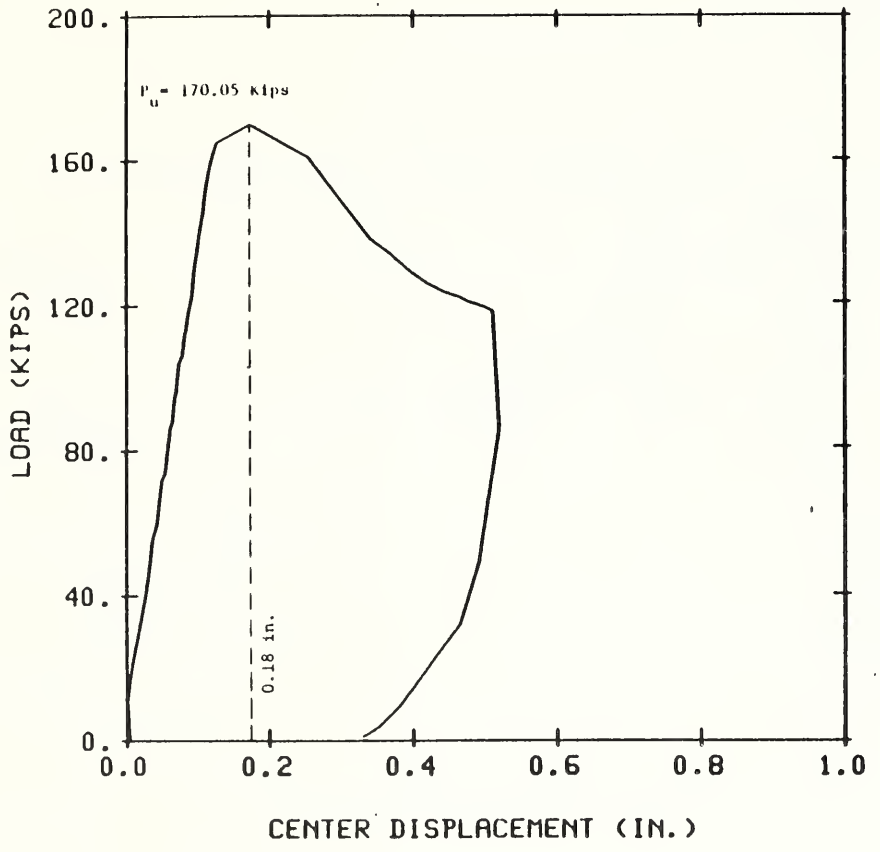

Figure 3.48 Load-Center Deflection Curve of Specimen AS12

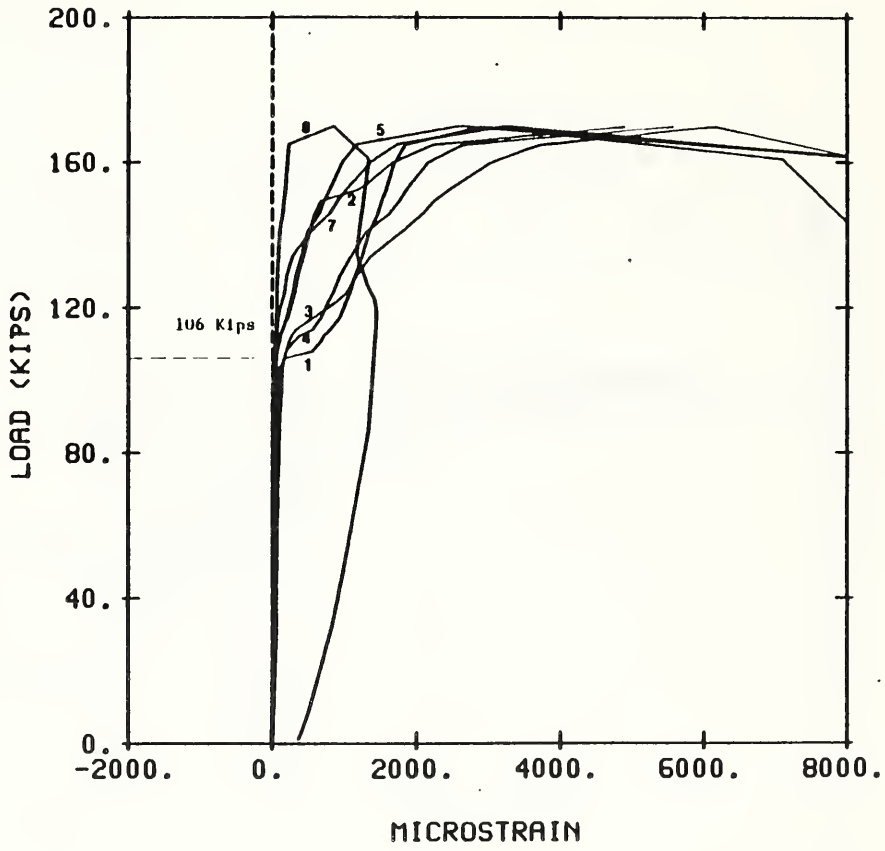

Figure 3.49 Load-Strain Curves for Gaged Shear Bars in AS12

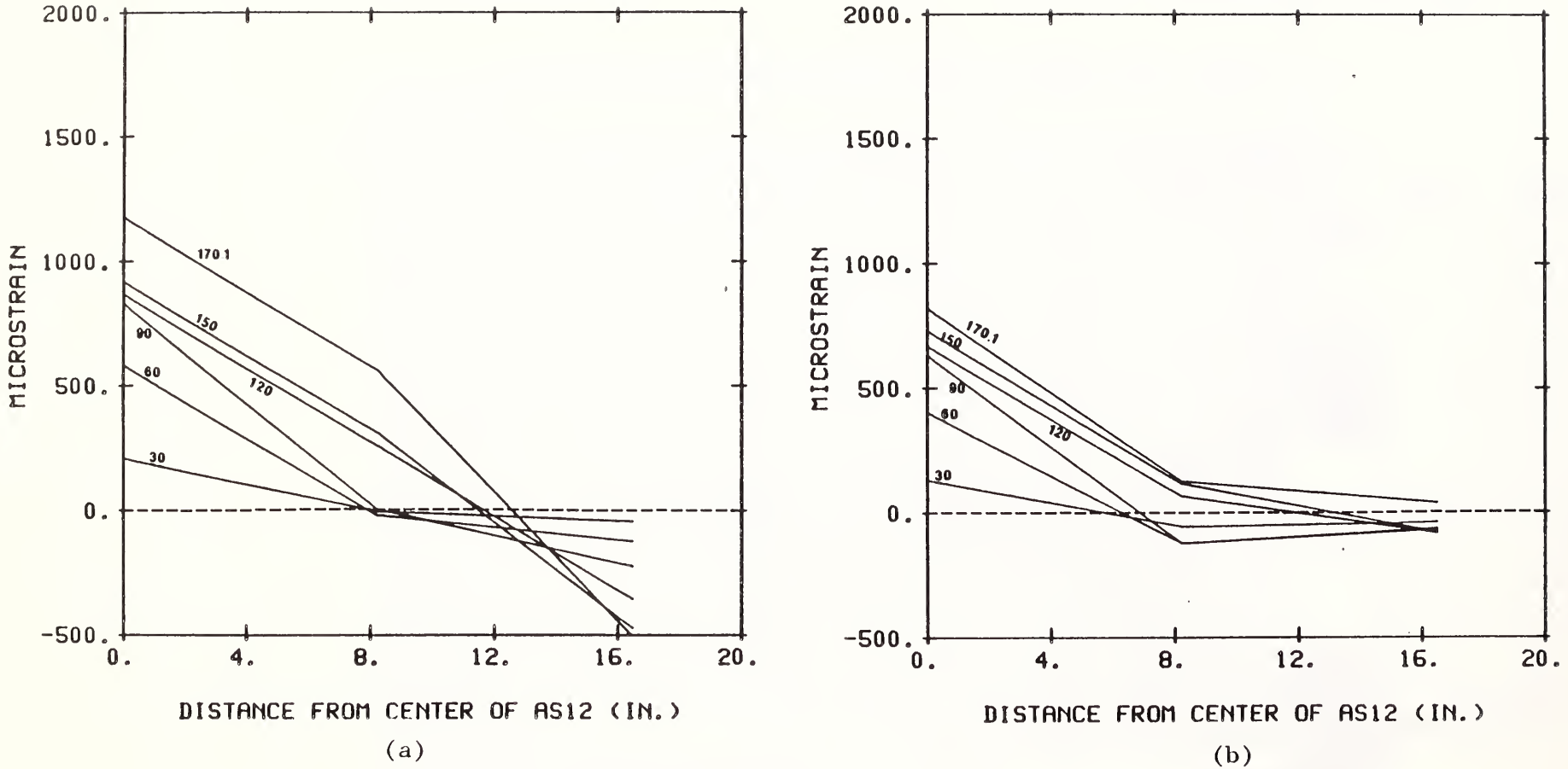

Figure 3.50 Flexural Strain Profiles of Specimen AS12
(a) in Span Tension Reinforcement
(b) in Transverse Tension Reinforcement
(c) in Span Compression Reinforcement

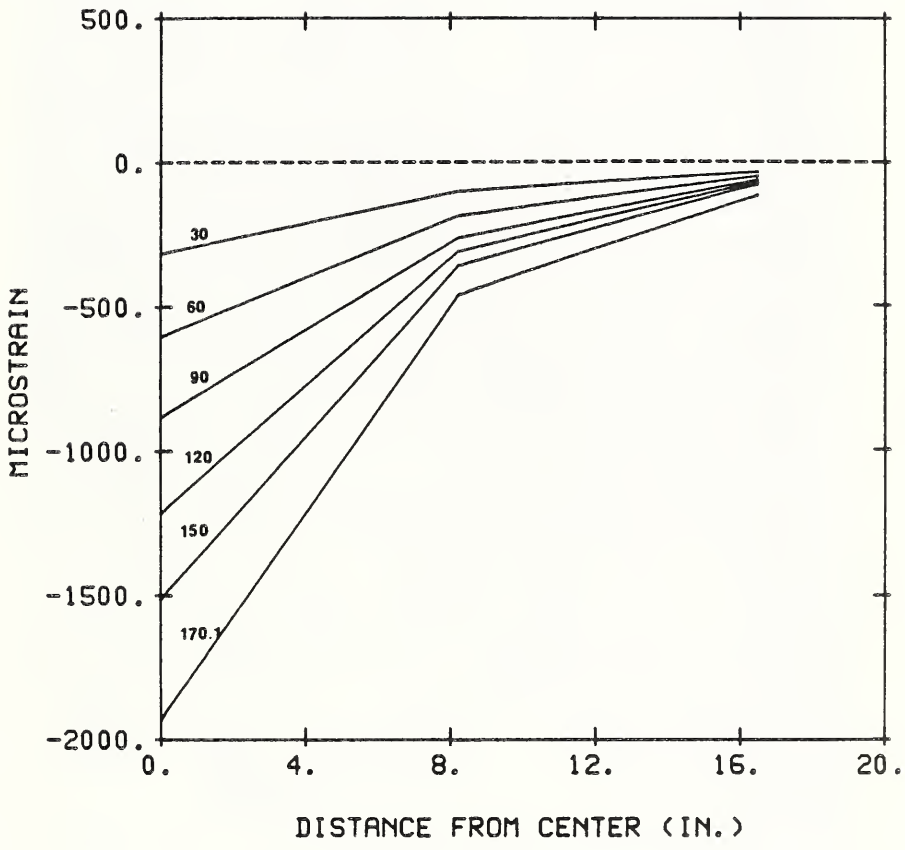

(c)

Figure 3.50 (continued)

Figure 3.51 Crack Patterns on the Underside of Specimen AS12

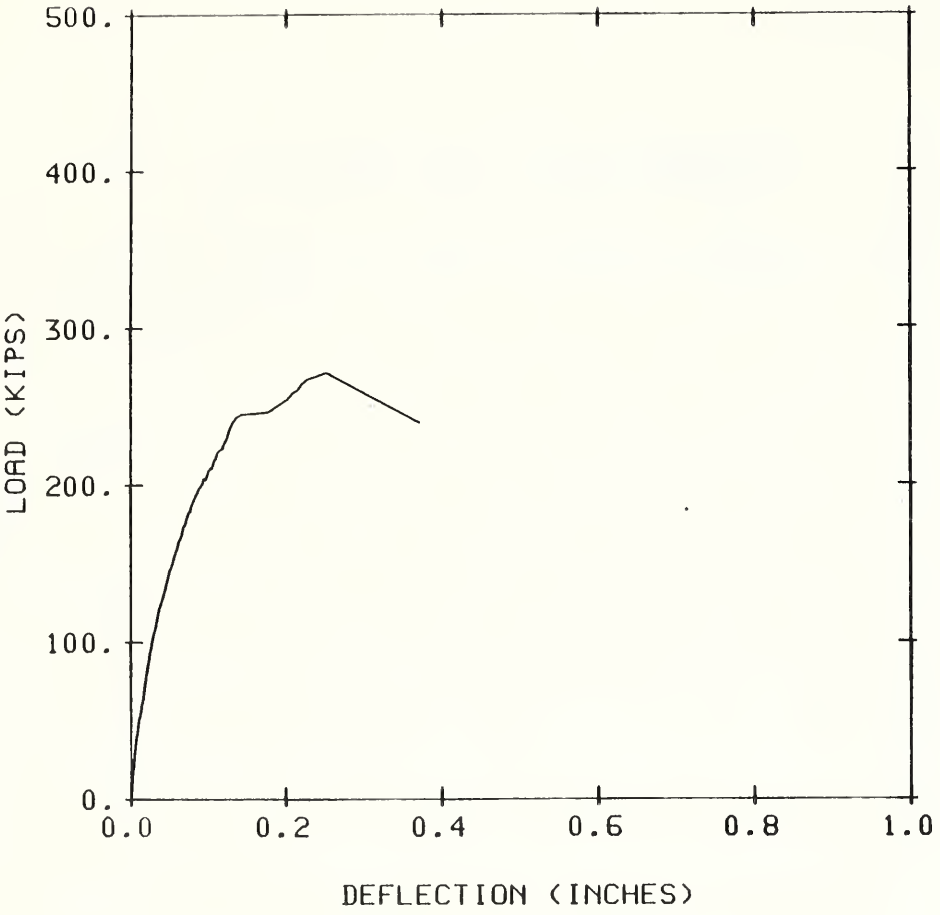

Figure 3.52 Load-Center Deflection Curve of Specimen 4FP2-1

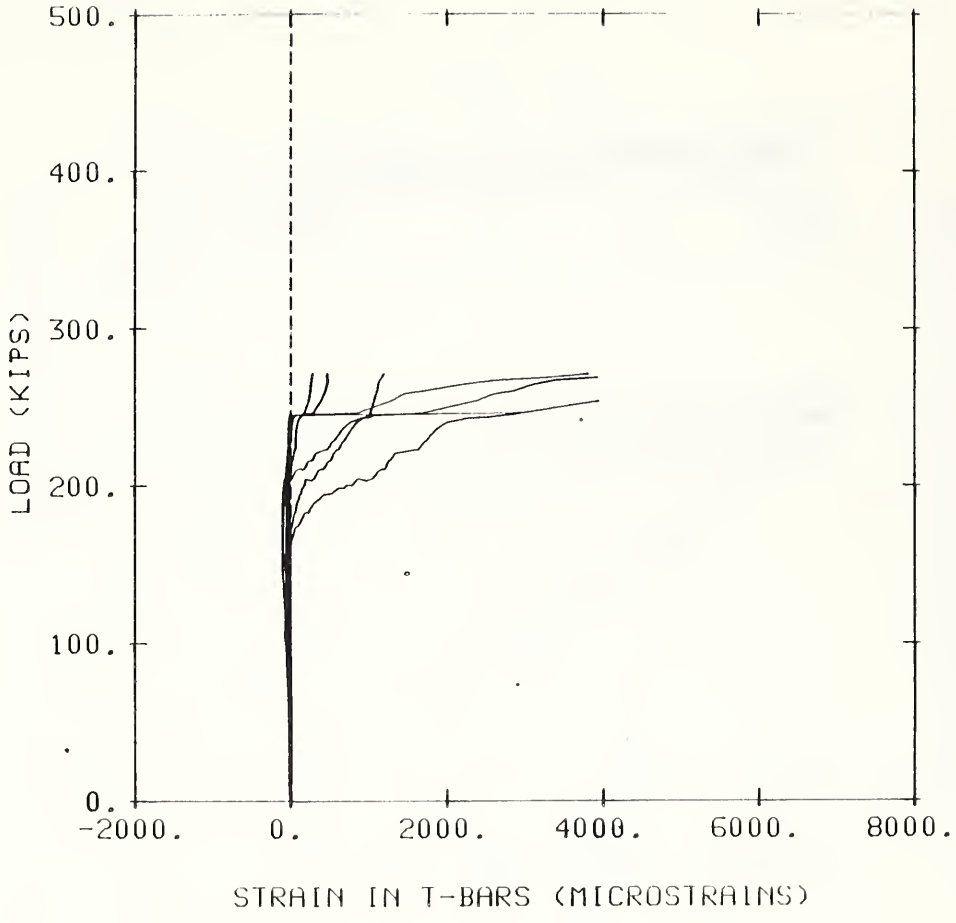

Figure 3.53 Load-Strain Curves for Gaged Shear Bars of 4FP2-1

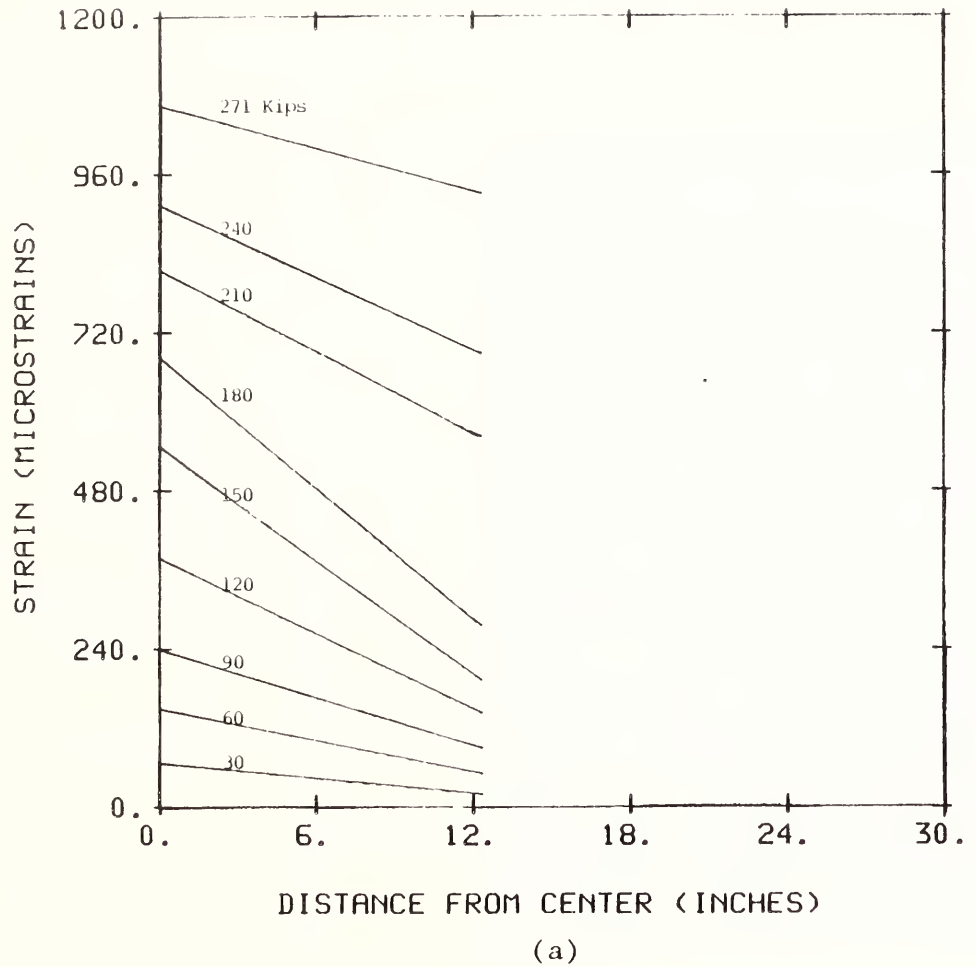

(a)

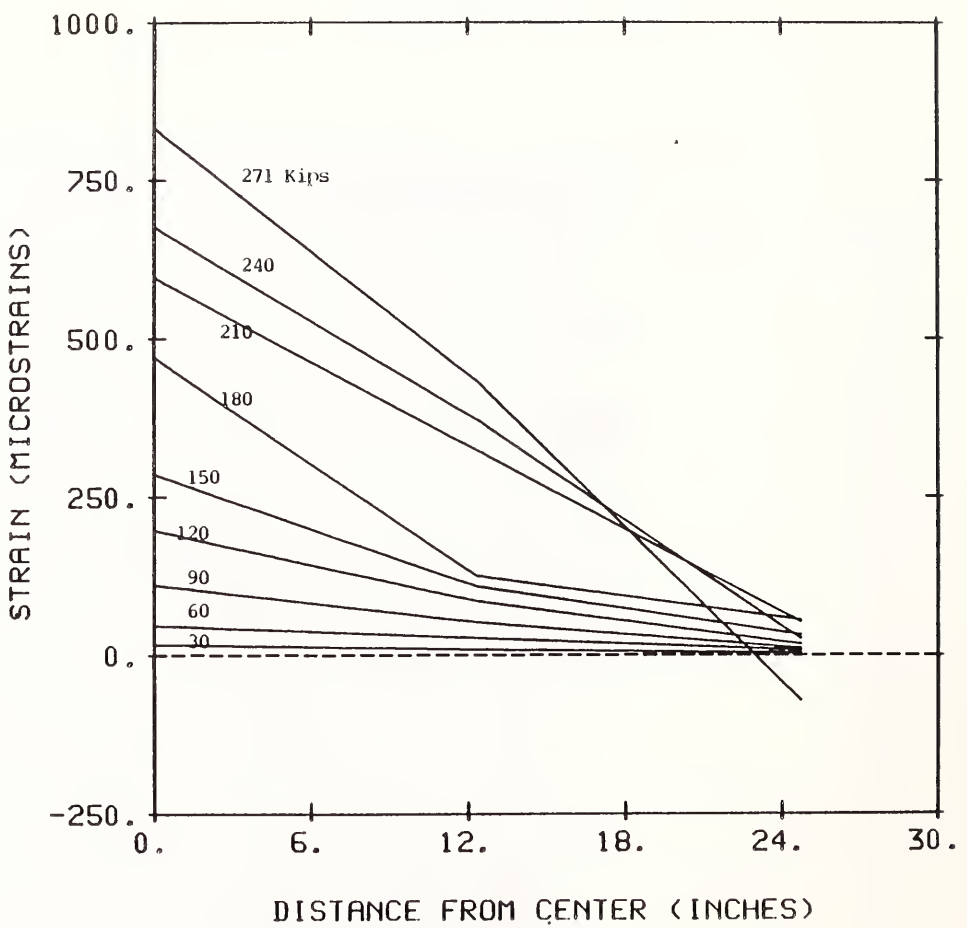

(b)

Figure 3.54 Flexural Strain Profiles of the Tension Reinforcement in 4FP2-1
(a) in Span Direction
(b) in Transverse Direction

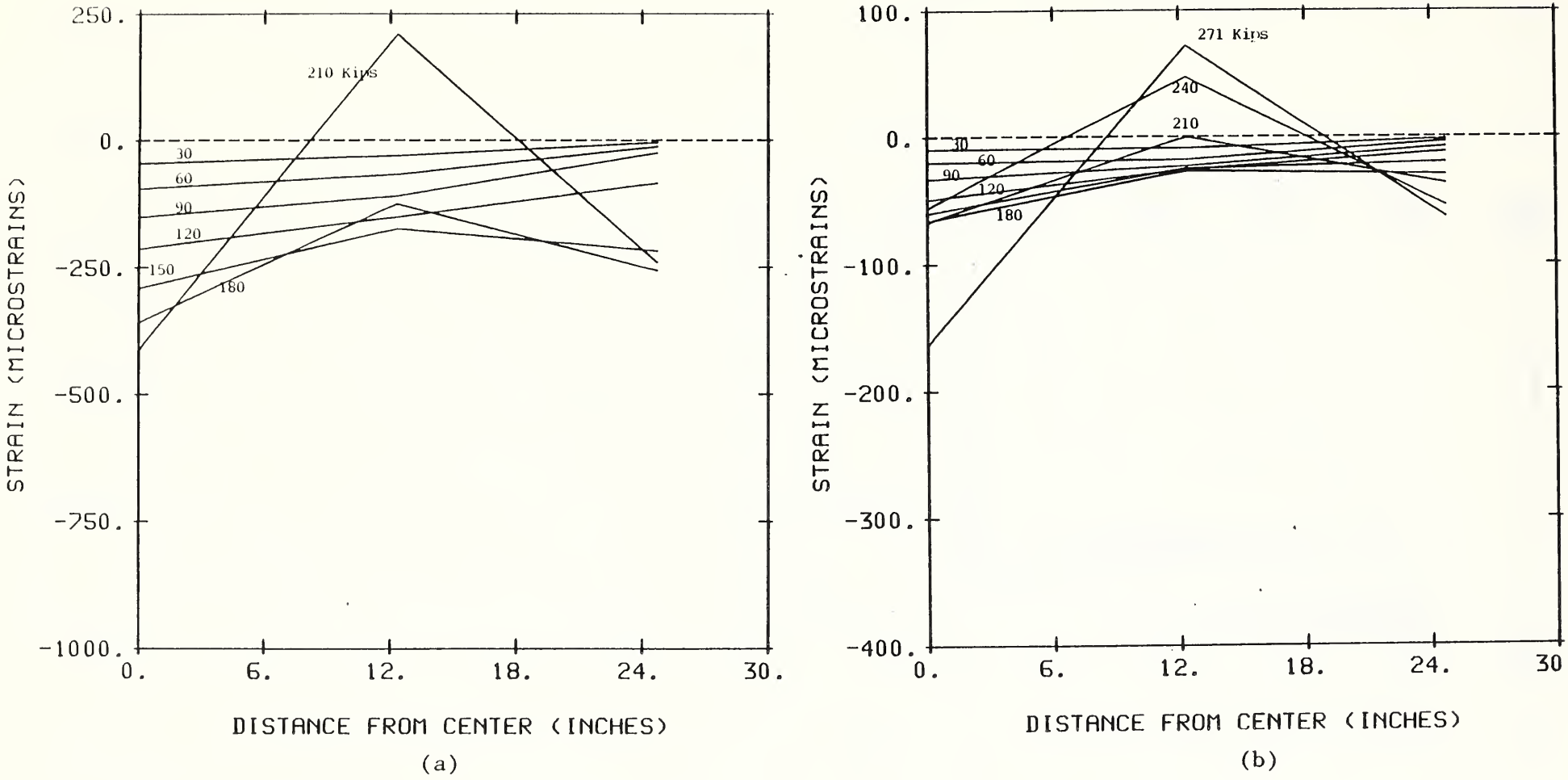

Figure 3.55 Flexural Strain Profiles of the Compression Reinforcement in 4FP2-1
(a) in Span Direction
(b) in Transverse Direction

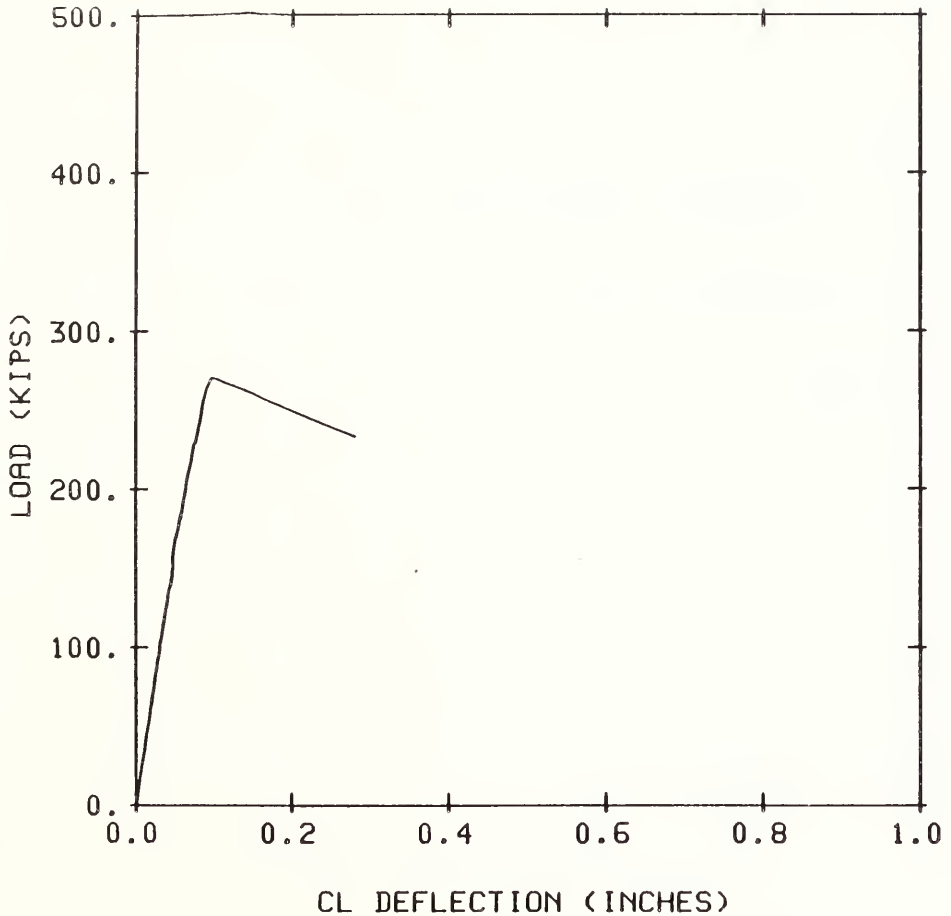

Figure 3.56 Load-Center Deflection Curve of Specimen 4FP2-2

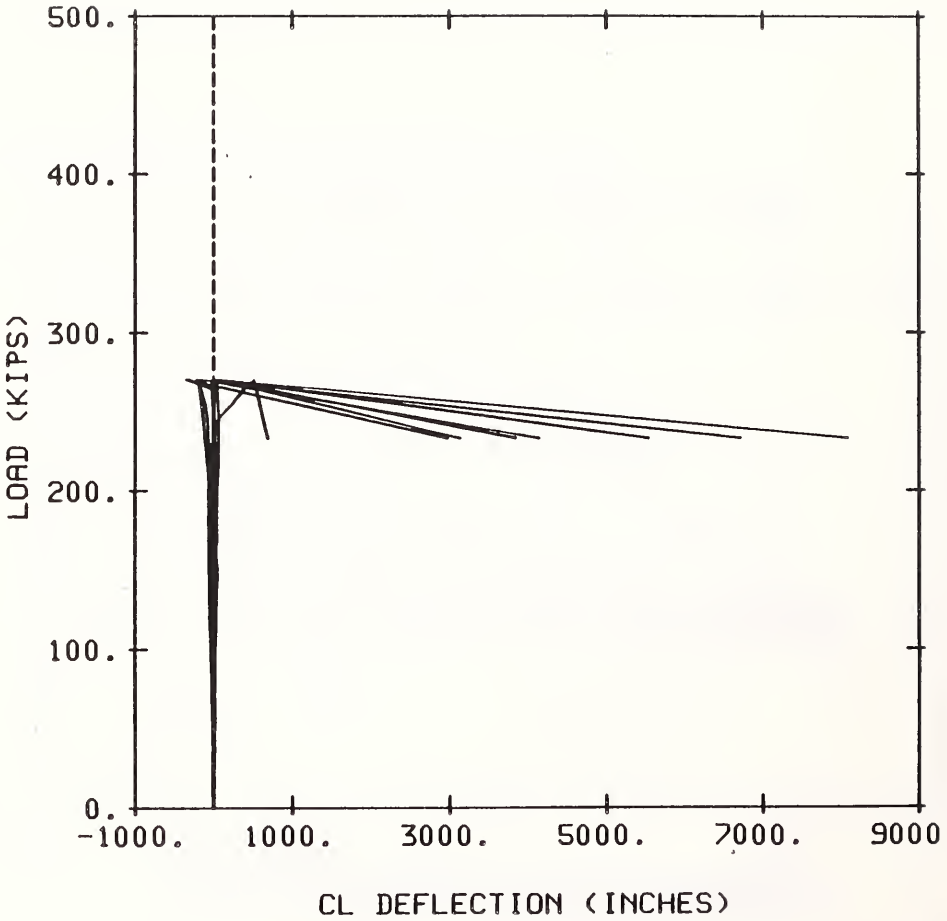

Figure 3.57 Load-Strain Curves for Gaged Shear Bars in 4FP2-2

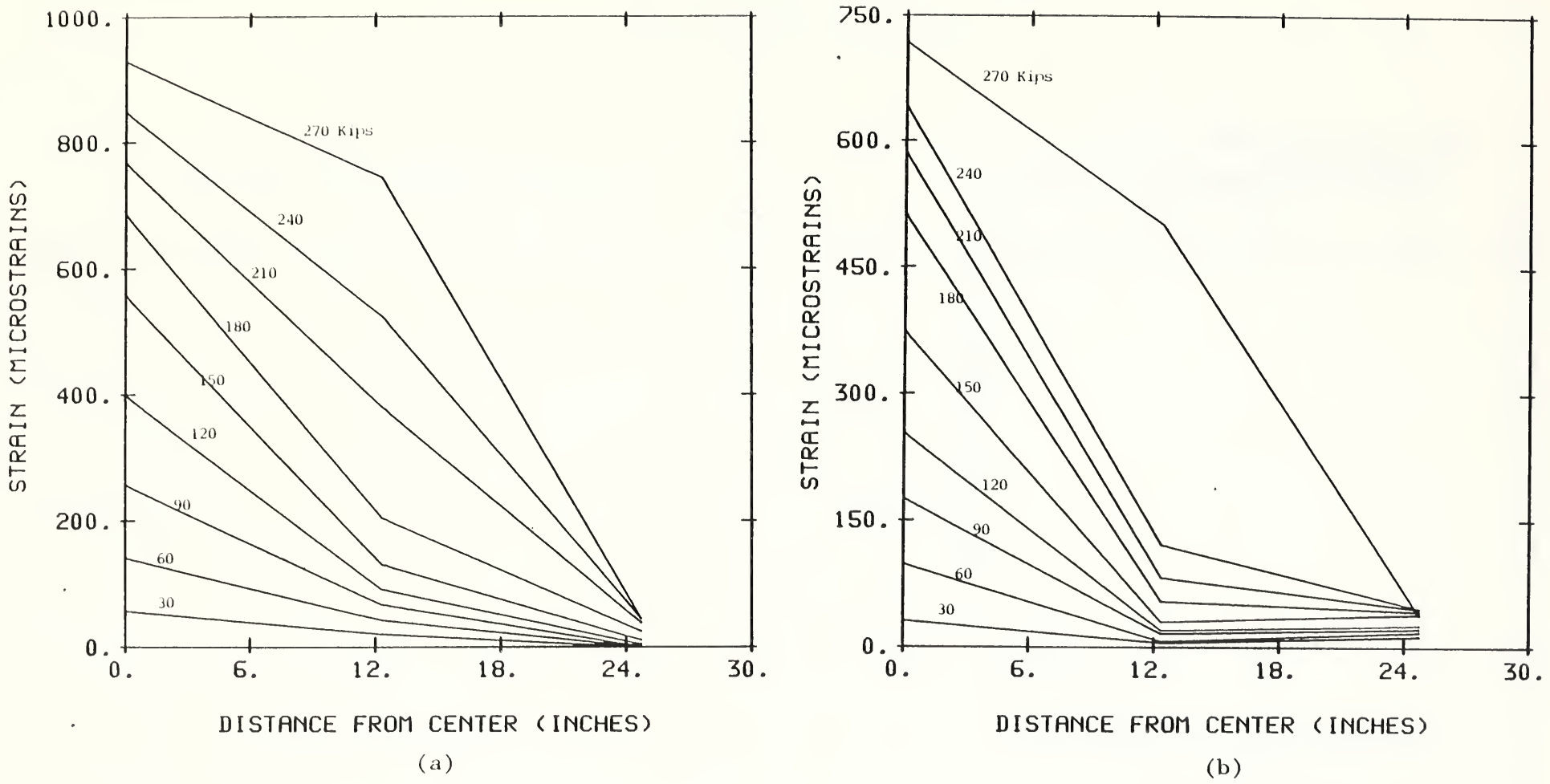

Figure 3.58 Flexural Strain Profiles of the Tension Reinforcement in 4FP2-2
(a) in Span Direction
(b) in Transverse Direction

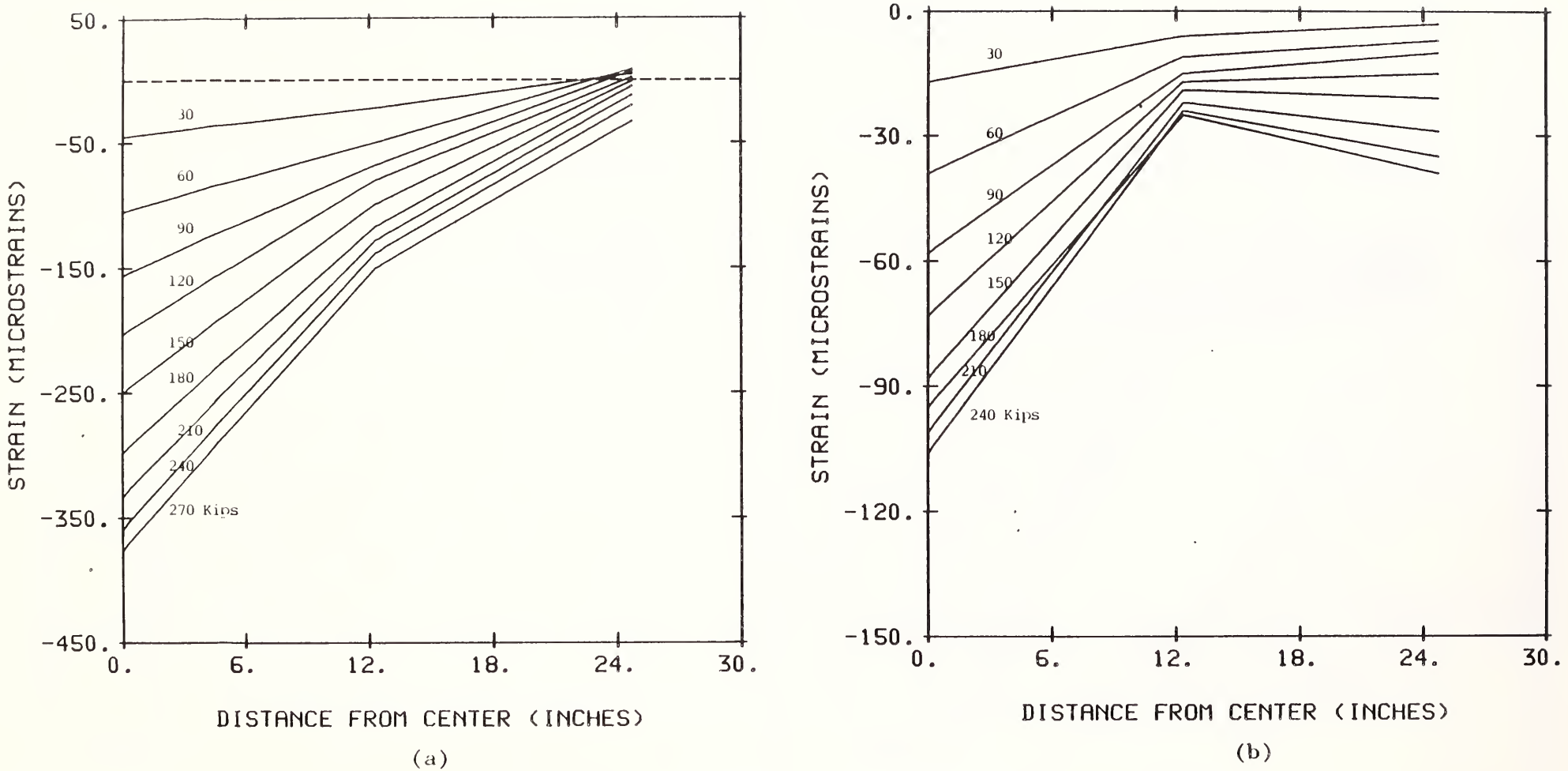

Figure 3.59 Flexural Strain Profiles of the Compression Reinforcement in 4FP2-2
(a) in Span Direction
(b) in Transverse Direction

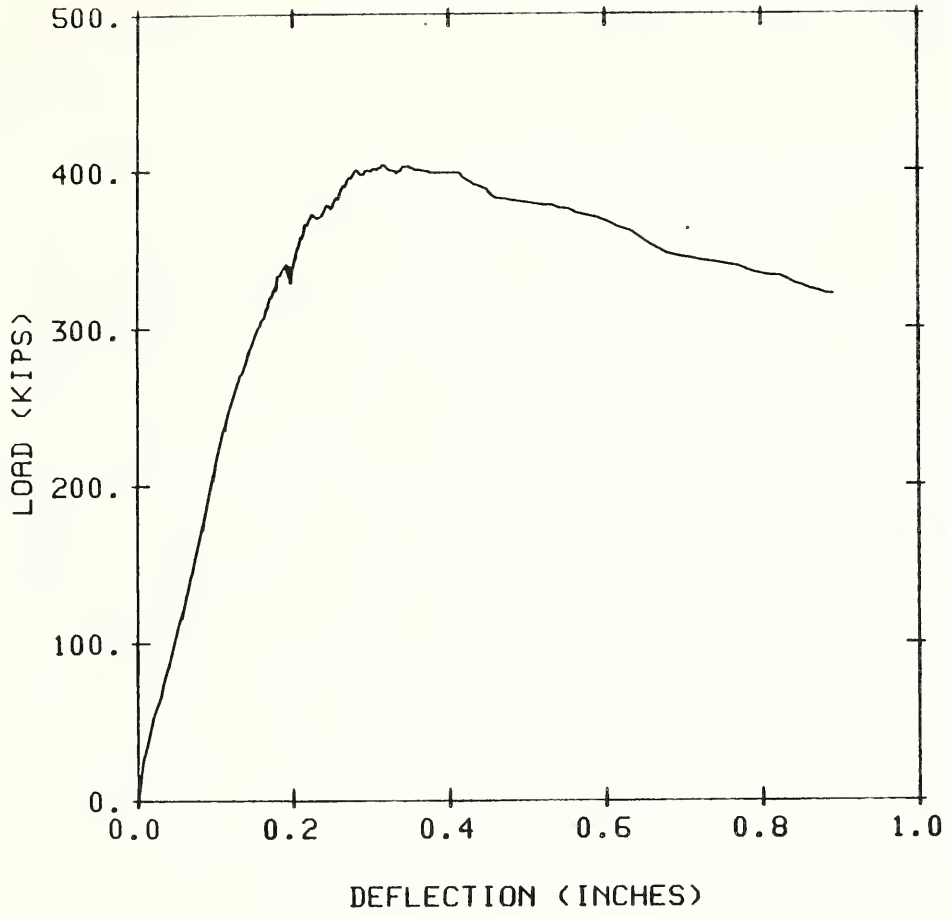

Figure 3.60 Load-Center Deflection Curve of Specimen 4FP3

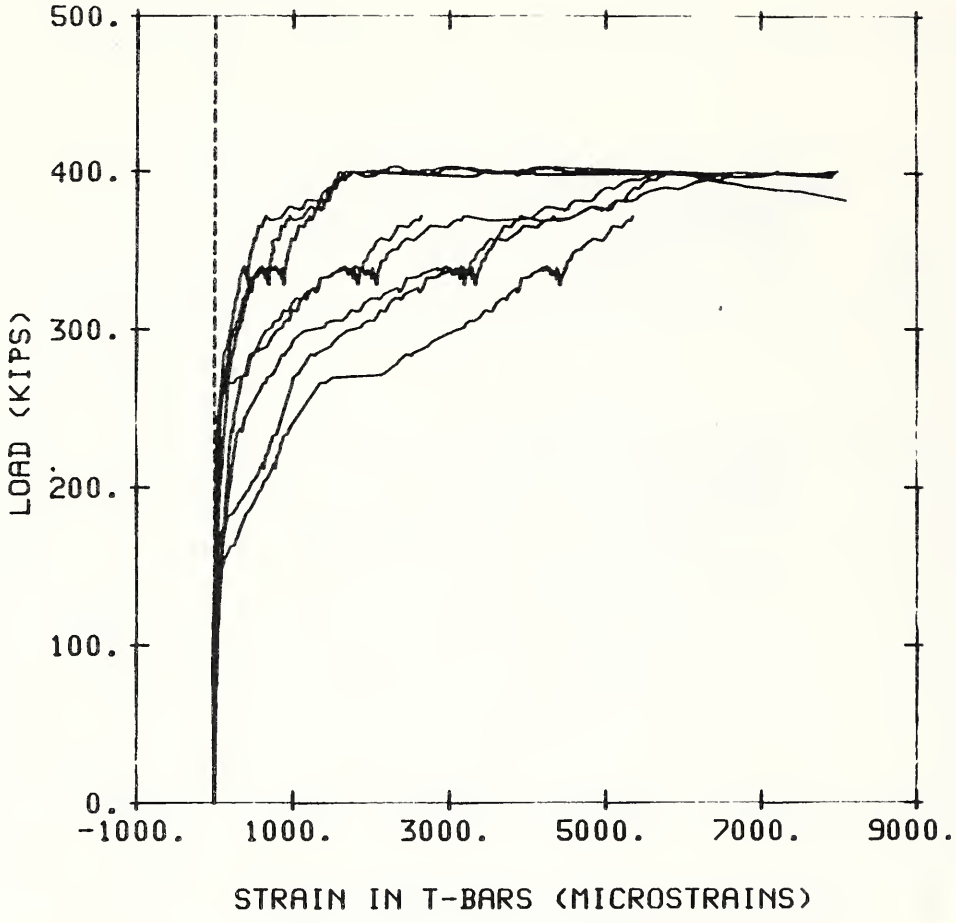

Figure 3.61 Load-Strain Curves for Gaged Shear Bars in 4FP3

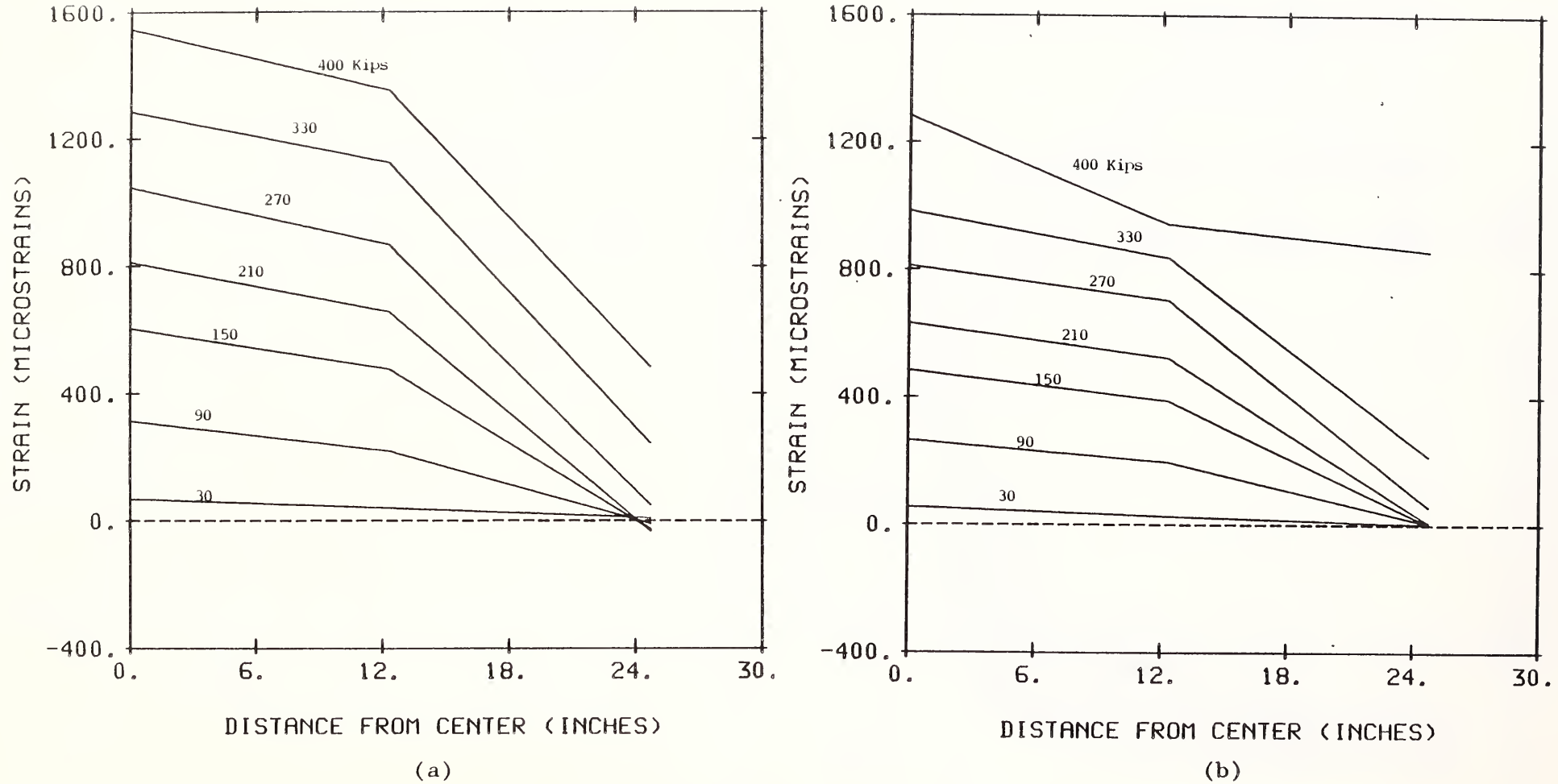

Figure 3.62 Flexural Strain Profiles of the Tension Reinforcement in 4FP3
(a) in Span Direction
(b) in Transverse Direction

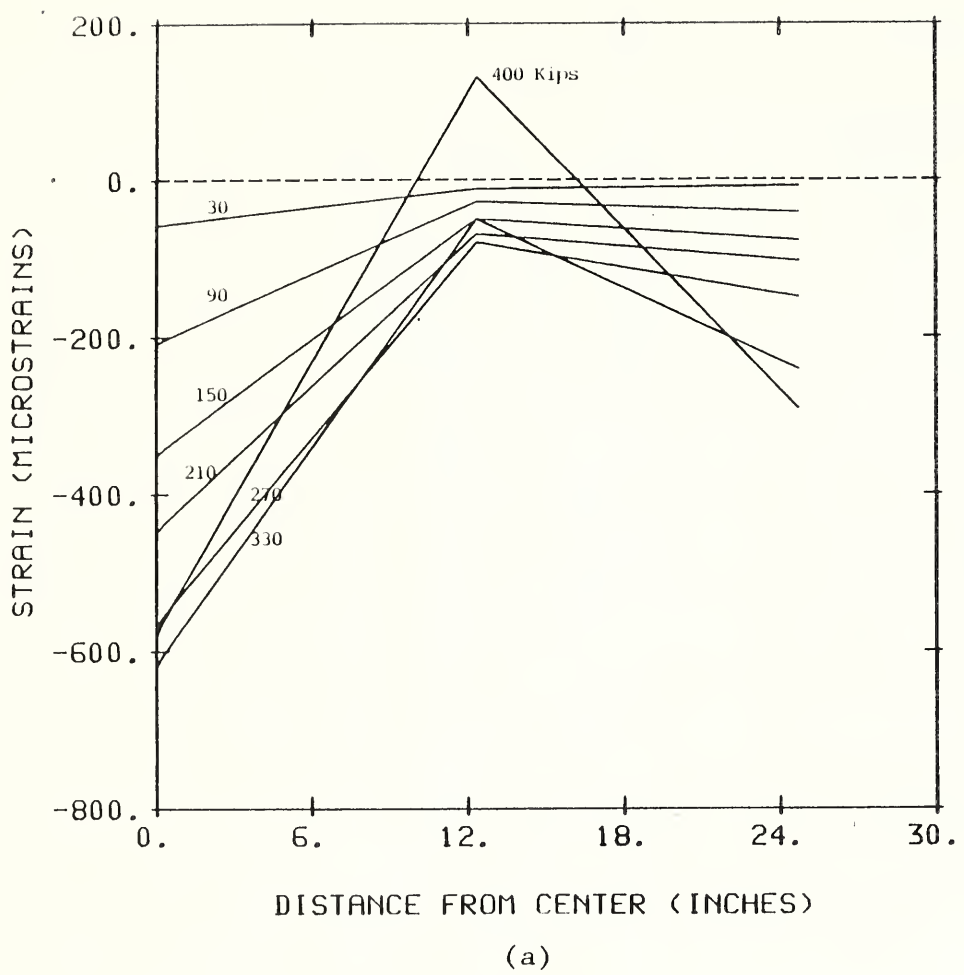

(a)

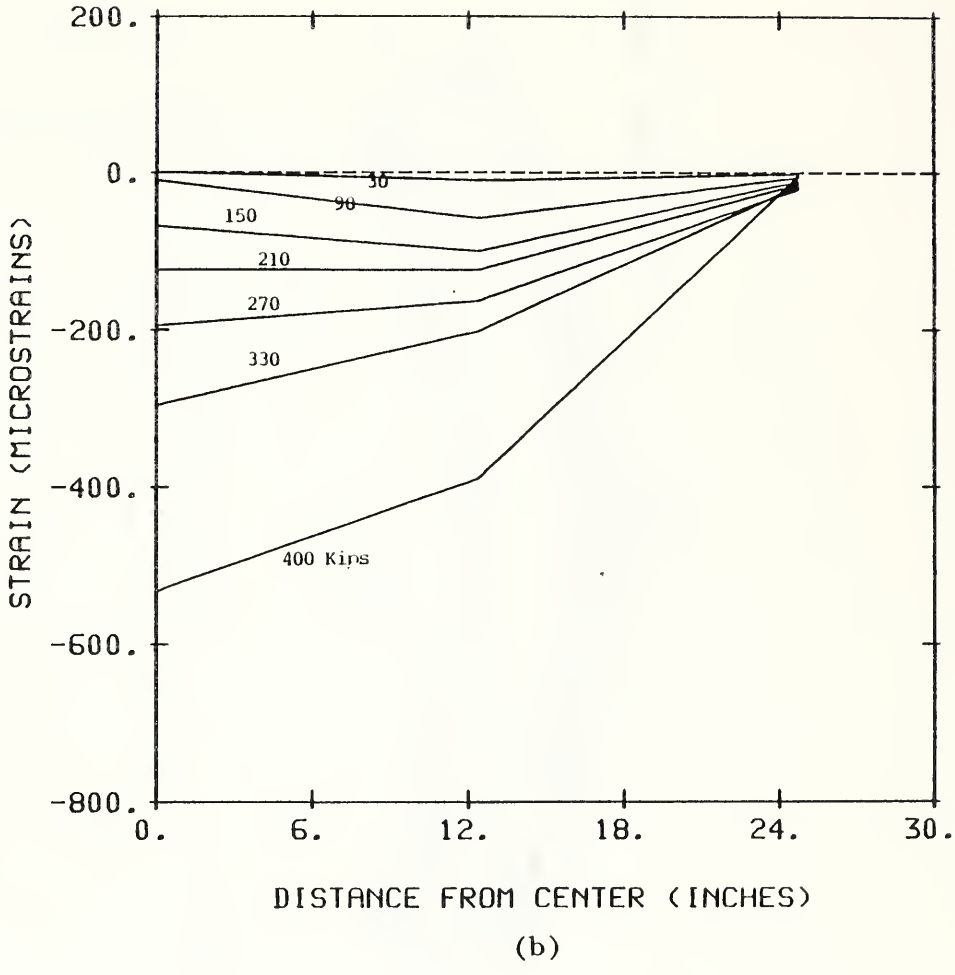

(b)

Figure 3.63 Flexural Strain Profiles of the Compression Reinforcement in 4FP3
(a) in Span Direction
(b) in Transverse Direction

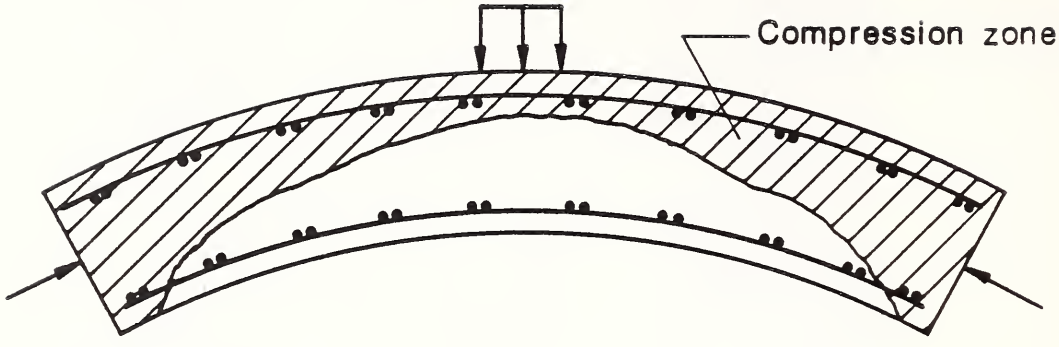

Figure 4.1 Idealized Compression Zone in Shell Specimens

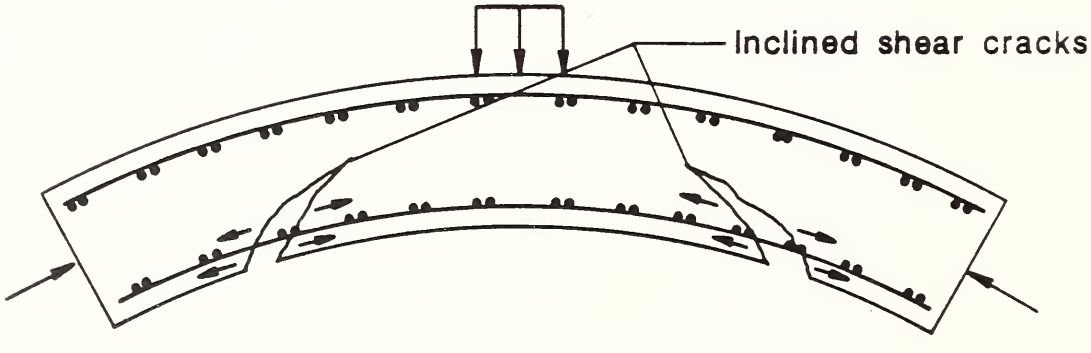

Figure 4.2 Effect of Inclined Shear Cracks in Shells

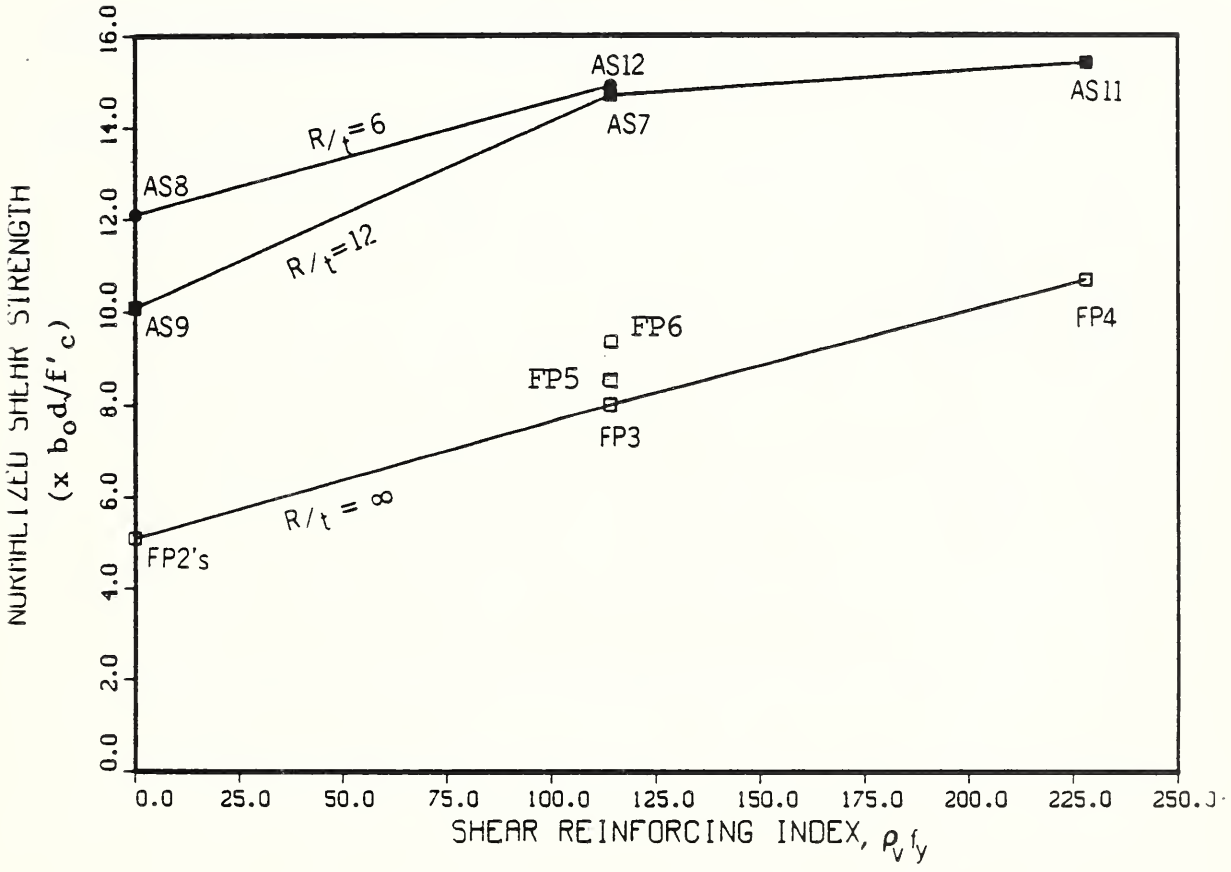

Figure 5.1 Normalized Shear Strength versus Shear Reinforcement Index

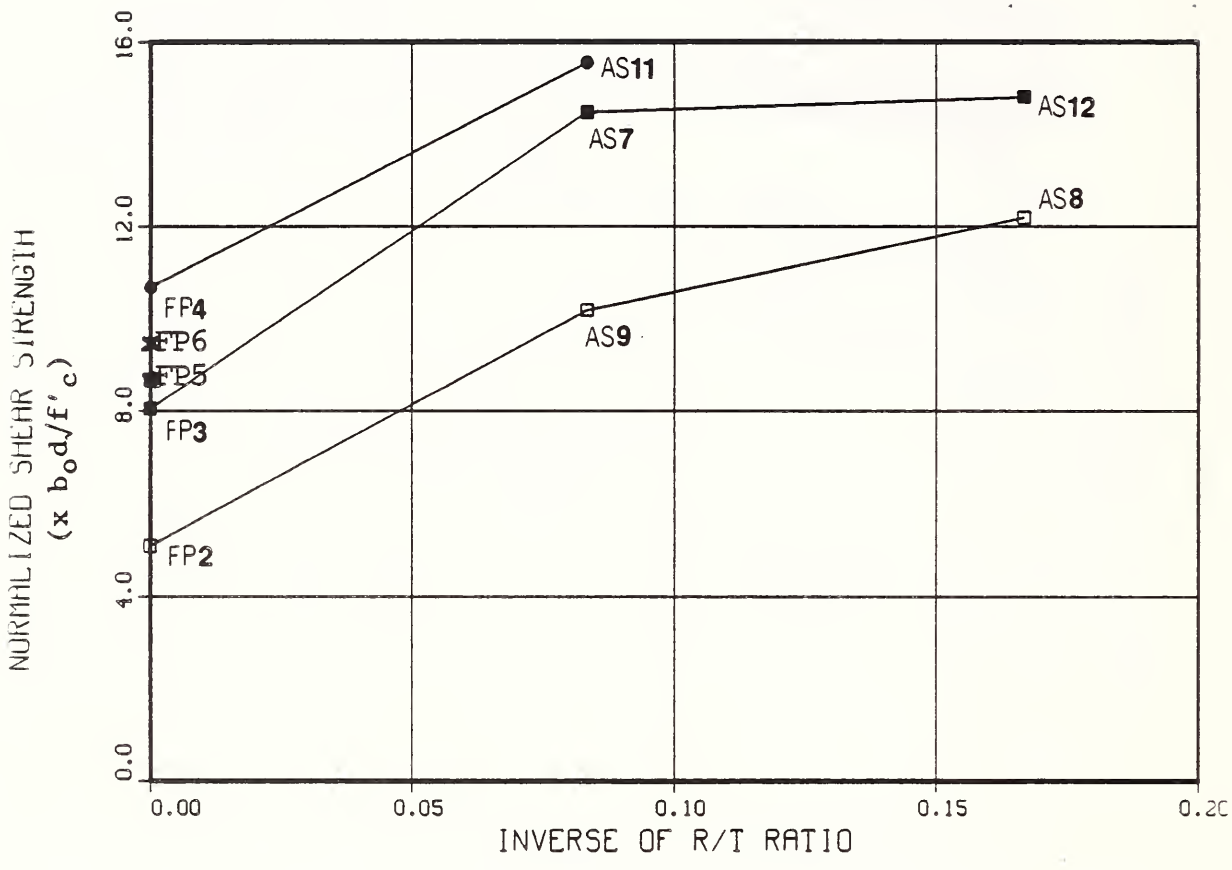

Figure 5.2 Normalized Shear Strength versus Inverse of R/t Ratios

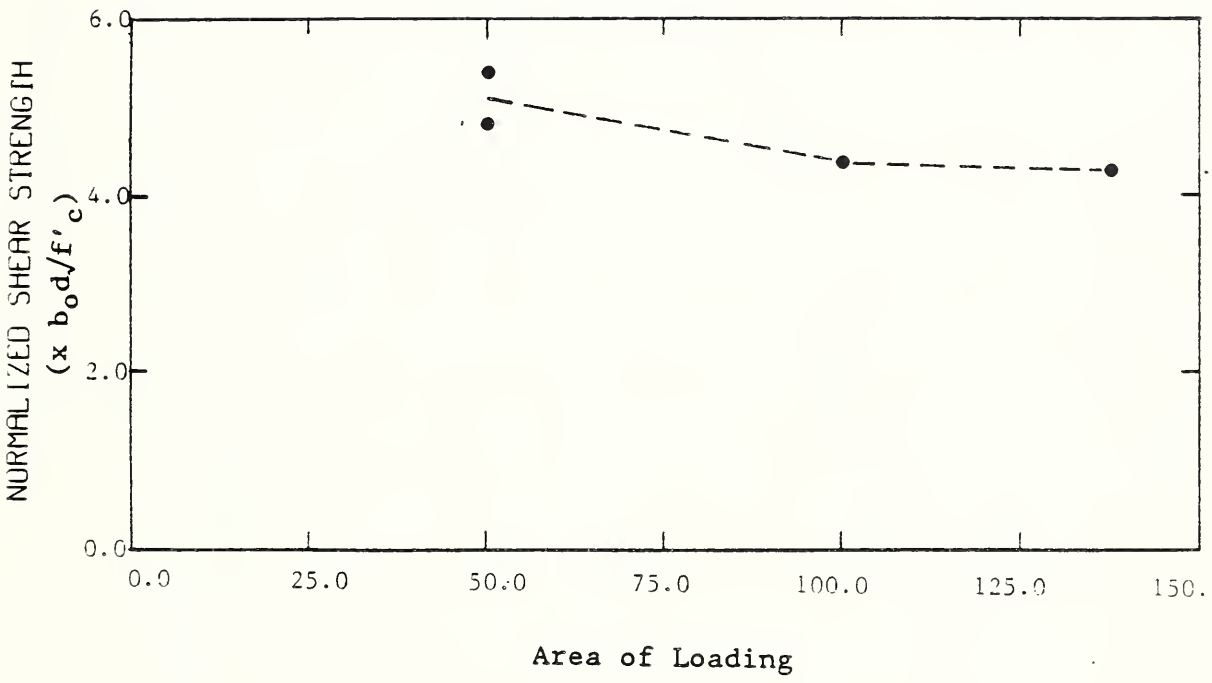

Figure 5.3 Normalized Shear Strength versus Area of Loading

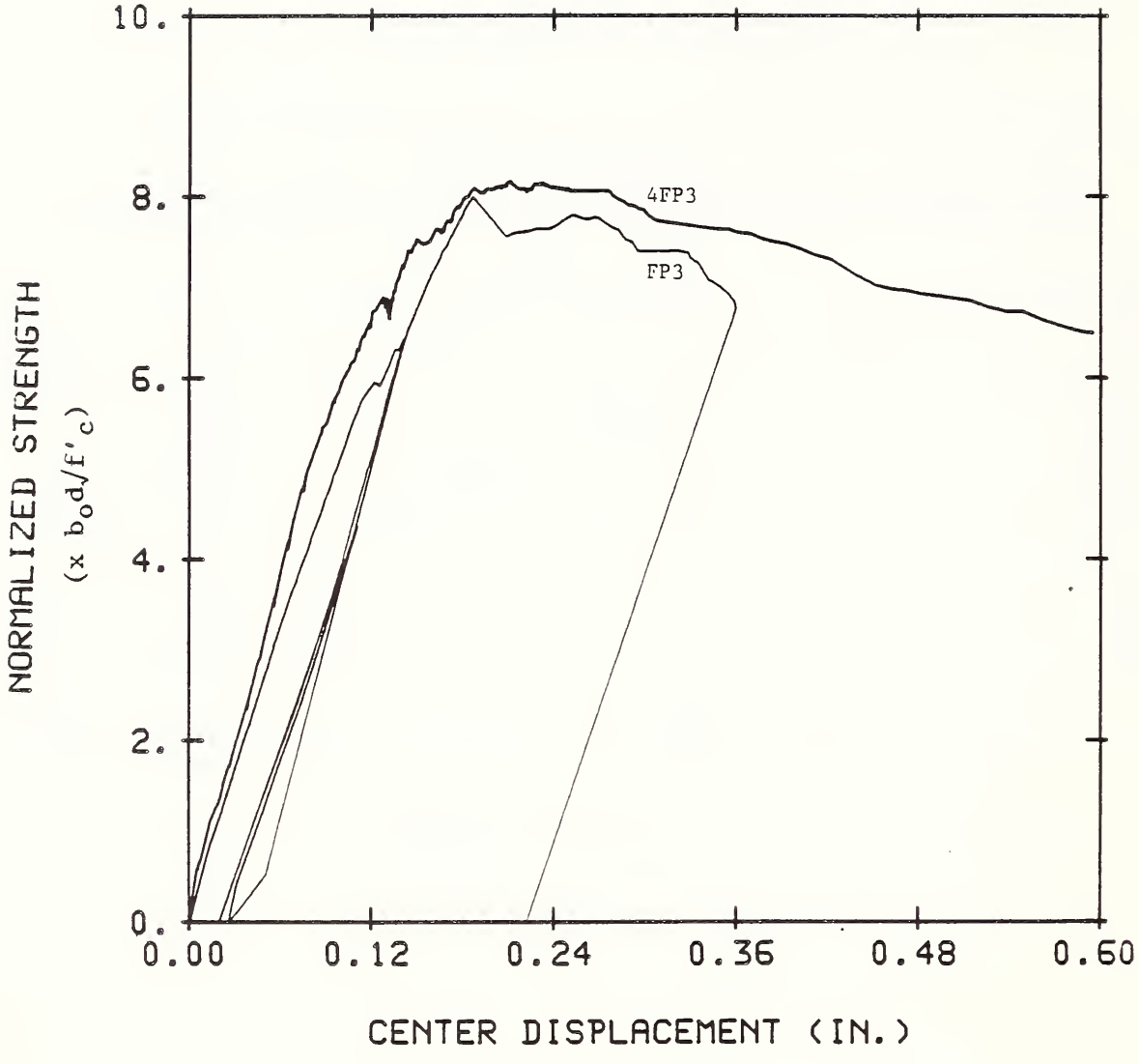

Figure 5.4 Comparison between Normalized Shear Strength-Displacement Relationships of Specimens FP3 and 4FP3

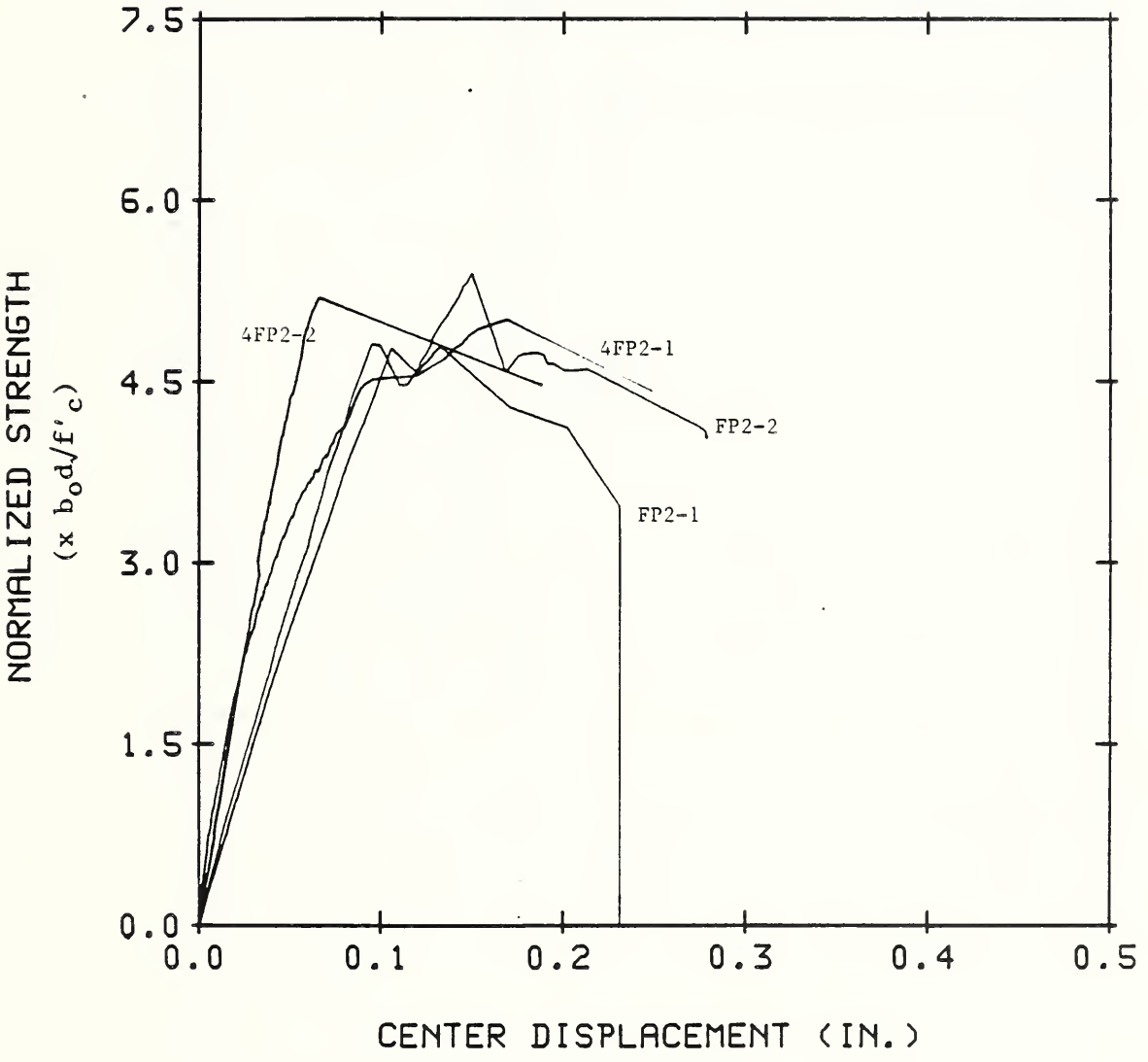

Figure 5.5 Comparison between Normalized Shear Strength-Displacement Relationships of Specimens FP2s and 4FP2s

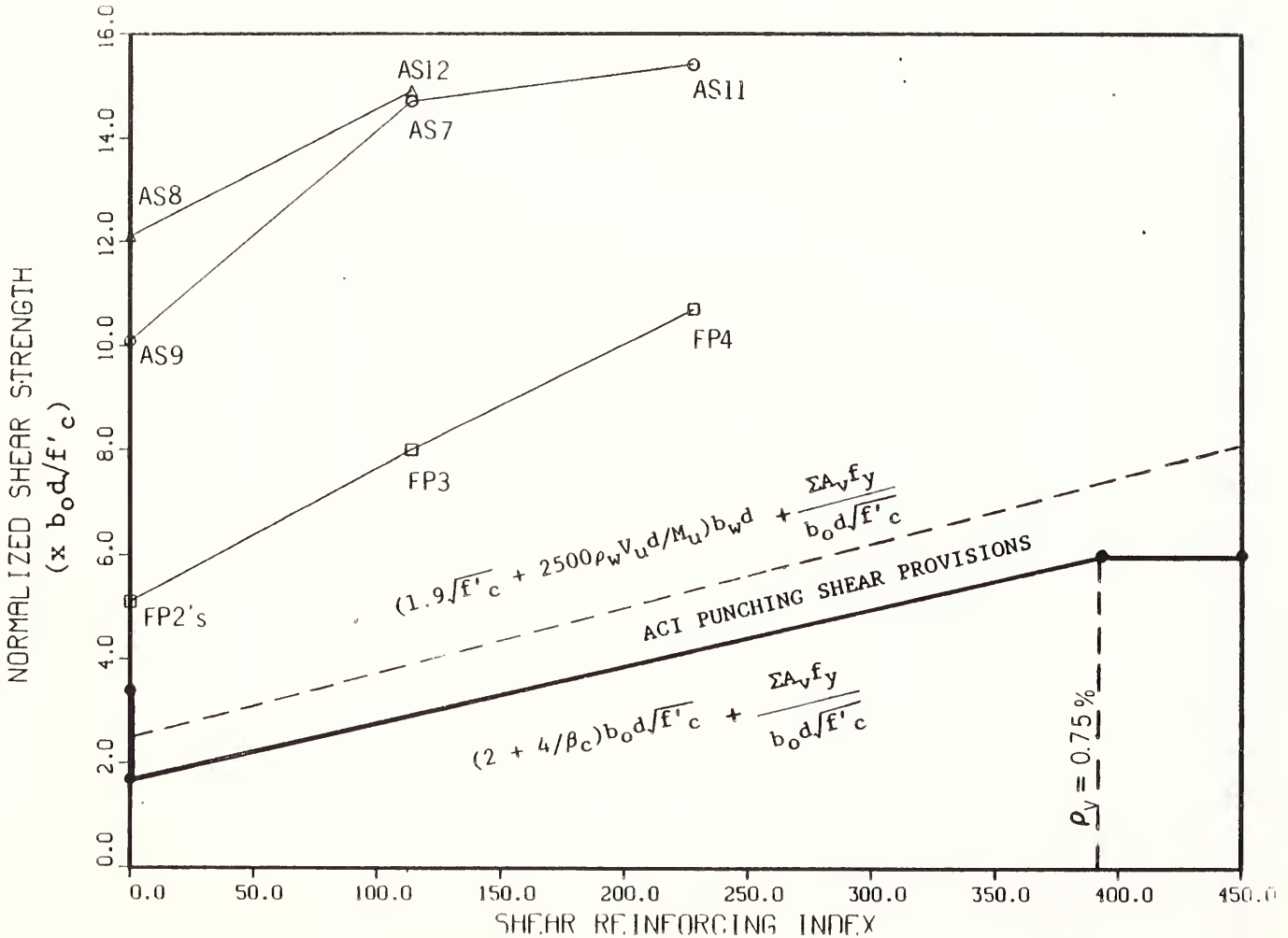

Figure 6.1 Comparison of Test Results and the ACI Predictions in terms of Shear Reinforcing Index ($\rho_v f_y$)

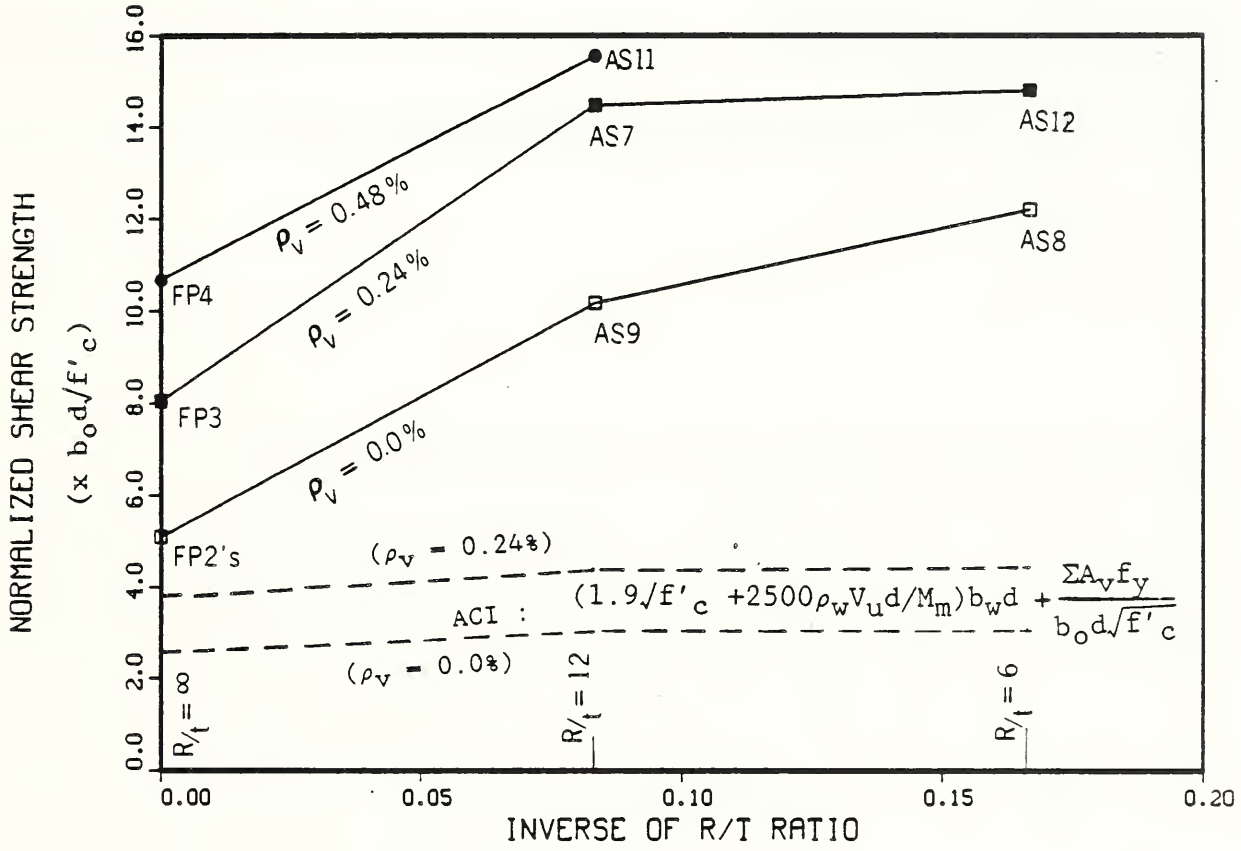

Figure 6.2 Comparison of Test Results and the ACI Predictions in terms of Curvature (t/R Ratio)

NBS-114A (REV. 2-8C)

U.S. DEPT. OF COMM. **BIBLIOGRAPHIC DATA SHEET** *(See instructions)*	1. PUBLICATION OR REPORT NO. NISTIR 88-4007	2. Performing Organ. Report No.	3. Publication Date NOVEMBER 1988

4. TITLE AND SUBTITLE

PUNCHING SHEAR RESISTANCE OF LIGHTWEIGHT CONCRETE OFFSHORE STRUCTURE FOR THE ARCTIC: RESULTS OF EXPERIMENTAL STUDY

5. AUTHOR(S)

Long T. Phan, H. S. Lew

6. PERFORMING ORGANIZATION *(If joint or other than NBS, see instructions)*

NATIONAL BUREAU OF STANDARDS
U.S. DEPARTMENT OF COMMERCE
GAITHERSBURG, MD 20899

7. Contract/Grant No.

8. Type of Report & Period Covered

9. SPONSORING ORGANIZATION NAME AND COMPLETE ADDRESS *(Street, City, State, ZIP)*

Technology Assessment and Research Branch
Minerals Management Service
U.S. Department of the Interior
Reston, VA 22091

10. SUPPLEMENTARY NOTES

☐ Document describes a computer program; SF-185, FIPS Software Summary, is attached.

11. ABSTRACT *(A 200-word or less factual summary of most significant information. If document includes a significant bibliography or literature survey, mention it here)*

This report presents the results of the experimental investigation on punching shear behavior of heavily reinforced, thick, lightweight concrete plates and shells. Eighteen concrete plate and shell specimens of 1/6- and 1/4-scale were tested. These were designed to represent typical panels of the perimeter walls of Arctic offshore structures. The specimens were subjected to high-intensity, concentrated load, applied at the center of each specimen. The results of tests indicated that shear reinforcement ratio (ρ_v) and curvature (R/t ratio) are the two most influencing factors affecting the punching shear strength and ductility of the specimens. Prestressing with uniform compressive prestress of 500 psi, either in one or both directions, was found to have very little effect in terms of improving the punching shear capacity of the specimens. Further, unlike the plates where ultimate punching shear failures were preceded by yielding of shear reinforcement on the crack surfaces, the presence of curvature-induced membrane compression in shells resulted in brittle failure which was caused by compression failure of concrete in the compression zone. More importantly, the test results showed that the current ACI Code provisions for punching shear are extremely conservative in predicting the punching shear strength of the specimens of this test program.

12. KEY WORDS *(Six to twelve entries; alphabetical order; capitalize only proper names; and separate key words by semicolons)*

Arctic offshore structures; experimental study; lightweight concrete; prestressing; punching shear; prototype; reinforced concrete; scale models.

13. AVAILABILITY

☐ Unlimited
☒ For Official Distribution. Do Not Release to NTIS
☐ Order From Superintendent of Documents, U.S. Government Printing Office, Washington, D.C. 20402.
☐ Order From National Technical Information Service (NTIS), Springfield, VA. 22161

14. NO. OF PRINTED PAGES 176

15. Price

USCOMM-DC 6043-P80